

**Surface Chemistry of  
Hexacyclic Aromatic Hydrocarbons  
on (2×1) and Modified Surfaces of Si(100)**

by

Qiang Li

A thesis  
presented to the University of Waterloo  
in fulfillment of the  
thesis requirement for the degree of  
Doctor of Philosophy  
in  
Chemistry

Waterloo, Ontario, Canada, 2004

© Qiang Li 2004

I hereby declare that I am the sole author of this thesis. This is a true copy of the thesis, including any required final revisions, as accepted by my examiners.

I understand that my thesis may be made electronically available to the public.

## Abstract

Room-temperature chemisorption of hexacyclic aromatic hydrocarbons on the  $2\times 1$ , sputtered, oxidized and H-terminated Si(100) surfaces, as well as those upon post treatments of hydrogenation, oxidization and electron irradiation have been investigated by using thermal desorption spectrometry (TDS), Auger electron spectroscopy (AES) and low energy electron diffraction (LEED). This work focuses on the effects of the functional groups (phenyl, methyl, vinyl, heteroatom, and H atom) in the chemisorbed aromatic hydrocarbons (benzene, toluene, xylene isomers, styrene and pyridine) on organic functionalization of the Si(100) surface, particularly on such surface processes as cycloaddition, dative adsorption, hydrogen abstraction, desorption, dissociation, diffusion, and condensation polymerization. Unlike the earlier notion that hydrogen evolution in the hydrocarbon/Si(100) systems is the result of hydrocarbon dissociation (into smaller hydrocarbon fragments and H atoms) on the surface, condensation polymerization of the adsorbed aromatic hydrocarbons is proposed in the present work, in order to explain the higher-temperature hydrogen evolution feature in the toluene/Si(100) system. This hypothesis is supported by our TDS results for other hydrocarbon adsorbates, especially in the pyridine/Si(100) system where electron-induced condensation polymerization has been observed at room temperature. The improved techniques in the TDS experiments developed in the present work have enabled us to observe condensation polymerization and the effect of H on the surface processes (via surface reconstruction) on Si(100) for the first time. New analysis methods have also been developed to determine the adsorption coverage from the AES data, and this work has not only improved the accuracy of the elemental-coverage evaluation, but also provided a means to estimate the rate and the order of chemisorption. By using the density functional theory with the Gaussian 98 program, the adsorption geometries and the corresponding adsorption energies of various adsorption phases have been calculated. These computational results have provided useful insights into the chemisorption structures on the Si(100) surface. The present work also presents the development of three kinetics models for hydrogen evolution in the aforementioned aromatic-hydrocarbon systems on Si(100). Based on a modified collision theory with consideration of diffusion, these theoretical models have proven to be quite successful in simulating the observed TDS profiles and in estimating the kinetic

parameters for the analysis of condensation polymerization in 2-dimensional diffusion systems. The present work illustrates that TDS experiments can be used effectively with quantum computation and theoretical kinetics modelling to elucidate the intricate nature of organosilicon surface chemistry.

## Acknowledgements

I am extremely grateful to my supervisor, Dr. K.T. Leung, for his kind support and encouragement during my work. His tireless guidance and great patience are indispensable to my successful completion of my Ph.D. study and research. I would also like to thank the members of my Ph.D. Advisory Committee, Dr. Dan Thomas, Dr. Jean Duhamel and Dr. Bruce Torrie for their helpful advice and information during my studies. Dr. Thomas' lecture had offered me a nice tour guide during my first journey in the beautiful world of Surface Science. I would express my thanks to all the members of WEPIL for their friendship and assistance. Thanks to Dr. Shihong Xu and Xiaojin Zhou for their help in proofreading my thesis. Thanks to Zhenhua He and Sergey Mitlin for their insightful discussions on the research problems. Thanks to Xiang Yang for his help in my computational study. Thanks to Dr. Nina Heinig and Qiang Gao for letting me feel at home. I would also like to thank the former coworkers in the lab, Dr. Hui Yu and Xiang He for their help in the experimental and software development. Thanks should also go to the entire staff of the Science Shops for their dedication in providing technical support that made this work possible. I do not know how I could have made it through the low points without my wife, Chunling, she is simply the best. To my parents and sister Lan, I would like to say thank you for everything you have done for me. Special thanks must go to my friends, Lili Zheng, Grace Yin, Jingying Yin, Ben Yang, Benda Liu, Yan Wu and their families. They let me have a good time in Kitchener-Waterloo. I should also thank Jilan Qi, Ling Nie and Jingyu Li for their kind help when I came to Canada.

This work was supported financially by the Natural Sciences and Engineering Research Council of Canada.

To my wife Chunling

## Table of Contents

Abstract.....	iii
Acknowledgements.....	v
Table of Contents.....	vii
List of Figures.....	x
List of Tables.....	xvii
Chapter 1 Introduction.....	1
1.1 Organic functionalization of semiconductors.....	1
1.2 Properties of the Si(100) substrate.....	2
1.3 Cycloaddition chemistry of alkenes on Si(100)2×1 surface.....	4
1.4 Aromatic hydrocarbons on 2×1 and modified surfaces of Si(100).....	7
1.5 Surface analysis techniques.....	9
1.5.1 Thermal desorption spectrometry.....	9
1.5.2 Auger electron spectroscopy, and low energy electron diffraction.....	12
1.6 Experimental details.....	13
1.6.1 UHV chamber and instrumentation.....	13
1.6.2 Development of the thermal desorption spectrometry system.....	15
1.6.3 Sample preparation and cleaning.....	20
1.6.4 Computational studies and kinetics modelling.....	21
1.7 Structure of this thesis.....	22
1.8 References.....	23
Chapter 2 Thermal chemistry of toluene and benzene on Si(100)2×1 and modified surfaces.....	27
2.1 Introduction.....	27
2.2 Results and Discussion.....	28
2.2.1 Room-temperature adsorption at various exposures.....	28
2.2.2 Hydrogen evolution.....	38
2.2.3 Effects of surface condition on thermal chemistry.....	41
2.2.4 Surface-mediated oxidation reaction.....	43
2.3 Concluding remarks.....	45

2.4	References.....	49
Chapter 3	Effects of methyl substitution on room-temperature chemisorption of <i>para</i> -xylene on Si(100)2×1 and modified surfaces: A thermal desorption and DFT study.....	51
3.1	Introduction.....	51
3.2	Results and Discussion .....	52
3.2.1	Molecular desorption .....	52
3.2.2	Hydrogen evolution .....	59
3.2.3	Surface conditions study.....	63
3.2.4	Surface-mediated reactions of <i>p</i> -xylene on Si(100)2×1 post-exposed to atomic H, molecular O <sub>2</sub> and low-energy electrons .....	66
3.3	Concluding remarks.....	69
3.4	Reference .....	73
Chapter 4	Thermal chemistry of styrene on Si(100)2×1 and modified surfaces: Electron-mediated condensation oligomerization, and post-hydrogenation reactions.....	75
4.1	Introduction.....	75
4.2	Results and Discussion .....	76
4.2.1	Room-temperature adsorption at various exposures.....	76
4.2.2	Hydrogen evolution .....	80
4.2.3	Electron irradiation of styrene on Si(100)2×1 .....	85
4.2.4	Surface conditions study.....	88
4.2.5	Surface-mediated hydrogenation reactions.....	90
4.3	Concluding remarks.....	97
4.4	Reference .....	99
Chapter 5	Thermally induced chemistry and electron-mediated processes of pyridine on (2×1) and modified Si(100) surfaces: Evidence of electron-induced condensation oligomerization.....	101
5.1	Introduction.....	101
5.2	Results and Discussion .....	103
5.2.1	Room-temperature adsorption of pyridine on Si(100)2×1 .....	103
5.2.2	Electron irradiation of pyridine on Si(100)2×1 .....	109



5.2.3	Surface condition studies .....	113
5.2.4	Post-adsorption surface-mediated oxidation and hydrogenation reactions .....	121
5.3	Concluding remarks .....	125
5.4	Reference .....	128
Chapter 6	Hydrogen evolution of aromatic hydrocarbons on Si(100) .....	133
6.1	Introduction.....	133
6.1.1	Hydrogen on Si(100)2×1: Adsorption, surface phases, diffusion and desorption.....	133
6.1.2	Hydrogen evolution in chemisorption systems of aromatic hydrocarbons on Si(100)2×1.....	135
6.2	Model I: hydrogen evolution from the vinyl group in styrene on Si(100)2×1 ..	138
6.3	Model II: hydrogen evolution from the methyl group in methyl-substituted aromatic hydrocarbons (toluene, xylene) on Si(100)2×1 .....	146
6.4	Model III: hydrogen evolution from the phenyl group - condensation polymerization and the collision theory for 2-dimensional diffusion systems..	151
6.5	Summary.....	162
6.6	References.....	164
Chapter 7	Concluding remarks and future outlook .....	167
Appendix A	Study of adsorption by Auger Electron Spectroscopy .....	173
Appendix B	Wepil_TDS - A self-developed software for TDS.....	185
Appendix C	Derivation of the equilibrium equation for surface adspecies .....	193

## List of Figures

Figure 1-1	The Si(100)-(2×1) Reconstruction: Comparison of (a) an unreconstructed Si(100) surface and (b) the more thermodynamically stable (2×1) reconstructed surface. WWW Picture Gallery based on the Surface Structure Database (SSD, NIST Standard Reference Database 42).....	3
Figure 1-2	Buckled Si(100)2×1 structure (unit-Å) obtained by using Gaussian 98 calculations with (a) a 3-dimer model (Si <sub>21</sub> H <sub>20</sub> ), and (b) a 1-dimer model (Si <sub>9</sub> H <sub>12</sub> ). (See Section 1.6.4).....	5
Figure 1-3	Cycloaddition reactions of alkenes: (a) The [2+2] cycloaddition between two alkenes forms a four-membered ring, and (b) [4+2] cycloaddition between an alkene and a diene forms a six-membered ring. The designations refer to the number of π electrons involved in the reaction.....	6
Figure 1-4	Cycloaddition reactions of hydrocarbons on Si(100)2×1: (a) [2+2] cycloaddition of styrene/Si(100)2×1, (b) [2+2] cycloaddition of benzene/Si(100)2×1, and (c) [4+2] cycloaddition of benzene/Si(100)2×1.....	8
Figure 1-5	Experimental setup - UHV chamber, apparatus and electronics.....	14
Figure 1-6	Schematic diagram of TPD experiment. A home-made digital signal processing (DSP) box is used to control the temperature by manipulating the “on-off” ratio of the AC power supply for sample heating, with a typical proportional-integral-differential (PID) algorithm. The computer is programmed to communicate with both the mass spectrometer and the DSP unit for data abstraction, display, storage, analysis, and system control. ....	15
Figure 1-7	Experimental setup for thermal desorption spectrometry with a differentially pumped quadrupole mass spectrometer. ....	16
Figure 1-8	A typical temperature ramping curve as a linear function of time. The error ΔT corresponds to the difference in temperature between the experiment and the predicted value. ....	17
Figure 1-9	The cracking pattern of toluene obtained by using our mass spectrometry. ....	19
Figure 2-1	Thermal desorption profiles of (a) Mass 92 (molecular toluene) and (b) Mass 78 (molecular benzene) as a function of room-temperature exposure of toluene and	

	benzene to Si(100)2×1. The desorption intensity of toluene is found to be considerably smaller than that of benzene. ....	29
Figure 2-2	Stable undissociated configurations for chemisorption of benzene on Si(100): (a) 1,4-single-dimer configuration, (b) 1,2-single-dimer configuration, (c) tight bridge double-dimer configuration, and (d) twisted bridge configuration. (White, black, and gray balls indicate H, C, and Si atoms, respectively.) .....	31
Figure 2-3	Carbon moiety as reflected by the peak-to-peak intensity ratio for the C(KLL) to Si(LVV) Auger transitions as a function of room-temperature exposure of toluene (triangle) and benzene (circle) to Si(100)2×1. The Auger peak-to-peak ratios for toluene and benzene converge to 11 % and 8 %, respectively, at saturation coverage.....	33
Figure 2-4	(a) Relative carbon moiety change as a function of annealing temperature for a 100 L room-temperature exposure of toluene on Si(100)2×1. (b) Typical lineshapes for the corresponding derivative C(KVV) Auger transitions after annealing the sample in 300-700 K (lower curve) and to 1100 K (upper curve). The lower and upper curves are characteristic of the lineshapes commonly found for SiC and graphite, respectively [24]. .....	35
Figure 2-5	LEED patterns collected at 71 eV electron beam energy for (a) clean Si(100)2×1 at 300 K, (b) the Si(100)2×1 surface exposed to 100 L of toluene at 300 K, followed by annealing to 700 K and (c) 1100 K for 10 minutes. (d) Schematic representation of the LEED pattern shown in (c). .....	37
Figure 2-6	Comparison of the molecular (solid lines) and Mass 4 (dashed lines) thermal desorption profiles of 100 L room-temperature exposures of (a) d <sub>8</sub> -toluene and (b) d <sub>6</sub> -benzene to Si(100)2×1. The parent masses for d <sub>8</sub> -toluene and d <sub>6</sub> -benzene correspond to Mass 100 and Mass 84, respectively. ....	39
Figure 2-7	Comparison of the molecular and Mass 4 TDS profiles for 100 L room-temperature exposures of (d <sub>8</sub> -)toluene to the (a) 2×1, (b) amorphous, (c) oxidized, and (d) H-terminated Si(100). An amorphous Si surface is obtained by ion sputtering in 2×10 <sup>-5</sup> Torr of Argon for 1 hour at 1 keV beam energy. An oxidized Si surface is produced by exposing a clean 2×1 surface with a 300 L exposure of O <sub>2</sub> while a H-terminated Si(100) is prepared by exposing 2000 L of	

	H <sub>2</sub> to a clean 2×1 surface (keep at RT with liquid nitrogen) with a hot W filament positioned 5 cm away, using liquid nitrogen . The parent masses for d <sub>8</sub> -toluene (a, b) and normal toluene (c, d) correspond to Mass 100 and Mass 92, respectively.....	42
Figure 2-8	Comparison of the molecular and Mass 4 thermal desorption profiles of 100 L room-temperature exposures of (a) d <sub>8</sub> -toluene and (b) d <sub>6</sub> -benzene to Si(100)2×1 with (dashed lines) and without (solid lines) 300 L of O <sub>2</sub> post-exposure. The parent masses for d <sub>8</sub> -toluene and d <sub>6</sub> -benzene correspond to Mass 100 and Mass 84, respectively.....	44
Figure 3-1	Relative carbon moiety as indicated by the peak-to-peak intensity ratio for the C(KLL) to Si(LVV) Auger transitions as a function of room-temperature exposure of (a) <i>p</i> -xylene, (b) toluene and (c) benzene to Si(100)2×1. The experimental data are found to follow first-order kinetics.....	53
Figure 3-2	Comparison of thermal desorption profiles of molecular (solid lines) and mass-4 (D <sub>2</sub> ) desorption (dashed lines) for saturation exposures of (a) <i>p</i> -xylene-d <sub>10</sub> , (b) toluene-d <sub>8</sub> , and (c) benzene-d <sub>6</sub> to Si(100)2×1 at room temperature.....	54
Figure 3-3	Schematic diagrams of the adsorption geometries and the corresponding adsorption energies ΔE for (a,b) [4+2] cycloaddition and (c) [2+2] cycloaddition of <i>p</i> -xylene on a model surface of Si <sub>21</sub> H <sub>20</sub> , obtained by a density functional calculation with B3LYP/6-31G(d).....	56
Figure 3-4	Schematic diagrams of the adsorption geometries and the corresponding adsorption energies ΔE for [4+2] cycloaddition of (a) benzene and (b,c) toluene on a model surface of Si <sub>21</sub> H <sub>20</sub> , obtained by a density functional calculation with B3LYP/6-31G(d).....	57
Figure 3-5	Comparison of thermal desorption profiles of mass-4 (D <sub>2</sub> ) desorption for a 10 L exposure of <i>p</i> -xylene-d <sub>10</sub> and that for a 10 L exposure of <i>p</i> -xylene-dimethyl-d <sub>6</sub> , both to Si(100)2×1 at room temperature. The two data sets have been arbitrarily normalized at 820 K and the difference is shown by a dashed line. The experimental desorption data for <i>p</i> -xylene-d <sub>6</sub> has been fitted with a near-second-order desorption kinetics model (solid line) as discussed in the text....	61

Figure 3-6	Thermal desorption profiles for (a) Mass 98 (molecular desorption), (b) Mass 28 (dissociative products), and (c) Mass 4 ( $D_2$ ) for a 5 L exposure of <i>p</i> -xylene- $d_{10}$ to Si(100)2×1 (solid lines), amorphous ( <i>a</i> -)Si (dashed lines), and oxidized surface of Si(100) (dotted lines) at room temperature. ....	64
Figure 3-7	Comparison of thermal desorption profiles of Mass 2, 4, 28, 30, and 98 for a 100 L room-temperature exposure of <i>p</i> -xylene- $d_{10}$ to Si(100)2×1 (solid lines), and with post-hydrogenation (PH, dashed lines), post-oxidation (PO, dotted lines), and post-electron-irradiation (EI, dashed-dotted lines) at 200 $\mu$ A and 80 eV for 30 minutes. ....	67
Figure 3-8	Schematic diagrams of the adsorption geometries and the corresponding adsorption energies $\Delta E$ for [4+2] cycloaddition of (a,b) <i>m</i> -xylene and (c,d) <i>o</i> -xylene on a model surface of $Si_{21}H_{20}$ , obtained by a density functional calculation with B3LYP/6-31G(d). ....	71
Figure 4-1	Relative carbon moiety as indicated by the peak-to-peak intensity ratio for the C(KLL) to Si(LVV) Auger transitions as a function of room-temperature exposure of (a) styrene and (b) benzene to Si(100)2×1. The experimental data are compared with fitted curves based on the first-order and second-order adsorption kinetic equations. ....	77
Figure 4-2	Thermal desorption profiles of Mass 112 (parent mass) and Mass 4 ( $D_2$ ) as a function of room-temperature exposure of styrene- $d_8$ to Si(100)2×1. ....	79
Figure 4-3	Schematic diagrams of the adsorption geometries in different perspectives and the corresponding adsorption energies $\Delta E$ obtained by a density functional calculation involving B3LYP/6-31G(d) for styrene on a model surface of $Si_{21}H_{20}$ : (a) vinyl-bonded adspecies; (b) phenyl-bonded adspecies. ....	81
Figure 4-4	Thermal desorption profiles (a) of Mass 109 (molecular desorption), Mass 4 ( $D_2$ ) and Mass 2 ( $H_2$ ) for a 10 L room-temperature exposure of styrene-ring- $d_5$ and (b) of Mass 112 (molecular desorption) and Mass 4 ( $D_2$ ) for a 10 L room-temperature exposure of styrene- $d_8$ , both to Si(100)2×1. ....	84
Figure 4-5	Thermal desorption profiles for (a) Mass 109 (molecular desorption) (b) Mass 28 (dissociative products), (c) Mass 4 ( $D_2$ ) and (d) Mass 2 ( $H_2$ ) for a 10 L room-temperature exposure of styrene-ring- $d_5$ to Si(100)2×1 without and with	

	electron irradiation (EI) at 200 $\mu$ A and 80 eV for 30 minutes, amorphous (a-) Si, and oxidized surface of Si(100). .....	86
Figure 4-6	Comparison of thermal desorption profiles of Mass 2, 4, 26, 28, 32, 83, 84 and 112 for a 100 L room-temperature exposure of styrene-d <sub>8</sub> to Si(100)2 $\times$ 1 surface, with and without post-hydrogenation (PH). .....	91
Figure 4-7	Comparison of thermal desorption profiles of (a) Mass 2 and (b) Mass 4 for a 100 L room-temperature exposure of styrene-d <sub>8</sub> with those of styrene-d <sub>5</sub> to Si(100)2 $\times$ 1, with and without post-hydrogenation (PH). .....	93
Figure 4-8	Proposed schemes for the adsorption, desorption, and surface reactions for styrene-d <sub>8</sub> on Si(100)2 $\times$ 1 followed by post-hydrogenation. ....	95
Figure 5-1	Relative carbon moiety as reflected by the peak-to-peak intensity ratio for the C(KLL) to Si(LVV) Auger transitions as a function of room-temperature exposure of (a) d <sub>5</sub> -pyridine and (b) benzene to Si(100)2 $\times$ 1. The experimental data are compared with fitted curves based on the first-order and second-order adsorption kinetic equations. ....	104
Figure 5-2	Thermal desorption profiles of Mass 84 (parent mass) and Mass 4 (D <sub>2</sub> ) as a function of room-temperature exposure of d <sub>5</sub> -pyridine to Si(100)2 $\times$ 1. ....	105
Figure 5-3	Schematic diagrams of the adsorption geometries in three different perspectives and the corresponding adsorption energies $\Delta E$ obtained by a density functional calculation involving B3LYP/6-31G(d) for pyridine on the model surface of Si <sub>21</sub> H <sub>20</sub> . ....	107
Figure 5-4	Thermal desorption profiles for (a) Mass 84 (molecular desorption) and dissociative products (b) Mass 28 and (c) Mass 4 for a 100 L room-temperature exposure of d <sub>5</sub> -pyridine with and without electron irradiation at 200 $\mu$ A and 80 eV for 30 minutes. The time difference between the first and second thermal desorption spectrometry (TDS) experiments was 60 minutes. ....	110
Figure 5-5	Thermal desorption profiles for (a) Mass 84, (b) Mass 28 and (c) Mass 4 for a saturation room-temperature exposure of d <sub>5</sub> -pyridine to the 2 $\times$ 1, amorphous (a-), oxidized and H-terminated surfaces of Si(100). ....	114

Figure 5-6	Thermal desorption profiles for (a) Mass 84, (b) Mass 28 and (c) Mass 4 for a 10 L room-temperature exposure of d <sub>5</sub> -pyridine to an amorphous (a-)Si surface with and without electron irradiation at 200 μA and 80 eV for 30 minutes. .	116
Figure 5-7	Thermal desorption profiles for (a) Mass 84, (b) Mass 28 and (c) Mass 4 for a 10 L room-temperature exposure of d <sub>5</sub> -pyridine to an oxidized Si surface. The time difference between the first and second thermal desorption spectrometry (TDS) experiments was 60 minutes. ....	118
Figure 5-8	Thermal desorption profiles of Mass 2, 3, 4, 26, 28, 30, and 84 for a 10 L room-temperature exposure of d <sub>5</sub> -pyridine to a H-terminated Si(100)2×1 surface. The time difference between the first and second thermal desorption spectrometry (TDS) experiments was 60 minutes. ....	120
Figure 5-9	Thermal desorption profiles of (a) Mass 84, (b) Mass 28 and (c) Mass 4 for a 10 L room-temperature exposure of d <sub>5</sub> -pyridine to Si(100)2×1 with and without a 30 L post-exposure of O <sub>2</sub> . ....	122
Figure 5-10	Thermal desorption profiles of Mass 2, 3, 4, 26, 28, 30, and 84 for a 10 L room-temperature exposure of d <sub>5</sub> -pyridine to a H-terminated Si(100)2×1 surface followed by post-exposure of hydrogen atoms. The time difference between the first and second thermal desorption spectrometry (TDS) experiments was 60 minutes. ....	124
Figure 6-1.	Structural model of hydrogen on Si(100) surface: (a) (2×1) reconstruction of clean Si(100); (b) (2×1) structure of hemihydride, single-occupied dimer (SOD), or Si–SiH, with a local coverage of 1/2 monolayer (ML); (c) (2×1) structure of monohydride, double-occupied dimer (DOD), or HSi–SiH, with a local coverage of 1 ML; (d) (1×1) structure of dihydride, with a local coverage of 2 ML; (e) (3×1) structure of the alternating monohydride and dihydride species, with a local coverage of 1.5 ML. ....	134
Figure 6-2	TDS profiles of D <sub>2</sub> and/or H <sub>2</sub> for (a) H/Si(100), (b) <i>p</i> -xylene-d <sub>10</sub> /Si, (c) <i>p</i> -xylene-d <sub>8</sub> /Si(100), (d) styrene-d <sub>8</sub> /Si(100), and (e) styrene-ring-d <sub>5</sub> /Si(100). ....	136
Figure 6-3	Process flow diagram for hydrogen evolution from the aromatic hexacyclic hydrocarbons adsorbed on Si(100) studied in the present work. ....	137

Figure 6-4	Fraction of hydrogen present in DOD as a function of total H coverage, for various values of enthalpy change for hydrogen pairing (Reaction 6.3). .....	141
Figure 6-5	The logarithm of H coverage in DOD ( $\theta'_2$ ) is plotted as a function of the logarithm of total H coverage ( $\theta'_H$ ) at various temperatures. ....	143
Figure 6-6	Desorption order n as a function of temperature and total H coverage for styrene-rind-d <sub>5</sub> /Si(100). ....	144
Figure 6-7	TDS profile of Mass-4 (D <sub>2</sub> ) desorption for a 5 L exposure of <i>p</i> -xylene-dimethyl-d <sub>6</sub> and has been fitted with the desorption kinetics model, Model II (solid line). ....	150
Figure 6-8	Effective order of H <sub>2</sub> Desorption as a function of temperature and initial coverage for <i>p</i> -xylene/Si(100). ....	152
Figure 6-9	Thermal desorption profiles of Mass 4 for 100 L RT exposure of d <sub>5</sub> -pyridine to Si(100)2×1 with and without electron irradiation (EI) at 200 μA and 80 eV for 30 minutes. ....	155
Figure 6-10	Experimental and fitted TDS profiles of D <sub>2</sub> desorption from the condensation of the phenyl groups for styrene-ring-d <sub>5</sub> /Si(100)2×1. (a) The total desorption includes the contributions involving the mobile monomers (b) and the mobile dimers (c). [Note: $r(i, j) = \sigma_i \sigma_j r_{i \rightarrow j}$ (i, j = 1, 2, or p) ] .....	160
Figure 6-11	Experimental and fitted TDS profiles of H <sub>2</sub> from the condensation of phenyl groups for pyridine/Si(100)2×1. [Note: $r(i, j) = \sigma_i \sigma_j r_{i \rightarrow j}$ (i, j = 1, 2, or p) ].	161



## List of Tables

Table 2-1	Summary of plausible surface processes of toluene on Si(100)2×1 in various temperature ranges. ....	46
Table 7-1	Summary of the involvement of functional groups in different surface processes: .....	167



# Chapter 1

## Introduction

### 1.1 Organic functionalization of semiconductors

For several decades, many breakthroughs have taken place in the field of microelectronics, which almost exclusively relies on advances in our understanding of semiconductors (typically Si, Ge, and GaAs). The rapid progress in the semiconductor industry is demonstrated by the “integration level”, and the so-called Moore’s Law (the number of components per chip doubles every 18-24 months) [1] has become not only a driving force but also a perpetual challenge to modern technologies. As the miniaturization of electronic devices is rapidly approaching the nanometer scale and even atomic dimensions [2], future technologies are becoming more and more dependent on the functionalities of individual atoms and molecules. Physical or chemical processes at a semiconductor surface, including epitaxy [3], chemical vapor deposition, etching, oxidation and passivation [4], have always been a cornerstone of micro-fabrication. Understanding the phenomena underlying these processes at the molecular (or atomic) level has become even more critical. Exploring surface chemistry at the molecular level is accelerated by the growing field of organic functionalization of semiconductors [5], which involves the deposition of organic molecules at the semiconductor surfaces, with the objective to create new devices by using this hybrid approach. Organic molecules comprise of over 95% of all known chemical compounds [6]. Carbon provides a myriad of molecules differing in shape, size and composition, and offers great flexibility for design and development of unique organic properties for new applications in optical, electronic, and mechanical functions as well as chemical and biological activities [7]. The applications of organic semiconductor devices include field-effect transistors [8], chemical or biological sensors, and switchable molecular devices, etc. [9,10].

Many applications of organic semiconductors rely on the synthesis of fully conjugated organic polymers, or conducting polymers [11,12,13,14]. Molecular engineering of  $\pi$ -conjugated oligomers and polymers has therefore become especially important to producing well characterized organic nanoscale structures and devices [15]. The conductivity of a polymer depends on the degree of conjugation in the  $\pi$ -bond backbone, and

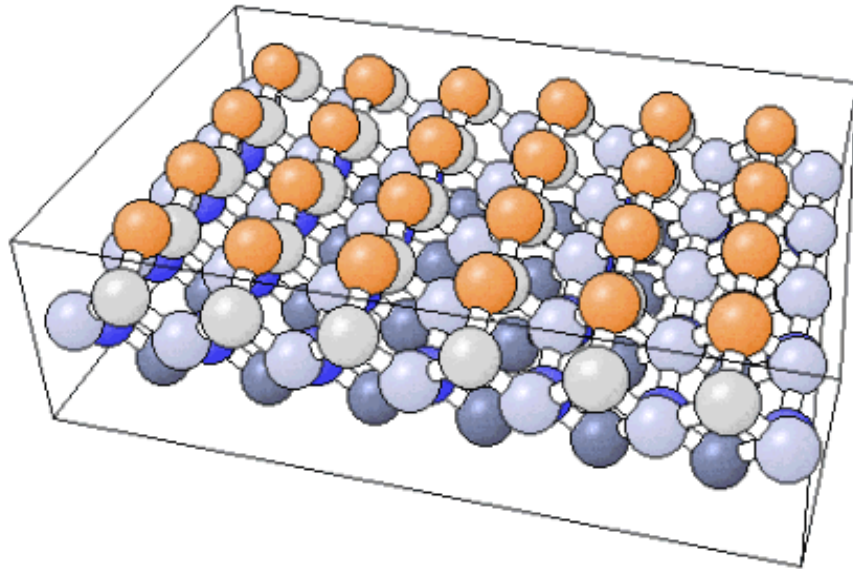
the chain alignment and extension. A conducting polymer film is often generated by chemical and electrochemical doping methods, in which the structure of the polymer film is generally ill-defined or highly disordered because it is difficult to control the factors that regulate the structure and organization of the polymer. A viable approach to improving the ordering of conducting polymers is to pre-align the monomers or oligomers on a well-defined single-crystal surface before initiating polymerization [16,17,18]. Since surfaces of most semiconductors for microelectronics have characteristics that enable organic molecules to be attached through a number of different chemical reactions with high surface selectivity, the semiconductor surface therefore offers a molecular template for further development in molecular engineering. Moreover, research on the surface chemistry of organic semiconductors not only provides an extended understanding of the reactivity of semiconductor surfaces, but also helps to create a variety of new applications based on the wealth of chemical knowledge over the past century in the field of organic chemistry.

The present work therefore seeks to investigate organic functionalization of silicon (the predominant semiconductor material used in the microelectronics industry) and in particular, the effects of the functional groups (phenyl, methyl, vinyl, heteroatom and H atom) in the chemisorbed hexacyclic aromatic hydrocarbons on the physical chemistry of the Si(100) surface. Since the interactions of aromatic hydrocarbons with the Si(111) surface have been studied previously in our group, it would also be of interest to compare the early work with the present study on Si(100) which is considered to be more reactive than Si(111).

## **1.2 Properties of the Si(100) substrate**

Silicon crystals have a diamond structure in which the atoms are  $sp^3$  hybridized to form a tetrahedral bonding configuration. The Si–Si covalent bond is 2.35 Å in length and 226 kJ/mol in strength [19]. When truncated at the (100) plane of the crystal, the stable tetrahedral bonding in the bulk is disturbed (Figure 1-1a). As a result, each Si atom at the surface bonds to two Si atoms in the sub-layer instead of four atoms as in the bulk, leaving two unpaired orbitals (the so-called dangling bonds) that increase the surface energy. In order to minimize the surface energy, the surface atoms reorganize the bonding among themselves to reduce the number of the dangling bonds (a process known as surface

(a)



(b)

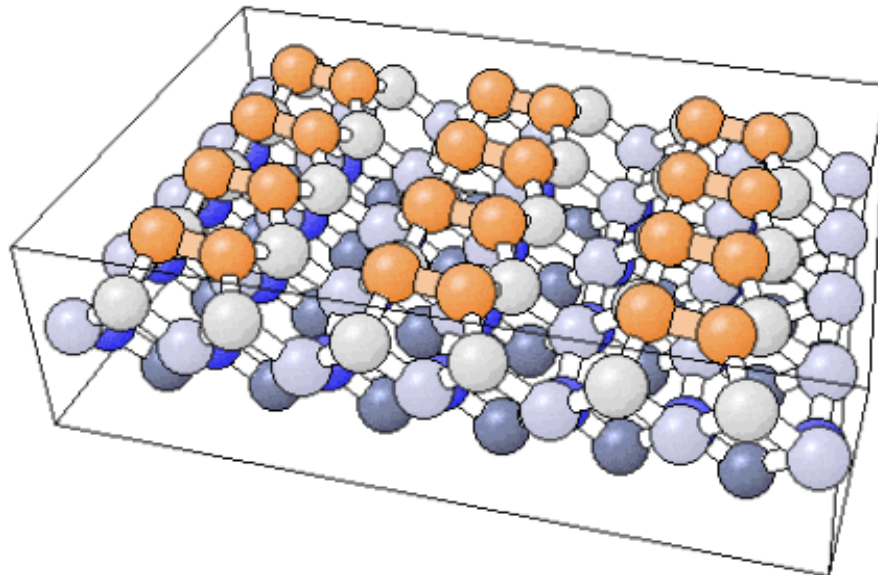


Figure 1-1 The Si(100)-(2x1) Reconstruction: Comparison of (a) an unreconstructed Si(100) surface and (b) the more thermodynamically stable (2x1) reconstructed surface. WWW Picture Gallery based on the Surface Structure Database (SSD, NIST Standard Reference Database 42).

reconstruction). The reconstruction of the Si(100) surface leads to a  $2\times 1$  structure (Figure 1-1b), which consists of Si dimer rows with periodicity of 1 unit along the dimer row and 2 units perpendicular to the row. The Si(100) $2\times 1$  reconstructed surface mimics an organic reagent because the two bonds of a surface Si dimer can be considered as double bonds consisting of a  $\sigma$  bond and a  $\pi$  bond.

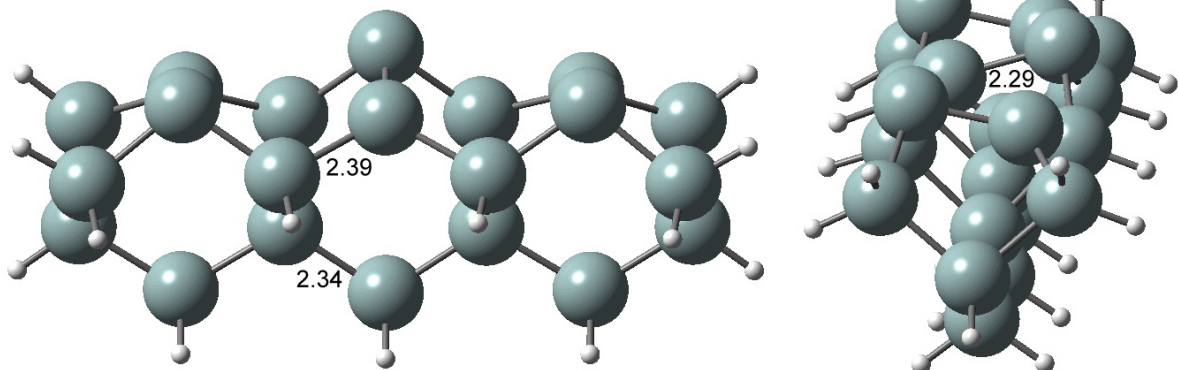
Si(100) is chosen as the substrate for all our studies in the present work because it is one of the most important substrates for fabrication of microelectronic devices. With its special structural and electronic properties [20,21], particularly the close analogy of a Si dimer on the  $2\times 1$  surface to an alkene group with a carbon-carbon double bond (C=C) [22], Si(100) provides an ideal platform for building hybrid devices by seeding unsaturated hydrocarbons on templates generated by the directional dangling bonds of the (100) surface. Recent studies of the interactions of unsaturated hydrocarbons with Si(100) have exploited promising opportunities for the development of atomically well-defined and ordered surface functionalities, which form the basis of molecular devices and nanoelectronics as well as biotechnology [5,23,24].

The Si dimers on the Si(100) surface play an important role in effecting surface reactions with incoming organic molecules. In contrast to the  $\pi$  bond in normal alkenes (e.g. ethylene), the “ $\pi$  bond” between two Si atoms of a Si dimer is sufficiently weak that the dimer is actually not held in a symmetric configuration (Figure 1-2). The energy of the Si(100) $2\times 1$  surface can be reduced further if the dimer is tilted into an asymmetric configuration at low temperature (200 K), revealing a  $c(4\times 2)$  long-range order as observed by using low energy electron diffraction (LEED) [25]. At higher temperatures, thermal energy induces a rapid change in the direction of the tilt which causes the dimers to appear symmetric and exhibit a typical two-domain ( $2\times 1$ ) LEED pattern for a clean Si(100) surface obtained at room temperature (RT).

### **1.3 Cycloaddition chemistry of alkenes on Si(100) $2\times 1$ surface**

The covalent nature of the Si(100) surface permits its reactivity to be described within a molecular framework, in which bonding is both localized and directional. The reactivity of

(a) Si(100)2x1 - 3-dimer Model  $\text{Si}_{21}\text{H}_{20}$



(b) Si(100)2x1 - 1-dimer Model  $\text{Si}_9\text{H}_{12}$

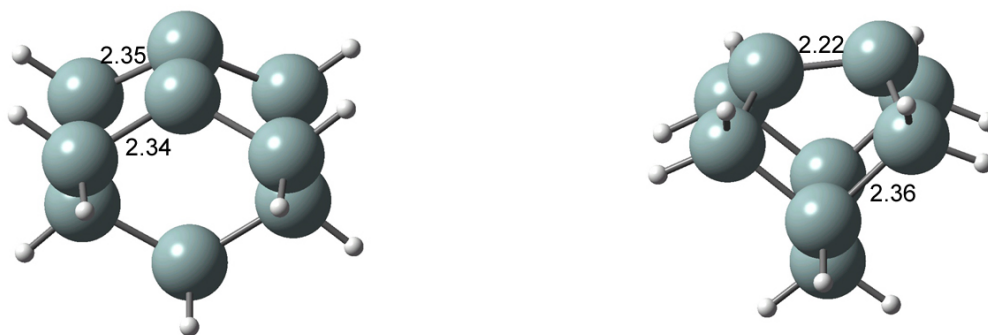
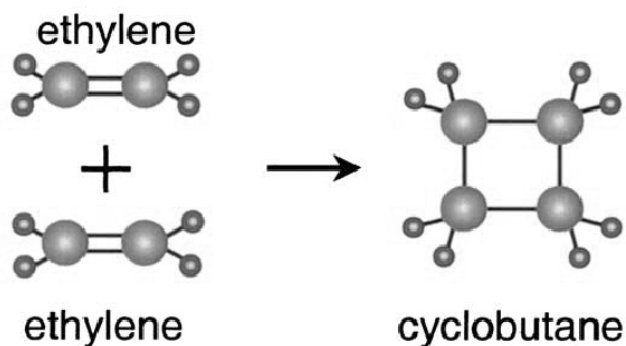


Figure 1-2 Buckled Si(100)2x1 structure (unit-Å) obtained by using Gaussian 98 calculations with (a) a 3-dimer model ( $\text{Si}_{21}\text{H}_{20}$ ), and (b) a 1-dimer model ( $\text{Si}_9\text{H}_{12}$ ). (See Section 1.6.4)

the silicon dimers on Si(100)2x1 surface can be understood by making analogies to alkenes in organic chemistry [26]. In particular, cycloaddition reactions of alkenes can be applied to investigate organic functionalization of Si(100) surface. Cycloaddition is widely used in organic synthesis as a means to form new carbon-carbon bonds and rings because of their versatility and high stereoselectivity [27]. Cycloadditions are reactions in which two molecules with  $\pi$  bonds come together to form a new cyclic molecule by creating two new  $\sigma$  bonds in the process. Depending on how many  $\pi$  electrons of each reactant molecule are involved in the reaction, there are two types of cycloaddition reactions (Figure 1-3). The first type (Figure 1-3a) is the [2+2] reaction, in which two  $\pi$  electrons in an alkene molecule (e.g. ethylene) are added to two  $\pi$  electrons in the another alkene to form a new (four-membered)

### a) [2+2] Cycloaddition



### b) [4+2] Cycloaddition

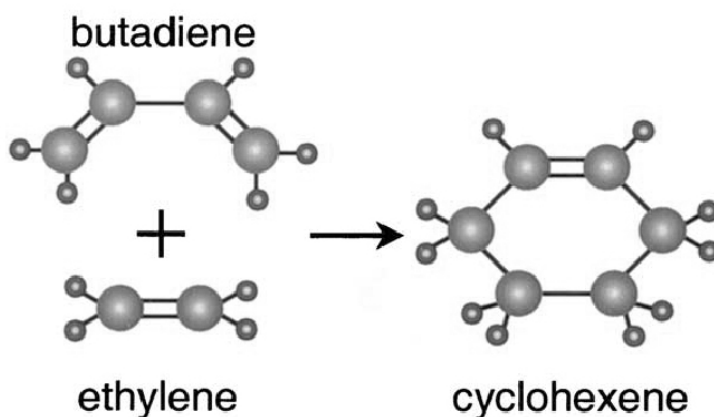


Figure 1-3 Cycloaddition reactions of alkenes: (a) The [2+2] cycloaddition between two alkenes forms a four-membered ring, and (b) [4+2] cycloaddition between an alkene and a diene forms a six-membered ring. The designations refer to the number of  $\pi$  electrons involved in the reaction.

ring. The second type (Figure 1-3b) is the [4+2] reaction, or the Diels-Alder reaction [28], in which a “diene” molecule with two neighboring (conjugated)  $\pi$  bonds (e.g. butadiene) reacts with an alkene (e.g. ethylene) to form a new (six-membered) ring. The cycloaddition reactions are subject to the Woodward-Hoffman selection rules [27], by which the [2+2] cycloaddition is found to be “symmetry forbidden” while the [4+2] reaction is “symmetry allowed”. The [2+2] reaction is largely limited to synthesis involving photochemical



activation, and the [4+2] reactions are commonly used in organic synthesis as a means to form new C–C bonds and ring structures.

Due to the analogy between the Si–Si dimer on the Si(100)2×1 surface and the C=C bond in an alkene, certain parallels might be expected to exist between reactions involving alkenes (or dienes) with the silicon surface and the cycloaddition reactions in organic chemistry. In addition, the [2+2] reactions symmetry-forbidden by the Woodward-Hoffman selection rules are allowed due to lower symmetry of the tilted Si dimer, and these [2+2] cycloaddition reactions on Si(100)2×1 are found to occur relatively fast at room temperature [23].

#### **1.4 Aromatic hydrocarbons on 2×1 and modified surfaces of Si(100)**

Aromatic hydrocarbons (e.g. benzene) and chain-like alkenes (e.g. ethylene) are the basic building blocks for constructing “conjugated” structures in most conducting polymer materials [11,15]. Unlike chain-like alkenes (or aliphatic hydrocarbons), aromatic hydrocarbons are more stable due to their ring structure. The cycloaddition principle applicable to adsorption of alkenes on Si(100)2×1 is also valid for adsorption of aromatic hydrocarbons. Figure 1-4 shows some examples of the [2+2] cycloaddition involving the vinyl group in styrene (Figure 1-4a) and the phenyl group in benzene (Figure 1-4b) \*, and of the [4+2] cycloaddition involving the phenyl group in benzene (Figure 1-4c). Details about the adsorption of these molecules will be discussed in the later chapters.

In the present work, planar aromatic hexacyclic hydrocarbons are investigated. In contrast to alkenes, the adsorption geometries of these molecules are more directional and easier to examine and control on the 2×1 template of Si(100). In addition, a collection of homocyclic (i.e. benzene) and heterocyclic (i.e. pyridine) conjugated molecules as well as

---

\* The [2+2] cycloaddition involving the phenyl group in benzene or other hexacyclic aromatic hydrocarbons is not very stable. The adsorption energy for benzene was calculated to be 3.9 kcal/mol by Wolkow et al. (See R.A. Wolkow, G.P. Lopinski, and D.J. Moffatt, Surf. Sci. 416 (1998) L1107), and that for xylene was calculated to be 5.5 kcal/mol in our group (See Chapter 3).

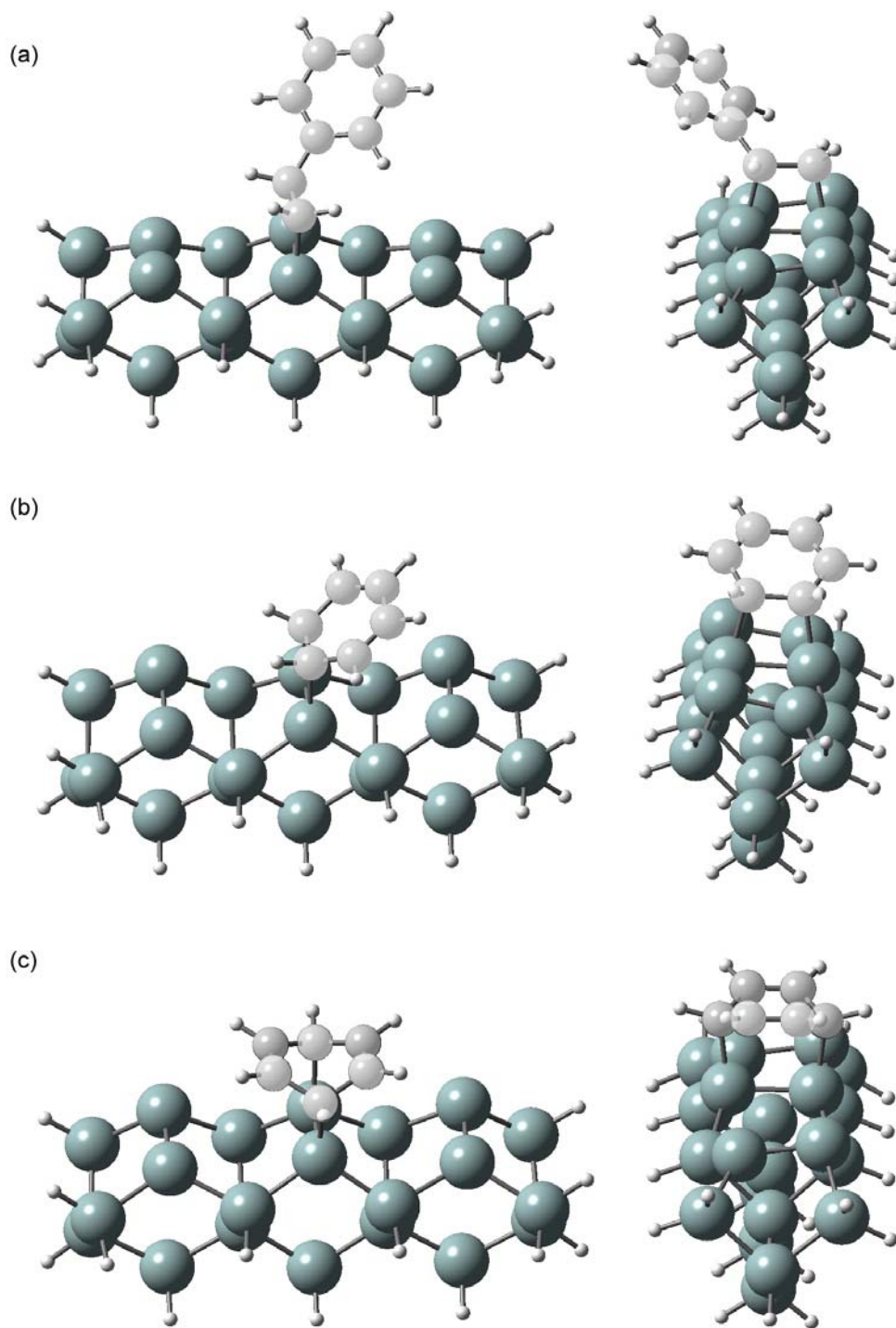


Figure 1-4 Cycloaddition reactions of hydrocarbons on Si(100)2x1: (a) [2+2] cycloaddition of styrene/Si(100)2x1, (b) [2+2] cycloaddition of benzene/Si(100)2x1, and (c) [4+2] cycloaddition of benzene/Si(100)2x1.

their substituted homologues (i.e. toluene, xylene and styrene) could provide additional functional groups for engineering of organic semiconductors. Different surface conditions, such as Ar<sup>+</sup> sputtered or amorphous silicon (*a*-Si), oxidized and H-terminated Si(100) surfaces, as well as post-treatments, including post-oxidization, post-hydrogenation and low energy electron irradiation, could also be employed to expose the nature of surface chemistry of aromatic hydrocarbons on the Si(100) surface.

## 1.5 Surface analysis techniques

During the past two decades, a great number of surface analysis techniques have been developed [29]. They include thermal desorption spectrometry (TDS), low energy electron diffraction (LEED), Auger electron spectroscopy (AES), scanning tunneling microscopy (STM), high-resolution electron energy loss spectroscopy (HREELS), and Fourier-transform infrared (FTIR) spectroscopy [29]. TDS, AES and LEED are the primary experimental techniques used in the present work. These techniques, respectively, provide important information about the thermal chemistry, elemental surface composition and surface crystallography of the organic materials of interest on Si(100) in the present work. In particular, when combined with the earlier results obtained by other research groups employing other techniques (STM, HREELS and FTIR), our TDS data has provided important complementary information and unique insights into new surface processes.

### 1.5.1 Thermal desorption spectrometry

TDS is a powerful surface science technique, in which adsorbates are thermally activated by raising the temperature of the substrate at a programmable rate (normally linear with respect to time) to induce desorption or thermal reactions or both, and the resulting desorbed products are monitored by mass spectrometry as a function of mass (in term of the mass-to-charge ratio) and temperature [29,30]. Desorption of the adsorbed species is one of the most elementary surface kinetic processes. It can be used to provide not only the thermodynamic information about the strength of the interactions between the substrate and the adsorbate, but also the kinetic information involving the adsorbate-adsorbate interaction. Qualitatively, the desorption products should be related to the adsorbed species. In the simplest case, the

adsorbed parent molecule is desorbed when the thermal energy exceeds the activation energy necessary to overcome the adsorbate-substrate interaction. In more complex cases, the adsorbate may fragment, recombine or rearrange to form new species that desorbs either promptly in what is known as reaction-limited desorption, or at a higher temperature when their own thermal activation barrier is surmounted in the so-called desorption-limited process.

TDS can also be used to provide quantitative information when the detected desorbates are related to the kinetics of surface species. Kinetic parameters for molecular desorption or reaction can be determined by analyzing the TDS profiles within the framework of an assumed model. The rates of desorption are often described by various approximated forms of a general rate equation, or the Polanyi-Wigner equation:

$$r(\theta) = -\frac{d\theta}{dt} = k_n \cdot \theta^n = \nu_n \cdot \theta^n \cdot e^{-E_d / RT} \quad (1.1)$$

where  $r(\theta)$  is the desorption rate of a single species, which is the derivative of the surface coverage of the adsorbate  $\theta$ , with respect to time  $t$ .  $n$  is the reaction order,  $k_n$  is the rate constant,  $\nu_n$  is the pre-exponential factor,  $E_d$  is the activation energy of the desorption process, and  $R$  is the gas constant. TDS profiles are usually represented by plots of the desorption intensities of preselected mass-channels (or mass-to-charge ratios of specific ions) against the substrate temperature  $T$ . Subsequent analysis of the TDS profiles collected at different initial coverages and surface conditions may be used to estimate the values of  $n$ ,  $E_d$ , and  $\nu$ , as well as the nature and strength of lateral interactions. In the present work, Redhead's Peak Temperature Method [31] and the Chan-Aris-Weinberg Method (CAW) [32] are used to analyze the TDS results.

In Redhead's method [31],  $E_d$  is approximated as a function of the temperature of the desorption maximum  $T_p$  during a linear annealing process:

$$T = T_0 + \beta \cdot t \quad (1.2)$$

where  $T_0$  is the initial temperature, and  $\beta$  is the heating rate. For first-order desorption, assuming  $\nu_n/\beta$  falls between  $10^8/\text{K}$  and  $10^{13}/\text{K}$ ,  $E_d$  is almost linear with respect to  $T_p$  (within 1.5%) for constant  $\nu_1$  and  $\beta$ , and it can be approximated by [31]:

$$E_d = RT_p \left[ \ln \left( \frac{\nu_1 T_p}{\beta} \right) - 3.64 \right] \quad (1.3)$$

This equation is often used to determine  $E_d$  from a single TDS profile of molecular desorption, after an appropriate choice of  $\nu_1$ , which is often set to  $10^{13}$ /s. Another equation proposed by Redhead gives a more general relation among the desorption parameters:

$$\nu = \frac{\beta E_d}{RT_p^2 \theta^{n-1}} \cdot e^{E_d / RT_p} \quad (1.4)$$

This equation can be used to determine  $\nu$  when  $E_d$  is already known from an alternative method.

Rather than relying on one parameter, the peak temperature  $T_p$ , as in Redhead's method, the CAW method [32] uses two peak characteristics: the peak temperature  $T_p$  and the Full Width at Half Maximum (FWHM) of the peak ( $W_{1/2}$ ). Because two independent characteristics are used, both  $\nu$  and  $E_d$  can be extracted from a single TDS profile, for a given reaction order. Assumptions of first or second order and a coverage-independent  $E_d$  are necessary in this method. For the first-order desorption kinetics:

$$E_d = RT_p \left[ \left( 1 + \frac{5.832 \cdot T_p^2}{W_{1/2}^2} \right)^{1/2} - 1 \right] \quad (1.5)$$

and

$$\nu = \frac{\beta E_d}{RT_p^2} \cdot e^{E_d / RT_p} \quad (1.6)$$

while for the second-order desorption kinetics:

$$E_d = 2RT_p \left[ \left( 1 + \frac{3.117 \cdot T_p^2}{W_{1/2}^2} \right)^{1/2} - 1 \right] \quad (1.7)$$

and

$$\nu = \frac{\beta E_d^2}{\theta \cdot RT_p^2 \cdot (E_d + 2RT_p)} \cdot e^{E_d / RT_p} \quad (1.8)$$

### 1.5.2 Auger electron spectroscopy, and low energy electron diffraction

AES is a standard elemental composition analysis technique in surface and interface science [29]. In AES, a high-energy incident electron beam (1000-10000 eV) is used to probe the surface, by inducing ionization of the surface atoms and followed by a radiationless relaxation of the excited state of the ion by ejection of an Auger electron. The kinetic energy of the Auger electron can be analysed by an electron energy analyser and is given by:

$$E_{AES} = E_1 - E_2 - E_3 \quad (1.9)$$

where  $E_1$  is the binding energy of the initial core-shell electron prior to ionization,  $E_2$  is that of the electron that fills the core hole, and  $E_3$  is the binding energy of the electron ejected as the Auger electron. The kinetic energy of the Auger electron is characteristic of the energy levels of the core hole and the upper state that fills the core hole. Due to the limited mean free path of the electrons in solids, AES is a very useful tool for elemental composition analysis of the surface, particularly to determine the cleanliness of the substrate surface. Moreover, the line shape of an AES peak also contains useful information for characterizing carbon nucleation (condensation polymerization as discussed in the later chapters) on a silicon surface [33]. Improved analysis methods have been developed for AES in the present work. In addition to an improved elemental composition analysis, the molecular adsorption coverages and kinetic parameters can also be analyzed by using these methods. These methods will be discussed in detail in Appendix A, and will be applied to the AES studies in later chapters.

LEED is used as the standard technique for checking the crystallographic quality of the surface, prepared either as a clean surface or in connection with an ordered adsorbate overlayer. In a typical LEED experiment, a beam of monochromatic electrons is incident on the surface at low energy (30–500 eV) and the elastically backscattered electrons give rise to diffraction spots that are imaged on a phosphorous screen. A LEED pattern corresponds to the structure of the reciprocal lattice, and it can be used to reveal the long-range order of the two-dimensional periodicity of a surface [29]. In the present work, LEED is mainly used to check the degree of surface order (or disorder) and cleanliness of the surface. A sharp and well-defined LEED pattern with low background intensity indicates a highly ordered surface

overlayer, while a weak and diffuse diffraction pattern with a high background intensity generally reflects a disordered surface.

## 1.6 Experimental details

### 1.6.1 UHV chamber and instrumentation

The experiments were conducted in a home-built double-chamber, ultra-high vacuum (UHV) system with a base pressure better than  $5 \times 10^{-11}$  Torr [34]. Figure 1-5 shows a photograph of the UHV chamber. The lower (analysis) chamber was equipped with a reverse-view four-grid retarding-field analyzer for LEED and AES measurements and with a 1-300 amu quadrupole mass spectrometer (QMS) for TDS experiments, while the upper (preparation) chamber was used for ion sputtering, sample annealing and gas dosing. The two chambers could be isolated from each other by a gate valve to minimize cross contamination during sample preparation ( $\text{Ar}^+$  sputtering) and sample dosing involving reactive gases. The upper chamber was evacuated with a turbomolecular pump and a titanium sublimation pump (TSP) to a vacuum better than  $1 \times 10^{-10}$  Torr. The lower chamber was evacuated with an ion pump and a TSP with a vacuum to below  $3 \times 10^{-11}$  Torr. The QMS was housed in a separated chamber that was differentially pumped by an ion gutter pump.

The electron beam energy used in the LEED experiments was typically 50-150 eV with an emission current of 0.1 mA. The sample was normally positioned about 2 inches away from the LEED optics. Within such energy range and emission current, surface damage due to the electron beam was usually undetectable, although the electron beam might induce desorption and/or surface reactions of the adsorbates as observed in some of our TDS experiments [35]. A CCD camera could also be used to record the LEED pattern.

AES was also performed by using the four-grid retarding-field LEED optics as a retarding field analyzer [36]. The LEED optics served as a high-pass energy filter, and together with a lock-in amplifier operating in second derivative mode, a differential energy distribution  $dN(E)/dE$  could be obtained [36]. The impact energy used in the present AES setup was usually 1.5 keV at 0.04 mA of emission current.

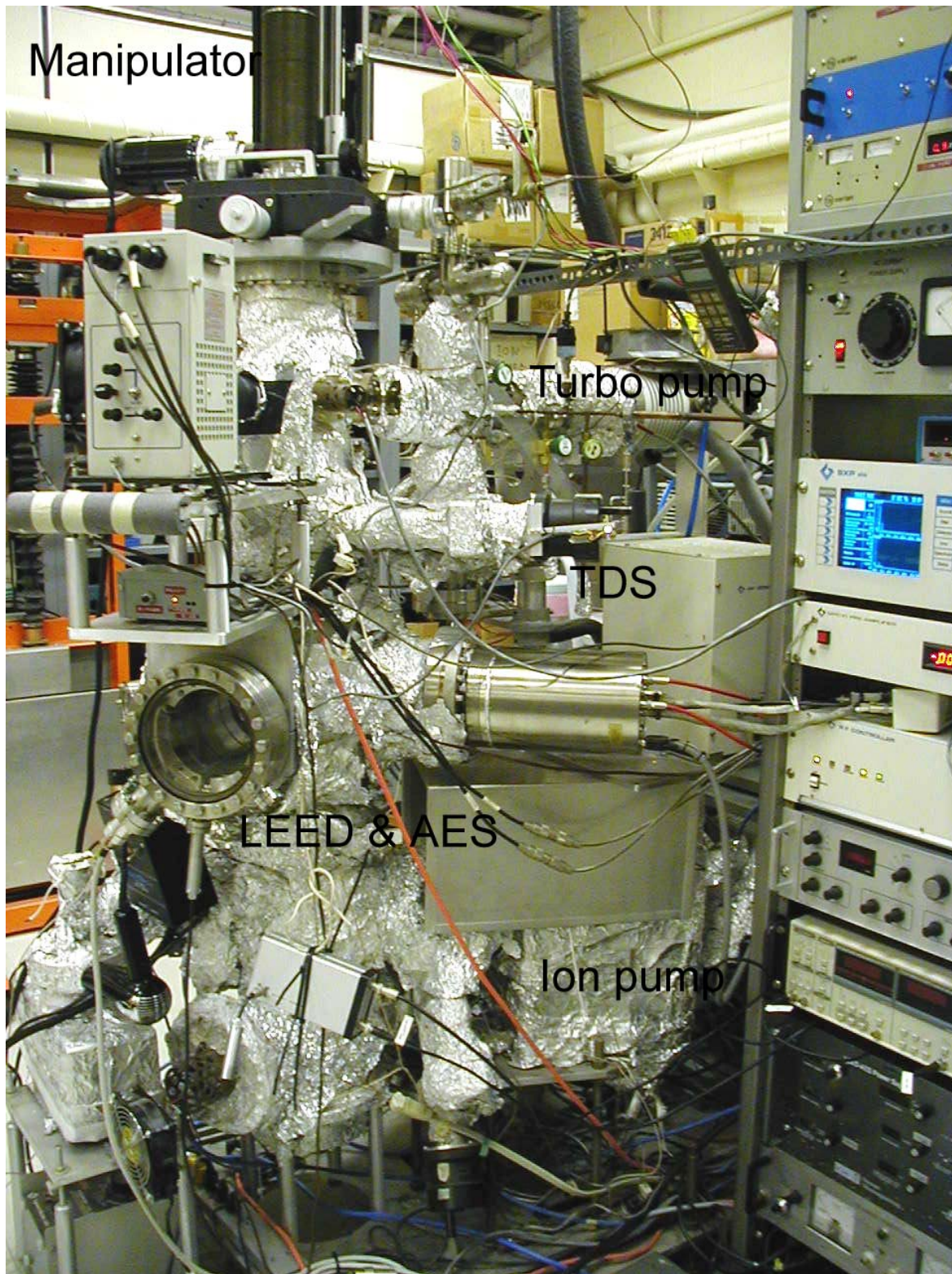


Figure 1-5 Experimental setup - UHV chamber, apparatus and electronics.



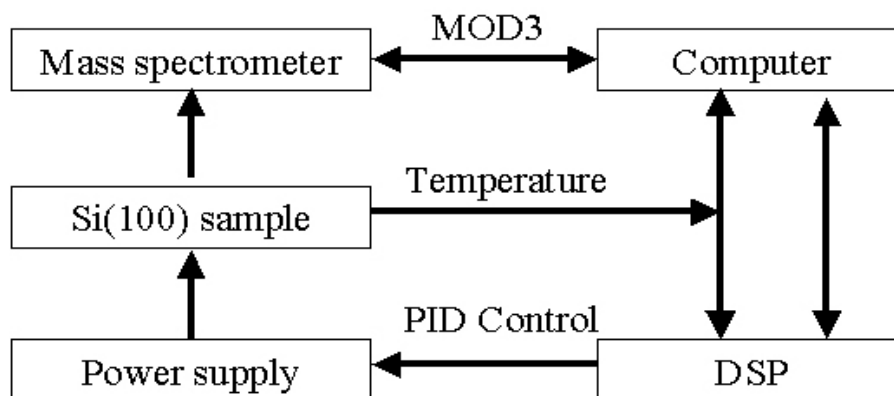


Figure 1-6 Schematic diagram of TPD experiment. A home-made digital signal processing (DSP) box is used to control the temperature by manipulating the “on-off” ratio of the AC power supply for sample heating, with a typical proportional-integral-differential (PID) algorithm. The computer is programmed to communicate with both the mass spectrometer and the DSP unit for data abstraction, display, storage, analysis, and system control.

### 1.6.2 Development of the thermal desorption spectrometry system

TDS is the main analysis method used in the present work. Based on the requirement of the present experiments, a home-built TDS system has been developed. Figure 1-6 shows a schematic diagram of the key components of a TDS system. A personal computer was used to communicate with a home-built digital signal processing (DSP) unit for temperature control and with the QMS controller.

The hardware setup of the sample in the UHV chamber is schematically shown in Figure 1-7. The only entrance to the ionization region of the QMS was a 2 mm diameter orifice in the QMS chamber, which was highly effective at reducing interference due to ambient desorption from the manipulator during a TDS experiment. A  $12.5 \times 3.5$  mm substrate was cut from a polished p-type boron-doped Si(100) wafer (0.38 mm thick) with a resistivity of 0.0080-0.0095  $\Omega \cdot \text{cm}$  at RT. The low resistivity of the sample allowed us to control the sample temperature smoothly by directly passing an appropriate current through the sample. The Si sample was mechanically fastened to a sample holder at both ends by Mo

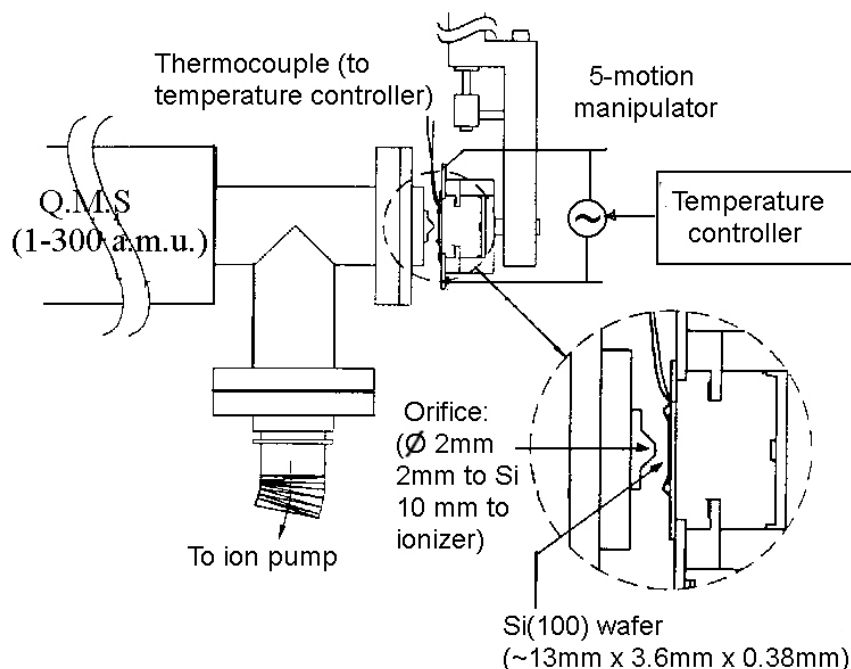


Figure 1-7 Experimental setup for thermal desorption spectrometry with a differentially pumped quadrupole mass spectrometer.

support plates and retaining bars, with small Si spacers sandwiched in between the Mo supports and the Si sample to minimize thermal contact between the sample and the rest of the manipulator while maintaining a good electrical connection. A type K thermocouple was inserted in between the Si spacers and mechanically fastened to one end of the Si sample by a Mo bar. In order to prevent any possible reaction between the Si sample and the thermocouple during annealing, the thermocouple was wrapped in a piece of Ta foil. Since the thermocouple was electrically in contact with the Si sample, an AC power supply was used to deliver the current in order to zero-average any voltage difference across the finite-sized thermocouple joint.

In order to satisfy the programmed control of the temperature ramp, a programmable DSP temperature controller based on the TMS320c50 microprocessor [37] was used to provide linear temperature ramping at an adjustable heating rate ( $\beta$ ), typically set at 1-2 K/s for the present TDS experiments (Figure 1-8). Physically, the temperature control was realized through regulation of an AC current power supply by modifying the on/off cycling ratio per second of a solid state relay. A typical proportional-integral-differential (PID)

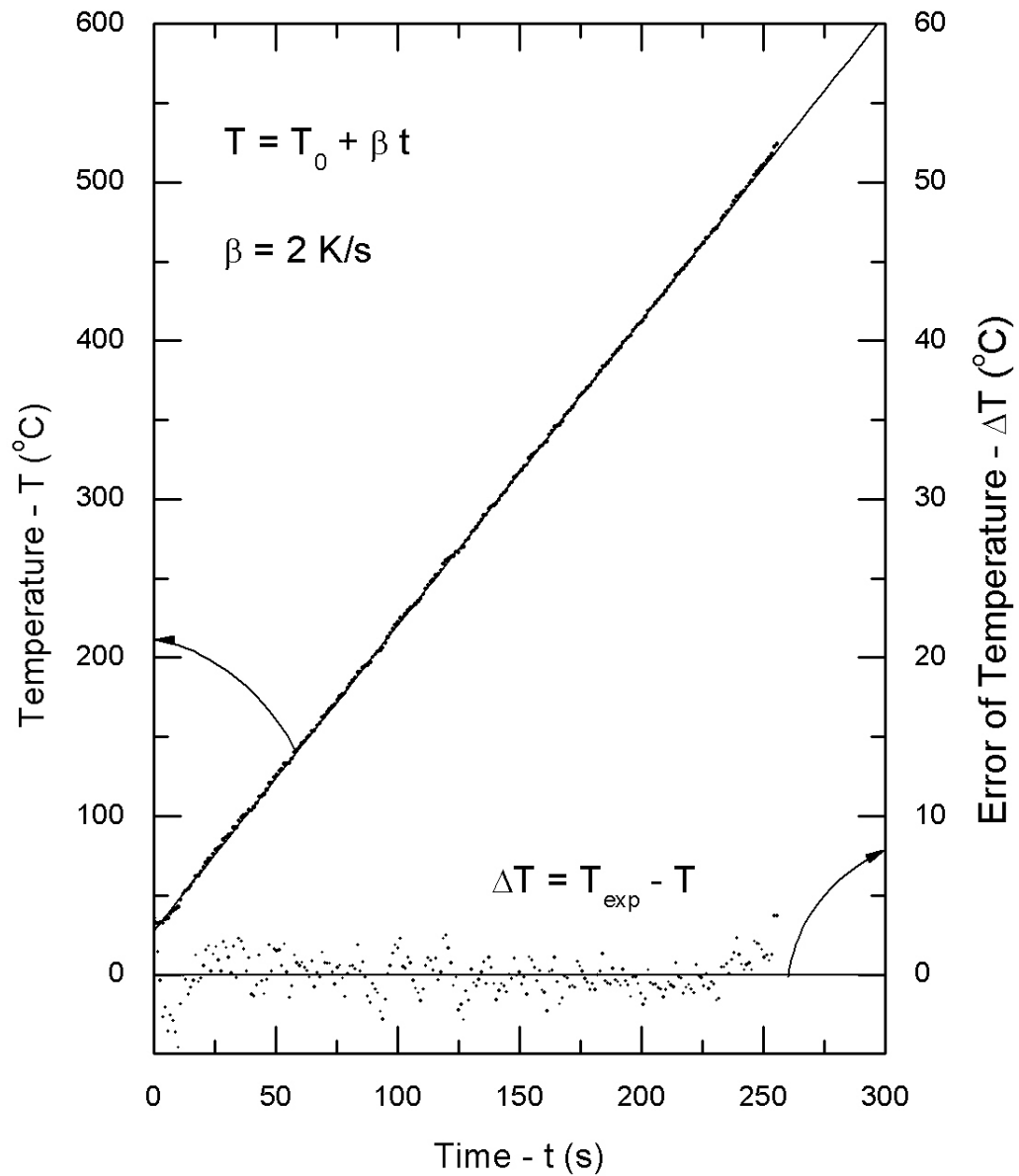


Figure 1-8 A typical temperature ramping curve as a linear function of time. The error  $\Delta T$  corresponds to the difference in temperature between the experiment and the predicted value.

algorithm [38] was used to adjust the on/off cycling ratio and hence the heating rate. In the present TDS experiment, the standard deviation of the linear temperature ramping was better than  $\pm 1\text{K}$ .

The standard software of the QMS provided by VG Quadrupoles could not satisfy our requirement for real-time multiple ion monitoring (MIM) as a function of the sample temperature. However, the manufacturer of the QMS has provided an option called MODE III that enabled us to develop our own program to realize real-time MIM. As a module of the home-built software WEPIL\_TDS, a Mode III object has been developed with all the necessary functions that operate on various QMS parameters (See Appendix B). In the present TDS system, the MIM can be obtained for up to 9 channels of integral mass-to-charge ratio (MCR) simultaneously. (The MCR has been referred to as mass in the subsequent chapters.)

The QMS can be used to analyse the gas species in the UHV chamber. In particular, a collection of the QMS signals from different MCR channels can be described as a vector  $\hat{s}_n$  in MCR channel space. Every gas species has its unique “fingerprint” of  $\hat{s}_n$ , or the so-called cracking pattern:

$$\hat{s}_n = \sum_m c_{mn} \cdot \hat{m} \quad (1.10)$$

where  $\hat{m}$  is the unit vector for the channel of a specific MCR in  $m$  atomic mass unit (amu), and the constant  $c_{mn}$  is the relative abundance of the species  $n$  in the channel  $m$ . Figure 1-9 gives an example of a cracking pattern  $\hat{s}_n$  for toluene that was obtained with the present QMS system. Suppose that there are  $N$  different species, a collection of QMS signals (from  $M$  MCR channels) for these species can be given as:

$$\begin{aligned} \hat{S} &= \sum_n a_n \cdot \hat{s}_n = \sum_n a_n \cdot \left( \sum_m c_{mn} \cdot \hat{m} \right) \\ &= \sum_m \hat{m} \cdot \left( \sum_n a_n \cdot c_{mn} \right) = \sum_m \hat{m} \cdot I_m \end{aligned} \quad (1.11)$$

where  $a_n$  is the amount of species  $n$ , and  $I_m$  is the intensity observed in the  $m^{\text{th}}$  channel of the mass spectrometer. Given the cracking patterns ( $c_{mn}$ ) and  $M \geq N$ , the distribution of each

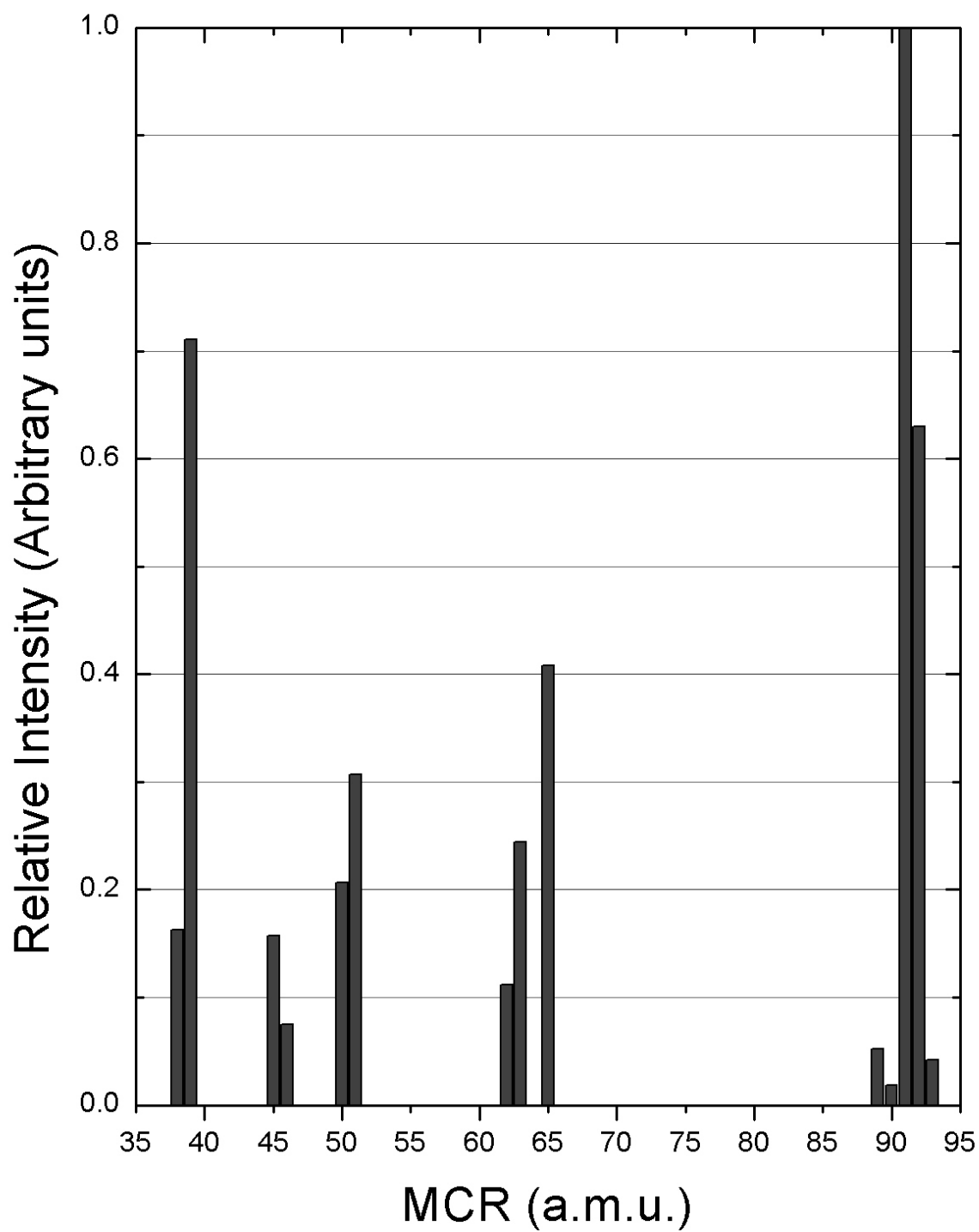


Figure 1-9 The cracking pattern of toluene obtained by using our mass spectrometry.

species ( $a_n$ ) can be obtained from intensities of mass spectrometry ( $I_m$ ) by solving the equation:

$$\begin{pmatrix} c_{11} & c_{12} & \cdots & c_{1N} \\ c_{21} & c_{22} & \cdots & c_{2N} \\ \vdots & \vdots & \ddots & \vdots \\ c_{M1} & c_{M2} & \cdots & c_{MN} \end{pmatrix} \cdot \begin{pmatrix} a_1 \\ \vdots \\ a_N \end{pmatrix} = \begin{pmatrix} I_1 \\ \vdots \\ I_M \end{pmatrix} \quad (1.12)$$

In the present TDS experiment, Equation 1.12 could be simplified in different ways as  $N$  is normally smaller than  $M$ . If a molecule has a component solely in the  $m^{\text{th}}$  channel, then the intensity  $I_m$  corresponds directly to the amount of this molecule. This is often the case for the molecular desorption of large hydrocarbons from Si(100), where the amount of the molecule can be represented by its parent ion and/or the base masses.

### 1.6.3 Sample preparation and cleaning

Before introduction into the vacuum chamber, the Si sample was first pre-cleaned by using a typical RCA procedure [39] that involves soaking in a basic peroxide solution consisting of equal parts of  $\text{H}_2\text{O}_2$  (~30%) and  $\text{NH}_4\text{OH}$  (~30%) in 5-20 parts of water. In an UHV environment, additional cleaning procedure was applied in order to obtain an atomically clean and well-ordered  $2 \times 1$  surface. After the bake-out, the sample was out-gassed at 900 K for 20 hours until the pressure recovered to the  $2 \times 10^{-10}$  Torr range. The temperature of the sample was then rapidly increased to 1500 K while carefully keeping the vacuum below  $1 \times 10^{-9}$  Torr [40]. Since most hydrocarbons used in the present experiment, except benzene, have been found to decompose easily upon annealing [34,35, 41], the resulting carbon could contaminate the bulk above 1400 K by diffusion [40], which would eventually accumulate in the sublayers and lead to a hazy surface after 3–5 experiments. (The haziness of the surface was thought to be caused by surface roughness of a ~100 nm size scale as a result of SiC formation [40,42]. A carbon-contaminated Si(100) surface was found to be roughened over the temperature range of 1150–1350 K by the formation of SiC clusters, which once formed could not be eliminated by further sputter-annealing cycles [40].) In order to prolong the repeated usage of the same Si sample after each TDS experiment, the near-surface carbon

concentration was first reduced to below an acceptable limit (as monitored by AES) by repeated cycles of Argon sputtering at a glancing angle (which reduced the roughness caused by Ar<sup>+</sup> sputtering) and low-temperature annealing to 850 K, before applying the high-temperature anneal to 1500 K. The resulting surface cleanliness was confirmed by a sharp 2×1 LEED pattern at RT, and by the lack of detectable Auger features attributable to C, O and S. Through high-temperature annealing, the majority of the surface defects could be eliminated and the small amount of surface C (< 1%) could be reduced by dissolving into the bulk. With this modified cleaning procedure, a Si sample could usually be maintained clean without the hazy appearance for about 50 TDS experiments.

The chemicals [toluene (99.8% purity), d<sub>8</sub>-toluene (98% D atom purity) and d<sub>6</sub>-benzene (99.6% D atom purity); pyridine (99.9+% purity) and d<sub>5</sub>-pyridine (99.5% D atom purity); *p*-xylene-d<sub>10</sub>, *m*-xylene-d<sub>10</sub>, *o*-xylene-d<sub>10</sub> (99+ atom% D) and *p*-xylene-dimethyl-d<sub>6</sub> (98+% D purity); styrene (99+% purity), styrene-d<sub>8</sub> (98+% D purity), and styrene-ring-d<sub>5</sub> (98% D purity)] used in this study were obtained commercially from BDH and Cambridge Isotope Laboratories. They are degassed by repeated freeze-pump-thaw cycles prior to use. Sample dosing was performed by back-filling the sample preparation chamber to an appropriate pressure, as monitored by an uncalibrated ionization gauge, with a precision leak valve. All exposures [in units of Langmuir (1L = 10<sup>-6</sup> Torr·second)] were performed at RT unless stated otherwise.

#### 1.6.4 Computational studies and kinetics modelling

Our theoretical approach is based on density functional theory (DFT) [43] with the electronic structure expanded in atomic Gaussian basis functions. By using the Gaussian 98 program [44], computational study on the Si(100)2×1 surface has been performed on Si<sub>21</sub>H<sub>20</sub> and Si<sub>9</sub>H<sub>12</sub> clusters with surfaces that simulate a 3-dimer model and a 1-dimer model, respectively. These models have been used in the computational studies presented in the following chapters. The hybrid functional consisting of Becke's 3-parameter non-local exchange functional and the correlation functional of Lee-Yang-Parr (B3LYP) was used along with the 6-31G(d) basis set [45], in order to determine the geometries of the critical points on the potential energy surface. Structures are fully optimized without geometrical

constraints on the clusters. The single-point energy calculations were performed on the optimized structures at the B3LYP/6-31G(d) level of theory. The resulting energies have been zero-point corrected. All calculated minima on the potential energy surfaces have been verified by frequency calculations to have no imaginary frequency.

## 1.7 Structure of this thesis

This thesis is organized as follow: First, the interactions of selected homocyclic aromatic hydrocarbons with Si(100) and related surfaces are investigated. In particular, benzene and toluene are described in Chapter 2, *para*-xylene in Chapter 3, and styrene in Chapter 4. In Chapter 5, a heterocyclic hydrocarbon, pyridine, is examined. Finally, in Chapter 6, the study of hydrogen evolution in thermal processes for hydrocarbons/Si(100) systems and their kinetics are given. Three kinetic models are proposed on the basis of the experimental results given in Chapters 2 to 5. In Chapter 7, some general observations about the organic functionalization of Si(100) and experimental developments in the present work are summarized and an outlook on future studies is presented. In Appendix A, the improved AES methods for the chemisorption analysis is presented. The structure and user manual of our software WEPIL-TDS are provided in Appendix B. In Appendix C, the equilibrium equation used in Chapter 6 is derived in detail.



## 1.8 References

- [1] G.E. Moore, *Electronics* 38 (1965) 114.
- [2] “International Technology Roadmap for Semiconductors”, Semiconductor Industry Association, (2002).
- [3] J.R. Arthur, *Surf. Sci.* 500 (2002) 189.
- [4] M.K. Weldon, K.T. Queeney, J. Eng Jr., K. Raghavachari, Y.J. Chabal, *Surf. Sci.* 500 (2002) 859.
- [5] S.F. Bent, *Surf. Sci.* 500 (2002) 879-903.
- [6] K.P.C. Vollhardt, N.E. Schore. “Organic Chemistry; 3rd ed. W. H. Freeman and Company”, New York, 1999.
- [7] J.W. Hill, D.K. Kolb, “Chemistry for Changing Times”, Prentice Hall, Englewood Cliffs, NJ, 1995.
- [8] A. Tsumura, H. Koezuka, and T. Ando, *Appl. Phys. Lett.* 49 (1986) 1210.
- [9] C.P. Collier, E.W. Wong, M. Belohradský, F.M. Raymo, J.F. Stoddart, P.J. Kuekes, R.S. Williams, J.R. Heath, *Science* 285 (1999) 391.
- [10] J. Liu, M. Gómez-Kaifer, A.E. Kaifer, *Structure and Bonding* 99 (2001) 141.
- [11] T.A. Skotheim, R.L. Elsenbaumer, and J.R. Reynolds (eds.), “Handbook of Conducting Polymers”, Dekker, New York (1998).
- [12] H. Shirakawa, E.J. Louis, A.G. MacDiarmid, C.K. Chiang, A.J. Heeger, *Chem. Commun.* (1977) 578.
- [13] C.K. Chiang, C.R. Fincher Jr., Y.W. Park, A.J. Heeger, H. Shirakawa, E.J. Louis, *Phys. Rev. Lett.* 39 (1977) 1098.
- [14] Nobel Lecture: H. Shirakawa, *Angew. Chem. Int. Ed.* 40 (2001) 2574-2580. “The Discovery of Polyacetylene Film: The Dawning of an Era of Conducting Polymers”; A.G. MacDiarmid, *Angew. Chem. Int. Ed.* 40 (2001) 2581-2590. “Synthetic Metals: A Novel Role for Organic Polymers”; A.J. Heeger *Angew. Chem. Int. Ed.* 40 (2001) 2591-2611.
- [15] J.L. Reddinger, J.R. Reynolds, *Advances in Polymer Science* 145 (1999) 57.
- [16] C.D. MacPherson, K.T. Leung, *Surf. Sci.* 324 (1995) 202.

- [17] R.J. Hamers, J.S. Hovis, C.M. Greenlief, D.F. Padowitz, *Jpn. J. Appl. Phys.* 38 (1999) 3879.
- [18] J.T. Yates, Jr., *Science* 279 (1998) 335.
- [19] R. Walsh, *Acc. Chem. Res.* 14 (1981) 246.
- [20] H.N. Waltenburg, J. T. Yates, *Chem. Rev.* 95 (1995) 1589.
- [21] R.J. Hamers, Y. Wang, *Chem. Rev.* 96 (1996) 1261.
- [22] R.J. Hamers, R.M. Tromp, J.E. Demuth, *Surf. Sci.* 181 (1987) 346.
- [23] R.A. Wolkow, *Annu. Rev. Phys. Chem.* 50 (1999) 413.
- [24] T. Bitzer, N.V. Richardson, *Appl. Phys. Lett.* 71 (1997) 662.
- [25] C.B. Duke, *Chem. Rev.* 96 (1996) 1237-1259.
- [26] J.J. Boland, *Adv. Phys.* 42 (1993) 129.
- [27] W. Carruthers, "Cycloaddition Reactions in Organic Synthesis", Pergamon Press, New York, 1990.
- [28] A. Wassermann, "Diels-Alder reactions; organic background and physicochemical aspects", Elsevier, New York, 1965.
- [29] A.T. Hubbard, ed., "The Handbook of Surface Imaging and Visualization", CRC Press, Inc., Boca Raton, Florida, 1995.
- [30] G. Attard, C. Barnes, "Surfaces", Oxford University Press Inc., New York,, USA, 1998.
- [31] P.A. Redhead, *Vacuum* 12 (1962) 203.
- [32] C.M. Chan, R. Aris, W.H. Weinberg, *Appl. Surf. Sci.* 1 (1978) 360-376.
- [33] E. Grossman, G.D. Lempert, J. Kulik, D. Matron, J.W. Rabalais, Y. Lifshitz, *Appl. Phys. Lett.* 68 (1996) 1214.
- [34] Q. Li, K.T. Leung, *Surf. Sci.* 479 (2001) 69.
- [35] Q. Li, K.T. Leung, *Surf. Sci.* 541 (2003) 111-125.
- [36] P.W. Palmberg, T.N. Rhodin, *J. Appl. Phys.* 39 (1969) 2425.
- [37] Texas Instruments TMS320C5X DSP Starter Kit User's Guide, Microprocessor Development Systems, Texas Instruments Inc., 1994, U.S.A.
- [38] K.J. Astrom and T.Hagglund, "Automatic Tuning of PID controllers", Instrument society of America, 1988.

- [39] W. Kern and D.A. Puotinen, *RCA Rev.* 31 (1970) 187.
- [40] B.S. Swartzentruber, Y.-W. Mo, M.B. Webb, and M.G. Lagally, *J. Vac. Sci. Technol. A* 7 (1989) 2901.
- [41] B. Borovsky, M. Krueger, E. Ganz, *Phys. Rev. B* 57 (1998) R4269.
- [42] A.W. Munz, Ch. Ziegler, and W. Gopel, *Surf. Sci.* 325 (1995) 177.
- [43] P. Hohenberg, W. Kohn, *Phys. Rev. B* 136 (1964) 864.
- [44] Gaussian 98 (Revision A.11.3), M.J. Frisch, G.W. Trucks, H.B. Schlegel, G.E. Scuseria, M.A. Robb, J.R. Cheeseman, V.G. Zakrzewski, J.A. Montgomery, Jr., R.E. Stratmann, J. C. Burant, S. Dapprich, J. M. Millam, A.D. Daniels, K.N. Kudin, M.C. Strain, O. Farkas, J. Tomasi, V. Barone, M. Cossi, R. Cammi, B. Mennucci, C. Pomelli, C. Adamo, S. Clifford, J. Ochterski, G.A. Petersson, P.Y. Ayala, Q. Cui, K. Morokuma, N. Rega, P. Salvador, J.J. Dannenberg, D.K. Malick, A.D. Rabuck, K. Raghavachari, J.B. Foresman, J. Cioslowski, J.V. Ortiz, A.G. Baboul, B.B. Stefanov, G. Liu, A. Liashenko, P. Piskorz, I. Komaromi, R. Gomperts, R.L. Martin, D.J. Fox, T. Keith, M.A. Al-Laham, C.Y. Peng, A. Nanayakkara, M. Challacombe, P.M.W. Gill, B. Johnson, W. Chen, M.W. Wong, J.L. Andres, C. Gonzalez, M. Head-Gordon, E.S. Replogle, J.A. Pople, Gaussian Inc., Pittsburgh PA (2002).
- [45] J.B. Foresman, A. Frisch, "Exploring Chemistry with Electronic Structure Methods", 2nd Ed., Gaussian Inc., Pittsburgh (1996); and references therein.



## Chapter 2

### Thermal chemistry of toluene and benzene on Si(100)2×1 and modified surfaces

#### 2.1 Introduction

Benzene and toluene are two of the most important unsaturated cyclic hydrocarbons in organic chemistry. Since toluene differs from benzene chemically only with the replacement of a hydrogen atom by a methyl group, comparison of the surface chemistries of these aromatic compounds on the technologically important silicon surfaces may provide new insight into the formation of multifunctional organic films involving unsaturated cyclic hydrocarbons. Although the interaction of benzene with silicon has been widely studied by a variety of theoretical [1,2,3] and experimental techniques including thermal desorption spectrometry (TDS) [4,5], high resolution electron energy loss spectroscopy (EELS) [5], photoemission [6,7], infrared spectroscopy and near-edge X-ray absorption fine structure [8], and scanning tunneling microscopy (STM) [9,10,11], only a limited amount of work has been found for toluene [12,13]. Previous studies from our group have shown that the methyl group could have interesting effects on the adsorption and reactivity of aromatic compounds on pristine and modified surfaces of Si(111)7×7 [12,14]. More recently, Borovsky, Krueger and Ganz reported a STM study on the adsorption of toluene on Si(100)2×1 [13], which suggests that room temperature (RT) adsorption occurs only on top of the dimer rows, giving rise to several binding geometries that closely resemble those of benzene. The interactions of toluene and xylenes with Si(100) were also investigated using Fourier-transform infrared (FTIR) spectroscopy by Coulter *et al.* [15]. These FTIR spectra show that the methyl-substituted aromatic hydrocarbons are chemisorbed on Si(100) in much the same way as benzene, with some dissociation occurring upon adsorption, which likely arises from C–H bond cleavage of the methyl group leaving the ring intact [15]. In the present work, we examine the interactions of toluene and benzene with the Si(100)2×1 and related surfaces using TDS, low energy electron diffraction (LEED) and Auger electron spectroscopy (AES), in order to compare the effects of methyl substitution between the (100) surface identified in the present work and the (111) surface observed in our earlier work [12,14]. Furthermore, the interactions of atomic hydrogen and O<sub>2</sub> with adsorbed toluene and benzene are also

investigated. It is important to emphasize that theoretical analysis of the TDS profiles [16] along with examples from our early work [12,17,18] have shown the potential ambiguities in the interpretation of multiple desorption peaks in TDS experiments. In particular, individual desorption features in a TDS profile may be attributed either to separate adsorption states with different binding energies (corresponding to different adsorption geometries) or to a single adsorption state with a coverage-dependent adsorption energy [16]. Such ambiguities make it difficult to definitely identify the number and nature of the adsorption states and their relative populations from TDS data alone. Recent STM experiments can however alleviate some of these problems by identifying different adsorption features. In the present work, we take advantage of corroborating evidence provided by other surface analysis technologies.

## 2.2 Results and Discussion

### 2.2.1 Room-temperature adsorption at various exposures

The TDS profiles of the parent mass (Mass 92) obtained as a function of RT exposure for toluene on Si(100)2×1 are shown in Figure 2-1a. In addition to the parent mass (Mass 92), other fragments including Mass 91 (C<sub>6</sub>H<sub>5</sub>CH<sub>2</sub>), Mass 65 (C<sub>5</sub>H<sub>5</sub>) and Mass 51 (C<sub>4</sub>H<sub>3</sub>) were also monitored during the TDS experiments. Since their corresponding peak intensity ratios were found to be in good accord with the respective ratios of the cracking pattern of toluene [19], the detected mass fragments could be attributed to dissociation of molecularly desorbed toluene in the ionizer of the QMS. These profiles therefore indicate that toluene desorbs from Si(100)2×1 molecularly. For exposures less than 0.25 L, a single desorption peak at 530 K ( $\gamma$  state) is observed. With increasing exposure, a new desorption peak at 430 K ( $\beta$  state) emerges along with the higher temperature peak ( $\gamma$  state). The  $\gamma$  state appears to reach saturation at a lower exposure than the  $\beta$  state. Within the absolute accuracy of our temperature measurement ( $\pm 20$  K), the desorption maxima of these states remain essentially unchanged with increasing exposure, indicating first-order desorption kinetics [20]. At higher exposure ( $> 4$  L), a third desorption state ( $\alpha$  state) appears as a small shoulder at 350 K, which is much higher than the temperature generally expected for desorption from

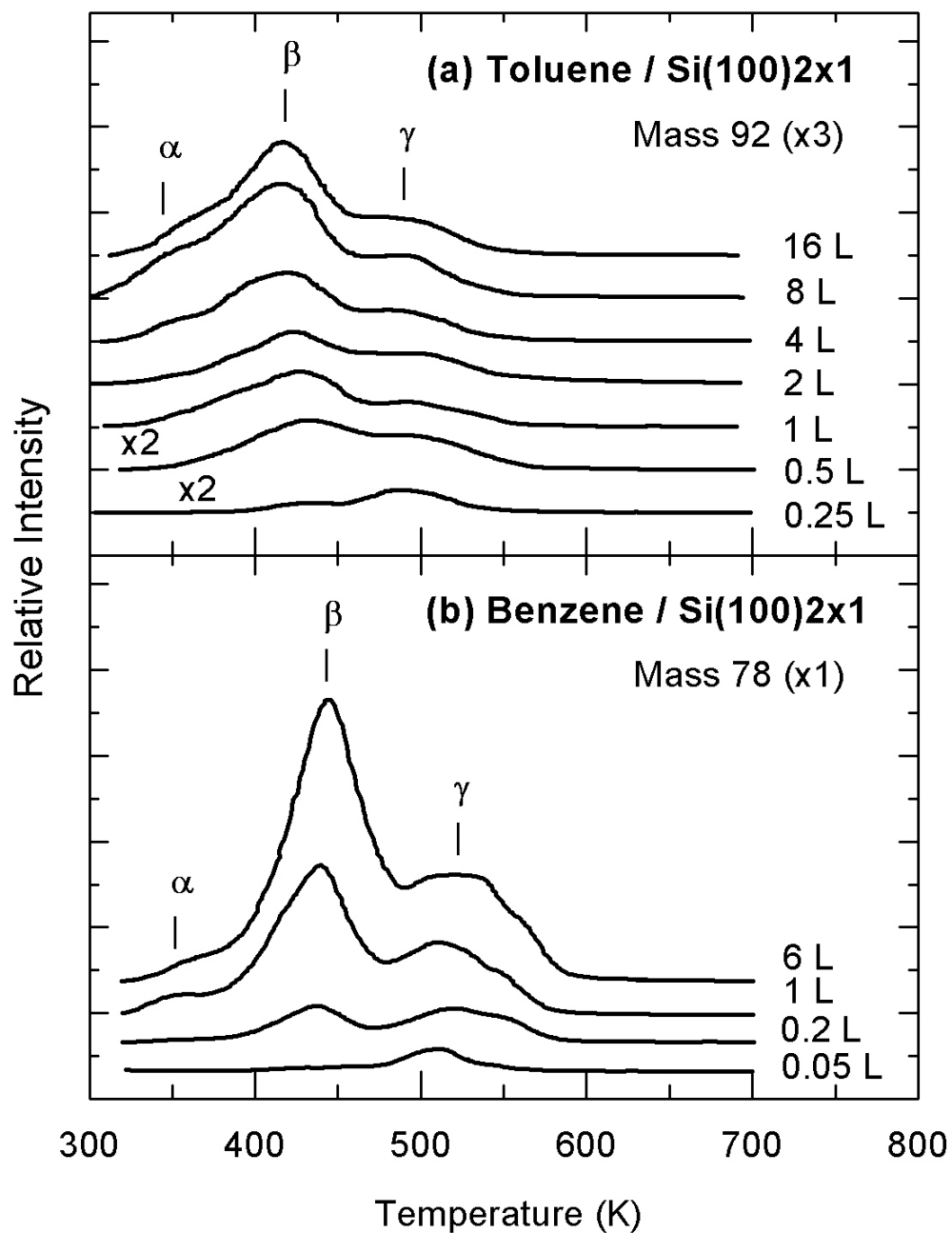


Figure 2-1 Thermal desorption profiles of (a) Mass 92 (molecular toluene) and (b) Mass 78 (molecular benzene) as a function of room-temperature exposure of toluene and benzene to Si(100)2 $\times$ 1. The desorption intensity of toluene is found to be considerably smaller than that of benzene.

physisorbed aromatic molecules (For example, the desorption temperature for physisorbed benzene is near 150 K [5]).

Figure 2-1b gives the corresponding TDS profiles of the parent mass (Mass 78) as a function of RT exposure for benzene on Si(100)2×1. Our data are found to be consistent with the earlier TDS results reported by Taguchi *et al.* [5]. Evidently, three desorption features are also observed. Except for the small differences in the desorption maxima from the corresponding TDS features for toluene (Figure 2-1a), all three states also appear to follow first-order desorption kinetics. A number of studies, including several theoretical studies [1,2,3,7,11], have been made in an attempt to better understand the nature of the two more prominent features ( $\beta$  and  $\gamma$  states) of benzene on Si(100)2×1. In particular, three types of chemisorbed states were discussed for the RT adsorption of benzene on Si(100) by using TDS [5] and STM [9]. Taguchi *et al.* attributed the two prominent TDS features for the  $\beta$  and  $\gamma$  states to benzene molecularly adsorbed on terrace and defect sites, respectively [5]. A recent study by Birkenheuer *et al.* suggested that a 1,4-cyclohexadiene-like “butterfly” structure di- $\sigma$  bonded to a dimer of the (2×1) surface (the so-called 1,4-single-dimer configuration) is energetically more favourable (Figure 2-2a) and should therefore be attributed to the lower-temperature desorption peak ( $\beta$  state) [3]. Another plausible bonding arrangement is a “tilted” 1,2-cyclohexadiene-like structure di- $\sigma$  bonded to a dimer of the surface (the 1,2-single-dimer configuration in Figure 2-2b). In addition to these single-dimer geometries, various cyclohexene-like or cyclohexane-radical structures tetra- $\sigma$  bonded to two dimers of the (2×1) surface are possible. These double-dimer configurations give rise to “tilted” tight bridge (Figure 2-2c) and twisted bridge (Figure 2-2d) geometries [9]. Lopinski *et al.* also suggested the 1,4-single-dimer configuration responsible for the  $\beta$  state is metastable and converts to the double-dimer configuration ( $\gamma$  state) [9]. Using more refined calculations, the same group later associated the  $\beta$  state to the double-dimer “tight bridge” configuration that is converted from a metastable 1,4 single-dimer configuration, and the  $\gamma$  state to a double-dimer “C defect-twisted bridge” geometry, which explains the saturation of the higher-temperature TDS feature at low exposures (benzene has been found to preferentially adsorb at type “C” defects) [11].



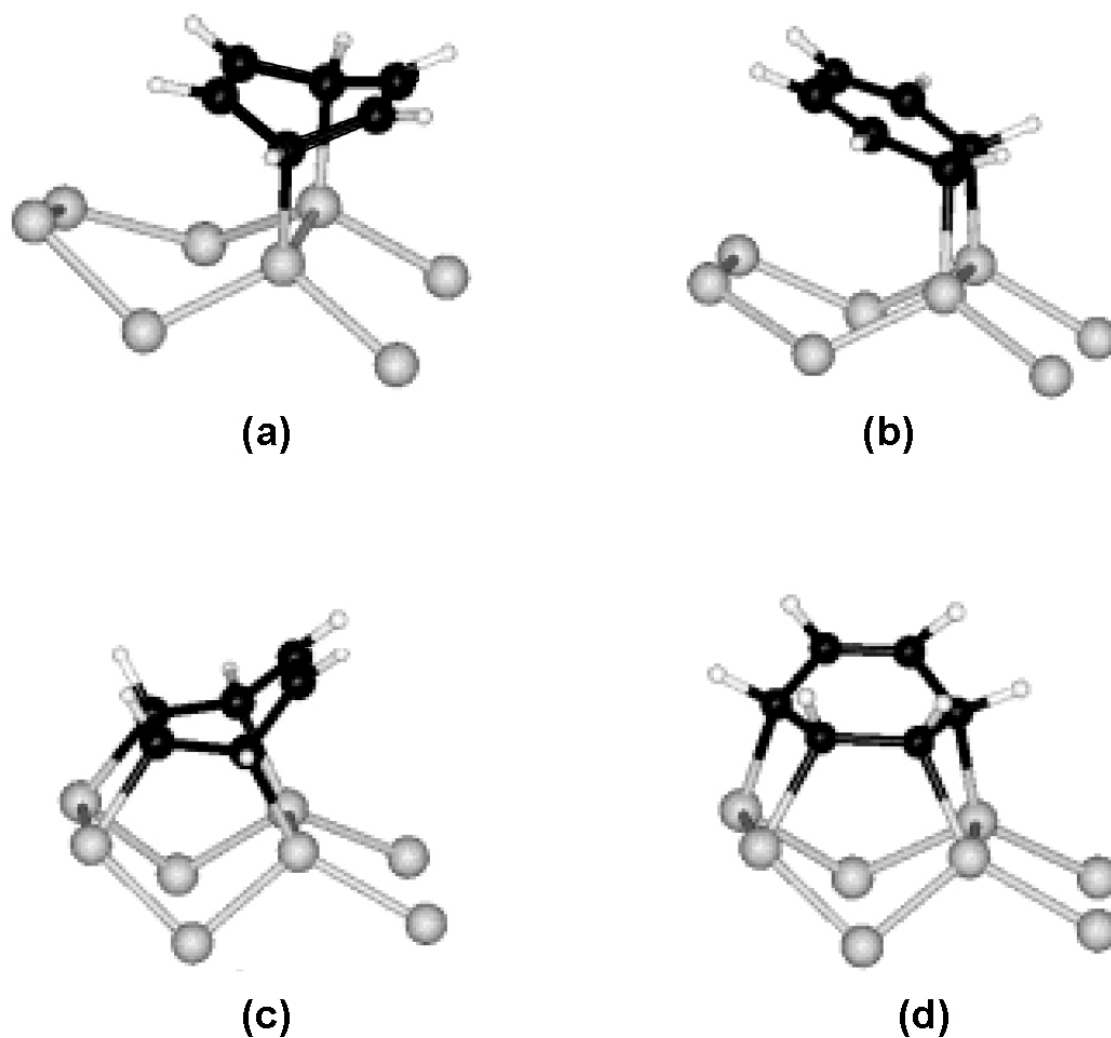


Figure 2-2 Stable undissociated configurations for chemisorption of benzene on Si(100): (a) 1,4-single-dimer configuration, (b) 1,2-single-dimer configuration, (c) tight bridge double-dimer configuration, and (d) twisted bridge configuration. (White, black, and gray balls indicate H, C, and Si atoms, respectively.)

As the molecular desorption features for both benzene and toluene on Si(100)2×1 are found to have very similar desorption maxima and desorption kinetics, we hypothesize that RT adsorption of toluene involves similar bonding arrangements to those of benzene, with  $\beta$  and  $\gamma$  states involving, respectively, single-dimer and double-dimer bonding configurations (similar to those aforementioned for benzene) and the  $\alpha$  state related to defect sites. Indeed,

the STM images of toluene on Si(100) at a low exposure (<0.1 L) reported by Borovsky *et al.* [13] have revealed two features that closely resemble those observed for benzene on Si(100) [9,10,11], except that toluene appears to interact with more than two dimers on the (2×1) surface. Based on the physical dimensions of a toluene molecule (whereby the diameter of the aromatic ring is 2.8 Å and the C–C bond length between the ring and the methyl group is 1.5 Å) and given that the dimer separation and bond length between the dimer molecules are 3.8 Å and 2.3 Å respectively [21], the methyl group can be sufficiently close to an adjacent dimer atom only for toluene adsorption with the 3,4 configuration (denoting C atoms 3 and 4 with respect to the C atom 1 that bonds to the methyl group) on a single-dimer. In the case of the double-dimer configurations (and other single-dimer configurations), the methyl group is oriented away from the Si back bond and any unoccupied dangling bonds. The β state should therefore be more reactive than the γ state.

One significant difference between the adsorption of the two aromatic compounds on Si(100)2×1 is that the desorption of toluene is considerably weaker than that of benzene for the same RT exposure. Assuming similar ionization cross sections for benzene and toluene (consistent with their similar gas-phase cracking patterns observed by QMS), the amount of molecular desorption for toluene is approximately 10% of that for benzene. This greatly reduced desorption can be attributed to either a lower initial adsorption of toluene than benzene, or the presence of subsequent reactions that reduce the concentration of adsorbed toluene, or both. AES measurements were also employed to study toluene adsorption on Si(100)2×1 at RT. Figure 2-3 compares the relative carbon concentration, as indicated by the peak-to-peak ratio of the C(KLL) Auger peak relative to that of the Si(LVV) Auger peak, as a function of RT exposure for toluene and benzene on Si(100)2×1. For each exposure, the average value of three measurements is used to prevent the possible errors due to electron beam effects [22]. The ratio appears to reach its maximum value at 10 L exposure, which indicates completion of adsorption of the first monolayer (ML). This adsorption uptake curve is nearly identical to that represented by the total desorption intensity for the

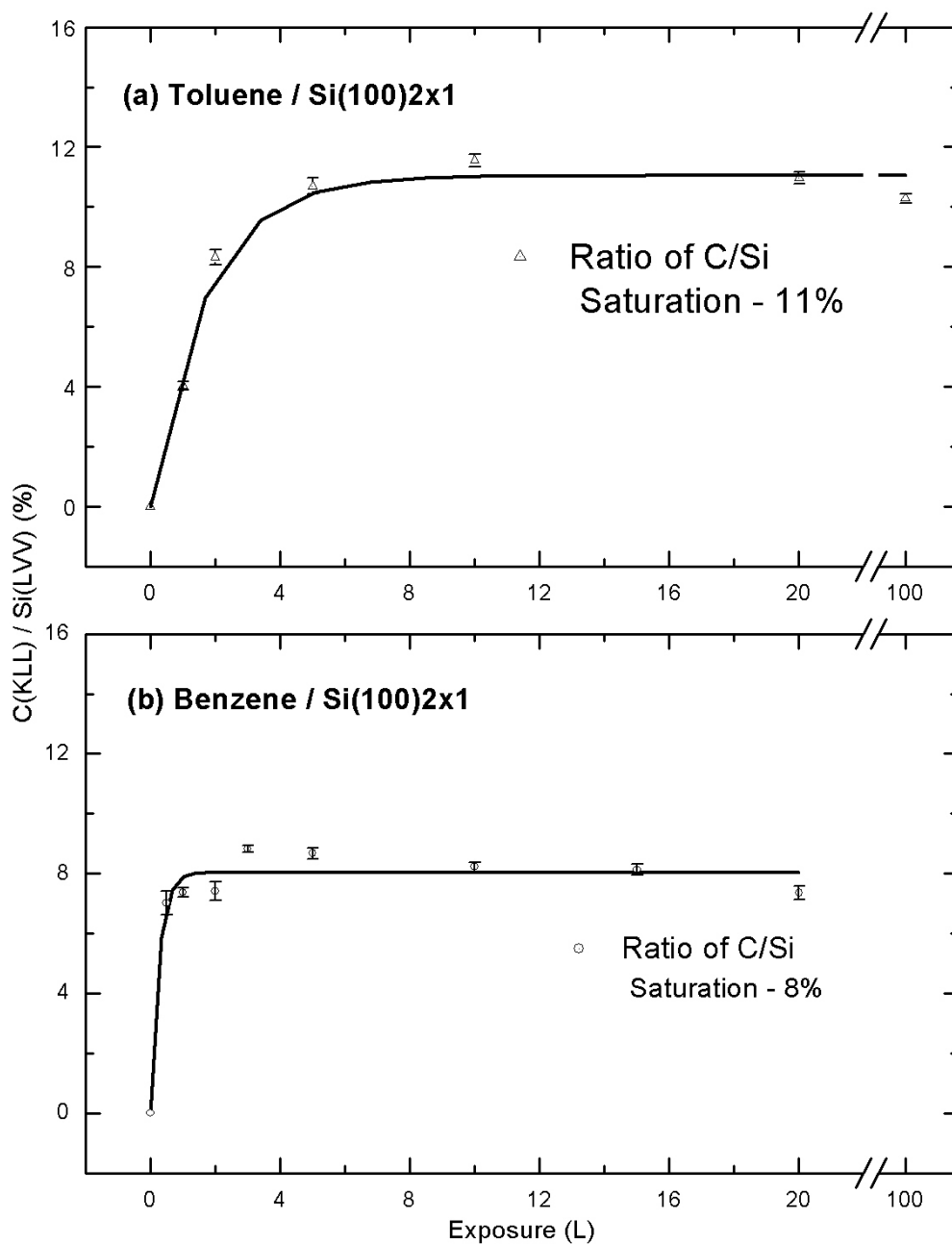


Figure 2-3 Carbon moiety as reflected by the peak-to-peak intensity ratio for the C(KLL) to Si(LVV) Auger transitions as a function of room-temperature exposure of toluene (triangle) and benzene (circle) to Si(100)2x1. The Auger peak-to-peak ratios for toluene and benzene converge to 11 % and 8 %, respectively, at saturation coverage.

corresponding TPD measurements (not shown).<sup>†</sup> The estimated saturation coverage of benzene has been determined to be 0.27 ML by Taguchi *et al.* [5]. From the ratio of the saturation ratios of toluene (11%) and benzene (8%) and after taking the number of carbon atoms in toluene (7) and benzene (6) into account, we determine the saturation coverage for toluene to be 0.33 ML. The adsorption of toluene on Si(100)2×1 is therefore ~20% higher than that of benzene, which corresponds approximately to one toluene molecule for two pairs of Si dimers on the 2×1 surface. This result suggests that the weak molecular desorption observed for toluene is not due to lower coverage but rather to possible reactions that reduce the toluene concentration. In addition, the higher saturation coverage for toluene relative to benzene indicates a stronger adsorbate-substrate interaction than adsorbate-adsorbate interaction in the case of toluene on Si(100)2×1.

In an attempt to quantify such surface reactions during the annealing process, we monitored the carbon moiety for a saturation (100 L) exposure of toluene on Si(100)2×1 after annealing the sample to successively higher temperature. Figure 2-4a shows that carbon depletion occurs in three stages involving different mechanisms. In accord with our TPD results (Figure 2-1) that show weak molecular desorption of toluene in 320-600 K, only 10% reduction in the relative C moiety is observed from the AES results, therefore suggesting that only 10% of the adsorbed toluene undergoes molecular desorption. Between 750 K and 950 K, a further 30% reduction in the carbon content is observed. Since our TDS experiments also reveal no significant molecular desorption in this temperature range, the considerable reduction in the C moiety can be attributed to thermal decomposition of toluene into hydrocarbon fragments that may undergo subsequent desorption in this temperature range. This could also be accompanied by associative hydrogen desorption with atomic hydrogen coming from the mono-hydride (Si-H) phase [23] (see Section 2.2.2 below). Finally, a significant carbon reduction occurs above 1200 K due to carbon diffusion into the bulk. The above picture is supported by the changes in the lineshape of the C(KLL) Auger peak for a

---

<sup>†</sup> The difference between the uptake curves of toluene and benzene is due to their differences in the reaction order and rate of the chemisorption. Detailed discussion about the study of chemisorption kinetics by using AES can be found in Appendix A.

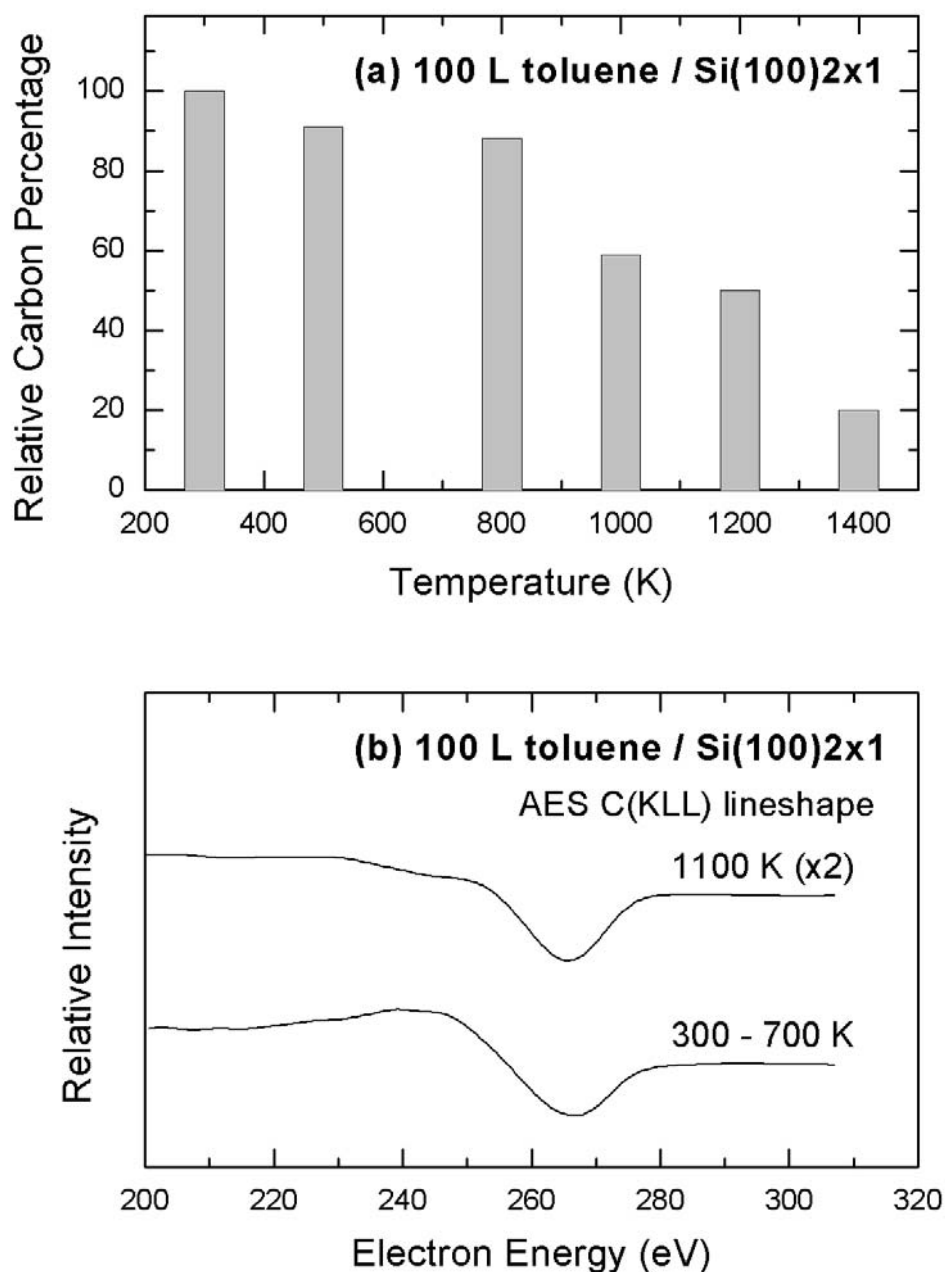


Figure 2-4 (a) Relative carbon moiety change as a function of annealing temperature for a 100 L room-temperature exposure of toluene on Si(100)2x1. (b) Typical lineshapes for the corresponding derivative C(KVV) Auger transitions after annealing the sample in 300-700 K (lower curve) and to 1100 K (upper curve). The lower and upper curves are characteristic of the lineshapes commonly found for SiC and graphite, respectively [24].

100 L RT exposure of toluene on Si(100)2×1 upon annealing the sample to different temperatures. In particular, Figure 2-4b shows that the Auger lineshape changes from that characteristic of tetrahedrally (sp<sup>3</sup>) bonded C between RT and 700 K, to that representative of graphite (sp<sup>2</sup> bonding) upon further annealing to 1100 K for 10 minutes [24]. The change in the Auger lineshape is therefore consistent with the above hypothesis of thermal decomposition of adsorbed toluene in the 750-950 K range, likely resulting in the formation of carbon cluster or graphite-like islands through a possible condensation polymerization reaction of the toluene adsorbed on the surface. This type of condensation reaction is known to be assisted by the presence of homosystemic or heterosystemic hydrogen acceptors [25]. The Si(100)2×1 surface with active dangling bonds along the dimer rows could serve as an ideal hydrogen acceptor.

Figure 2-5a shows a typical two-domain (2×1) LEED pattern of a clean Si(100) surface at RT collected at 71 eV electron energy. Upon exposure of 100 L of toluene to the clean surface at RT (Figure 2-5a), the (2×1) LEED pattern remains essentially unchanged with a slight increase in the background intensity (Figure 2-5b). It should be noted that, like benzene, a saturation coverage of toluene exhibits a two-domain (2×1) LEED pattern, and not a (2×2) or c(4×2) LEED pattern as would be expected from a well-ordered overlayer (0.25 ML). Although benzene adsorption takes place in a regular fashion along the dimer rows of the domain by forming chains of benzene molecules bound to every other Si dimer, these chains are very likely randomly registered relative to each other, resulting in an adsorption phase with one-dimensional disorder perpendicular to the Si(100) dimer rows, which slightly increases the background intensity [1]. Such a model proposed by Birkenheuer *et al.* [3] for benzene may be used to explain the similar LEED patterns observed for toluene adsorption, because there is no discernible difference observed in the LEED patterns for toluene or benzene adsorption on Si(100)2×1. Annealing a saturation coverage of toluene (0.33 ML) on the 2×1 surface to 700 K does not appear to affect the (2×1) LEED pattern. However, further annealing the sample to 850 K for 5 minutes causes the LEED pattern to become diffuse (not shown), which indicates that the sample has undergone considerable reorganization. Adsorbate relocation, decomposition and other surface reactions contribute to binding of different fragments to the Si surface involving

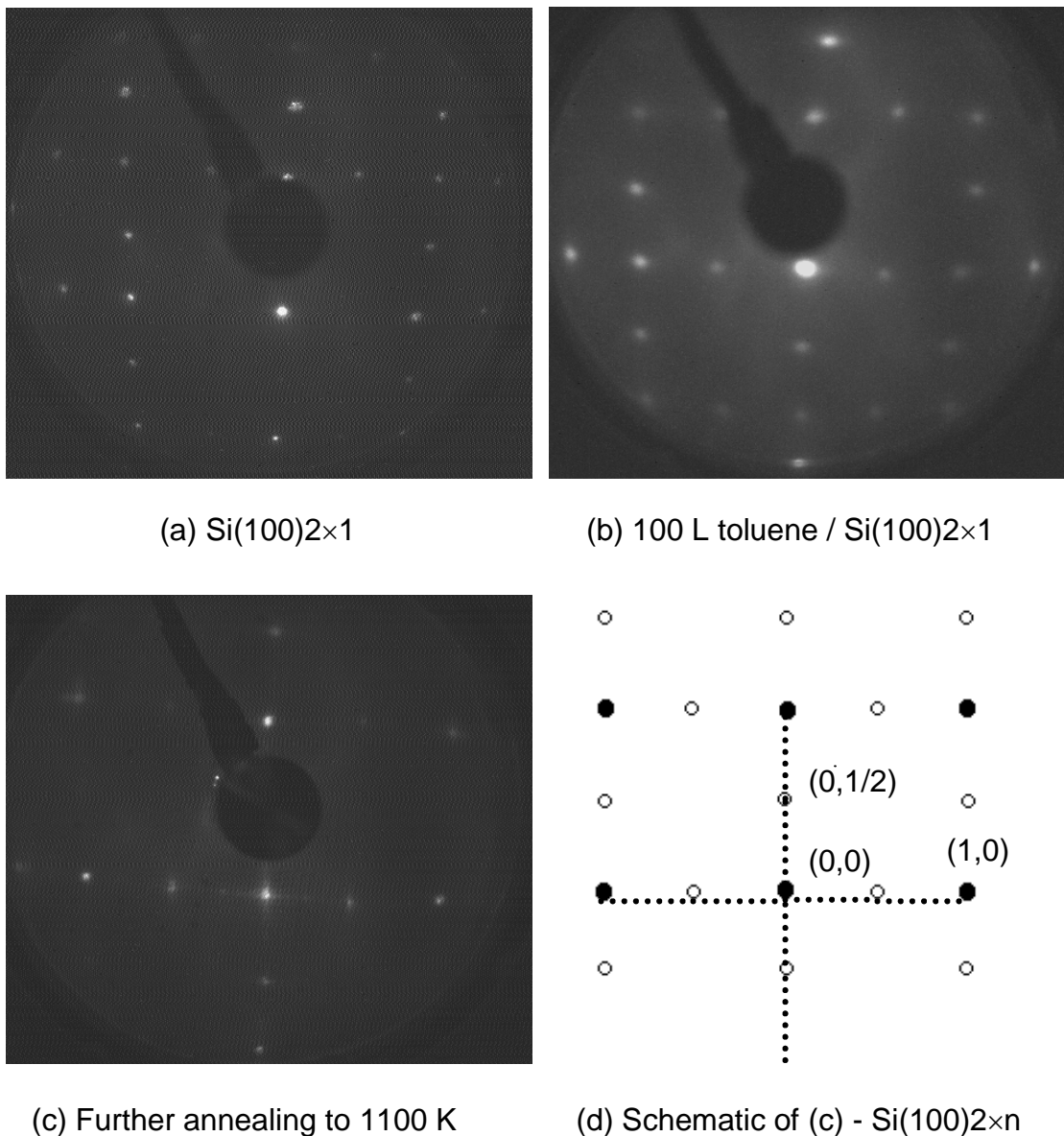


Figure 2-5 LEED patterns collected at 71 eV electron beam energy for (a) clean Si(100)2×1 at 300 K, (b) the Si(100)2×1 surface exposed to 100 L of toluene at 300 K, followed by annealing to 700 K and (c) 1100 K for 10 minutes. (d) Schematic representation of the LEED pattern shown in (c).

different bonding geometries, all of which can lead to a more diffuse LEED pattern. Further annealing the sample to 1100 K for 10 minutes recovers the basic two-domain (2×1) LEED pattern found for the clean surface but with additional streaks between the (2×1) spots, which can also be described as (2×n) features Figure 2-5c). The 2×n overlayer has been regarded as an intermediate structure between the (2×1) and c(4×4) structures [26], and is likely due to carbon contamination [27,28]. The present LEED result is consistent with the STM results by Borovsky *et al.* [13], which also suggest that toluene decomposes upon annealing and the resulting dissociated hydrocarbon fragments form SiC and eventually coalesce to form graphite islands. The open areas not covered by those carbon islands would exhibit the normal (2×1) LEED pattern.

### 2.2.2 Hydrogen evolution

In addition to the weak molecular desorption features observed earlier (Figure 2-1a), Figure 2-6 shows considerably stronger Mass 4 desorption at 820 K for a saturation exposure of deuterated toluene relative to that of deuterated benzene on Si(100)2×1 at RT. ‡ It should be noted that the TDS profiles for normal and deuterated toluene are found to be identical, indicating no isotopic effect on the adsorption process. Deuterated toluene is used in the present TDS experiment to avoid the large H<sub>2</sub> background commonly found in stainless steel ultrahigh vacuum chambers. The temperature of D<sub>2</sub> evolution (820 K) is indicative of associative desorption of D atoms from mono-deuteride (Si–D) on the silicon surface, rather than from the di-deuteride (Si–D<sub>2</sub>) with a characteristic desorption maximum at 700 K [29]. Hydrogen evolution for d<sub>8</sub>-toluene on Si(100)2×1 may therefore involve partial dehydrogenation of adsorbed toluene to form Si–D and other fragments (e.g. C<sub>7</sub>-benzyl

---

‡ Unlike the benzene TDS with two features in Figure 2-1b, the molecular desorption of benzene in Figure 2-6b appears to be only one peak. It is because of the intense desorption from the β state overlaps the γ-state desorption at saturation exposures. At low coverage, if it takes a while before starting TDS, some adsorbates in the β state may convert to the γ state, and make more desorption from the γ state.



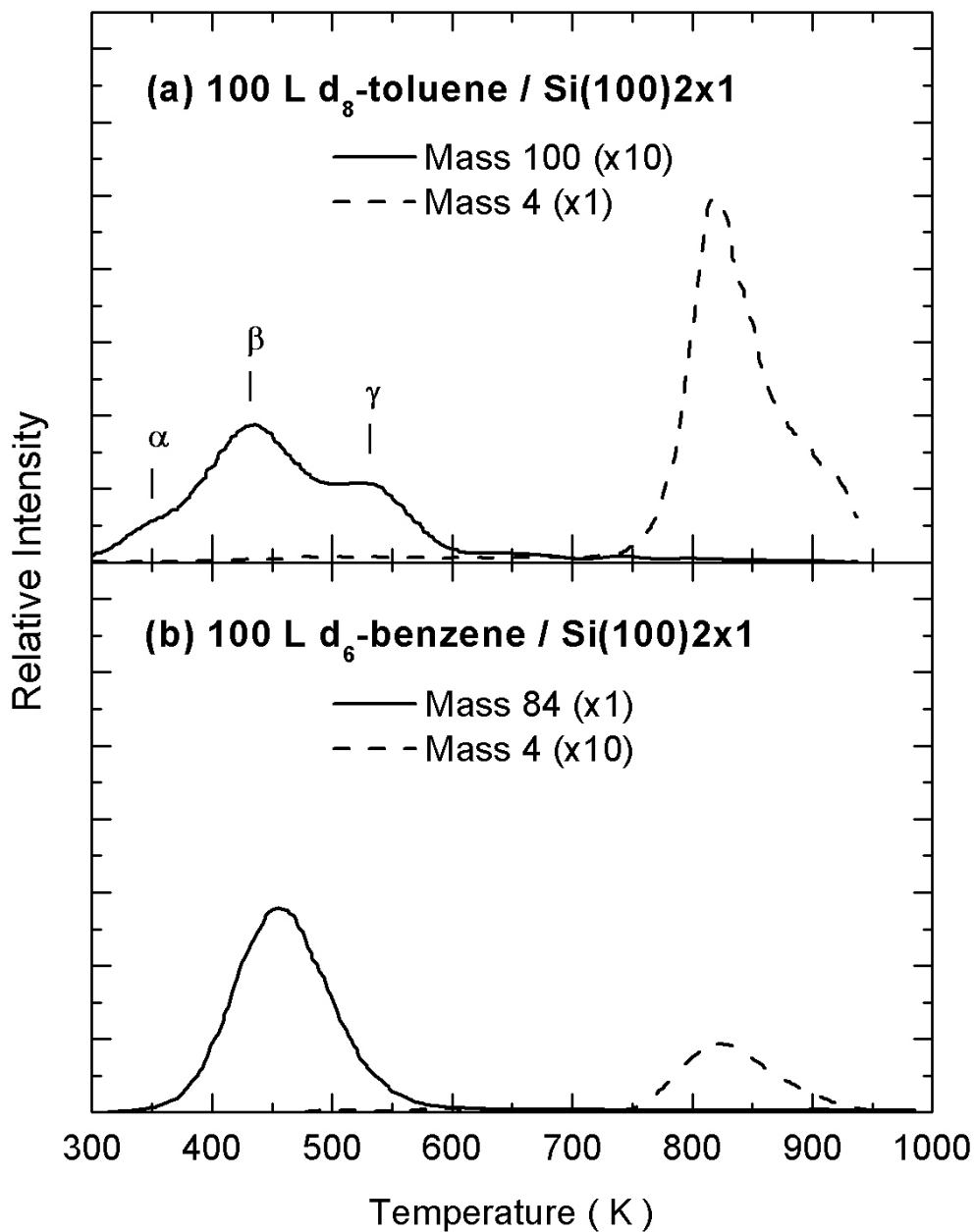


Figure 2-6 Comparison of the molecular (solid lines) and Mass 4 (dashed lines) thermal desorption profiles of 100 L room-temperature exposures of (a)  $d_8$ -toluene and (b)  $d_6$ -benzene to Si(100)2 $\times$ 1. The parent masses for  $d_8$ -toluene and  $d_6$ -benzene correspond to Mass 100 and Mass 84, respectively.

species [30]) and/or to complete dissociation of toluene into C and D atoms on the Si surface. In contrast to the small ratio of D<sub>2</sub> evolution (Mass 4) relative to molecular desorption (parent mass) for d<sub>6</sub>-benzene (0.030), the corresponding ratio for d<sub>8</sub>-toluene (15) is found to be significantly larger, indicating that hydrogen evolution is a predominant pathway over molecular desorption for toluene. Given that the C–H bond strengths of C<sub>6</sub>H<sub>5</sub>–H and C<sub>6</sub>H<sub>5</sub>CH<sub>2</sub>–H are typically 110 kcal/mol and 85 kcal/mol respectively [31], hydrogen evolution from the aromatic ring (aromatic hydrogen) for both benzene and toluene below the molecular desorption temperature (<600 K) therefore appears unlikely. Rather, the D atoms predominantly come from the methyl group (benzylic hydrogen) at this lower temperature. However, the prospect of minor hydrogen evolution pathways for benzene involving adsorption on defect sites cannot be ruled out [8]. Since a saturation coverage corresponds to one d<sub>8</sub>-toluene molecule for every two Si dimers, only one out of the three possible benzylic D atoms can be sufficiently close to be abstracted by a neighbouring Si dimer on the surface, which is consistent with the formation of Si–D structure. Finally, in order to determine whether hydrogen abstraction could occur upon adsorption of toluene, we saturated any unoccupied bonding sites with hydrogen atoms for a saturation coverage of d<sub>8</sub>-toluene on Si(100)2×1 at RT. Dosing of atomic hydrogen was accomplished by exposing the sample with 2000 L of H<sub>2</sub> with a hot W filament positioned 3 cm from the sample. Since blocking of the active sites by atomic hydrogen would prevent hydrogen abstraction (from the methyl group) to take place during the subsequent thermal annealing process, the lack of any increase in the molecular desorption features suggests that hydrogen abstraction has already occurred upon adsorption of toluene at RT. The abundance of hydrogen atoms on the surface after the post-exposure also does not appear to reverse the benzylic hydrogen abstraction of the methyl group in toluene, suggesting it to be an irreversible process at RT. The recent FTIR study by Coulter *et al.* also confirms that the dissociation of substituted aromatic molecules upon adsorption arises almost entirely by C–H bond cleavage of the functional group external to the aromatic ring [15].

For TDS for the saturation chemisorption, the molecular desorption intensity for the β state relative to that for the γ state for d<sub>8</sub>-toluene adsorption on Si(100)2×1 (Figure 2-6a) is found to be considerably smaller than that for d<sub>6</sub>-benzene adsorption (Figure 2-6b – See also

Figure 2-1b). Since the adsorption of the benzene ring is expected to involve similar adsorption geometries, the presence of the methyl group in toluene evidently only affects the  $\beta$  state, which is consistent with the bonding model that the  $\beta$  state involves single-dimer configurations that are more susceptible to steric effects acting on the methyl group. On the other hand, the  $\gamma$  state involves the double-dimer configurations, whereby the methyl group is oriented away from the surface and hence should have little effect on the adsorption.

Hydrogen evolution involving the Si–D bonding structure should follow the first-order desorption kinetics [23,32,33]. In contrast to a typical first-order desorption peak shape (i.e. with a faster drop-off at the higher temperature side), the slower drop-off at the higher temperature side of the Mass 4 TDS peak observed in Figure 2-6a indicates additional processes that increase hydrogen evolution at the higher temperature. According to our AES results that show increased depletion of carbon moiety in this temperature range (Figure 2-4), we expect desorption of hydrocarbon fragments as a result of dissociation of adsorbed toluene. Associative desorption of D atoms also frees up more active sites on the surface, further enhancing hydrogen abstraction from the dissociated hydrocarbon fragments.

### **2.2.3 Effects of surface condition on thermal chemistry**

Figure 2-7 compares the TDS profiles of the parent mass (Mass 100) and Mass 4 for 100 L RT exposure of  $d_8$ -toluene on the  $2\times 1$  and amorphous Si(100) surfaces. An amorphous Si surface was produced by ion sputtering in  $2\times 10^{-5}$  torr of Argon for 1 hour at 1 keV beam energy, and the lack of any long-range order was confirmed by the absence of a LEED pattern. The total areas for Mass 100 and Mass 4 for the amorphous surface (Figure 2-7b) have been reduced by 1/3 and 3/5, respectively, relative to the  $2\times 1$  surface (Figure 2-7a). The general decrease in the overall intensity for the parent mass indicates reduction in the number of active sites available for molecular adsorption after Ar sputtering. The weakening of peaks at 430 K ( $\beta$  state) and 530 K ( $\gamma$  state) for the amorphous Si surface is consistent with the general assignment of these states to terrace sites, while the strengthening of the TDS feature near 350 K clearly indicates that the  $\alpha$  state involves adsorption on defect sites. In Section 2.2.1, we propose that the  $\beta$  state involves adsorption in the single-dimer

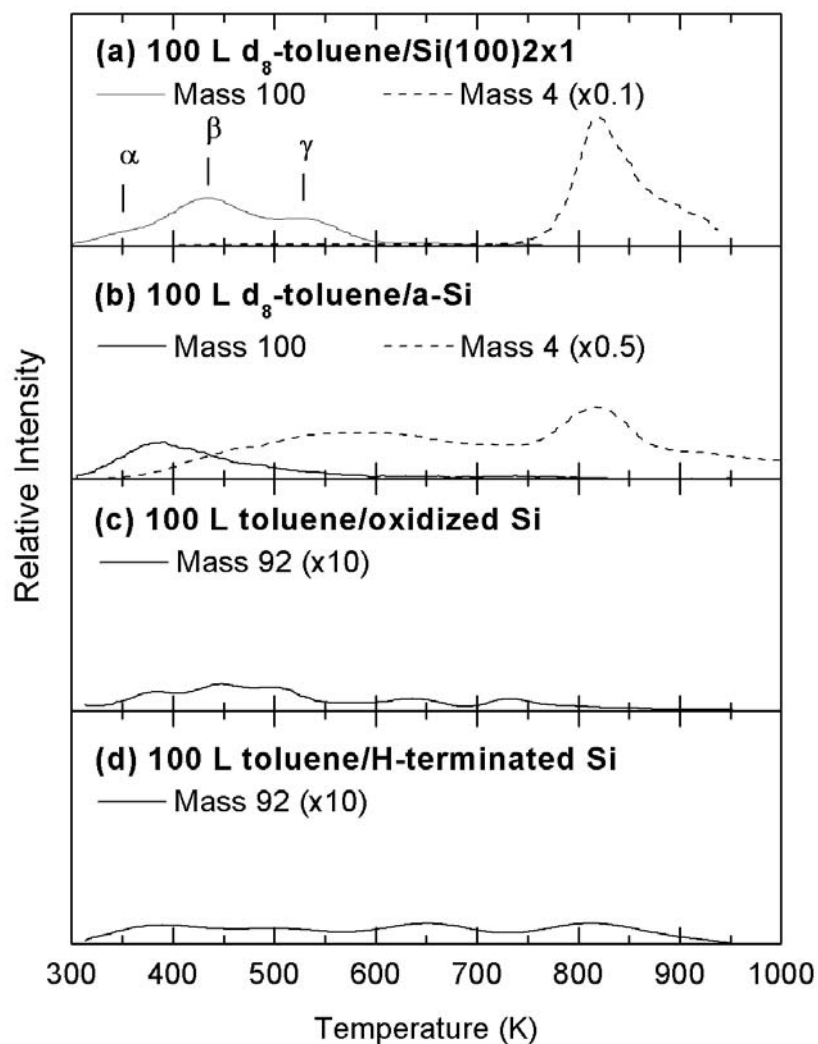


Figure 2-7 Comparison of the molecular and Mass 4 TDS profiles for 100 L room-temperature exposures of (d<sub>8</sub>-)toluene to the (a) 2×1, (b) amorphous, (c) oxidized, and (d) H-terminated Si(100). An amorphous Si surface is obtained by ion sputtering in 2×10<sup>-5</sup> Torr of Argon for 1 hour at 1 keV beam energy. An oxidized Si surface is produced by exposing a clean 2×1 surface with a 300 L exposure of O<sub>2</sub> while a H-terminated Si(100) is prepared by exposing 2000 L of H<sub>2</sub> to a clean 2×1 surface (keep at RT with liquid nitrogen) with a hot W filament positioned 5 cm away, using liquid nitrogen. The parent masses for d<sub>8</sub>-toluene (a, b) and normal toluene (c, d) correspond to Mass 100 and Mass 92, respectively.

configurations, while the  $\gamma$  state involves the double-dimer bonding geometries. Furthermore, the presence of a broad new desorption band centered at 600 K in the Mass 4 TDS profile indicates that hydrogen evolution originates from a variety of bonding geometries (all with its own adsorption energies). The source of the hydrogen atoms can be the absorbed toluene itself or any fragments resulting from thermal decomposition during the TDS experiment. Hydrogen abstraction from the methyl group opens up new opportunity for  $\sigma$ -bonding of the methylene group to the Si surface, which could provide the possibility for further reactions. In the case of  $d_6$ -benzene on sputtered Si [18], there is an increase in hydrogen evolution at  $\sim 800$  K, without any broad TDS feature near 600 K, indicating that the majority of benzene molecules have already desorbed molecularly before reaching this temperature.

The TDS profiles for a saturation coverage of normal toluene on an oxidized and H-terminated Si(100) are also shown in Figure 2-7. An oxidized Si surface was obtained by exposing a clean Si(100)2 $\times$ 1 with 300 L of O<sub>2</sub> while a H-terminated Si(100) was prepared by exposing 2000 L of H<sub>2</sub> to the 2 $\times$ 1 sample with a hot W filament positioned 5 cm away. The TDS profiles for the parent mass are found to be featureless and greatly reduced in intensity after exposure of O<sub>2</sub> or atomic H, suggesting that pre-exposure of oxygen and hydrogen has the effect of filling the active sites and hence preventing subsequent adsorption of toluene on Si(100)2 $\times$ 1.

#### **2.2.4 Surface-mediated oxidation reaction**

As shown in Figure 2-8a, a 300 L O<sub>2</sub> post-exposure to Si(100)2 $\times$ 1 saturated with 100 L of  $d_8$ -toluene at RT is found to have a dramatic effect on the TDS profiles of Mass 100 (molecular desorption) and Mass 4 (D<sub>2</sub> evolution). The post-oxidation appears to greatly reduce molecular desorption of toluene while enhancing hydrogen evolution. In particular, the ratio of the integrated area for the Mass 100 TDS profile to that of the Mass 4 TDS profile is

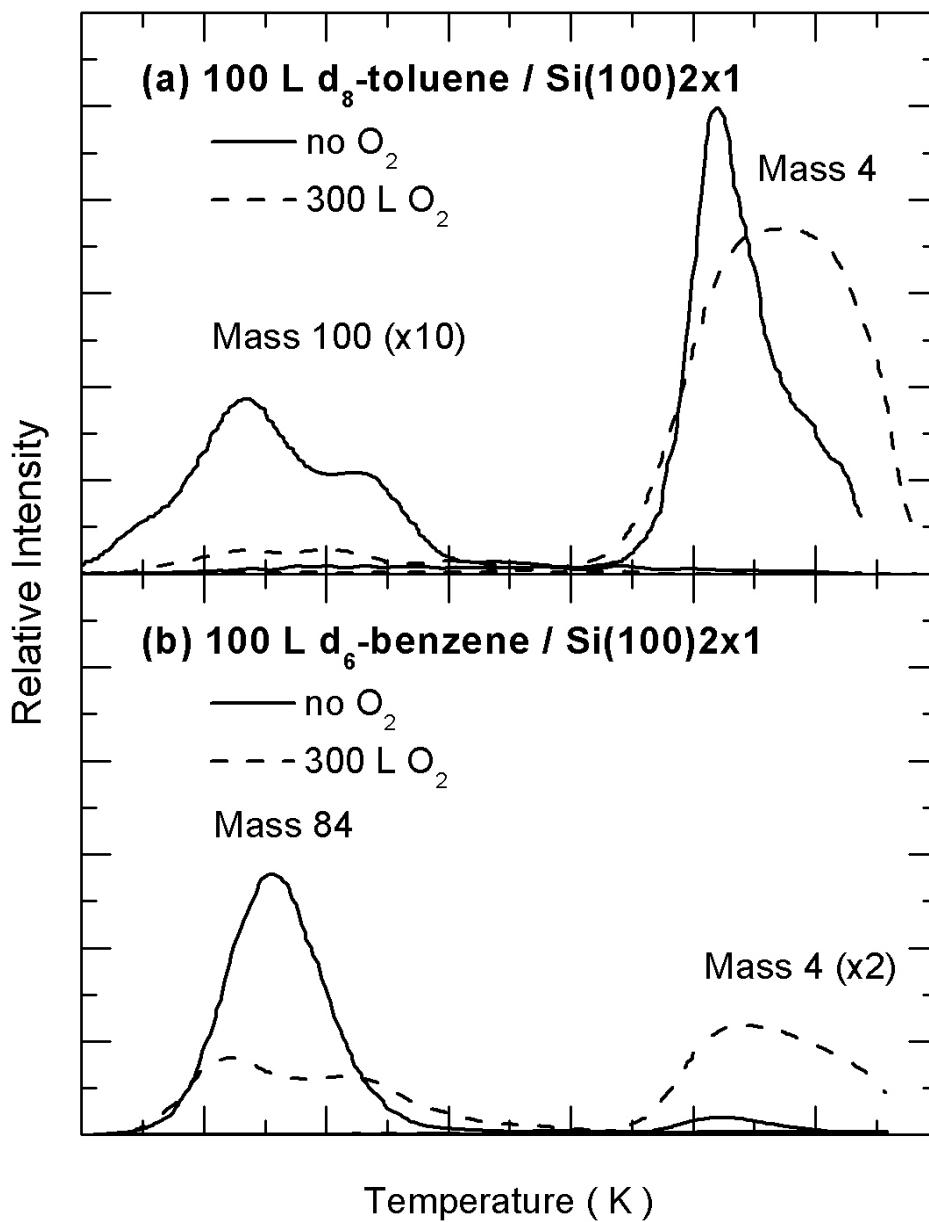


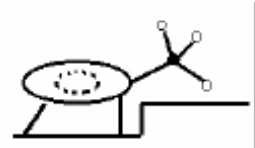
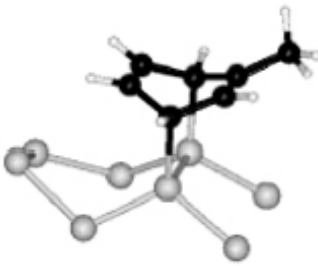
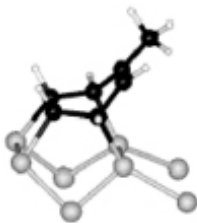

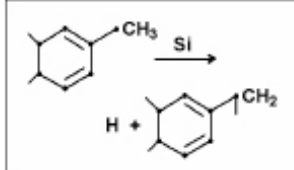
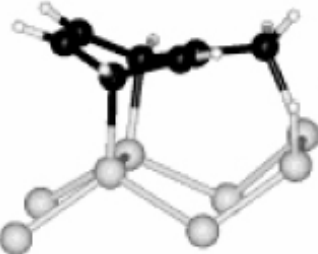
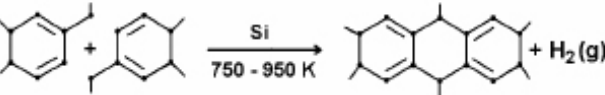
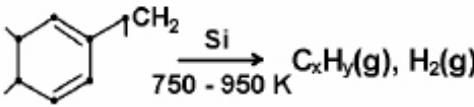
Figure 2-8 Comparison of the molecular and Mass 4 thermal desorption profiles of 100 L room-temperature exposures of (a) d<sub>8</sub>-toluene and (b) d<sub>6</sub>-benzene to Si(100)2×1 with (dashed lines) and without (solid lines) 300 L of O<sub>2</sub> post-exposure. The parent masses for d<sub>8</sub>-toluene and d<sub>6</sub>-benzene correspond to Mass 100 and Mass 84, respectively.

found to decrease from 0.07 to 0.01 by the O<sub>2</sub> post-exposure. It therefore appears that post-oxidation greatly enhances the dissociation of d<sub>8</sub>-toluene into C and D atoms on the Si surface. Figure 2-8b shows similar effects for a 300 L post-exposure of O<sub>2</sub> on Si(100)2×1 saturated with 100 L of d<sub>6</sub>-benzene, whereby the ratio of the integrated area for the Mass 84 TDS profile to that of the Mass 4 TDS profile is found to reduce from 30 to 2 by the post-oxidation. Evidently, the enhanced dissociation of adsorbed toluene caused by post-oxidation is not exclusively related to oxygen interaction with the methyl group, because post-oxidation also appears to facilitate dissociation of both toluene and benzene on Si(100)2×1. It should be noted that neither benzene nor toluene readily reacts with O<sub>2</sub> (g) in the absence of a catalyst [34,35]. The low temperature at which toluene (benzene) begins to desorb (~350 K) would suggest that either O reacts with the adsorbed toluene (benzene) directly near RT in a surface-mediated type reaction, or O stabilizes the adsorption of toluene (without a direct reaction) to a higher temperature at which hydrogen evolution occurs. The complete disappearance of the 2×1 LEED pattern after O<sub>2</sub> post-exposure is in favour of the former mechanism. The coadsorption with O<sub>2</sub> has also been found to increase the adsorption energy of NH<sub>3</sub> on a Cu surface, resulting in the N–H bond breakage and the subsequent formation of hydroxyl species or H<sub>2</sub>O [36].

### 2.3 Concluding remarks

Room-temperature adsorption of toluene on the 2×1 and modified Si(100) surfaces has been investigated by using TDS, AES and LEED, and the results are compared to that of benzene. Table 2-1 illustrates the key observations for toluene adsorption obtained in the present work. In particular, three molecular desorption states are observed at 350 K ( $\alpha$ ), 430 K ( $\beta$ ) and 530 K ( $\gamma$ ), which involve RT adsorption on defect sites, single-dimer and double-dimer geometries of Si(100), respectively. The TDS data for toluene on sputtered Si surface confirms that the desorption peak at 350 K is related to adsorption on defect sites. Toluene in the double-dimer adsorption configuration ( $\gamma$  state) undergoes molecular desorption, while those in the  $\alpha$  and  $\beta$  states involve the loss of benzylic hydrogen at RT, leaving the methylene group bound to a neighbouring dimer on the surface. This result also favours the

Table 2-1 Summary of plausible surface processes of toluene on Si(100)2×1 in various temperature ranges.

Molecular Desorption	$\alpha$ state 350 K	$\beta$ state 430 K	$\gamma$ state 485 K
Adsorption Configuration	 <p>Defect site</p>	 <p>Single-dimer</p>	 <p>Double-dimer</p>
H Abstraction at RT	 		N / A
Condensation Polymerization			N / A
Dissociative Desorption			N / A
Carbon dissolving into the Si bulk	1200 - 1400 K		N / A



transformation from the  $\gamma$  state to the  $\beta$  state, and the resulting higher saturation coverage (0.33 M) for toluene than benzene (0.27 M) is supported by our AES results. Such hydrogen abstraction appears to stabilize the adsorbate on Si(100) at higher temperature and facilitate further reactions, such as condensation polymerization and/or dissociation at 750-950 K. Further annealing to above 1200 K causes carbon diffusion into the bulk. In the case of benzene, three molecular desorption peaks are also observed and found to have similar desorption maxima to those of the corresponding peaks for toluene. These TDS data therefore reflect the similarity in the nature of the adsorption states of these aromatic molecules on Si(100)2 $\times$ 1. However, almost all of the adsorbed benzene undergoes molecular desorption without any evidence of further reactions at higher temperature. These differences show that toluene is more reactive than benzene toward the Si(100) surfaces. Surface roughness and post-oxidation also significantly improve the reactivity of aromatic compounds on Si surface.

In our previous TDS study of  $d_8$ -toluene on Si(111)7 $\times$ 7 [12], two intense well-defined desorption peaks for the parent mass were observed at 370 K and 420 K, which appear to have similar exposure dependence as the  $\beta$  and  $\gamma$  states for the Si(100)2 $\times$ 1 surface observed in the present work. A weak Mass 4 desorption at 800 K involving the Si–D configuration was also observed for the exposure of  $d_8$ -toluene to the 7 $\times$ 7 surface. A broad Mass 4 desorption peak at 540 K was observed for sputtered Si(111) surface and can be attributed to direct evolution of D<sub>2</sub> during thermal dissociation of the adsorbed toluene. The presence of the Mass 4 desorption peak at 800 K for the exposure of other selected deuterated isotopes (CH<sub>3</sub>-C<sub>6</sub>D<sub>5</sub> and CD<sub>3</sub>-C<sub>6</sub>H<sub>5</sub>) and the lack of Mass 4 evolution for the  $d_6$ -benzene exposure to Si(111)7 $\times$ 7 suggest that deposition of D atoms on Si(111) is due to a methyl-to-surface interaction, which results in complete dissociation of the deuterated toluene samples. As with the Si(100)2 $\times$ 1 surface, dissociation of toluene is found to be dramatically increased by a 2000 L O<sub>2</sub> post-exposure on Si(111)7 $\times$ 7. The present study therefore shows that the general molecular desorption behaviour of toluene on Si(100)2 $\times$ 1 is similar to that on Si(111)7 $\times$ 7 [12], with minor differences in the temperatures for various desorption maxima. The significant differences in the extent for molecular desorption and hydrogen evolution show that Si(100) is more reactive than Si(111).

In summary, the present work shows the intricate thermal chemistry of toluene on Si(100). On the one hand, upon adsorption on such a well-ordered surface as Si(100) $2\times 1$ , the aromatic ring of these cyclic hydrocarbon compounds exerts significant selectivity on the bonding configurations, and bonding through specific functional groups (such as the methyl group) might be enhanced by annealing [37]. On the other hand, the methyl group plays a decisive role in the subsequent thermal surface reactions, such as decomposition and condensation polymerization. Additional studies involving other techniques will be of great interest in providing further insights into the surface chemistry of aromatic hydrocarbons on Si(100).

## 2.4 References

- [1] B.I. Craig, Surf. Sci. 280 (1993) L279.
- [2] H.D. Jeong, S. Ryu, Y.S. Lee, and S. Kim, Surf. Sci. 344 (1995) L1226.
- [3] U. Birkenheuer, U. Gutdeutsch, and N. Rosch, Surf. Sci. 409 (1998) 213.
- [4] C.D. MacPherson, D.Q. Hu, and K.T. Leung, Solid State Comm. 80 (1991) 217.
- [5] Y. Taguchi, M. Fujisawa, T. Takaoka, T. Okada, and M. Nishijima, J. Chem. Phys. 95 (1991) 6870.
- [6] Y. Taguchi, Y. Ohta, T. Katsumi, K. Ichikawa, and O. Aita, J. Electron Spectrosc. Relat. Phenom. 88-91 (1998) 671.
- [7] S. Gokhale, P. Trischberger, D. Menzel, W. Widdra, H. Droge, H.-P. Steinruck, U. Birkenheuer, U. Gutdeutsch, and N. Rosch, J. Chem. Phys. 108 (1998) 5554.
- [8] M.J. Kong, A.V. Teplyakov, J.G. Lyubovitsky, and S.F. Bent, Surf. Sci. 411 (1998) 286.
- [9] G.P. Lopinski, D.J. Moffatt, and R.A. Wolkow, Chem. Phys. Lett. 282 (1998) 305.  
Also: G.P. Lopinski, T.M. Fortier, D.J. Moffatt, and R.A. Wolkow, J. Vac. Sci. Tech. A 16 (1998) 1037.
- [10] B. Borovsky, M. Krueger, and E. Ganz, Phys. Rev. B 57 (1998) R4269.
- [11] R.A. Wolkow, G.P. Lopinski, and D.J. Moffatt, Surf. Sci. 416 (1998) L1107.
- [12] C.D. MacPherson and K.T. Leung, Surf. Sci. 326 (1995) 141.
- [13] B. Borovsky, M. Krueger, and E. Ganz, J. Vac. Sci. Technol. B 17 (1999) 7.
- [14] C.D. MacPherson, D.Q. Hu, and K.T. Leung, Surf. Sci. 322 (1995) 58.
- [15] S.K. Coulter, J.S. Hovis, M.D. Ellison, and R.J. Hamers, J. Vac. Sci. Technol. A 18 (2000) 1965.
- [16] H. Froitzheim, P. Schenk, and G. Wedler, J. Vac. Sci. Technol. A 11 (1993) 345.
- [17] C.D. MacPherson, D.Q. Hu, and K.T. Leung, Surf. Sci. 276 (1992) 156.
- [18] C.D. MacPherson and K.T. Leung, Surf. Sci. 324 (1995) 202.
- [19] NIST/EPA/NIH Mass Spectral Library, NIST'98 with Windows, Version 1.7 software (1996).
- [20] P.A. Redhead, Vacuum 12 (1962) 203.
- [21] J.A. Kubby and J.J. Boland, Surf. Sci. Rep. 26 (1996) 62.

- [22] C.C. Cheng, R.M. Wallace, P.A. Taylor, W.J. Choke, and J.T. Yates, Jr., *J. Appl. Phys.* 67 (1990) 3693.
- [23] K. Sinniah, M.G. Sherman, L.B. Lewis, W.H. Weinberg, J.T. Yates, Jr., and K.C. Janda, *Phys. Rev. Lett.* 62 (1989) 567. Also: K. Sinniah, M.G. Sherman, L.B. Lewis, W.H. Weinberg, J.T. Yates, Jr., and K.C. Janda, *J. Chem. Phys.* 92 (1990) 5700.
- [24] A.K. Green and V. Rehn, *J. Vac. Sci. Technol A* 1 (1983) 1877; and references therein.
- [25] J.R. Anderson, Q.N. Dong, Y.F. Chang, and R.J. Western, *J. Catal.* 127 (1991) 113.
- [26] D.-S. Lin and P.-H. Wu, *Surf. Sci.* 397 (1998) L273.
- [27] K. Miki, K. Sakamoto, and T. Sakamoto, *Appl. Phys. Lett.* 71 (1997) 3266.
- [28] H. Norenberg and G.A.D. Briggs, *Surf. Sci.* 430 (1999) 154.
- [29] M. Suemitsu, H. Nakazawa, and N. Miyamoto, *Appl. Surf. Sci.* 82/83 (1994) 449.
- [30] N.R. Avery, *J. Am. Chem. Soc., Chem. Comm.* 3 (1988) 153.
- [31] “CRC Handbook of Chemistry and Physics”, 64<sup>th</sup> edition, Ed. R.C. Weast (CRC Press Inc., Boca Raton, 1983).
- [32] U. Hofer, L. Li, and T.F. Heinz, *Phys. Rev. B* 45 (1992) 9485.
- [33] L.A. Okada, M.L. Wise, and S.M. George, *Appl. Surf. Sci.* 82/83 (1994) 410.
- [34] R.A. Sheldon and N. de Heij, in: “The Role of Oxygen in Chemistry and Biochemistry,” Eds. W. Ando and Y. Moro-Oka (Elsevier, Amsterdam, 1988) p. 243.
- [35] R.N. Patel, in “Catalysis of Organic Reactions”, Ed. R.L. Augustine (Dekker, New York, 1985) p. 327.
- [36] G.J.C.S. van de Kerkhof, W. Biemolt, A.P.J. Jansen, and R.A. van Santen, *Surf. Sci.* 284 (1993) 361; and references therein.
- [37] R.J. Hamers, J.S. Hovis, C.M. Greenlief, and D.F. Padowitz, *Jpn. J. Appl. Phys.* 38 (1999) 3879.

## Chapter 3

# Effects of methyl substitution on room-temperature chemisorption of *para*-xylene on Si(100)2×1 and modified surfaces: A thermal desorption and DFT study

### 3.1 Introduction

The thermal chemistry of benzene and toluene (or methylbenzene) on Si(100) surface has been investigated in our early work [1]. The methyl group in toluene appears to introduce more reactivity and additional surface processes than benzene. The presence of two methyl groups in xylene (or dimethylbenzene) may also produce similar effects as those of toluene on Si(100). The relative positions of the two methyl groups on the benzene ring give rise to different isomers, which may in turn affect their surface chemistry and other properties. Using Fourier-transform infrared (FTIR) spectroscopy, Coulter *et al.* observed the same bonding structures for methyl-substituted aromatic hydrocarbons (toluene and xylene) as benzene on Si(100), and further suggested that dissociation occurs predominantly *via* C–H bond cleavage of the methyl group after adsorption [2].

In the present work, the room-temperature (RT) adsorption, thermal desorption and other surface chemical processes of *p*-xylene on Si(100) have been investigated. Of the three xylene isomers: *p*-xylene (or 1,4-dimethylbenzene), *m*-xylene (or 1,3-dimethylbenzene) and *o*-xylene (or 1,2-dimethylbenzene), *p*-xylene represents the most symmetrical isomer with the two methyl groups farthest apart, which therefore provides a more appropriate platform for investigating the effect of methyl content when compared with benzene and toluene. The effects of the relative locations of the methyl groups on silicon surface chemistry will be the subject of future work. Both *p*-xylene-d<sub>10</sub> and *p*-xylene-dimethyl-d<sub>6</sub> are used in the present experiment to investigate the selective reactivity of the phenyl and methyl groups on Si(100).

## 3.2 Results and Discussion

### 3.2.1 Molecular desorption

The adsorption of *p*-xylene on Si(100)2×1 at RT has been studied as a function of exposure by LEED and AES. Upon different exposures of *p*-xylene to the Si(100) surface at RT, only a slight increase in the background intensity was observed in the two-domain (2×1) LEED pattern characteristic of a clean Si(100) surface, which suggests that the dimer-row structure of the Si substrate is generally preserved after the adsorption of *p*-xylene. The peak-to-peak ratio of the C(KLL) Auger peak to that of the Si(LVV) Auger peak is used to indicate the relative carbon moiety on the surface. Figure 3-1 shows this ratio as a function of RT exposure for *p*-xylene, toluene and benzene on Si(100)2×1. The data for each of the adsorbates was compared with first-order and second-order adsorption kinetics [3] and they are all found to follow the first-order kinetics, indicating a non-dissociative, i.e. molecular, chemisorption. The observed non-dissociative nature of the adsorption process for *p*-xylene, toluene and benzene therefore suggests that the adsorption of these aromatic molecules involves a common mechanism, likely via cycloaddition of the aromatic ring. For *p*-xylene, the ratio appears to reach its saturation value at 2 L exposure, which generally marks the completion of adsorption of the first monolayer (ML). The saturation coverage of benzene has been estimated to be 0.27 ML by Taguchi *et al.* [4]. From the ratio of the saturation values for relative C surface moiety of *p*-xylene (12%) and benzene (8.0%) and after taking into account the number of carbon atoms in *p*-xylene (8) and benzene (6), the saturation coverage for *p*-xylene is estimated to be 0.30 ML, which corresponds approximately to two molecules for every three Si dimers on the 2×1 surface. It should be noted that the slightly higher value of the saturation coverage for *p*-xylene on Si(100)2×1 relative to that for benzene could be attributed to additional interaction due to one of its methyl groups with the Si surface. On the other hand, that this saturation coverage of *p*-xylene (0.30 ML) is lower than that of toluene on Si(100)2×1 (0.33 ML) could be the result of steric effects due to the presence of the second methyl group in *p*-xylene.

Figure 3-2a shows the TDS profiles of Mass 98 (base-ion mass) and Mass 4 (D<sub>2</sub>) for a 5 L RT exposure of *p*-xylene-d<sub>10</sub> on Si(100)2×1. It should be noted that deuterated *p*-xylene

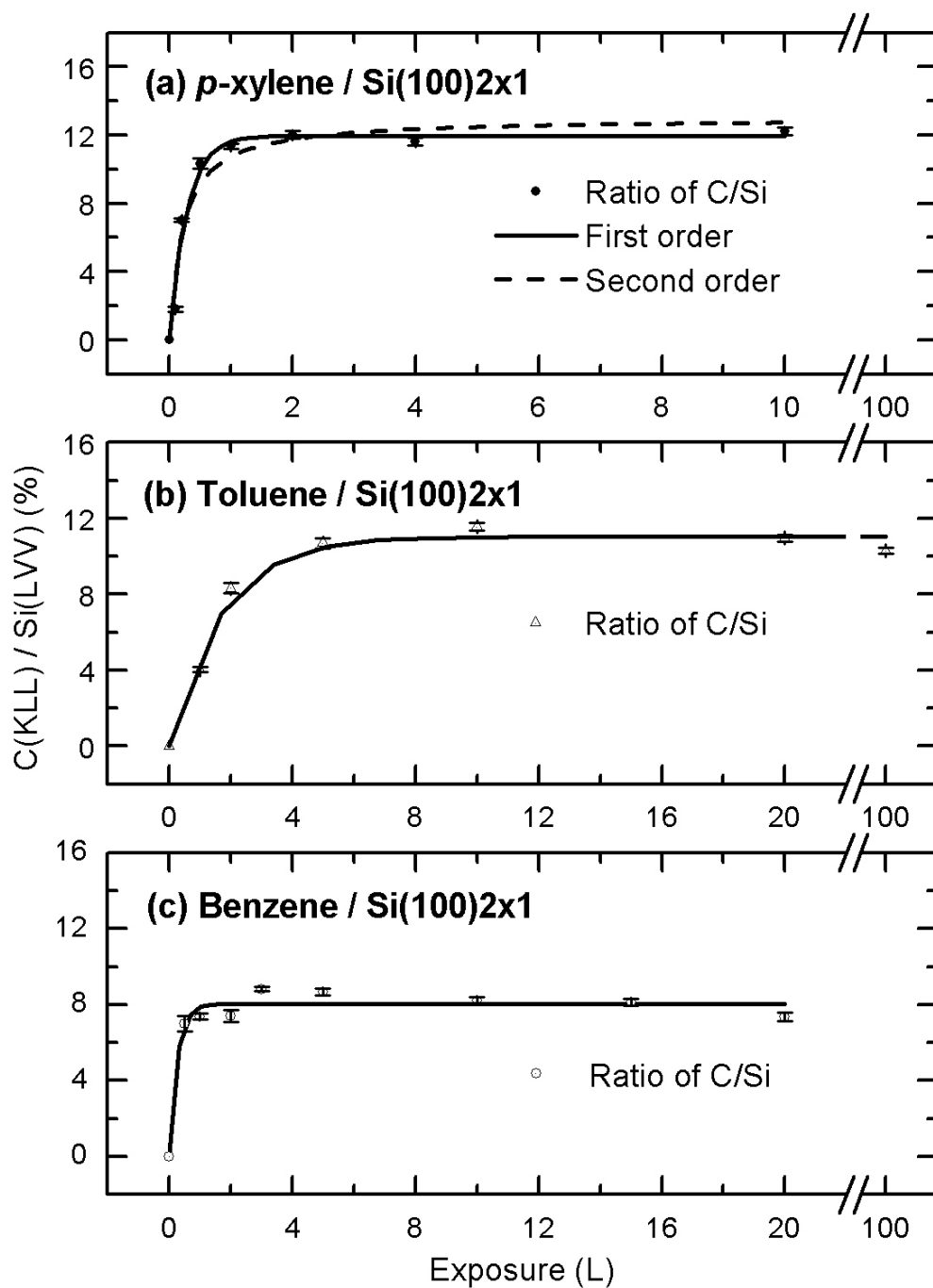


Figure 3-1 Relative carbon moiety as indicated by the peak-to-peak intensity ratio for the C(KLL) to Si(LVV) Auger transitions as a function of room-temperature exposure of (a) *p*-xylene, (b) toluene and (c) benzene to  $Si(100)2 \times 1$ . The experimental data are found to follow first-order kinetics.

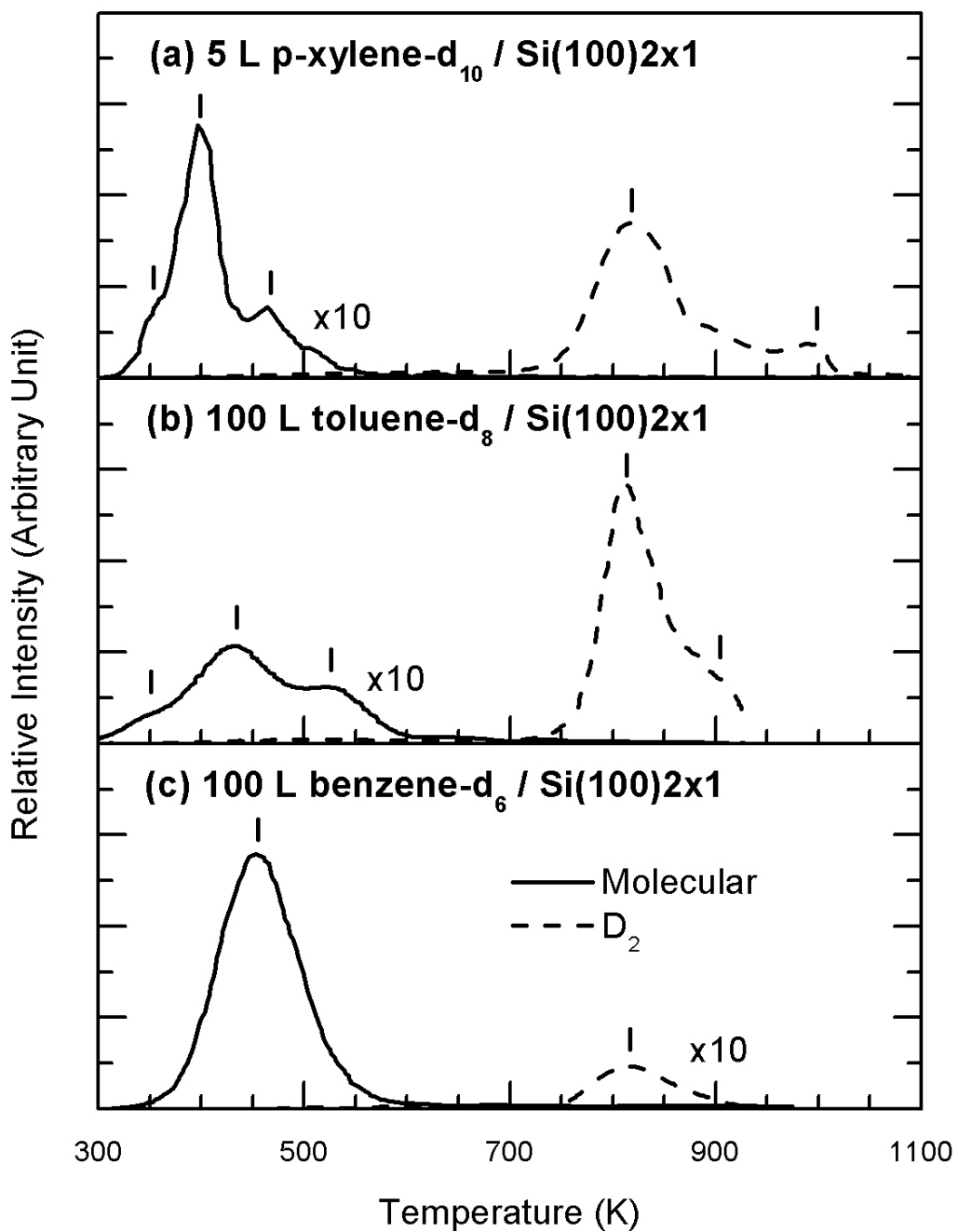


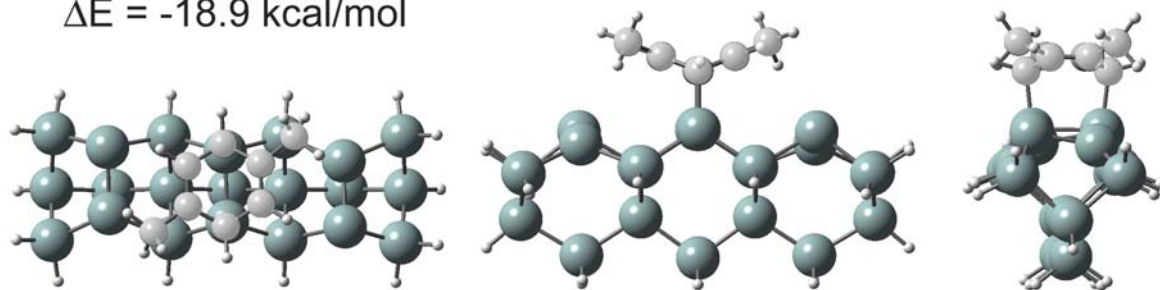
Figure 3-2 Comparison of thermal desorption profiles of molecular (solid lines) and mass-4 ( $D_2$ ) desorption (dashed lines) for saturation exposures of (a)  $p$ -xylene- $d_{10}$ , (b) toluene- $d_8$ , and (c) benzene- $d_6$  to Si(100)2x1 at room temperature.



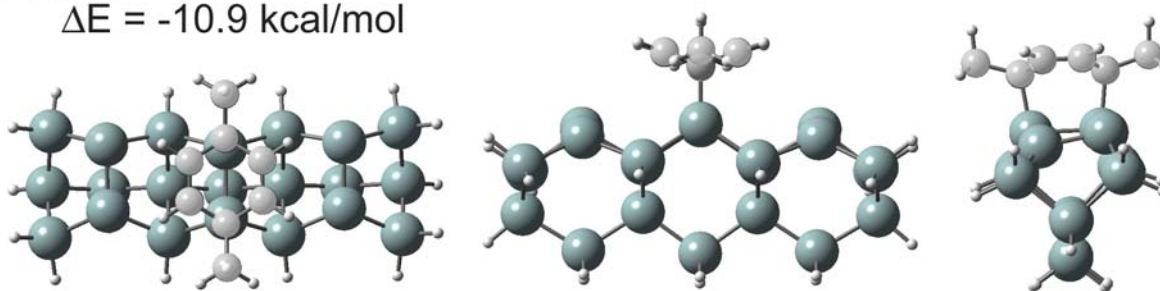
was used in our TDS experiments in order to avoid the large H<sub>2</sub> background commonly found in stainless steel UHV chambers [5]. In addition to the base-ion mass (Mass 98, C<sub>7</sub>D<sub>7</sub>), the parent-ion mass (Mass 116) and other ionic fragments including Mass 110 (C<sub>8</sub>D<sub>7</sub>) and Mass 82 (C<sub>6</sub>D<sub>5</sub>) were also monitored during the TDS experiments (not shown). Since their corresponding TDS peak intensities were found to follow the cracking pattern of *p*-xylene-d<sub>10</sub> [6] over the same temperature range for the profile of Mass 98, these ionic fragments could be attributed to dissociation of molecularly desorbed *p*-xylene-d<sub>10</sub> in the ionizer of the quadrupole mass spectrometer (QMS). The TDS profile of Mass 98 can therefore be used to indicate molecular desorption of *p*-xylene-d<sub>10</sub> from Si(100)2×1. Evidently, two molecular desorption states with desorption maxima at 400 K and 470 K for *p*-xylene-d<sub>10</sub> are found to be similar in temperature to those of the corresponding primary molecular desorption from single-dimer geometry for toluene (at 430 K, Figure 3-2b) and benzene (at 460 K, Figure 3-2c) [1,4] on Si(100)2×1.

In order to understand the equilibrium geometries and enthalpy changes for different adsorption structures, we performed density functional theory (DFT) calculations for *p*-xylene interacting with a triple-dimer surface of a Si<sub>21</sub>H<sub>20</sub> cluster by using the B3LYP/6-31G(d) level of theory [7]. As a result, Figure 3-3 shows the optimized geometries for *p*-xylene/Si<sub>21</sub>H<sub>20</sub> involving bonding through the phenyl group, which include the [4+2] cycloaddition structures of 2,5-dimethylcyclohexa-2,5-diene-1,4-diyl (Figure 3-3a) and 1,4-dimethylcyclohexa-2,5-diene-1,4-diyl (Figure 3-3b) adspecies, as well as the [2+2] cycloaddition structure of 3,6-dimethylcyclohexa-3,5-diene-1,2-diyl adspecies (Figure 3-3c). The corresponding enthalpy changes with zero-point energy corrections, ΔE, are found to be -18.9 kcal/mol, -10.9 kcal/mol and -5.5 kcal/mol, respectively. In our earlier work, we attributed the molecular desorption peak at 460 K of benzene/Si(100)2×1 to a [4+2] cycloaddition (cyclohexa-2,5-diene-1,4-diyl) adspecies (Figure 3-4a), with ΔE = -16.7 kcal/mol obtained by a similar DFT calculation for benzene/Si<sub>21</sub>H<sub>20</sub> [1]. The similarity in ΔE to that of benzene/Si<sub>21</sub>H<sub>20</sub> for both [4+2] cycloaddition adspecies (Figure 3-3a and b) of *p*-xylene/Si<sub>21</sub>H<sub>20</sub> found in the present DFT calculations suggests that the prominent molecular desorption features at 400 K and 470 K can be similarly assigned to 1,4-dimethylcyclohexa-2,5-diene-1,4-diyl (Figure 3-3b) adspecies and 2,5-dimethylcyclohexa-2,5-diene-1,4-diyl

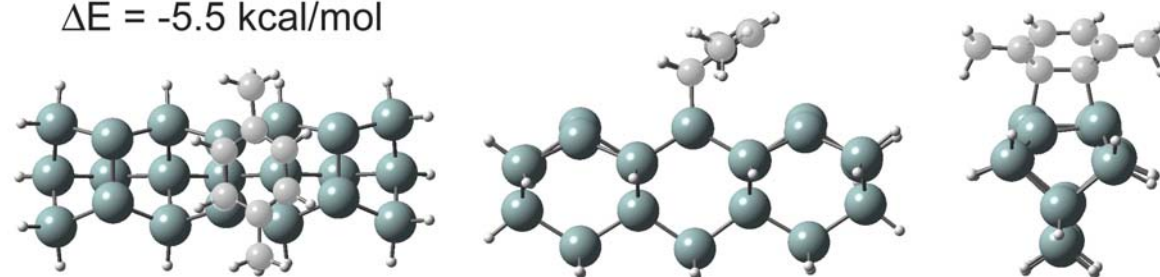
(a) *p*-xylene-2,5-cycloaddition  
 $\Delta E = -18.9$  kcal/mol



(b) *p*-xylene-1,4-cycloaddition  
 $\Delta E = -10.9$  kcal/mol



(c) *p*-xylene-2,3-cycloaddition  
 $\Delta E = -5.5$  kcal/mol



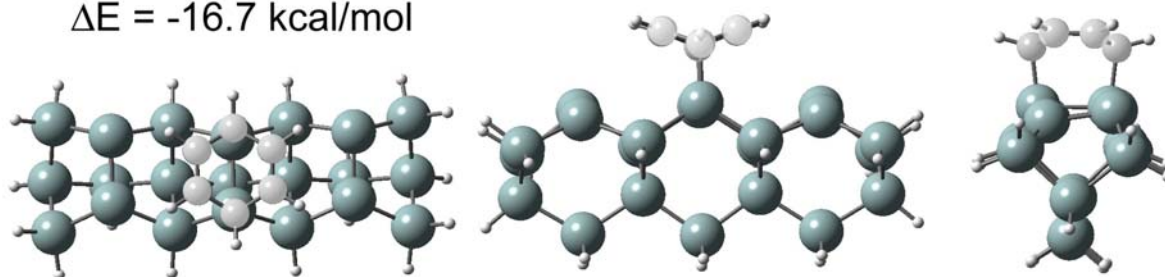
● - Si

● - C

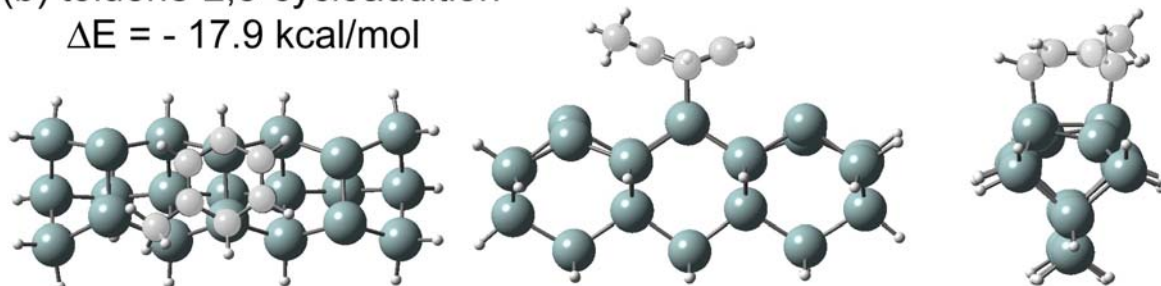
● - H

Figure 3-3 Schematic diagrams of the adsorption geometries and the corresponding adsorption energies  $\Delta E$  for (a,b) [4+2] cycloaddition and (c) [2+2] cycloaddition of *p*-xylene on a model surface of  $\text{Si}_{21}\text{H}_{20}$ , obtained by a density functional calculation with B3LYP/6-31G(d).

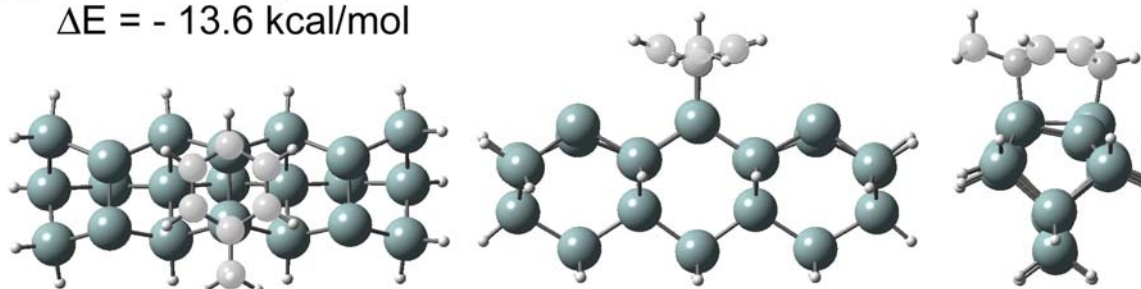
(a) benzene-1,4-cycloaddition  
 $\Delta E = -16.7$  kcal/mol



(b) toluene-2,5-cycloaddition  
 $\Delta E = -17.9$  kcal/mol



(c) toluene-1,4-cycloaddition  
 $\Delta E = -13.6$  kcal/mol



● - Si

● - C

● - H

Figure 3-4 Schematic diagrams of the adsorption geometries and the corresponding adsorption energies  $\Delta E$  for [4+2] cycloaddition of (a) benzene and (b,c) toluene on a model surface of  $\text{Si}_{21}\text{H}_{20}$ , obtained by a density functional calculation with B3LYP/6-31G(d).

(Figure 3-3a), respectively. The least stable [2+2] cycloaddition adspecies (Figure 3-3c) could be attributed to the intensity at the lower desorption temperature (350 K, Figure 3-2a), which could be shown later to be related to adsorption on defect sites. The fact that the less stable structure is more predominant can be understood by the steric effect. Because two methyl groups in *p*-xylene-2,5-cycloaddition (Figure 3-3a) covers more surface area on the dimer row than in *p*-xylene-1,4-cycloaddition (Figure 3-3b), and becomes less possible due to adsorbate-adsorbate interaction. It should be noted that all of these molecular adsorption structures only involve bonding between the phenyl group and the Si dimer, which is consistent with an earlier FTIR study reported by Coulter *et al.* [2]. Furthermore, the temperature difference for the desorption features of the [4+2] cycloaddition adspecies is evidently due to the relative positions of the methyl groups to the C–Si bonding points.

In the case of benzene and toluene on Si(100), a more stable double-dimer adsorption geometry with the so-called “tight bridge” (TiB) configuration has been reported previously [4, 8]. This adsorption configuration was believed to be converted from the initial “metastable” single-dimer [4+2] cycloaddition geometry upon chemisorption [4,8]. In the TDS profiles of benzene and toluene, the respective molecular desorption feature with desorption maximum in the range of 520-550 K has been attributed to the TiB state. By using the aforementioned DFT computational method, the corresponding enthalpy change of the TiB adsorption state of *p*-xylene on Si(100) is calculated to be –26.4 kcal/mol [compared to –18.9 kcal/mol (Figure 3a) and –10.9 kcal/mol (Figure 3b) for the single-dimer states]. These values are found to be on a similar relative scale as those for benzene/Si(100) [8] and toluene/Si(100) [9], which suggests a similar temperature range for the desorption maximum of *p*-xylene from the TiB state (520–550 K). However, the TiB state for benzene and toluene could only be clearly observed in the case of low coverage (<0.1 L) and was found not to be prominent at higher coverage in the earlier [1,10] and the present work (Figure 2). Evidently, molecular desorption above 500 K for a saturation coverage of *p*-xylene/Si(100) is also found to be relatively weak (Figure 3-2a), therefore suggesting that the TiB state does not predominate at high coverage or TiB state does not desorb molecularly (i.e. decomposes). At high coverage, steric effects arising from the two methyl groups in *p*-xylene therefore appear to be more important in controlling the adsorption geometry. Furthermore, the unexpected higher saturation coverage for *p*-xylene/Si(100) than that for benzene/Si(100) as observed

from our AES data (Figure 1) is consistent with the lower relative population of the double-dimer adsorption geometry for *p*-xylene. Finally, as all of the TDS experiments were performed immediately after sample exposure in the present work, there would not be sufficient time for the single-dimer state to convert to the TiB state [4,8] although upon heating conversion will be rapid. As such, while we acknowledge the plausible existence of the TiB state, we will not consider it further in the present work.

In order to investigate the influence of the methyl group on the [4+2] cycloaddition of aromatic hydrocarbons on Si(100), two adsorption geometries of toluene/Si(100), 2-methylcyclohexa-2,5-diene-1,4-diyl (Figure 3-4b) and 1-methylcyclohexa-2,5-diene-1,4-diyl (Figure 3-4c), are also determined with a similar DFT calculation, and compared with that of benzene/Si(100) as cyclohexa-2,5-diene-1,4-diyl adspecies (Figure 3-4a). The adsorption enthalpy changes ( $\Delta E$ ) of toluene/Si(100) with a methyl group that is attached to an ipso C (i.e. a C atom in the phenyl group that is attached to a substrate atom) and that to a non-ipso C are found to be 3.1 kcal/mol lower and 1.2 kcal/mol higher, respectively, than the enthalpy change of benzene/Si(100). Furthermore, it is of interest that the enthalpy changes of *p*-xylene/Si(100), with an additional methyl group that is attached to an ipso C and a non-ipso C, are found to be 2.7 kcal/mol lower and 1.0 kcal/mol higher, respectively, than that of toluene/Si(100). Qualitatively, the enthalpy changes for the [4+2] cycloaddition of *p*-xylene on Si(100) can be used to infer the relative position of the methyl group(s) to the ipso C, and this picture is consistent with the TDS features shown in Figure 3-2a.

### 3.2.2 Hydrogen evolution

In addition to the molecular desorption profile, the mass-4 ( $D_2$ ) TDS profile for *p*-xylene- $d_{10}$  on Si(100) $2\times 1$  is also shown in Figure 2a and found to have a desorption maximum at 820 K, similar in temperature to that of recombinative hydrogen desorption from Si monohydride (at 800 K) [11,12]. The slightly higher temperature of the desorption maximum from that of desorption from monohydride by 20 K [11,12] and the broad mass-4 profile extending to 1000 K (Figure 2a) can be attributed to different H sources on the surface during the thermal desorption process. As observed in our previous TDS studies for toluene [1], pyridine [3] and styrene [13] on Si(100), hydrogen abstraction of *p*-xylene near or below its molecular

desorption temperature could stabilize the adsorbate on Si(100) at higher temperature and further facilitate other reactions. For example, after H has been abstracted from a methyl group of *p*-xylene to the surface, the resulting radical would become more tightly bound to the surface through the methyl C (if the two strained  $\sigma$  bonds from the phenyl group are broken to yield a fully-aromatic benzene ring). This hypothesis is also supported by earlier studies for acetylene on Si(100) [14,15]. In particular, similar TDS profiles for hydrogen desorption have also been obtained by Taylor *et al.* for the adsorption and decomposition of  $C_2H_2$  on Si(100)2 $\times$ 1 [14]. Using high-resolution electron energy-loss spectroscopy, Huang *et al.* later found that the dissociation of adsorbed acetylene occurs via C–H bond breakage over a wide temperature range of 750-900 K, which evidently starts below the molecular desorption maximum of  $C_2H_2$  at 760 K [15].

Figure 3-2 also compares TDS profiles of mass-4 ( $D_2$ ) for a RT saturation exposure of *p*-xylene- $d_{10}$  with those of toluene- $d_8$  and benzene- $d_6$  on Si(100)2 $\times$ 1, which show similar temperature values of the desorption maxima for all three molecules. Similar to those observed for the adsorption of toluene on Si(100)2 $\times$ 1 (Figure 3-2b) [1], the intensity of  $D_2$  desorption for *p*-xylene- $d_{10}$  on Si(100)2 $\times$ 1 (Figure 3-2a) is considerably higher (almost 10-fold) than that for the corresponding molecular desorption. However, the intensity of  $D_2$  desorption for benzene- $d_6$  is significantly lower than that of molecular desorption (Figure 3-2c), which clearly indicates that molecular desorption is the predominant process for benzene but not for its methyl-substituted derivatives. In addition, a weaker  $D_2$  desorption feature is also observed for *p*-xylene- $d_{10}$  and for toluene- $d_8$  with desorption maxima near 1000 K and 900 K respectively, which further suggests the presence of an additional pathway for hydrogen evolution for these methyl-substituted benzene derivatives.

In order to determine whether the methyl group or the phenyl group is involved in the hydrogen abstraction process of *p*-xylene, the TDS profile of Mass 4 for a 5 L exposure of *p*-xylene-dimethyl- $d_6$  (i.e. with just the methyl groups deuterated) is compared with that of a 5 L exposure of *p*-xylene- $d_{10}$  (i.e. with both the phenyl and the methyl groups deuterated) to Si(100)2 $\times$ 1 at RT in Figure 3-5. The two desorption profiles have been arbitrarily normalized at the peak maxima of 820 K. Evidently, the desorption of  $D_2$  at 1000 K is only found in the TDS profile for *p*-xylene- $d_{10}$  but not that for *p*-xylene-dimethyl- $d_6$  on

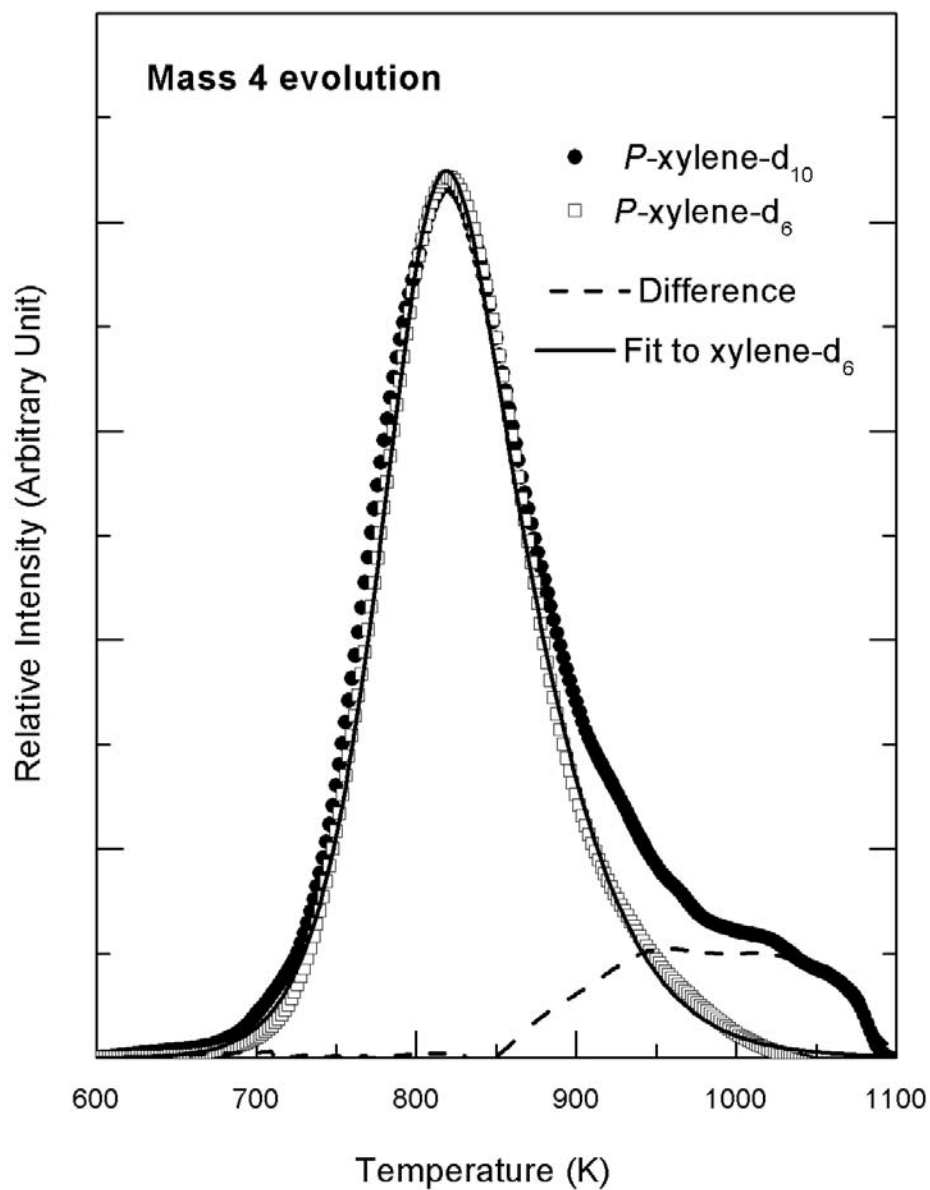
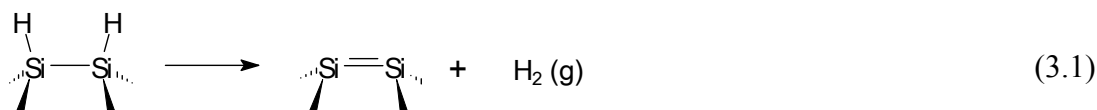


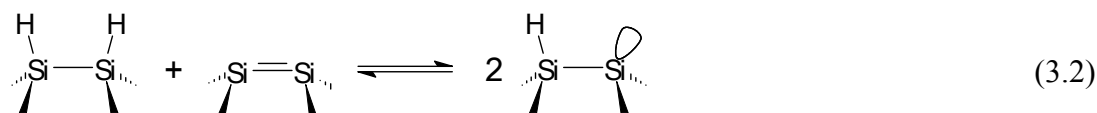
Figure 3-5 Comparison of thermal desorption profiles of mass-4 ( $D_2$ ) desorption for a 10 L exposure of *p*-xylene-d<sub>10</sub> and that for a 10 L exposure of *p*-xylene-dimethyl-d<sub>6</sub>, both to Si(100)2×1 at room temperature. The two data sets have been arbitrarily normalized at 820 K and the difference is shown by a dashed line. The experimental desorption data for *p*-xylene-d<sub>6</sub> has been fitted with a near-second-order desorption kinetics model (solid line) as discussed in the text.

Si(100)2×1. Hydrogen evolution originated from the methyl groups (*p*-xylene-dimethyl-d<sub>6</sub>) could therefore occur only through surface-mediated abstraction followed by recombination desorption from monohydride sites at 820 K. Although the desorption intensity at 1000 K could only come from hydrogen evolution from the phenyl group [as shown in Figure 3-5 for the lack of D<sub>2</sub> desorption in the *p*-xylene-d<sub>6</sub>/Si(100)], we cannot rule out any plausible contribution of the phenyl group to the TDS feature at 820 K. Indeed, the TDS profile of Mass 3 (not shown), corresponding to recombinative desorption of methyl D and phenyl H, for *p*-xylene-dimethyl-d<sub>6</sub> has also been observed at 820 K.

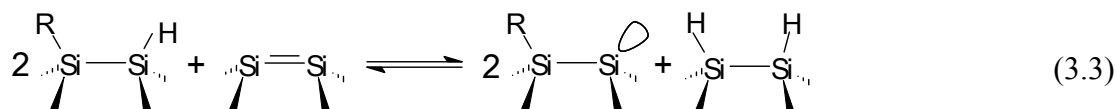
The shape of the desorption feature at 820 K for *p*-xylene-dimethyl-d<sub>6</sub> on Si(100)2×1 can be understood by a pseudo second-order desorption kinetics model [16]. In particular, the kinetics of hydrogen evolution from the methyl group can be investigated using a simple lattice gas model similar to that for the H-terminated Si(100) surface proposed by D'Evelyn *et al.* [17]. In this model, there is only one desorption channel of H<sub>2</sub> resulting from monohydride (two H atoms paired on the same silicon dimer on Si(100)2×1), i.e.



In the present case where aromatic hydrocarbons (R) are involved, the distributions of species, including doubly occupied dimers, are determined by two independent equilibria:



and



It should be noted that Equilibria 3.2 and 3.3 are used only to define the distributions of species present on the surface, and they are not meant to be part of the mechanism by which these equilibrium distributions are established. The reaction enthalpy changes for equilibria 3.2 and 3.3 could be estimated by a DFT calculation similar to that used in Section 3.2.1 and



were found to be +6.0 kcal/mol and +5.4 kcal/mol, respectively. The equilibrium concentration of monohydride on Si(100) can therefore be calculated for any given coverages of *p*-xylene and of overall surface hydrogen at a given temperature. The desorption rate of H<sub>2</sub> can then be obtained as:

$$-\frac{d\theta_H}{dt} = \theta_2 \cdot \nu \cdot e^{-E_d/RT} \quad (3.4)$$

where  $\theta_H$  is the overall coverage of H atoms on the surface,  $\theta_2$  is the coverage of H atoms at the monohydride sites,  $\nu$  and  $E_d$  are, respectively, the preexponential factor and activation energy for hydrogen desorption. Figure 3-5 shows that experimental TDS profile for 5 L of *p*-xylene-methyl-d<sub>6</sub> can be effectively simulated using fitted parameters  $\nu_d = 5.6 \times 10^{14} \text{ s}^{-1}$  and  $E_d = 53 \text{ kcal/mol}$ , which are found to be similar to the results obtained for hydrogen desorption from monohydrides [17]. From this numerical analysis, the desorption rate for H<sub>2</sub> is found to follow a near-second-order desorption kinetics with respect to the overall H coverage  $\theta_H$ . The good accord between the experimental TDS profile of *p*-xylene-dimethyl-d<sub>6</sub> and the fitted profile shown in Figure 3-5 therefore supports the hypothesis that hydrogen evolution from the methyl groups of *p*-xylene on Si(100)2×1 follows a near-second-order desorption kinetics, even though hydrogen evolution from monohydrides on Si(100)2×1 follows a near-first-order desorption kinetics [17]. The presence of Equilibrium 3.3 therefore could greatly affect the desorption kinetics of hydrogen evolution. In addition, the desorption feature at ~1000 K for the hydrogen evolution from the phenyl group could be the result of a condensation polymerization process that can be understood with a two-dimensional diffusion model in a “modified” collision theory, and this will be discussed in a later study [16].

### 3.2.3 Surface conditions study

Figure 3-6 compares the TDS profiles for molecular desorption (Mass 98) and desorption of dissociative products (Mass 28 and Mass 4) for a saturation exposure (5 L) of *p*-xylene-d<sub>10</sub> to a 2×1, amorphous and oxidized surfaces of Si(100) at RT. The amorphous surface (*a*-Si) was produced by ion sputtering in  $4 \times 10^{-5}$  Torr of Ar at 1 keV impact energy for 20 minutes, while

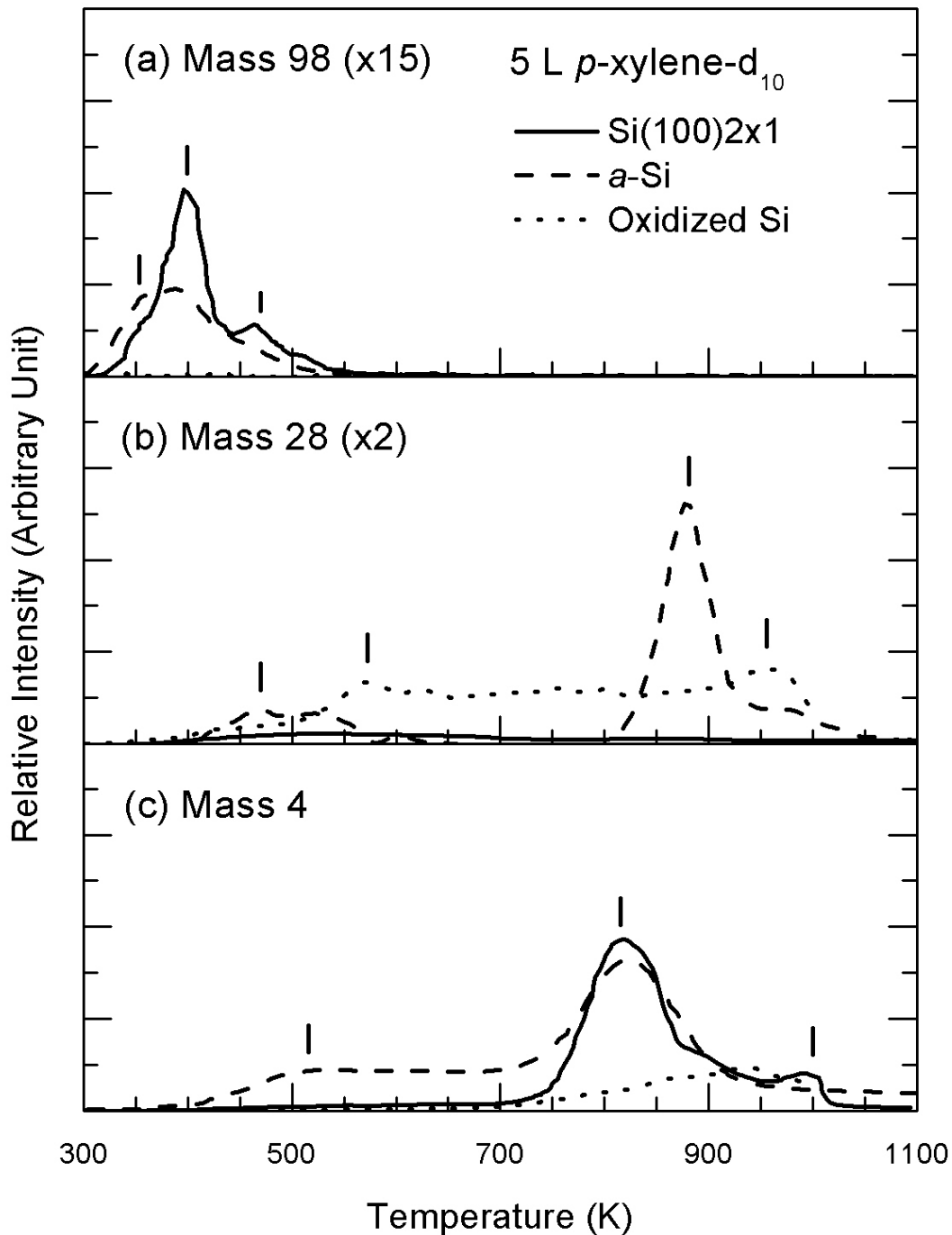


Figure 3-6 Thermal desorption profiles for (a) Mass 98 (molecular desorption), (b) Mass 28 (dissociative products), and (c) Mass 4 (D<sub>2</sub>) for a 5 L exposure of *p*-xylene-d<sub>10</sub> to Si(100)2x1 (solid lines), amorphous (*a*-)Si (dashed lines), and oxidized surface of Si(100) (dotted lines) at room temperature.

the oxidized Si surface was obtained by exposing a clean  $2\times 1$  surface with 100 L of  $O_2$  at RT. The lack of any long-range order for both  $a$ -Si and oxidized Si surfaces was confirmed by the absence of a LEED pattern.

In the TDS profiles of molecular desorption on  $a$ -Si (Figure 3-6a), the desorption features at 400 K and 470 K, both corresponding to [4+2] cycloaddition adspecies shown in Figure 3-3b and Figure 3-3a respectively, are found to be reduced in intensity relative to the corresponding features observed for the  $2\times 1$  surface. On the other hand, enhanced desorption intensity is observed for the feature at 350 K for  $a$ -Si, suggesting molecular desorption from defect sites likely involving the [2+2] cycloaddition adspecies shown in Figure 3-3c. The enhancement of the low-temperature desorption feature on the sputtered surface is similar to that observed for toluene on  $a$ -Si [1]. In contrast to the weak and broad band of Mass 28 for the  $2\times 1$  surface in the 400-800 K region, the desorption intensity in the same temperature region is found to increase noticeably for the sputtered surface, which suggests enhanced desorption of smaller fragments. Furthermore, as was previously observed for pyridine and styrene on  $a$ -Si, a strong mass-28 TDS feature at 880 K (Figure 3-6b) is also found for  $p$ -xylene and can be attributed to dissociative desorption of larger hydrocarbon adspecies. Since a significant amount of mass-40 desorption was also observed at 880 K (not shown), which corresponds to desorption of ion-implanted Ar due to the sputtering process, this mass-28 TDS feature at 880 K could therefore be attributed to dissociative desorption of hydrocarbon fragments from a fairly active surface as a result of significant structural rearrangement accompanied with Ar desorption near 880 K. The shapes and desorption maxima of the TDS profiles of  $D_2$  (Mass 4, Figure 3-6c) for  $a$ -Si are found to be generally similar to those observed on a  $Si(100)2\times 1$  surface. The enhanced intensity observed in the lower-temperature region (400-700 K) for the sputtered surface is likely related to the desorption of smaller fragments found in the mass-28 TDS profile.

Figure 3-6 also shows the TDS profiles of Mass 98, Mass 28 and Mass 4 for a 5 L RT exposure of  $p$ -xylene- $d_{10}$  to an oxidized Si surface. Evidently, significant reductions in molecular desorption (Mass 98, Figure 3-6a) and hydrogen evolution (Mass 4, Figure 3-6c) are found for the oxidized surface, which could be attributed to the loss of active adsorption sites due to oxidation. Furthermore, the discernible desorption features of Mass 28 (along

with Mass 26 and Mass 30, not shown) in the 450-700 K region depicted in Figure 3-6b could be attributed to desorption of small hydrocarbons. However, the lack of corresponding mass-26 and mass-30 desorption intensities for the mass-28 feature near 960 K suggests that the latter intensity could be due to recombinative desorption of CO formed from surface C with O on the oxidized surface, as was previously proposed for styrene on an oxidized Si surface [13]. The latter desorption channel for Mass 28 is evidently accompanied by D<sub>2</sub> (Mass 4) desorption in the same temperature region (Figure 3-6c).

Finally, passivation of the active sites can also be achieved by H atoms as demonstrated in a separate TDS experiment for *p*-xylene-d<sub>10</sub> on a H-terminated Si(100)1×1 surface, in which desorption of Mass 98 (base mass of *p*-xylene-d<sub>10</sub>), Mass 28 and Mass 4 is not observed (not shown). The lack of reactivity of a H-terminated Si(100) surface towards *p*-xylene-d<sub>10</sub> is therefore similar to that found for benzene and toluene [1].

### **3.2.4 Surface-mediated reactions of *p*-xylene on Si(100)2×1 post-exposed to atomic H, molecular O<sub>2</sub> and low-energy electrons**

In order to investigate the interaction of atomic hydrogen with *p*-xylene adsorbed on Si(100)2×1, the sample saturated with a 5 L exposure of *p*-xylene-d<sub>10</sub> was post-exposed with H atoms generated from 3000 L of H<sub>2</sub> with a hot W filament positioned 2 cm away. Liquid nitrogen was used to maintain the sample near or below RT during the post-hydrogenation experiment. After the post-hydrogenation, the 2×1 LEED pattern for the *p*-xylene-d<sub>10</sub>-saturated surface was found to revert back to a 1×1 pattern, indicating total de-reconstruction of the surface structure. Evidently, the TDS features for the molecular (Mass 98) desorption are totally diminished upon post-hydrogenation (Figure 3-7). The mass-30 TDS features in the 500-700 K region and the weaker feature at 750 K could be attributed to desorption of C<sub>2</sub>D<sub>2</sub>H<sub>2</sub>. In particular, the lower-temperature mass-30 TDS features along with the weaker mass-28 and mass-2 desorption features at 510 K are typical of molecular desorption of ethylene [18,19]. On the other hand, the unusually strong mass-28 TDS feature at 710 K relative to the mass-30 feature could be attributed to an additional pathway of dehydrogenation desorption of ethyl adspecies on a H-terminated Si(100) surface [13,20], indicating that post-hydrogenation could enhance the dissociation of the adsorbate as a result

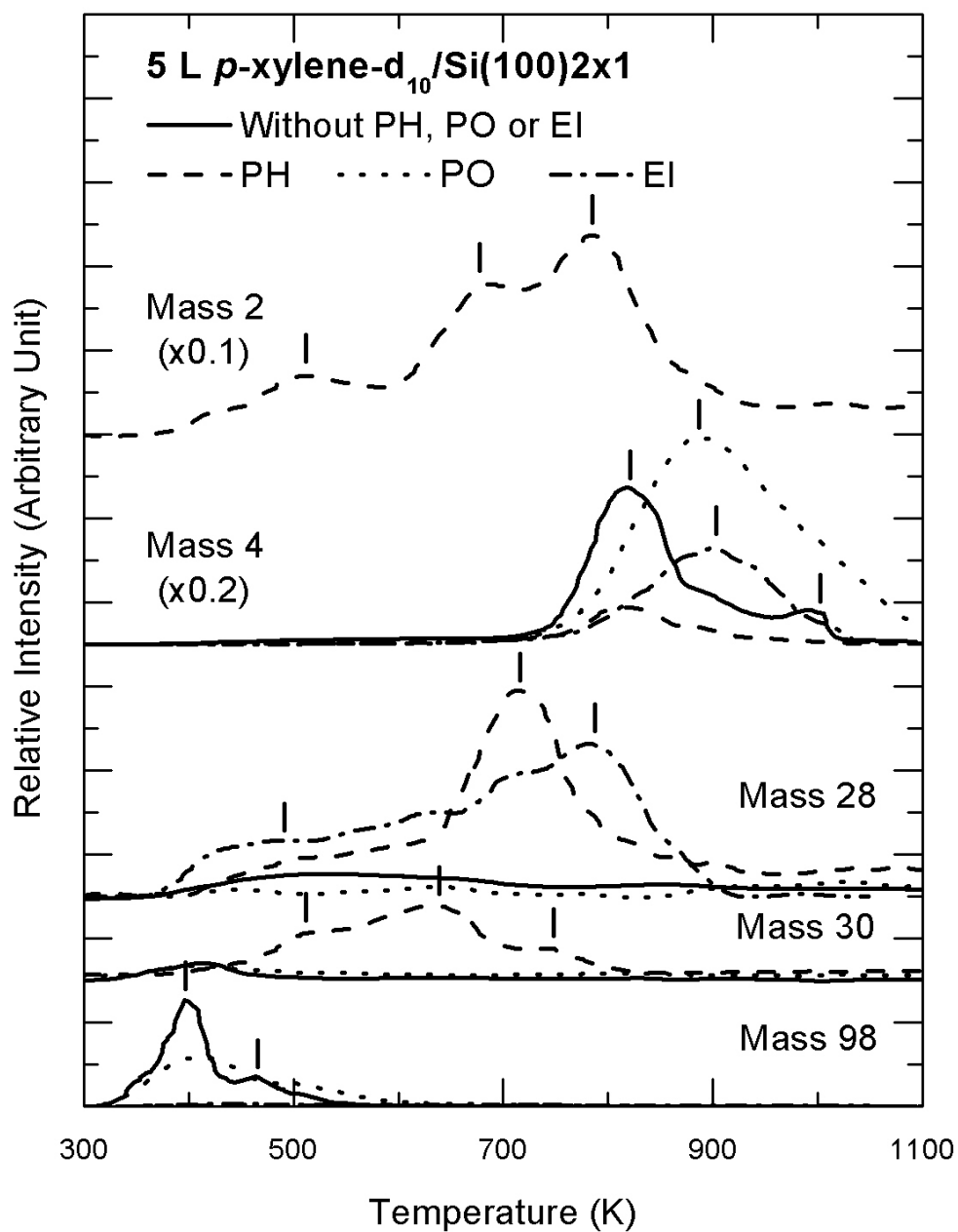


Figure 3-7 Comparison of thermal desorption profiles of Mass 2, 4, 28, 30, and 98 for a 100 L room-temperature exposure of *p*-xylene-d<sub>10</sub> to Si(100)2×1 (solid lines), and with post-hydrogenation (PH, dashed lines), post-oxidation (PO, dotted lines), and post-electron-irradiation (EI, dashed-dotted lines) at 200 μA and 80 eV for 30 minutes.

of bond saturation. The two mass-30 features at 630 K and 750 K can be attributed to ethylene evolution from two separated H-terminated Si(100) phases (dihydride and alternating dihydride-monohydride) in surface-mediated processes driven by thermal diffusion and desorption of hydrogen [13]. In addition, the two intense TDS features of Mass 2 at 680 K and 790 K for the post-hydrogenated sample could be assigned to recombinative desorption from dihydride and monohydride, respectively, on a H-terminated Si(100) surface [11,12]. At 820 K, the mass-4 desorption from post-hydrogenated sample is found to be greatly reduced while the corresponding mass-3 desorption is evidently similar to that of the 2×1 surface at 820 K (not shown), which suggests strong recombinative desorption involving post-adsorbed H atoms and D atoms from the *p*-xylene-d<sub>10</sub> adspecies.

Figure 3-7 also shows the TDS profiles for 5 L of *p*-xylene-d<sub>10</sub> on Si(100)2×1 post-exposed with 100 L of O<sub>2</sub> at RT. As in the case of toluene and benzene [1], post-oxidation appears to partially reduce molecular (Mass 98) desorption of *p*-xylene-d<sub>10</sub>, which indicates the presence of surface-mediated interactions of oxygen with *p*-xylene-d<sub>10</sub>. Furthermore, the mass-4 (D<sub>2</sub>) evolution for *p*-xylene-d<sub>10</sub>/Si(100)2×1 upon post-oxidation is found to be broadened and shifted to a higher temperature (from 820 K to 890 K). Similar results have been reported and discussed in our earlier TDS studies on benzene and toluene [1], and they could be similarly attributed to be the result of surface-mediated oxidation of xylene. Similar to that on the Si(100)2×1 surface, the desorption intensities of Mass 28 and Mass 30 for the post-oxidized sample are found to be very weak, suggesting that post-oxidation will not help in producing fragments of adsorbed *p*-xylene.

Figure 3-7 depicts the effects of low-energy electron irradiation on the TDS profiles of Mass 98 (base mass), Mass 28 and Mass 4 for 5 L RT exposure of *p*-xylene-d<sub>10</sub> to Si(100)2×1. Electron irradiation was performed on the Si sample (held at 80 V bias potential) for 30 minutes at 0.2 mA with electrons thermionically emitted from a hot W filament positioned 5 cm away. Evidently, electron irradiation greatly diminishes molecular desorption, which is likely due to electron-induced desorption [21] and/or conversion to other smaller dissociated or larger oligomerized adspecies. The TDS profile of Mass 28 shows a marked increase in the desorption of dissociated fragments C<sub>2</sub>D<sub>2</sub> (arising from molecular desorption of C<sub>2</sub>D<sub>2</sub> or further dissociation of C<sub>2</sub>D<sub>4</sub>) caused by electron-induced dissociation

of the adsorbed *p*-xylene-d<sub>10</sub>. In particular, two enhanced desorption features of Mass 28 are observed, with a maximum at 790 K and with a broad structure in the region of 400-700 K. Because molecular desorption of smaller hydrocarbons such as C<sub>2</sub>H<sub>4</sub> on Si(100)2×1 generally occurs near 550 K [18,19], the broad mass-28 TDS feature in the region of 400-700 K can be attributed to the cracking patterns of desorbed fragments caused by electron irradiation. The mass-28 desorption feature at 790 K can be assigned to molecular desorption of acetylene (arising from electron dissociation), which has been reported to exhibit a desorption maximum at 690-740 K from Si(100)2×1 [14]. In addition, the intensity for the mass-4 TDS profile for the electron-irradiated sample appears to have been reduced by half relative to that for the 2×1 surface with its desorption maximum shifted from 820 K to 900 K. The reduction in the relative intensity of the mass-4 TDS profile could be due to reduced moiety of hydrocarbons as a result of desorption of these fragments at a lower temperature. The increase in the temperature of the desorption maximum found in the present case has also been observed in our previous studies on electron irradiation of pyridine [3] and styrene on Si(100) [13]. Such an increase can also be similarly explained by a proposed mechanism involving electron-induced oligomerization of the adsorbate [3,13,16].

### 3.3 Concluding remarks

The RT adsorption and thermal reactions of *p*-xylene on Si(100)2×1 and related sputtered and oxidized surfaces have been investigated by using TDS, AES and LEED. *P*-xylene is found to adsorb on the Si(100)2×1 surface predominantly through [4+2] cycloaddition and to have little effect on the two domain (2×1) long-range order of the Si(100) surface. The saturation coverage at RT is estimated to be 0.30 ML, in between that of benzene (0.27 ML) and toluene (0.33 ML), which illustrates the interplay between the effect of methyl substitution in enhancement and that of steric hindrance on chemisorption. Upon annealing, the adsorbate is found to desorb in part molecularly with desorption states at 400 K and 470 K, while the majority of the adsorbate remains on the surface after hydrogen abstraction from the methyl group. Two hydrogen evolution states are observed at 820 K and 1000 K, with the former involving H atoms abstracted from the methyl group followed by recombinative

desorption of H<sub>2</sub> from the monohydride sites, and the latter involving H atoms released from the phenyl group as H<sub>2</sub> during condensation polymerization.

The sputtered Si surface exhibits additional adsorption that leads to molecular desorption at 350 K, and potentially opens up new reaction pathways for decomposition into acetylene (as shown in the mass-28 TDS profile at 880 K). On the other hand, considerably reduced molecular desorption and diminished hydrogen evolution on the oxidized Si surface are observed, due to oxygen passivation of the available active sites. Other processes such as CO production and/or condensation polymerization near 1000 K are found to be plausible on post-oxidized Si(100)2×1 surface saturated with *p*-xylene. Furthermore, a saturation exposure of atomic H is also found to totally passivate the Si(100)2×1 surface, producing a 1×1 surface that is inert to *p*-xylene adsorption. High post-exposure of atomic hydrogen, on the other hand, appears to saturate some of the double bonds of the adsorbed *p*-xylene on Si(100) that lead to further evolution of ethyl, ethylene and acetylene adspecies and a 1×1 structure. Moreover, dehydrogenation, diffusion and desorption of surface hydrogen appear to lead to more surface-mediated processes upon annealing.

Finally, preliminary studies on the adsorption of other xylene isomers, including *m*-xylene (1,3-dimethylbenzene) and *o*-xylene (1,2-dimethylbenzene) on Si(100)2×1 have also been performed. Figure 3-8 compares the adsorption geometries and corresponding enthalpy changes  $\Delta E$  of the [4+2] cycloaddition adspecies of *m*-xylene and *o*-xylene on Si(100)2×1. Similar to the results found for the adsorption of *p*-xylene and toluene, the adsorption structure with a methyl group attached to an ipso C is less stable than that without any methyl group attached to an ipso C. For example,  $\Delta E$  for 1,4-dimethylcyclohexa-2,5-diene-1,4-diyl (−14.9 kcal/mol, Figure 3-8b) is less negative than that for 2,6-dimethylcyclohexa-2,5-diene-1,4-diyl (−17.9 kcal/mol, Figure 3-8a). Similarly,  $\Delta E$  for 1,2-dimethylcyclohexa-2,5-diene-1,4-diyl (−13.9 kcal/mol, Figure 3-8d) is less negative than that for 2,3-dimethylcyclohexa-2,5-diene-1,4-diyl (−16.4 kcal/mol, Figure 3-8c). The differences of enthalpy changes between the ipso-C and non-ipso-C types of adsorption structures are 8.0, 3.0 and 2.5 kcal/mol for *p*-xylene, *m*-xylene and *o*-xylene, respectively. The larger difference for *p*-xylene relative to those for *m*-xylene and *o*-xylene is likely due to the attachment of two



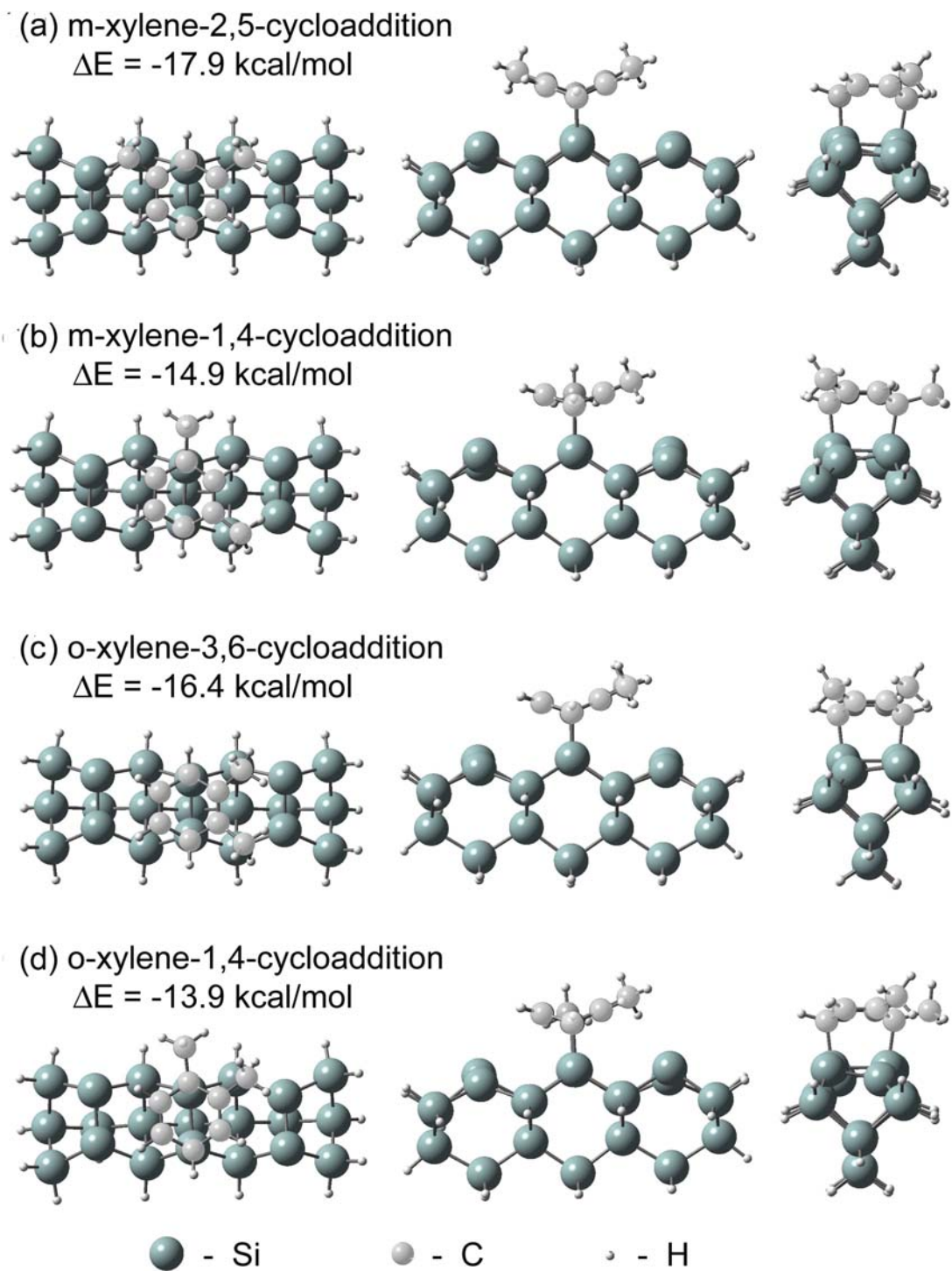


Figure 3-8 Schematic diagrams of the adsorption geometries and the corresponding adsorption energies  $\Delta E$  for [4+2] cycloaddition of (a,b) *m*-xylene and (c,d) *o*-xylene on a model surface of  $\text{Si}_{21}\text{H}_{20}$ , obtained by a density functional calculation with B3LYP/6-31G(d).

methyl groups to two ipso C atoms. It would be of great interest to deploy surface analysis techniques (including TDS) to obtain more insights into the intricate adsorption structures and thermal chemistry of these xylene isomers on Si(100) and related surfaces.

### 3.4 Reference

- [1] Q. Li, K.T. Leung, Surf. Sci. 479 (2001) 69. See also Chapter 2.
- [2] S.K. Coulter, J.S. Hovis, M.D. Ellison, R.J. Hamers, J. Vac. Sci. Technol. A 18 (2000) 1965.
- [3] Q. Li, K.T. Leung, Surf. Sci. 541 (2003) 111. See also Chapter 5.
- [4] Y. Taguchi, M. Fujisawa, T. Takaoka, T. Okada, M. Nishijima, J. Chem. Phys. 95 (1991) 6870.
- [5] J.-P. Bacher, C. Benvenuti, P. Chiggiato, M.-P. Reinert, S. Sgobba, A.-M. Brass, J. Vac. Sci. Technol. A 21 (2003) 167.
- [6] “NIST/EPA/NIH Mass Spectral Library”, NIST’98 with Windows, Version 1.7, (1996).
- [7] J.B. Foresman, *Æ.* Frisch, “Exploring Chemistry with Electronic Structure Methods”, 2nd Ed., Gaussian Inc., Pittsburgh (1996); and references therein.
- [8] R.A. Wolkow, G.P. Lopinski, D.J. Moffatt, Surf. Sci. 416 (1998) L1107.
- [9] F. Costanzo, C. Sbraccia, P.L. Silvestrelli, F. Ancilotto, J. Phys. Chem. B 107 (2003) 10209.
- [10] B. Borovsky, M. Krueger, E. Ganz, J. Vac. Sci. Technol. B 17 (1999) 7.
- [11] M. Suemitsu, H. Nakazawa, N. Miyamoto, Appl. Surf. Sci. 82/83 (1994) 449.
- [12] S.M. Gates, R.R. Kunz, C.M. Greenlief, Surf. Sci. 207 (1989) 364.
- [13] Q. Li, K.T. Leung, Surf. Sci. (2003) submitted.
- [14] P.A. Taylor, R.M. Wallace, C.C. Cheng, W.H. Weinberg, M.J. Dresser, W.J. Choyke, and J.T. Yates, Jr., J. Am. Chem. Soc. 114 (1992) 6754.
- [15] C. Huang, W. Widdra, X.S. Wang, W.H. Weinberg, J. Vac. Sci. Technol. A 11 (1993) 2550.
- [16] Q. Li, K.T. Leung, to be submitted. See also in Chapter 6.
- [17] M.P. D'Evelyn, Y.L. Yang, L.F. Sutcu, J. Chem. Phys. 96 (1992) 852.

- [18] C.C. Cheng, W.J. Choyke, J.T. Yates, Jr., Surf. Sci. 231 (1990) 289.
- [19] L. Clemen, R.M. Wallace, P.A. Taylor, M.J. Dresser, W.J. Choyke, W.H. Weinberg, J.T. Yates, Jr., Surf. Sci. 268 (1992) 205.
- [20] W. Widdra, C. Huang, S.I. Yi, W.H. Weinberg, J. Chem. Phys. 105 (1996) 5605.
- [21] V.N. Ageev, Prog. Surf. Sci. 47 (1994) 55; and references therein.

## Chapter 4

# Thermal chemistry of styrene on Si(100)2×1 and modified surfaces: Electron-mediated condensation oligomerization, and post- hydrogenation reactions

### 4.1 Introduction

Aromatic hydrocarbons (e.g. benzene) and chain-like alkenes (e.g. ethylene) are the basic building blocks for constructing “conjugated” structures in most conducting polymer materials [1,2]. Styrene (or vinyl benzene) therefore represents one of the most fundamental combinations of a hexacyclic aromatic unit (the phenyl group) with the smallest alkene (the vinyl group). The interaction of benzene with silicon has been the subject of extensive experimental [3,4,5,6,7,8] and theoretical studies [9,10,11,12,13,14]. These studies show that chemisorption of this homocyclic aromatic compound on Si(100)2×1 follows the Diels-Alder cycloaddition mechanism, giving rise to a di- $\sigma$  bonded cyclohexa-2,5-dien-1,4-diyl (and cyclohexa-3,5-dien-1,2-diyl) adsorption species which may be converted to tight-bridge double bonding structure. Adsorption of ethylene on Si(100) has also been well studied both experimentally [15,16,17,18,19,20] and theoretically [21,22,23], and is found to form a di- $\sigma$ -bonded ethane-1,2-diyl with a Si dimer. Styrene is a particularly interesting molecule because, unlike benzene, the presence of a vinyl group in styrene provides the prospect of polymerization. Adsorption of styrene on Si(100) could therefore provide a benchmark system for investigation of surface interactions and processes that are prototypical of organic semiconductors [24]. Relative to benzene and ethylene, styrene is expected to undergo more complex yet selective chemisorption on Si(100). To date, only a limited number of studies have been made for styrene on Si(100) surfaces, and none on the respective thermally or electron induced surface processes. In particular, a recent Fourier-Transform Infrared (FTIR) spectroscopic study by Schwartz *et al.* has shown that this high selectivity involves bonding through the vinyl group with the aromatic ring (the phenyl group) unperturbed [25]. Using the tip of a scanning tunnelling microscope to initiate adsorption of styrene on a H-terminated Si(100)2×1 surface, Lopinski *et al.* have demonstrated self-directed growth of molecular wires along the direction of the Si-dimer row [26].

In the present work, we examine the interactions of styrene with the  $2\times 1$  and modified surfaces of Si(100) using thermal desorption spectrometry (TDS), low energy electron diffraction (LEED) and Auger electron spectroscopy (AES), in order to better understand not only the important roles of the vinyl and phenyl groups in organosilicon surface chemistry, but also the nature of different thermal surface processes for different surface conditions. Factors that could be used to monitor and control plausible synthesis steps of well-defined organic semiconductors in the nanoscale are of particular interest. The present result is also compared with our earlier work on homocyclic (benzene and toluene) [27] and heterocyclic (pyridine) unsaturated hydrocarbons on Si(100) [28]. In addition to the multitude of thermally induced processes (other than molecular desorption), the effects of low-energy electron irradiation and post-exposure of atomic hydrogen to the adsorbed styrene are also investigated.

## 4.2 Results and Discussion

### 4.2.1 Room-temperature adsorption at various exposures

The adsorption of styrene on Si(100) $2\times 1$  at RT was studied as a function of exposure by LEED and AES. Upon different exposures of styrene to the Si(100) surface at RT, only a slight increase in the background intensity was observed in the two-domain ( $2\times 1$ ) LEED pattern characteristic of a clean Si(100) surface, which shows that the dimer-row structure of the Si substrate is generally preserved after the adsorption of styrene. The peak-to-peak ratio of the C(KLL) Auger peak to that of the Si(LVV) Auger peak is used to indicate the relative carbon moiety. Figure 4-1 compares this ratio as a function of RT exposure for styrene and benzene on Si(100) $2\times 1$ , and each with the corresponding results expected from first-order and second-order adsorption kinetics. Evidently, both the first-order and second-order kinetics are in good accord with the experimental data, indicating that our present data may not be sufficiently sensitive to differentiate the adsorption order. For styrene, the ratio appears to reach its saturation value at 10 L exposure, which generally marks the completion of adsorption of the first monolayer (ML). The saturation coverage of benzene has been estimated to be 0.27 ML by Taguchi *et al.* [4]. From the ratio of the saturation values of styrene (21.3%) and benzene (8.0%) and after taking the number of carbon atoms in styrene

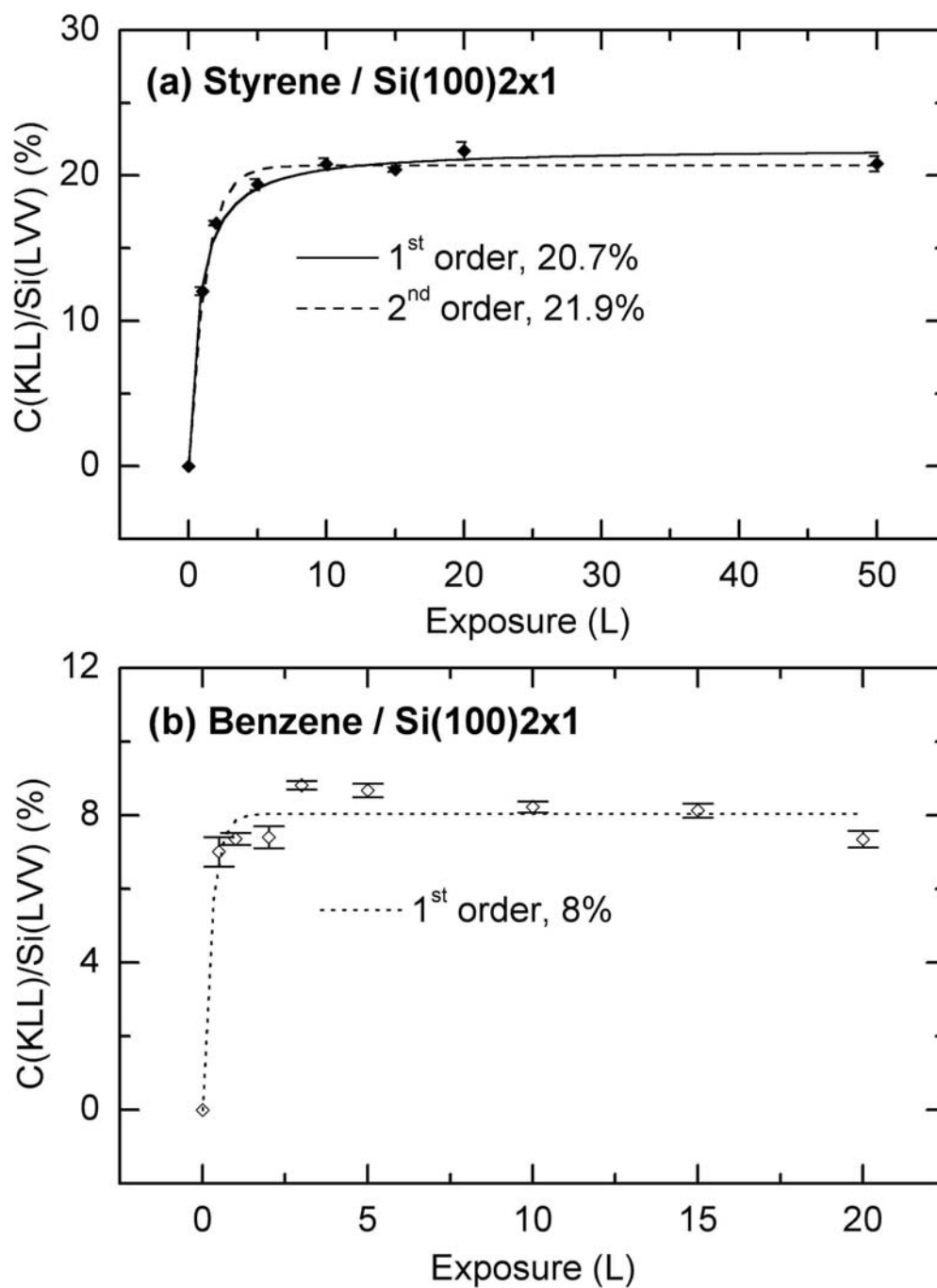


Figure 4-1 Relative carbon moiety as indicated by the peak-to-peak intensity ratio for the C(KLL) to Si(LVV) Auger transitions as a function of room-temperature exposure of (a) styrene and (b) benzene to Si(100)2×1. The experimental data are compared with fitted curves based on the first-order and second-order adsorption kinetic equations.

(8) and benzene (6) into account, we determine the saturation coverage for styrene to be 0.5 ML, which corresponds approximately to one styrene molecule per Si dimer on the 2×1 surface.

Figure 4-2 shows the TDS profiles of Mass 112 (parent mass) and Mass 4 corresponding to molecular and recombinative D<sub>2</sub> desorption, respectively, for different RT exposures of styrene-d<sub>8</sub> on Si(100)2×1. It should be noted that deuterated styrene was used in our TDS experiments in order to avoid the large H<sub>2</sub> background commonly found in stainless steel UHV chambers. In addition to the parent mass (Mass 112), other smaller ionic fragments including Mass 110 (C<sub>8</sub>D<sub>7</sub>), Mass 84 (C<sub>6</sub>D<sub>6</sub>) and Mass 56 (C<sub>4</sub>D<sub>4</sub>) were also monitored during the TDS experiments (not shown). Since their corresponding peak intensity ratios were found to be in good accord with the respective ratios in the cracking pattern of styrene-d<sub>8</sub> [29] over the same temperature range (of 350-700 K) as that for Mass 112, these smaller mass fragments could be attributed to dissociation of molecularly desorbed styrene-d<sub>8</sub> in the ionizer of the quadrupole mass spectrometer (QMS). These TDS profiles therefore indicate that styrene-d<sub>8</sub> desorbs molecularly from Si(100)2×1 over this temperature range. The TDS intensity for molecular desorption reaches saturation at ~10 L exposure (not shown), which is in good accord with the AES result for the adsorption of styrene (Figure 4-1). Evidently, two desorption states are observed for molecular desorption (Figure 4-2). The desorption maximum at 430 K is similar to those of the primary molecular desorption feature found in our previous TDS studies on benzene, toluene [27] and pyridine on Si(100)2×1 [28], suggesting a similar molecular adsorption state that corresponds to a [4+2] di-σ bonding geometry between the phenyl group and the Si dimer. Furthermore, a new peak with a much stronger intensity for the molecular desorption of styrene is found at 560 K. The similarity in the temperature of this desorption maximum to that for ethylene on Si(100)2×1 [18,19] suggests that the predominant chemisorption configuration involves bonding through the vinyl group. This di-σ bonding geometry for styrene on Si(100)2×1 has also been concluded from an earlier FTIR study by Schwartz *et al.* [25]. The relative intensity ratio of two molecular desorption features at saturation coverage in Figure 4-2a shows that only 15% of desorption comes from phenyl-bonded structures (at 430 K) while the majority originates from vinyl-bonded structures (at 560 K). The present TDS result is



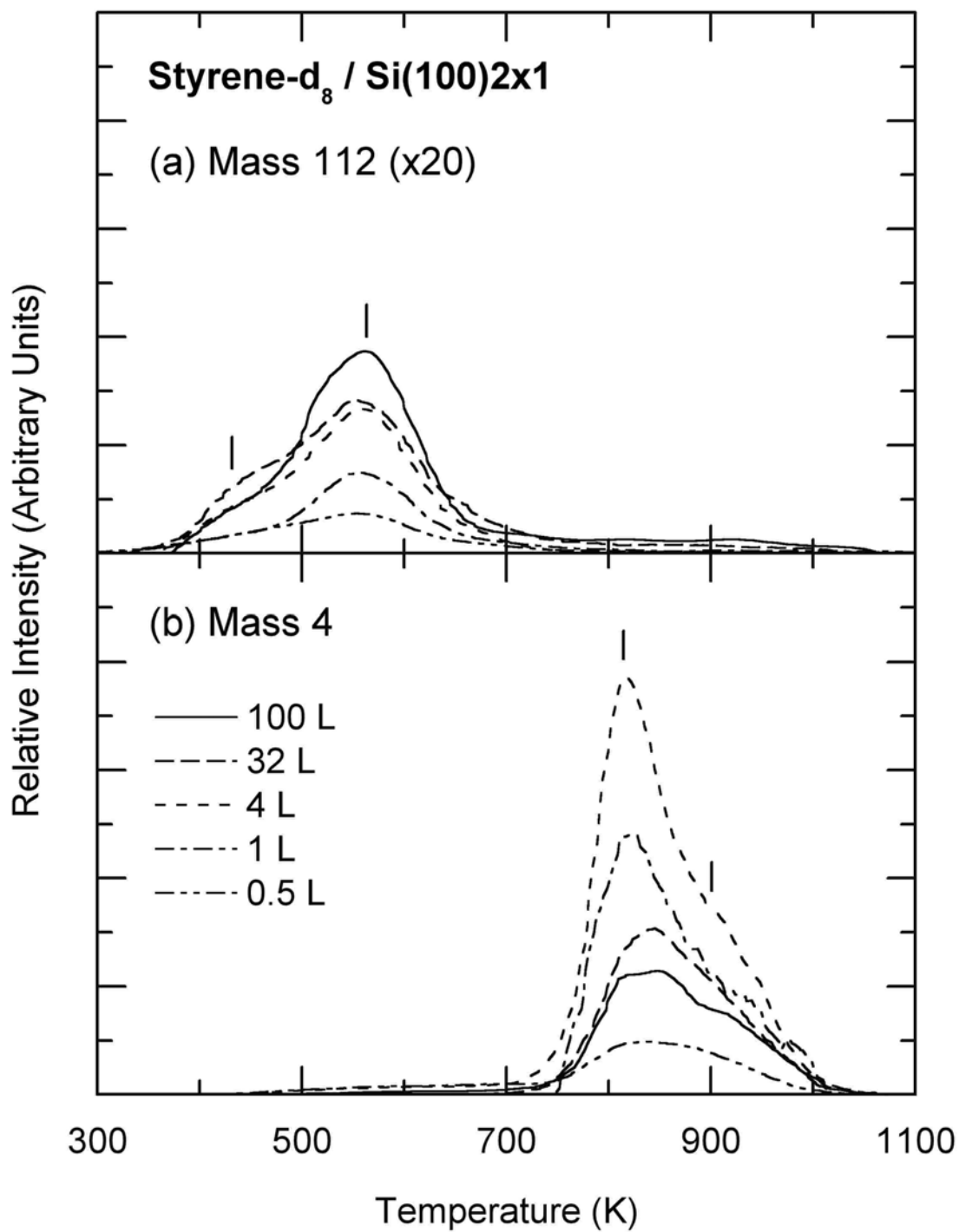


Figure 4-2 Thermal desorption profiles of Mass 112 (parent mass) and Mass 4 (D<sub>2</sub>) as a function of room-temperature exposure of styrene-d<sub>8</sub> to Si(100)2x1.

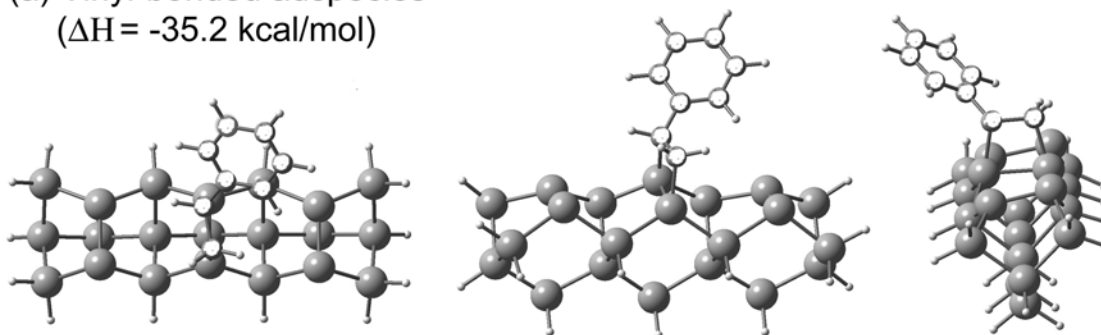
therefore in general accord with the earlier work [25]. The “absence” of the phenyl-bonded structure concluded in the earlier work [25] may be explained by the nearly surface-parallel orientation of the phenyl group, which does not give a strong FTIR signature. Furthermore, the TDS feature for the phenyl-bonded adspecies (at 430 K) appears to reach saturation at a lower exposure than the feature for the vinyl-bonded adspecies (at 560 K), which is consistent with the larger footprint required for the phenyl-bonded structure.

To understand the geometries and bonding energies for different adsorption structures, we performed *ab-initio* density functional calculations for styrene interacting with a Si<sub>21</sub>H<sub>20</sub> triple-dimer cluster employed for modelling the Si(100)2×1 surface [30]. Figure 4-3 shows the optimized geometries for the vinyl-bonded (*cis*-phenylethen-1,2-diyl) and phenyl-bonded (2-vinylcyclohexa-2,5-diene-1,4-diyl) adsorption structures. The corresponding enthalpy change with zero-point energy corrections, ΔH, are found to be -35.2 kcal/mol and -23.4 kcal/mol, respectively, which are consistent with our assignment that the phenyl-bonded adspecies would be desorbed at a lower temperature than the vinyl-bonded adspecies (Figure 4-2a). The higher adsorption energy of the phenyl-bonding structure for styrene than that for benzene is due to the less stability of the aromatic structure in styrene. It should be noted that improved calculations involving a larger basis set are not expected to significantly change the qualitative nature of the adsorption configurations. Other conformers of the cyclohexadienediyl adspecies have also been considered and found to have a smaller magnitude for the binding energy. It is of interest to note that the most stable conformer obtained for the adsorption of benzene on Si<sub>21</sub>H<sub>20</sub> was also found to correspond to the cyclohexa-2,5-diene-1,4-diyl adspecies [11].

#### 4.2.2 Hydrogen evolution

In addition to the molecular desorption profiles, Figure 4-2 also shows the mass-4 (D<sub>2</sub>) TDS profiles with maxima at 810 K for RT exposures of styrene-d<sub>8</sub> on Si(100)2×1. It should be noted that the TDS profiles for normal and deuterated styrene are found to be identical in our TDS experiment, indicating that isotopic effect is not important for the adsorption process. The desorption maximum at 810 K appears to be quite stationary with increasing exposure in the D<sub>2</sub> TDS profile (Figure 4-2b), which suggests predominant first-order kinetics as a result

(a) Vinyl-bonded adspecies  
( $\Delta H = -35.2$  kcal/mol)



(b) Phenyl-bonded adspecies  
( $\Delta H = -23.4$  kcal/mol)

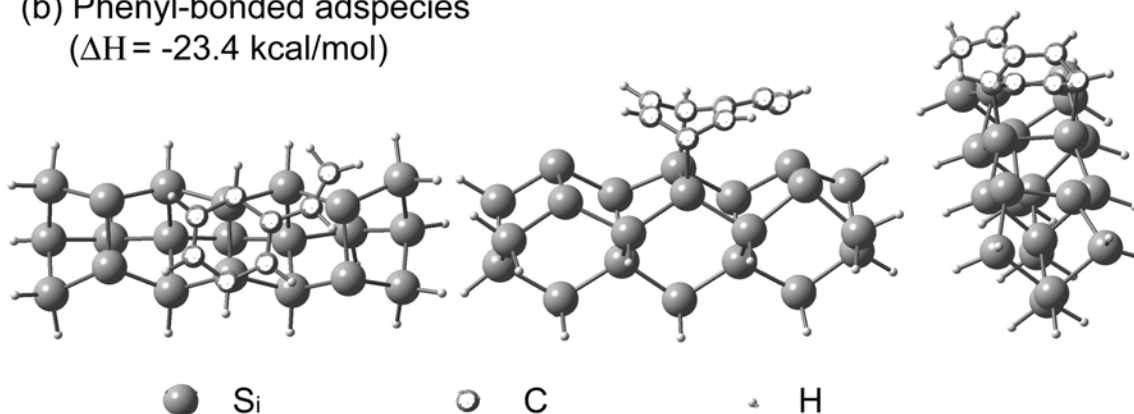
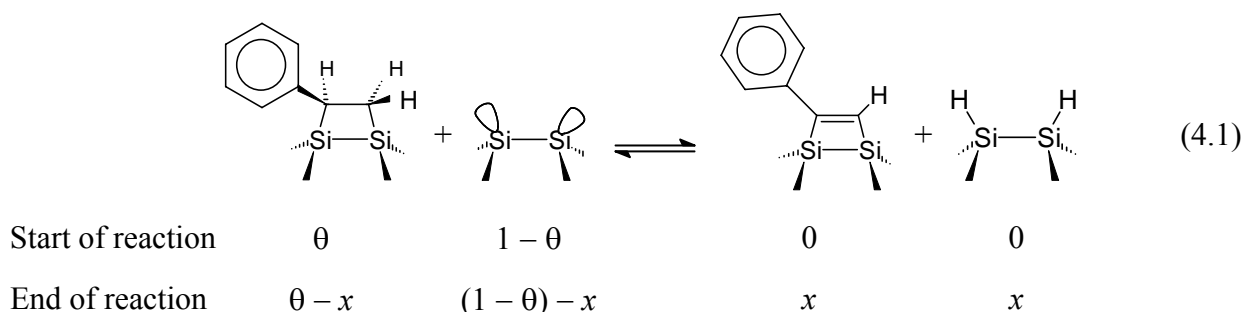


Figure 4-3 Schematic diagrams of the adsorption geometries in different perspectives and the corresponding adsorption energies  $\Delta E$  obtained by a density functional calculation involving B3LYP/6-31G(d) for styrene on a model surface of  $\text{Si}_{21}\text{H}_{20}$ : (a) vinyl-bonded adspecies; (b) phenyl-bonded adspecies.

of recombinative molecular desorption from Si monohydride [31,32]. The slightly higher temperature of the desorption maximum from that of monohydride desorption by 20 K [11,12] and the broad mass-4 profile extending to 1000 K (Figure 4-2b) are related to contributions from different sources of atomic hydrogen on the surface during the thermal desorption process. As observed in our previous TDS studies for toluene [27] and pyridine on Si(100) [28], hydrogen abstraction of styrene near or below its molecular desorption temperature could generate a comparable moiety of atomic hydrogen and other dissociated products, which could undergo further hydrogen abstraction mediated by the surface at a

higher temperature than that of molecular desorption. This hypothesis is supported by earlier studies [25,33,34]. In particular, the FTIR study by Schwartz *et al.* also reported a Si–H stretching feature indicative of C–H bond cleavage in the vinyl group of styrene upon adsorption at RT [25]. Furthermore, similar TDS behaviour for hydrogen desorption has also been obtained by Taylor *et al.* for the adsorption and decomposition of acetylene on Si(100)2×1 [14]. Using high-resolution electron energy-loss spectroscopy, Huang *et al.* later found that the dissociation of adsorbed acetylene occurs via C–H bond breakage over a wide temperature range (>150 K) starting from 750 K, which is below the molecular desorption temperature of C<sub>2</sub>H<sub>2</sub> [15].

Similar to those observed for the adsorption of toluene on Si(100)2×1 [27], the intensity of D<sub>2</sub> desorption (Figure 4-2b) in the adsorption of styrene on Si(100)2×1 is over ten-fold higher than that for the corresponding molecular desorption (Figure 4-2a). However, unlike the molecular desorption that increases to a saturation level with exposure (10 L), the D<sub>2</sub> desorption reaches its maximum at ~4 L exposure of styrene-d<sub>8</sub> and then evidently decreases at a higher exposure (Figure 4-2b). This “anomalous” desorption behavior can be explained if the hydrogen abstraction is not instantaneous upon adsorption of styrene and it could be approximated as a separate step after the completion of the RT adsorption. As an example, we consider the simple case of complete hydrogen abstraction. Starting with an initial coverage of styrene  $\theta$  (with its value between 0 and 1), which corresponds in effect to the occupancy per Si dimer, the change in the surface concentration of the adsorbed styrene,  $x$ , that undergoes hydrogen abstraction can be written as follows:



The maximum change  $x_{\max}$  for complete hydrogen abstraction (reaction going to the right) would occur when  $\theta - x \rightarrow 0$  or  $(1 - \theta) - x \rightarrow 0$ , i.e. when  $\theta = 0.5$  in this case. In our

experiment,  $x_{\max}$  is found to occur at a coverage of 0.8-0.9, which is larger than the value obtained for complete abstraction (0.5). This difference could be due to incomplete abstraction reaction at RT as demonstrated by the amount of molecular desorption at a lower exposure (Figure 4-2a). Furthermore, the availability of vacated sites released in the thermal desorption process could also shift  $x_{\max}$  to a larger exposure.

In order to determine whether the phenyl group is involved in the hydrogen abstraction of styrene, the TDS profiles for a 10 L RT exposure of styrene-ring-d<sub>5</sub> (i.e. with just the phenyl group deuterated) are compared with those of a similar exposure of styrene-d<sub>8</sub> to Si(100)2×1 in Figure 4-4. Similarly to that shown in Figure 4-4b, the molecular desorption depicted in Figure 4-4a is considerably weaker than the hydrogen evolution. The TDS profiles of the parent mass for styrene-ring-d<sub>5</sub> (Mass 109) and styrene-d<sub>8</sub> (Mass 112) are effectively identical. The sum of the mass-2 TDS profile (with desorption maximum at 800 K) and mass-4 TDS profile (with desorption maximum at 870 K) for styrene-ring-d<sub>5</sub> (Figure 4-4a) is remarkably similar to the mass-4 TDS profile for styrene-d<sub>8</sub> (Figure 4-4b), which indicates that hydrogen abstraction can occur not just from the vinyl group but also from the phenyl group at a higher temperature. Below 700 K, the hydrogen atoms abstracted from the vinyl group of the adsorbed styrene evidently dominate the monohydride state on the Si(100)2×1 surface, and these hydrogen atoms start to desorb near 600 K. Above 700 K, on the other hand, the majority of hydrogen abstraction comes from the phenyl group. The present TDS results are consistent with the FTIR study by Schwartz *et al.* [25]. In particular, from the FTIR spectra recorded at RT for a 10 L RT exposure of d<sub>3</sub>-styrene (i.e. with just the vinyl group deuterated) to Si(100)2×1, Schwartz *et al.* observed the emergence of the Si–H stretching mode (at 2060 cm<sup>-1</sup>) upon annealing to 500-700 K (in addition to the Si–D stretch found at RT) [25], which indicates that hydrogen evolution from the phenyl group occurs at the higher temperature. In the aforementioned di-σ vinyl-bonded geometry of styrene on Si(100)2×1 observed at RT, the “dangling” phenyl group is unattached to the Si surface, which gives rise to a similar FTIR spectrum as that of a free benzene molecule, but different from that of benzene adsorbed on Si(100)2×1 in a cyclohexadiene-like adsorption geometry (as supported by the lack of C–H stretching vibration involving sp<sup>3</sup>-hybridized (alkane-like)

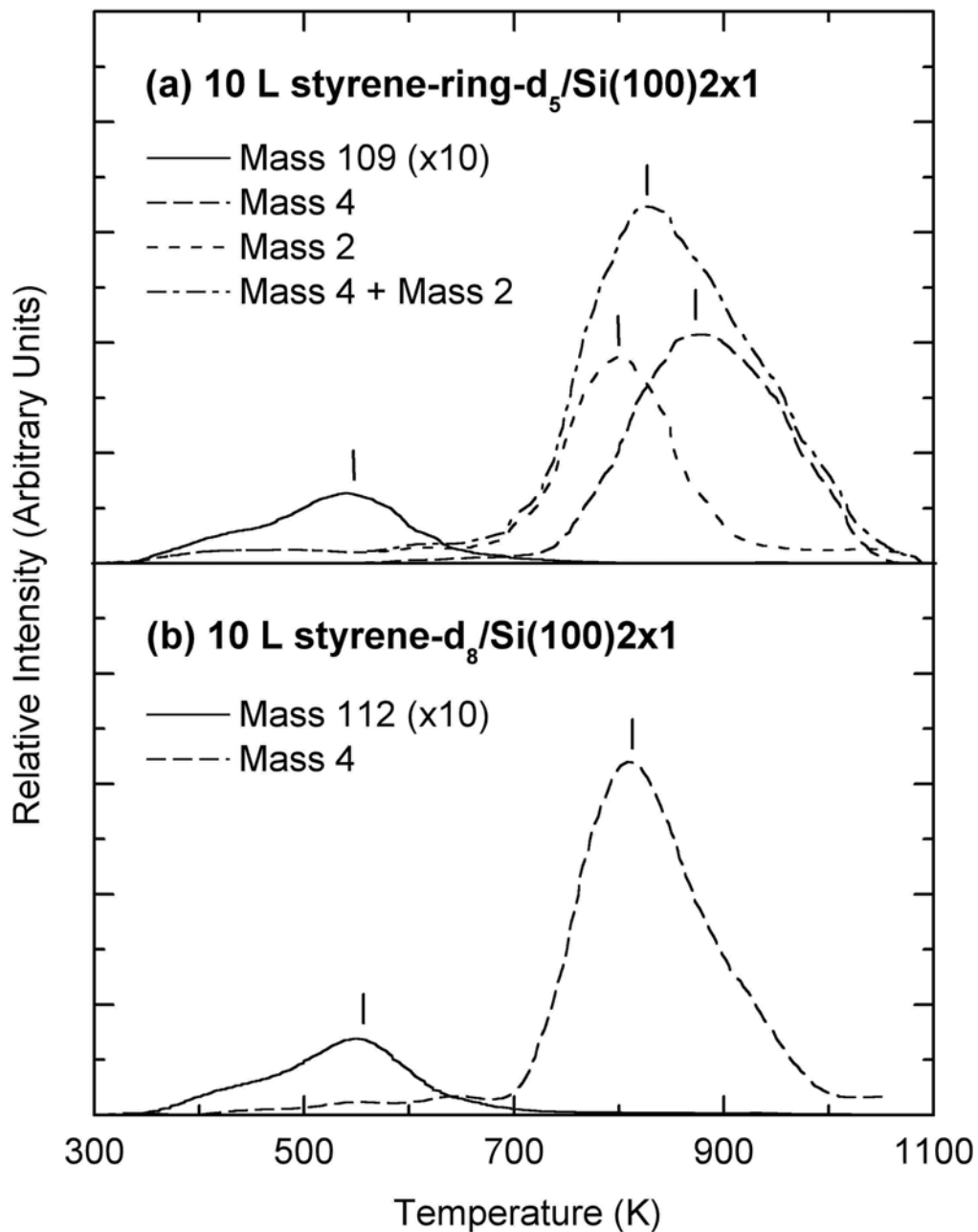
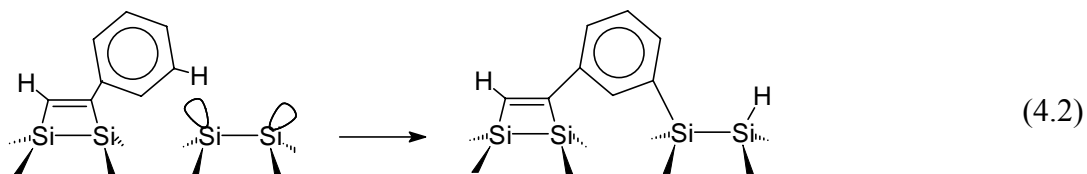


Figure 4-4 Thermal desorption profiles (a) of Mass 109 (molecular desorption), Mass 4 ( $D_2$ ) and Mass 2 ( $H_2$ ) for a 10 L room-temperature exposure of styrene-ring- $d_5$  and (b) of Mass 112 (molecular desorption) and Mass 4 ( $D_2$ ) for a 10 L room-temperature exposure of styrene- $d_8$ , both to Si(100)2 $\times$ 1.

carbons) [25]. Upon thermal excitation during annealing, the “dangling” phenyl group could become sufficiently close to the Si for the following reaction to occur



The attachment (bridging) of the phenyl group onto a second Si dimer is supported by the reduction in the number of the FTIR features in the 3010-3080  $\text{cm}^{-1}$  region [25], indicative of the general increase in the number of hydrogen substitution and replacement by bonding to the surface [35]. This picture is also consistent with a higher desorption maximum for recombinative desorption of the phenyl H atoms (870 K) than that of the vinyl H atoms (800 K). Another possible pathway for hydrogen evolution from the phenyl group is through adsorbate-adsorbate interaction, i.e. condensation oligomerization, which will be discussed in more detail elsewhere [36].

#### 4.2.3 Electron irradiation of styrene on Si(100)2×1

Figure 4-5 shows the effects of low-energy electron irradiation on the TDS profiles of Mass 109 (parent mass), Mass 28, Mass 4 and Mass 2 for 10 L RT exposure of styrene-ring-d<sub>5</sub> to Si(100)2×1. Electron irradiation (EI) was performed on the Si sample (held at 80 V bias potential) for 30 minutes at 0.2 mA with electrons thermionically emitted from a hot W filament positioned 5 cm away. Evidently, electron irradiation greatly diminishes desorption of the parent mass, suggesting a significantly reduced moiety of molecularly adsorbed styrene on the electron-irradiated sample, which is likely due to electron-induced desorption [37] or to conversion to other (smaller dissociated or larger oligomerized) adspecies. In addition to the parent mass (Mass 109), other smaller ionic fragments including Mass 108 (C<sub>6</sub>D<sub>5</sub>C<sub>2</sub>H<sub>2</sub>), Mass 83 (C<sub>6</sub>D<sub>5</sub>H) and Mass 54 (C<sub>4</sub>D<sub>2</sub>H<sub>2</sub>) were also monitored during the TDS experiments. The TDS profiles of these smaller fragments (not shown) closely follow that of the parent mass, indicating that they originate from dissociation of the molecularly desorbed styrene-ring-d<sub>5</sub> in the ionizer of the QMS. On the other hand, the TDS profile of Mass 28 (Figure 4-5b) corresponds to desorption of dissociated fragments (C<sub>2</sub>D<sub>2</sub> or C<sub>2</sub>H<sub>4</sub>) arising from

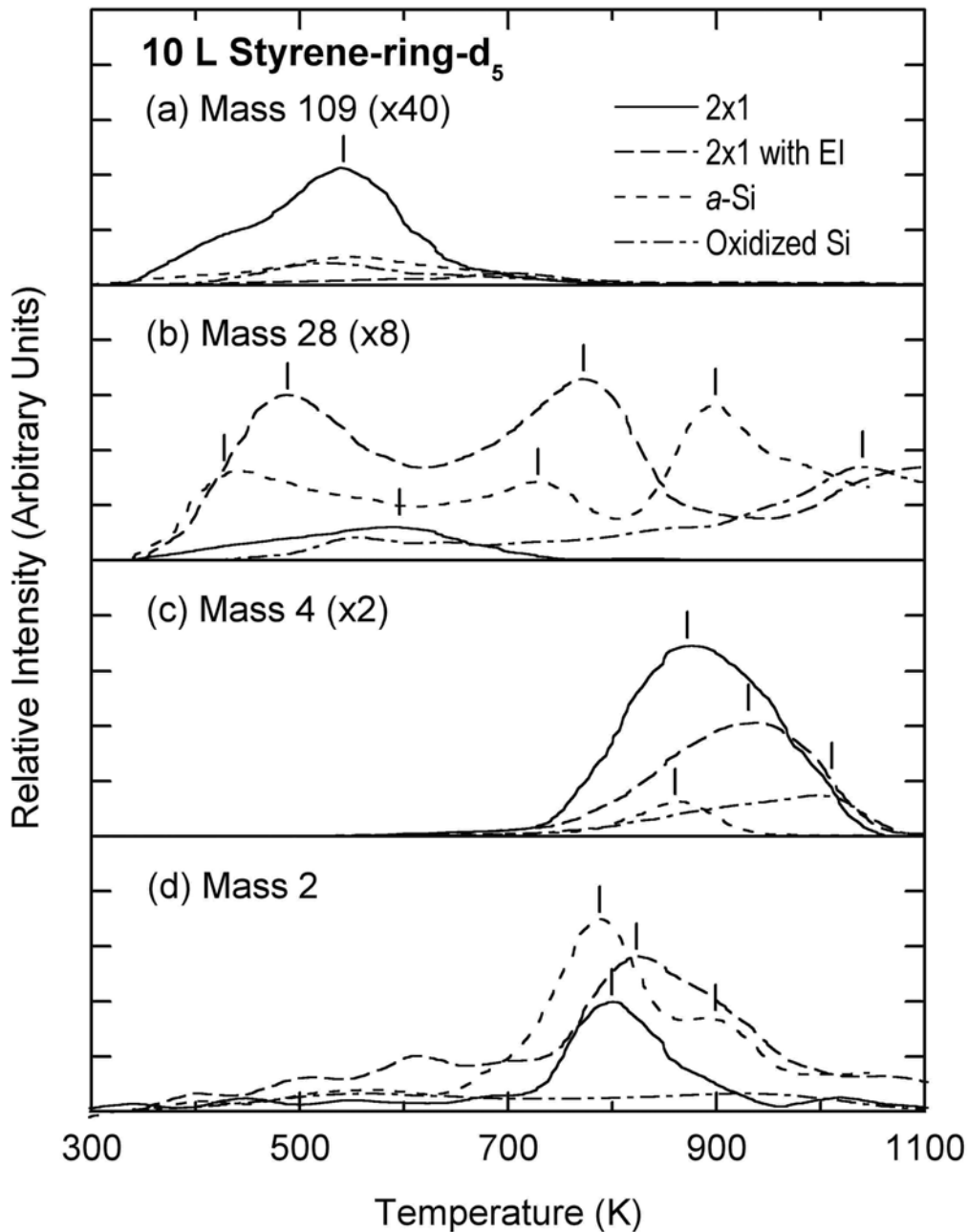


Figure 4-5 Thermal desorption profiles for (a) Mass 109 (molecular desorption) (b) Mass 28 (dissociative products), (c) Mass 4 ( $D_2$ ) and (d) Mass 2 ( $H_2$ ) for a 10 L room-temperature exposure of styrene-ring- $d_5$  to Si(100)2 $\times$ 1 without and with electron irradiation (EI) at 200  $\mu$ A and 80 eV for 30 minutes, amorphous (*a*-) Si, and oxidized surface of Si(100).



electron irradiation of the adsorbed styrene. Without electron irradiation, only very weak mass-28 desorption feature can be found in the 350-700 K region, generally indicating negligible dissociation of styrene upon adsorption and during the TDS experiment. Electron irradiation appears to significantly enhance the desorption profile of Mass 28 (Figure 4-5b) with two desorption maxima at 480 K and 760 K. Because the molecular desorption maximum for  $C_2H_4$  on  $Si(100)2\times 1$  is normally found at 550 K [19], the desorption maximum of Mass 28 at 480 K can be attributed to the dissociative desorption of fragments resulting from electron-induced dissociation of the vinyl group. Furthermore, molecular desorption of acetylene from  $Si(100)2\times 1$  has been reported with desorption maximum at 690-740 K [14]. The desorption maximum for the higher-temperature feature of Mass 28 (at 760 K) could therefore correspond to electron-induced dissociation of the phenyl group of the adsorbed styrene-ring- $d_5$  at RT.

The majority (~90%) of the mass-2 desorption for the electron-irradiated sample is found to occur above 700 K with a desorption maximum at ~800 K, which is similar to that found for styrene-ring- $d_5/Si(100)2\times 1$  without electron irradiation (Figure 4-5d). The small amount of desorption at 450-650 K could correspond to  $H_2$  originated from the cracking of some dissociative products. On the other hand, there is a considerable reduction in the relative intensity and a discernible shift in the desorption maximum from 870 K to 930 K for the mass-4 TDS profile for the adsorbed styrene-ring- $d_5$  upon electron irradiation (Figure 4-5c). The reduction in the relative intensity of the mass-4 TDS profile could be due to the reduced moiety of phenyl group caused by electron-induced dissociation to produce fragments such as  $C_2D_2$  (Mass 28). Hydrogen evolution from the adsorbate can result from either adsorbate-substrate substitution or adsorbate-adsorbate condensation oligomerization reaction. In both cases, the reduced surface mobility and enhanced steric effect of larger molecules are expected to require a higher temperature in order to overcome the respective activation barrier. Detailed mechanisms about hydrogen evolution in cyclic hydrocarbons on  $Si(100)$  are discussed elsewhere [36]. In particular, surface condensation oligomerization of pyridine on  $Si(100)2\times 1$  at RT was found upon low-energy electron irradiation at RT [28]. In this case, the condensation oligomerization process was marked by a shift in the TDS maximum for hydrogen evolution to a higher temperature relative to that of recombinative desorption from monohydrides abstracted from adsorbed pyridine monomers or its smaller

fragments. Together with the small shoulder appearing at 930 K of the mass-2 TDS profile (Figure 4-5d), the similarity in the observed shift in the desorption maximum for Mass 4 in styrene-ring-d<sub>5</sub> (Figure 4-5c) suggests electron-induced oligomerization of styrene at RT, as in the case proposed for pyridine [28]. In accord with our previous TDS experiments [36], the present work appears to support the general observation that the larger the size of the unsaturated organic adsorbate, the higher the temperature for hydrogen evolution. For instance, the desorption maximum for hydrogen evolution is found to increase from 790 K for surface monohydride to 800 K for vinyl group (Figure 4-4a), 870 K for phenyl group (Figure 4-4a), and 930 K for oligomers (Figure 4-5c) observed in the present work.

#### 4.2.4 Surface conditions study

Figure 4-5 also compares the TDS profiles for molecular desorption (Mass 109) and desorption of dissociative products (Mass 28, Mass 4 and Mass 2) for the 2×1 and modified surfaces of Si(100) exposed with 10 L of styrene-ring-d<sub>5</sub> at RT. The amorphous Si (*a*-Si) surface was produced by ion sputtering in 4×10<sup>-5</sup> Torr of Ar at 1 keV ion impact energy for 20 minutes, while the oxidized Si(100) surface was obtained by exposing a clean 2×1 surface with 100 L of O<sub>2</sub> at RT. The lack of any long-range order for both *a*-Si and oxidized Si surfaces was confirmed by the absence of a LEED pattern (below 100 eV electron beam energy).

In contrast to the generally weak and broad band of Mass 28 for the 2×1 surface at 600 K, there are three strong mass-28 desorption features centered at 440 K, 730 K, and 900 K for *a*-Si Figure 4-5b). On the other hand, the TDS profile of Mass 26 (not shown) reveals a single desorption feature near 730 K for the *a*-Si sample. From the earlier work [14], the mass-28 desorption feature at 730 K could only come from desorption of acetylene (C<sub>2</sub>D<sub>2</sub>), which should also exhibit a corresponding mass-26 (C<sub>2</sub>D) TDS profile at approximately 20% of the TDS intensity of the parent mass (C<sub>2</sub>D<sub>2</sub>) according to the cracking pattern of acetylene [6]. After removal of this contribution due to C<sub>2</sub>D<sub>2</sub> (with its origin likely coming from the dissociation of the phenyl group of the adsorbed styrene-ring-d<sub>5</sub>) in the mass-26 TDS profile, we obtain a similar amount of contribution from the parent mass of C<sub>2</sub>H<sub>2</sub> (as that originated from C<sub>2</sub>D<sub>2</sub>), which could come from dissociation of the vinyl group. Given the lack of any

discernible features of Mass 26 at the corresponding temperatures, the other TDS features of Mass 28 at 440 K and 900 K (Figure 4-5b) can be attributed to dissociative desorption of  $C_2D_2$  from the phenyl group of adsorbed styrene-ring- $d_5$ . Furthermore, the prominent mass-28 TDS peak at 900 K (Figure 4-5b) is found to be accompanied with significant desorption of Mass 40 at 880 K, which corresponds to desorption of ion-implanted Ar as a result of the sputtering process (not shown). The mass-28 TDS feature at 900 K could therefore also be attributed to dissociative desorption of hydrocarbon fragments from a fairly active surface as a result of significant structural rearrangement due to Ar desorption near 880 K.

The shapes and desorption maxima of the TDS profiles for molecular desorption (Mass 109, Figure 4-5a),  $D_2$  (Mass 4, Figure 4-5c) and  $H_2$  (Mass 2, Figure 4-5d) for  $\alpha$ -Si are found to be similar to those observed on the clean Si(100) $2\times 1$  surface. For  $\alpha$ -Si, the TDS intensities for molecular and  $D_2$  desorption are found to be greatly reduced (by over 70%), in contrast to an increase in the hydrogen desorption, all relative to the clean  $2\times 1$  surface. The reduction in molecular desorption is likely due to the loss of Si dimer sites (appropriate for molecular adsorption) on the  $\alpha$ -Si surface. On the other hand, the increase in the mass-28 TDS profile for  $\alpha$ -Si surface with respect to that for the  $2\times 1$  surface (Figure 4-5b) suggests that there are evidently more active sites available for dissociation on the  $\alpha$ -Si surface. Stoichiometrically, a dissociated phenyl group would need to acquire a hydrogen atom in order to generate three acetylene molecules, while a vinyl group would be required to release a hydrogen atom to produce one acetylene molecule. The increase of the acetylene desorption (Figure 4-5b) is consistent with the observed reduction in the mass-4 desorption (Figure 4-5c) and increase in the mass-2 desorption (Figure 4-5d) observed for the  $\alpha$ -Si surface.

Figure 4-5 also shows the TDS profiles of Mass 109, Mass 28, Mass 4 and Mass 2 for a 10 L RT exposure of styrene-ring- $d_5$  on an oxidized Si(100) surface. Evidently, the total amounts of desorption of molecular (Mass 109, Figure 4-5a) and dissociative products (Mass 28, Figure 4-5b) are found to decrease significantly with respect to that for Si(100) $2\times 1$ , while the corresponding TDS profile of Mass 2 (Figure 4-5d) is reduced to featureless, which could be attributed to the loss of active adsorption sites due to oxidation. In particular, the lack of any discernible mass-2 ( $H_2$ ) desorption suggests that hydrogen abstraction from the vinyl

group on the  $2\times 1$  surface is blocked by the passivation of Si dangling bonds by oxygen. Passivation of the active sites can also be achieved by H atoms as demonstrated in a separate TDS experiment for styrene- $d_8$  on a H-terminated Si(100) $1\times 1$  surface, in which no desorption of Mass 112 (parent mass of styrene- $d_8$ ), Mass 28 and Mass 4 was observed (not shown). On the other hand, the TDS intensity of Mass 28 for the oxidized surface is found to increase considerably and shift toward a higher temperature with respect to that for the  $2\times 1$  surface (Figure 4-5b). The lack of any corresponding lower mass fragments, e.g. Mass 26, suggests that Mass 28 is not due to desorption of  $C_2D_2$  or  $C_2H_4$  fragments, but possibly to associative desorption of CO. Since the temperature of desorption maximum for molecular desorption of CO on Si(100) (180 K) [38] (with the corresponding adsorption energy of CO on Si(100) $2\times 1$  estimated to be 17–19 kcal/mol [39]) is found to be considerably lower than the observed desorption maximum (1040 K) in Figure 4-5b, other dissociation channels by which C readily combines with O on the oxidized surface to produce the desorbed CO could be activated (Figure 4-5b). The latter is consistent with an ascending shape and shift of the observed mass-4 TDS intensity toward the higher temperature side (Figure 4-5c) similar to the mass-28 profile (Figure 4-5b), which could be due to hydrogen evolution in this high temperature region.

#### 4.2.5 Surface-mediated hydrogenation reactions

In order to investigate the interaction of atomic hydrogen with styrene adsorbed on Si(100) $2\times 1$ , the sample saturated with a 100 L RT exposure of styrene- $d_8$  was post-exposed with H atoms generated from 3000 L of  $H_2$  with a hot W filament positioned 2 cm away. To minimize the effect of radiative heating from the hot filament during the hydrogen activation, liquid nitrogen was used to keep the sample near or below RT. After the post-hydrogenation (PH), the diffused  $2\times 1$  LEED pattern for the styrene- $d_8$  saturated surface was changed to a  $1\times 1$  pattern, which indicates total destruction of the surface reconstruction involving the Si dimers. Evidently, the TDS features for the molecular (Mass 112) desorption from both phenyl-bonded adspecies (at 460 K) and vinyl-bonded adspecies (at 560 K) shown in Figure 4-6 are greatly diminished. However, new desorption states with maxima at 700 K and 750 K are observed for the post-hydrogenated sample. The nature of these two states will be

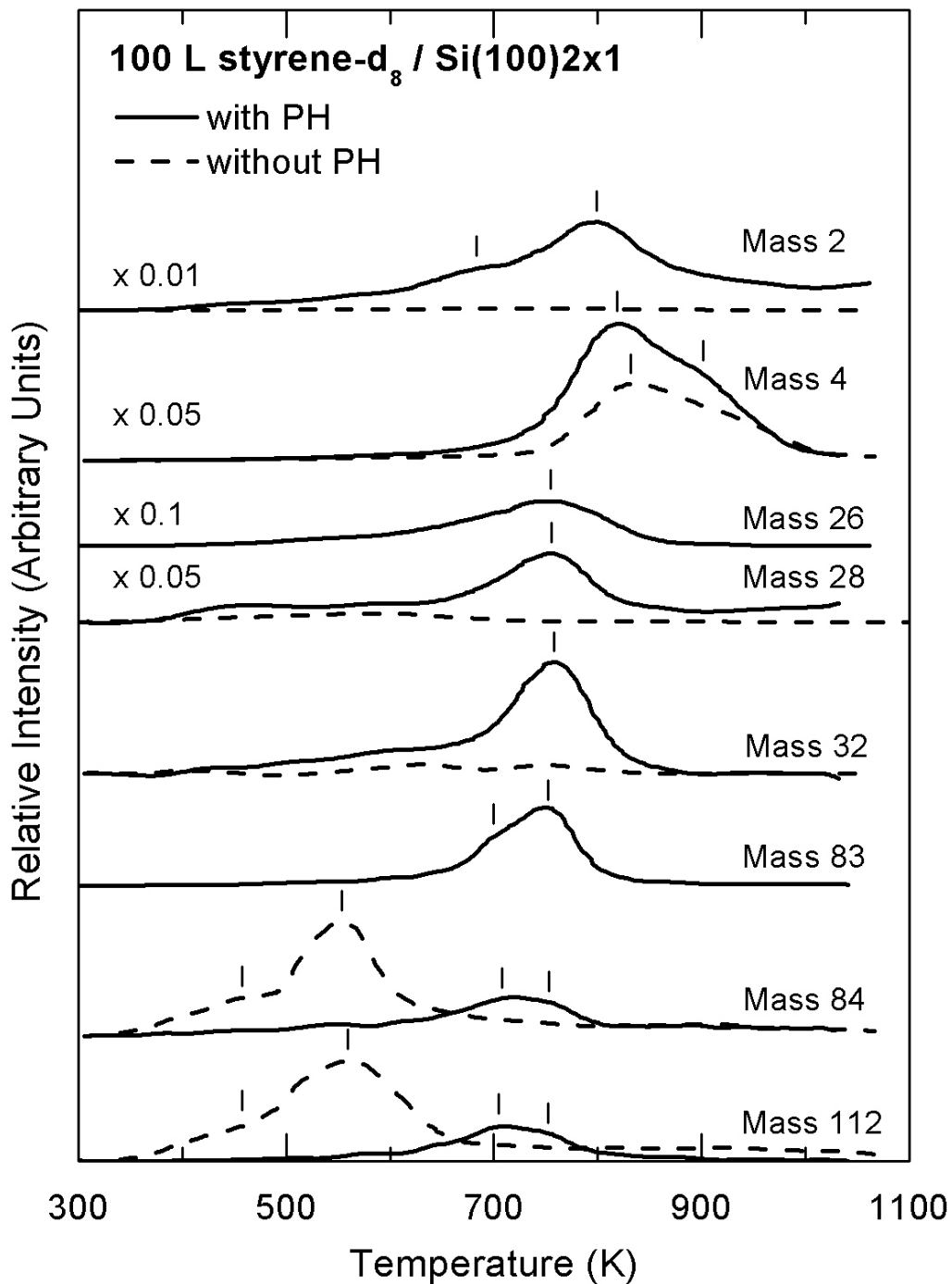


Figure 4-6 Comparison of thermal desorption profiles of Mass 2, 4, 26, 28, 32, 83, 84 and 112 for a 100 L room-temperature exposure of styrene-d<sub>8</sub> to Si(100)2×1 surface, with and without post-hydrogenation (PH).

discussed below. Like the case without post-hydrogenation, the mass-84 ( $C_6D_6$ ) TDS profile for the sample with post-hydrogenation appears to follow the TDS profile of the parent mass, which suggests that Mass 84 is due to electron dissociation of the molecularly desorbed styrene- $d_8$  in the ionizer of the QMS. The stronger TDS maxima of Mass 83 ( $C_6D_5H$ ), and of Mass 32 ( $C_2D_4$ ), Mass 28 ( $C_2D_2$  or  $C_2H_4$ ), and Mass 26 ( $C_2H_2$ ), all at 750 K, suggest that these fragments are predominantly due to associative desorption of H (from the surface) with the phenyl group and with the vinyl group, respectively, both of which involve isotopic mixing of H and D. Similar increase in the temperature of desorption maxima for molecular desorption has also been reported in our earlier studies on (methyl-)cyclohexene and (methyl-)cyclohexadiene on Si(111)7 $\times$ 7 [40,41,42], the TDS profiles of which provide strong evidence for the production of (toluene) benzene by dehydrogenation on Si(111)7 $\times$ 7 upon the TDS process. The desorption maxima for both molecular and dehydrogenated products were also found to be shifted by 100 K to 670 K, similar to the desorption maximum of dihydride (650 K). We have also performed the same TDS experiment for 100 L exposure of styrene-ring- $d_5$  with post-hydrogenation. Results similar to those for styrene- $d_8$  have been observed for the corresponding masses: Mass 109 (parent mass of  $C_6D_5C_2H_3$ ), Mass 83 ( $C_6D_5H$ ), Mass 30 ( $C_2D_2H_2$ ), Mass 28 ( $C_2D_2$  or  $C_2H_4$ ) and Mass 26 ( $C_2H_2$ ) – not shown.

In Figure 4-6, the two intense TDS features of Mass 2 with maxima at 680 K and 800 K for the post-hydrogenated styrene- $d_8$ /Si(100)2 $\times$ 1 sample are found to be similar to those arising from recombinative thermal desorption, respectively, from dihydride and monohydride on a H-terminated Si(100) surface [11,12]. Two mass-4 TDS features with maxima located at 820 K and 900 K are found for the post-hydrogenated sample (Figure 4-6). In comparison with the TDS profile for the styrene- $d_8$ /Si(100) sample without H post-exposure, the corresponding mass-4 TDS profile for the post-hydrogenated styrene- $d_8$ /Si(100) sample nearly doubles in intensity, in marked contrast to that for the post-hydrogenated styrene-ring- $d_5$ /Si(100) sample, which is at about the same intensity as the styrene- $d_8$ /Si(100) sample without H post-exposure (Figure 4-7b). The increase in the  $D_2$  desorption for the styrene- $d_8$ /Si(100) sample with H post-exposure can therefore be attributed to hydrogen abstraction from the vinyl group.

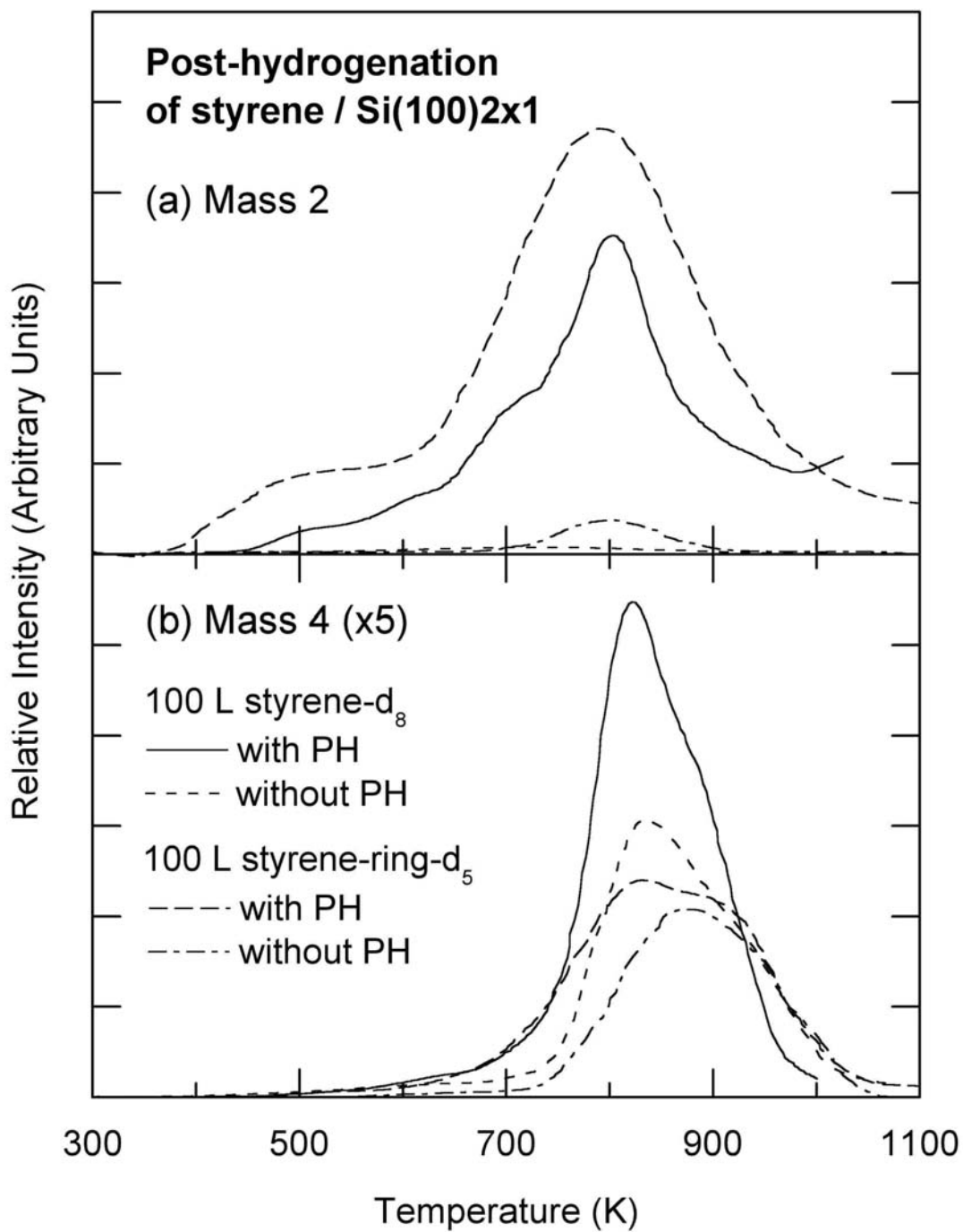


Figure 4-7 Comparison of thermal desorption profiles of (a) Mass 2 and (b) Mass 4 for a 100 L room-temperature exposure of styrene-d<sub>8</sub> with those of styrene-d<sub>5</sub> to Si(100)2×1, with and without post-hydrogenation (PH).

It is of interest to note that the TDS profile has not revealed any higher masses than the parent mass (e.g. Mass 114), which would correspond to desorption of hydrogenated products of the adsorbed styrene. However, the TDS profiles of lower masses such as Mass 84 (benzene-d<sub>6</sub>) and Mass 83 (benzene-d<sub>5</sub>) follow that of Mass 112 (parent mass of styrene-d<sub>8</sub>), which suggests that hydrogenation occurs primarily for the vinyl group of the adsorbed styrene (Figure 4-6). Furthermore, the “dangling” phenyl group of the adsorbed styrene appears to be not directly involved in bonding to the Si surface and therefore not reactive toward H. The highly stable aromatic ring structure remains intact during the H post-exposure and the subsequent thermal desorption process, which is also confirmed by the weaker mass-4 TDS profile for styrene-ring-d<sub>5</sub> relative to that for styrene-d<sub>8</sub> with H post-exposure shown in Figure 4-7. The post-hydrogenation process is therefore site-selective and occurs at the vinyl group likely via surface mediated enhancement. Widdra *et al.* reported a similar elevation in the molecular desorption temperature (from 590 K to 700 K) after a high H post-exposure to Si(100)2×1 exposed with ethylene [19]. The 1,2-ethanediyl adspecies is believed to undergo hydrogenation upon high exposure of H atoms to form a surface ethyl species by breaking a Si–C  $\sigma$ -bond [and the (2×1) reconstruction by breaking Si-Si dimer bond]. Further stabilization of the ethyl-Si structure is also obtained by blocking reactive sites for both molecular desorption and decomposition pathways [20]. In the case of the styrene/Si(100)2×1 system, the adsorption is found to primarily involve a vinyl-bonded adspecies, with molecular desorption maxima found at similar temperatures for both the 2×1 and post-hydrogenated sample as that for ethylene/Si(100)2×1 [20]. A similar mechanism for the corresponding surface thermal chemistry could therefore be used to explain the TDS spectra in Figure 4-6 (and Figure 4-7), with the difference in the replacement of a H atom with a phenyl group on the ethylene molecule.

Figure 4-8 shows a proposed model for the thermal evolution of styrene-d<sub>8</sub> upon molecular adsorption on Si(100)2×1 at RT followed by H post-exposure. Structure I illustrates the initial molecular adsorption of styrene-d<sub>8</sub> involving the saturation of the  $\pi$  bond in the vinyl group by the dangling bonds of the Si dimer and the formation of di- $\sigma$  bonded phenylethane-1,2-diyl adspecies as the [2+2] cycloaddition product [25]. As confirmed by the observed LEED pattern, such type of interaction does not significantly affect the (2×1)



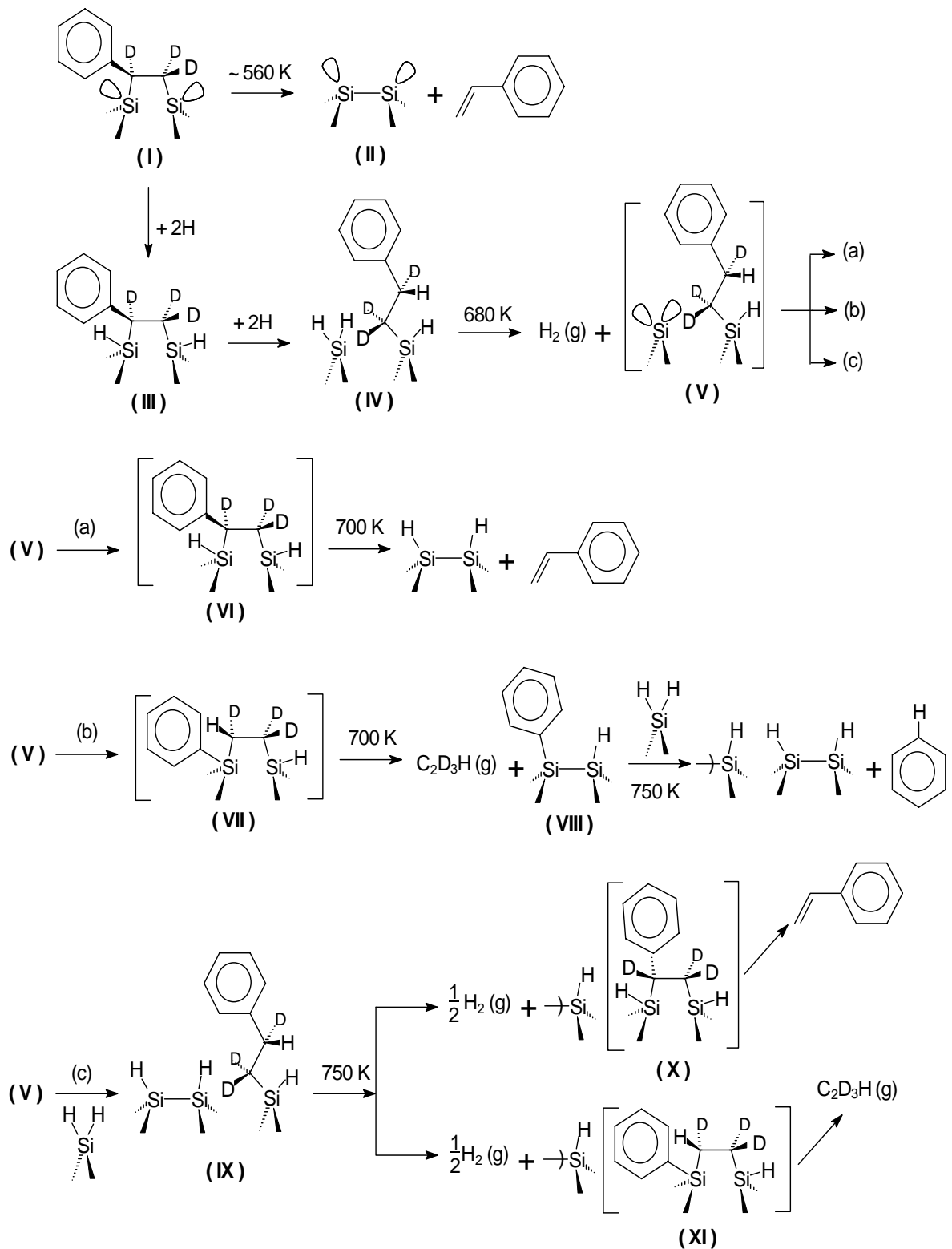


Figure 4-8 Proposed schemes for the adsorption, desorption, and surface reactions for styrene- $\text{d}_8$  on  $\text{Si}(100)2\times 1$  followed by post-hydrogenation.

surface structure, which can be recovered upon molecular desorption near 560 K (II). Post-exposure of H is believed to saturate the remaining “outside” dangling bonds of the Si dimer that is already di- $\sigma$  bonded to styrene- $d_8$  (III), and break the Si-Si dimer bond. At higher exposures, H atoms could not only attack one of the  $\sigma$ -bonds of the adsorbed styrene to form phenylethyl adspecies (IV) but also saturate the vacated dangling bond site, disrupting the (2 $\times$ 1) reconstruction and generating the observed (1 $\times$ 1) LEED pattern. The adsorbed H is stable up to the recombinative desorption temperature of H from silicon dihydride (~680 K). In the absence of coadsorbed hydrogen at the silicon dihydride sites, an ethyl adspecies was reported to further decompose into ethylene and hydrogen in effect by insertion of a Si dimer atom at 600 K [43,44]. This decomposition pathway could be hindered by hydrogen occupation on the dihydride sites, which blocks the reactive neighbouring sites during H post-exposure, and could become available only upon annealing to 680 K. A similar mechanism could apply to the phenylethyl adspecies on Si(100), if one of the hydrogen on the adsorbed ethyl group is replaced by a phenyl group.

After the neighbouring dangling bond sites have been vacated by recombinative desorption of H upon annealing to 680 K, the single- $\sigma$  bonded phenylethyl adspecies (V) could undergo three possible processes upon further annealing. The phenylethyl adspecies could reoccupy the adjacent dangling bond site by an insertion reaction of a neighbouring Si atom either into the  $C_\beta$ -H bond to form a di- $\sigma$  bonded phenylethane-1,2-diyl adspecies (VI) in process (a) or into  $C_\beta$ -phenyl bond to produce a di- $\sigma$  bonded ethane-1,2-diyl adspecies (VII) with a mono- $\sigma$  bonded phenyl adspecies in process (b). Because the temperature (680 K) is already higher than the molecular desorption temperatures of styrene (560 K, Figure 4-6) and of ethylene (560 K) [20], once the surface hydrogen atoms begin to desorb, the as-formed di- $\sigma$  bonded phenylethane-1,2-diyl adspecies in a [2+2] geometry (VI) in process (a) and the ethane-1,2-diyl adspecies (VII) in process (b) would be expected to undergo immediate desorption, which accounts for the slightly higher desorption maximum of Mass 112 (parent mass of styrene) and Mass 31 ( $C_2D_3H$ ) (not shown), respectively, at 700 K. In process (b) the phenyl group (VIII) recombines with a neighbouring H on a dihydride site and desorbs as benzene ( $C_6D_5H$ , Mass 83) at 750 K. Because the formation of benzene involves the surface reconstruction from a phase consisting of a mixture of monohydride and

dihydride (i.e. a  $3\times 1$  structure with alternating dihydride and monohydride-dimer rows) to a phase with just monohydride (i.e. a  $2\times 1$  structure), the corresponding temperature of benzene formation and desorption is therefore expected to be in between the hydrogen desorption temperatures for dihydride (680 K) and monohydride (800 K), which is in accord with the observed TDS maximum of Mass 83 at 750 K. Finally, when the empty dangling bond sites of the single- $\sigma$  bonded phenylethyl adspecies (V) have been converted to a monohydride dimer after reacting with one of its neighbouring dihydride in process (c), the resulting phenylethyl adspecies (IX) could undergo similar pathways as in processes (a) and (b). In particular, upon further annealing to 750 K in process (c), the recombinative desorption of  $H_2$  involving H atoms from a dihydride and a monohydride would induce similar Si insertion reactions in the formation of metastable di- $\sigma$  bonded phenylethane-1,2-diyl adspecies (X) and ethane-1,2-diyl adspecies (XI) that lead to desorption of styrene and ethylene, respectively. It should be noted that the difference in the  $H_2$  recombinative desorption temperature is due to hydrogen evolution from a dihydride pair (680 K) and from a dihydride-monomer pair (750 K). Following these three reaction pathways (a, b, and c), the remaining hydrocarbons on the surface may undergo further decomposition into silicon carbide while the remaining H, present in the form of monohydride (on the Si dimer), could undergo recombinative desorption at 800 K. The observation of the dihydride-monomer feature (at 750 K) is of interest because even though such a feature could exist for the H-terminated Si(100) surface it would likely be obscured by the strong overlapping monohydride feature.

### 4.3 Concluding remarks

The adsorption and thermal reactions of styrene- $d_8$  on the  $2\times 1$  and modified Si(100) surfaces have been investigated by using TDS, AES and LEED. At RT, the saturation coverage of styrene on Si(100) $2\times 1$  is found to be nearly identical to that of ethylene, i.e. 0.5 ML (one styrene for every surface Si dimer), and it appears to have little effect on the ( $2\times 1$ ) LEED pattern of the Si(100) surface. Chemisorption occurs primarily by bonding through the vinyl group, with only 15% of the adsorbed styrene involving bonding through the phenyl group. Upon annealing, the adsorbate is found to undergo several plausible reactions, including

molecular desorption, hydrogen abstraction, fragmentation, and/or condensation oligomerization. Similar to pyridine/Si(100)2×1 [28], the elevation of the TDS maximum for recombinative desorption involving H from the phenyl group after electron irradiation on styrene/Si(100)2×1 also suggests electron-induced oligomerization at RT.

The surface roughness of the sputtered Si surface generally provides more adsorption states and open up new thermal dissociation pathways resulting in less molecular desorption. On the oxidized Si(100) surface, considerably reduced molecular desorption and diminished hydrogen abstraction from the vinyl group are observed, while CO production and condensation oligomerization near 1000 K are found to be plausible. Furthermore, saturation exposure of atomic H totally passivates the Si(100)2×1 surface, producing a 1×1 surface that is inert to styrene adsorption.

High post-exposure of atomic hydrogen is found to stabilize the adsorption on Si(100)2×1 by transforming the di- $\sigma$  vinyl-bonded cycloaddition structure of styrene (phenylethane-1,2-diyl adspecies) into a substitution adsorption structure of phenylethyl adspecies. Given the stability of the aromatic ring structure and the lack of direct bonding with the Si substrate, it is not surprising that the “dangling” phenyl group remains intact upon H post-exposure at RT. Driven by thermal diffusion and desorption of hydrogen upon annealing, surface-mediated reforming of the resulting adspecies and evolution of ethylene and benzene are observed likely from dihydride and monohydride structures. Hydrogen therefore appears to play an important role in affecting the outcome of different chemical processes on the Si(100) surfaces.

In summary, the two functional groups (vinyl and phenyl groups) in styrene are found to exhibit different selectivity toward RT chemisorption on Si(100)2×1. In addition to different surface conditions, remarkably different surface chemical processes have been observed and could effectively be controlled on the 2×1 surface thermally and by low-energy electron irradiation and post-hydrogenation.

## 4.4 Reference

- [1] T.A. Skotheim, R.L. Elsenbaumer, and J.R. Reynolds (eds.), "Handbook of Conducting Polymers", Dekker, New York (1998).
- [2] J.L. Reddinger, J.R. Reynolds, *Advances in Polymer Science* 145 (1999) 57.
- [3] Y. Taguchi, M. Fujisawa, T. Takaoka, T. Okada, M. Nishijima, *J. Chem. Phys.* 95 (1991) 6870.
- [4] Y. Taguchi, Y. Ohta, T. Katsumi, K. Ichikawa, O. Aita, *J. Electron Spectrosc. Relat. Phenom.* 88-91 (1998) 671.
- [5] S. Gokhale, P. Trischberger, D. Menzel, W. Widdra, H. Droge, H.-P. Steinruck, U. Birkenheuer, U. Gutdeutsch, N. Rosch, *J. Chem. Phys.* 108 (1998) 5554.
- [6] M.J. Kong, A.V. Teplyakov, J.G. Lyubovitsky, S.F. Bent, *Surf. Sci.* 411 (1998) 286.
- [7] G.P. Lopinski, T.M. Fortier, D.J. Moffatt, R.A. Wolkow, *J. Vac. Sci. Tech. A* 16 (1998) 1037.
- [8] B. Borovsky, M. Krueger, E. Ganz, *Phys. Rev. B* 57 (1998) R4269.
- [9] B.I. Craig, *Surf. Sci.* 280 (1993) L279.
- [10] H.D. Jeong, S. Ryu, Y.S. Lee, S. Kim, *Surf. Sci.* 344 (1995) L1226.
- [11] U. Birkenheuer, U. Gutdeutsch, N. Rosch, *Surf. Sci.* 409 (1998) 213.
- [12] R.A. Wolkow, G.P. Lopinski, D.J. Moffatt, *Surf. Sci.* 416 (1998) L1107.
- [13] P.L. Silvestrelli, F. Ancilotto, F. Toigo, *Phys. Rev. B* 62 (2000) 1596.
- [14] X. Lu, M.C. Lin, X. Xu, N. Wang, Q. Zhang, *Phys. Chem. Comm.* 13 (2001) 1.
- [15] C.C. Cheng, W.J. Choyke, J.T. Yates, Jr., *Surf. Sci.* 231 (1990) 289.
- [16] L. Clemen, R.M. Wallace, P.A. Taylor, M.J. Dresser, W.J. Choyke, W.H. Weinberg, J.T. Yates, Jr., *Surf. Sci.* 268 (1992) 205.
- [17] L.H. Chua, R.B. Jackman, J.S. Foord, *Surf. Sci.* 315 (1994) 69.
- [18] C. Huang, W. Widdra, W.H. Weinberg, *Surf. Sci.* 315 (1994) L953.
- [19] W. Widdra, C. Huang, S.I. Yi, W.H. Weinberg, *J. Chem. Phys.* 105 (1996) 5605.
- [20] M. Ikeda, T. Maruoka, N. Nagashima, *Surf. Sci.* 416 (1998) 240.
- [21] W. Pan, T. Zhu, W. Yang, *J. Chem. Phys.* 107 (1997) 3981.
- [22] A.J. Fisher, P.E. Blöchl, G.A.D. Briggs, *Surf. Sci.* 374 (1997) 298.
- [23] R. Konečný, D.J. Doren, *Surf. Sci.* 417 (1998) 169.

- [24] S.F. Bent, *Surf. Sci.* 500 (2002) 879-903.
- [25] M.P. Schwartz, M.D. Ellison, S.K. Coulter, J.S. Hovis, R.J. Hamers, *J. Am. Chem. Soc.* 122 (2000) 8529.
- [26] G.P. Lopinski, D.D.M. Wayner, R.A. Wolkow, *Nature* 406 (2000) 48.
- [27] Q. Li, K.T. Leung, *Surf. Sci.* 479 (2001) 69. See also Chapter 2
- [28] Q. Li, K.T. Leung, *Surf. Sci.* 541 (2003) 111. See also Chapter 5
- [29] "NIST/EPA/NIH Mass Spectral Library", NIST'98 with Windows, Version 1.7, (1996).
- [30] J.B. Foresman, Æ. Frisch, "Exploring Chemistry with Electronic Structure Methods", 2nd Ed., Gaussian Inc., Pittsburgh (1996); and references therein.
- [31] M. Suemitsu, H. Nakazawa, N. Miyamoto, *Appl. Surf. Sci.* 82/83 (1994) 449.
- [32] S.M. Gates, R.R. Kunz, C.M. Greenlief, *Surf. Sci.* 207 (1989) 364.
- [33] P.A. Taylor, R.M. Wallace, C.C. Cheng, W.H. Weinberg, M.J. Dresser, W.J. Choyke, and J.T. Yates, Jr., *J. Am. Chem. Soc.* 114 (1992) 6754.
- [34] C. Huang, W. Widdra, X.S. Wang, W.H. Weinberg, *J. Vac. Sci. Technol. A* 11 (1993) 2550.
- [35] G. Socrates, "Infrared Characteristic Group Frequencies", Wiley, New York (1980).
- [36] Q. Li, K.T. Leung, to be submitted. See also Chapter 6.
- [37] V.N. Ageev, *Prog. Surf. Sci.* 47 (1994) 55; and references therein.
- [38] R.Y. Young, K.A. Brown, W. Ho, *Surf. Sci.* 336 (1995) 85.
- [39] Y. Imamura, N. Matsui, Y. Morikawa, M. Hada, T. Kubo, M. Nishijima, H. Nakatsuji, *Chem. Phys. Lett.* 287 (1998) 131.
- [40] D.Q. Hu, C.D. MacPherson, K.T. Leung, *Surf. Sci.* 273 (1992) 21.
- [41] C.D. MacPherson, D.Q. Hu, M. Doan, K.T. Leung, *Surf. Sci.* 310 (1992) 231.
- [42] C.D. MacPherson, D.Q. Hu, K.T. Leung, *Surf. Sci.* 322 (1995) 58.
- [43] L.A. Keeling, L. Chen, C.M. Greenlief, *Chem. Phys. Lett.* 217 (1994) 136.
- [44] J. Schmidt, C. Stuhlmann, H. Ibach, *Surf. Sci.* 302 (1994) 10.

## Chapter 5

# Thermally induced chemistry and electron-mediated processes of pyridine on (2×1) and modified Si(100) surfaces: Evidence of electron-induced condensation oligomerization

### 5.1 Introduction

Organic semiconductors have attracted much recent attention because of their unique physical and electronic properties associated with many potential applications in the microelectronics industry [1,2,3,4]. The interactions of heterocyclic hydrocarbons, such as thiophene (C<sub>4</sub>H<sub>4</sub>S) and furan (C<sub>4</sub>H<sub>4</sub>O), with semiconductor surfaces are of practical importance to the development of highly ordered thin-film conducting polymers [5,6]. The conductivity of a polymer depends on the degree of conjugation in the  $\pi$ -bond backbone, and the chain alignment and extension [6]. Polymers are often generated electrochemically and made (semi)conducting upon doping. In such a process, the structure of the polymer film is usually ill-defined and highly disordered because it is difficult to control the factors that regulate the structure and organization of the polymer. Consequently, the conductivity of the resulting polymer is usually low. A viable approach to improve the ordering of conducting polymers is to pre-align the monomers or oligomers on a well-defined single-crystal surface before initiating polymerization. The two-dimensional periodicity of the surface can be used as a template to produce a highly ordered thin-film polymer. Silicon with its directional bonding and special electronic properties [7,8] is an ideal choice for use as a template [9,10]. In addition to thermally induced chemistry, different forms of radiation (ultraviolet light, low-energy electrons and/or ions) have also been used to mediate surface polymerization upon monomer adsorption. An improved understanding of the factors that govern the adsorption and reactivity of heterocyclic hydrocarbons on silicon surfaces with and without mediation by thermal or non-thermal irradiation is therefore of fundamental technological interest.

Pyridine (C<sub>5</sub>H<sub>5</sub>N) is one of the most common hetero-hexacyclic hydrocarbons, with a dipole moment of 2.215 D due largely to the lone-pair electrons on the N heteroatom [11]. Unlike the adsorption of pyridine on Si(111) surfaces that has been studied extensively

[12,13,14,15], only a limited number of theoretical studies have been reported for pyridine on Si(100) [16,17,18]. Based on the photoemission result, Piancastelli *et al.* proposed that the adsorption of pyridine on Si(111)2×1 involves an interaction of the lone-pair electrons of the N heteroatom and, to a lesser extent, an out-of-plane  $\pi$ -bond interaction with the ring tilted from the Si surface [12]. However, a high-resolution electron energy loss spectroscopy (HREELS) investigation later showed that the adsorption mechanism involves the breakage of C–H bonds and the formation of Si–C bonds [13]. A scanning tunneling microscopy study by Yagi *et al.* suggested a dipole-dipole interaction between pyridine and the Si(111)7×7 surface, and the interaction is electrostatic and not chemical in nature [15]. An earlier low-energy electron diffraction (LEED) and thermal desorption spectrometry (TDS) study by our group showed that the N heteroatom appears to cause reduced adsorption of pyridine on the Si surface but enhanced surface reactivity, relative to benzene [16]. In the case of benzene (C<sub>6</sub>H<sub>6</sub>), a large number of experimental [19,20,21,22,23,24,25] and theoretical studies [17,21,26,27,28,29,30] revealed that the chemisorption of this homocyclic aromatic compound on Si(100)2×1 follows the Diels-Alder cycloaddition mechanism, giving rise to a di- $\sigma$  bonded, cyclohexadiene-like adsorption species [31]. Although pyridine is isoelectronic with benzene with a similar ring structure, it is not clear whether a similar chemisorption mechanism would apply. After investigating an N-end-on adsorption state and two side-on adsorption states by means of density functional calculations, Lu *et al.* proposed that the most favorable adsorption geometry for pyridine on Si(100) is the N-end-on geometry [16]. In addition, rapid electron-induced dissociation of pyridine on Si(111)7×7 was also observed by our group [16]. It is unclear whether pyridine would exhibit similar adsorption behaviour and electron-mediated processes on the structurally different Si(100)2×1 surface.

In the present work, the surface chemistry of pyridine on Si(100)2×1 and related surfaces is investigated by using TDS, LEED, and Auger electron spectroscopy (AES), with the goal to determine the role of the N heteroatom on thermal and electron-mediated surface reactions. The results are compared with those of pyridine on Si(111) surfaces [12,13,15,16] and with other hexacycles (benzene [17,19,20,21,22,23,24,25,26,27,28,29,30] and toluene [32]) on Si(100).



## 5.2 Results and Discussion

### 5.2.1 Room-temperature adsorption of pyridine on Si(100)2×1

AES was used to study pyridine adsorption on Si(100)2×1 at RT. Figure 5-1 compares the relative carbon concentration, as indicated by the peak-to-peak ratio of the C(KLL) Auger peak at 272 eV to the Si(LVV) Auger peak at 92 eV, as a function of RT exposure for pyridine and benzene on Si(100)2×1. The ratio appears to level off to its maximum value at a pyridine (benzene) exposure of 20 L (2 L), which indicates completion of adsorption of the first monolayer (ML). The saturation coverage of benzene has been estimated to be 0.27 ML by Taguchi *et al.* [19]. From the ratios of saturation for pyridine (10.2%) and benzene (8.0%) and after taking into account the numbers of carbon atoms in pyridine (5) and benzene (6), we determine the saturation coverage for pyridine to be 0.41 ML. The adsorption of pyridine on Si(100)2×1 is therefore over 50% higher than that of benzene, which corresponds approximately to two d<sub>5</sub>-pyridine molecules for every three Si dimers on the 2×1 surface. Furthermore, we have fitted the experimental data according to the following equations derived from first-order and second-order adsorption kinetics [33]:

$$\theta = \theta_0(1 - e^{-k\Lambda}), \text{ for first-order adsorption } ; \text{ and} \quad (5.1)$$

$$\theta = \theta_0 \frac{k\Lambda}{1 + k\Lambda}, \quad \text{for second-order adsorption;} \quad (5.2)$$

where  $\theta$  is the coverage and  $\Lambda$  is the exposure in L. The fitting parameters are the saturation coverage  $\theta_0$  and the adsorption rate constant  $k$ . As shown in Figure 5-1, the amount of adsorbed pyridine on the surface evidently follows a second-order kinetics in terms of the fraction of unoccupied sites, which suggests that the adsorption of pyridine is a more complicated process (relative to benzene) possibly involving hydrogen abstraction and/or fragmentation at RT. For benzene on Si(100)2×1, the saturation coverage was found to be insensitive to the order of the adsorption kinetics, which has been shown to be first order by Taguchi *et al.* [19] but could not be determined with our data set.

Figure 5-2 shows the TDS profiles of Mass 84 and Mass 4 (corresponding to molecular and D<sub>2</sub> desorption, respectively) obtained at different RT exposures of d<sub>5</sub>-pyridine on Si(100)2×1. It should be noted that deuterated pyridine was used in the present TDS

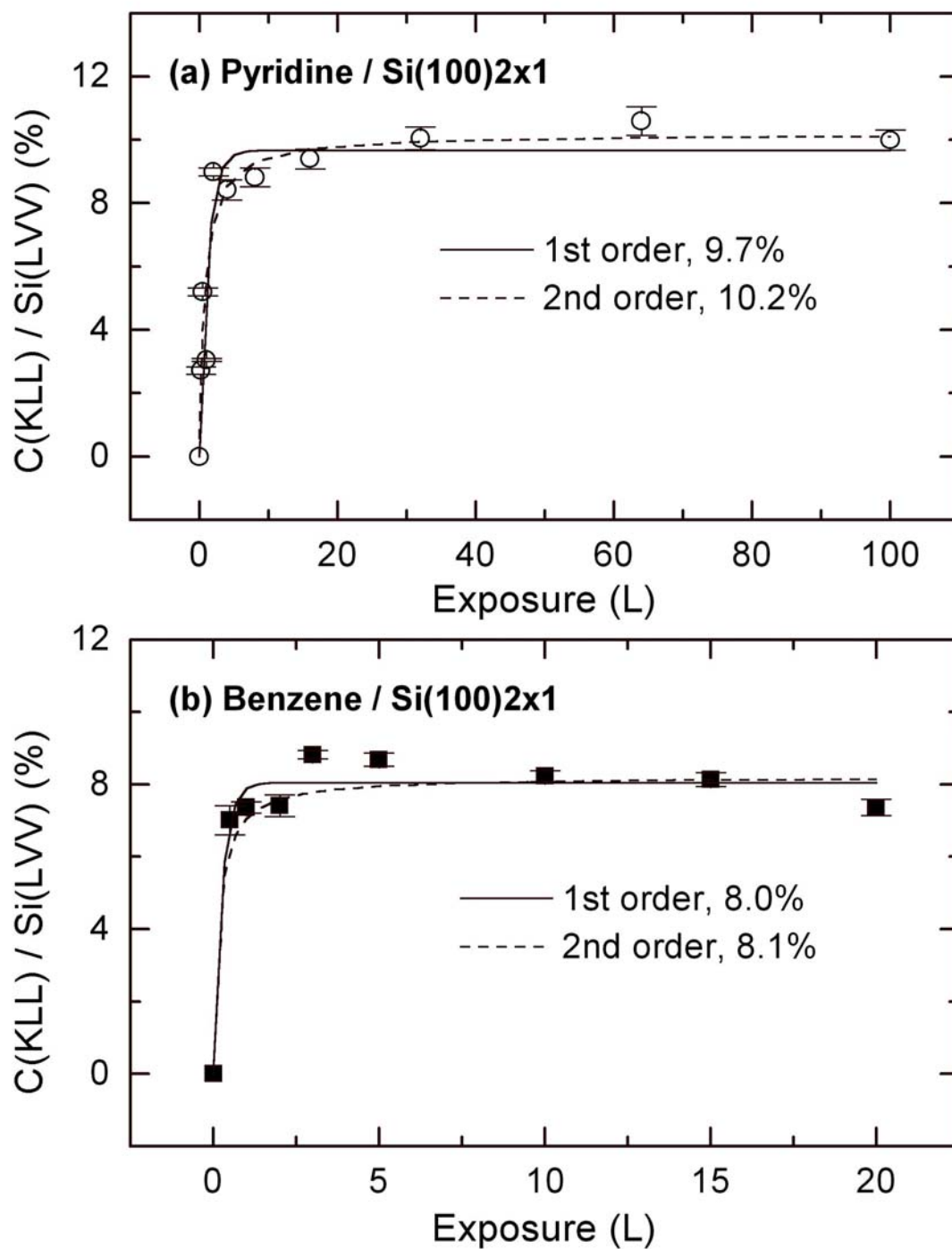


Figure 5-1 Relative carbon moiety as reflected by the peak-to-peak intensity ratio for the C(KLL) to Si(LVV) Auger transitions as a function of room-temperature exposure of (a) d<sub>5</sub>-pyridine and (b) benzene to Si(100)2×1. The experimental data are compared with fitted curves based on the first-order and second-order adsorption kinetic equations.

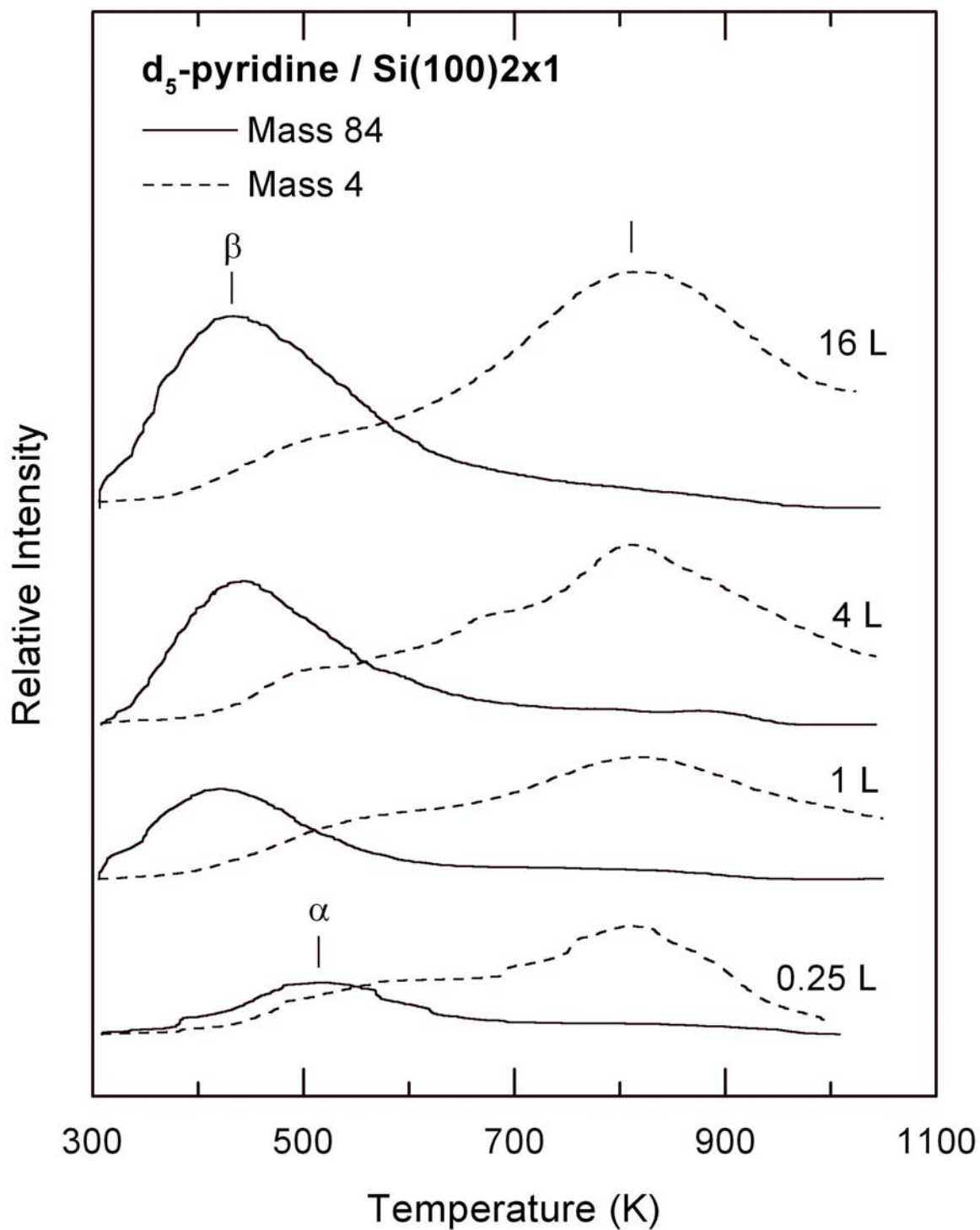
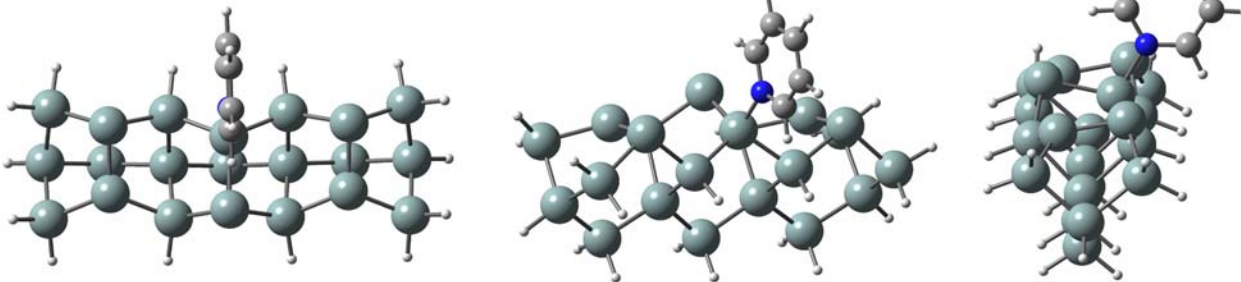


Figure 5-2 Thermal desorption profiles of Mass 84 (parent mass) and Mass 4 ( $D_2$ ) as a function of room-temperature exposure of  $d_5$ -pyridine to  $Si(100)2 \times 1$ .

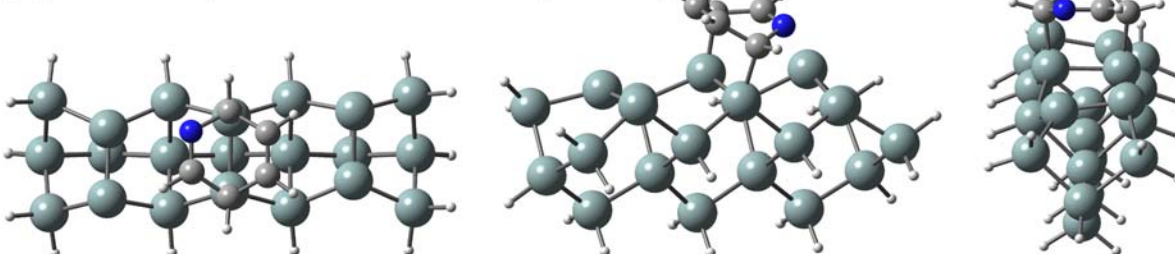
study in order to avoid the large H<sub>2</sub> background commonly found in stainless steel UHV chambers. In addition to the parent ion (Mass 84), other fragments including C<sub>4</sub>D<sub>4</sub> (Mass 56) and C<sub>4</sub>D<sub>3</sub> (Mass 54) were also monitored during the TDS experiments. Since the relative intensities of the corresponding peaks were found to be in good accord with those found in the cracking pattern of d<sub>5</sub>-pyridine [34], the detected mass fragments could be largely attributed to dissociation of molecularly desorbed d<sub>5</sub>-pyridine in the ionizer of the QMS. For exposures less than 0.25 L, a single desorption peak at 520 K ( $\alpha$  state) is observed (Figure 5-2). With increasing exposure, a new desorption peak emerges at 430 K ( $\beta$  state) along with the higher temperature peak ( $\alpha$  state). The  $\alpha$  state appears to reach saturation at a lower exposure than the  $\beta$  state. Within the absolute accuracy of our temperature measurement ( $\pm 10$  K), the desorption maxima of the  $\alpha$  and  $\beta$  states remain essentially unchanged with increasing exposure, generally indicating first-order desorption kinetics [35]. The two molecular desorption maxima for pyridine/Si(100)2 $\times$ 1 are located very close in temperature to those of the corresponding peaks for benzene/Si(100)2 $\times$ 1 and for toluene/Si(100)2 $\times$ 1 [31]. The similarities found in the molecular desorption states indicate common chemisorption mechanisms for pyridine, benzene and toluene on Si(100)2 $\times$ 1, in particular involving the [2+2] and/or [4+2] cycloaddition reactions.

To identify the plausible adsorption geometries for the adsorption states of pyridine/Si(100)2 $\times$ 1, we performed *ab-initio* density functional calculations using Gaussian 98 [36] with hybrid functionals consisting of Becke's 3-parameter non-local exchange functional and the correlation functional of Lee-Yang-Parr (the so-called B3LYP method in Gaussian 98) [37]. Three different basis sets including STO-3G, 3-21G and 6-31G(d) have been used and found to give qualitatively similar adsorption geometries. A triple-dimer Si<sub>21</sub>H<sub>20</sub> model was used to approximate the Si(100)2 $\times$ 1 surface, and three local energy minima have been found for C<sub>5</sub>H<sub>5</sub>N on this model surface. Figure 5-3 shows the corresponding adsorption geometries obtained with the 6-31G(d) basis set. The first local minimum corresponds to an N-end-on atop configuration (Figure 5-3a), with the N end of the pyridine molecule (and its ring in plane with the Si dimer) datively bonded to the buckled-down Si atom of the dimer. The corresponding energy change  $\Delta E$  with the zero-point energy correction for the adsorption of C<sub>5</sub>H<sub>5</sub>N on the Si<sub>21</sub>H<sub>20</sub> cluster is calculated to be -32.3

**(a) N-end-on ( $\Delta E = -32.3$  kcal/mol)**



**(b) 2,5 di- $\sigma$  ( $\Delta E = -20.7$  kcal/mol)**



**(c) 1,4 di- $\sigma$  ( $\Delta E = -14.2$  kcal/mol)**

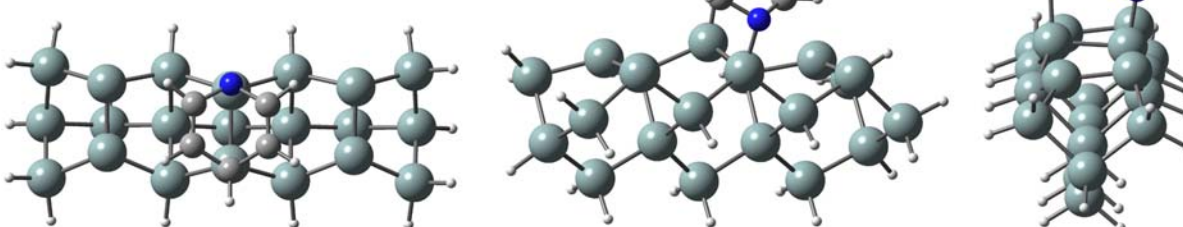


Figure 5-3 Schematic diagrams of the adsorption geometries in three different perspectives and the corresponding adsorption energies  $\Delta E$  obtained by a density functional calculation involving B3LYP/6-31G(d) for pyridine on the model surface of  $\text{Si}_{21}\text{H}_{20}$ .

kcal/mol (i.e. an exothermic process). The other two adsorption geometries follow the [4+2] cycloaddition mechanism, with the pyridine molecule di- $\sigma$  bonded to the Si surface dimer *via* the  $\text{C}_2$  and  $\text{C}_5$  atoms (2,5 di- $\sigma$  configuration, with  $\Delta E$  of -20.7 kcal/mol, Figure 5-3b) or *via* the N atom and the  $\text{C}_4$  atom (1,4 di- $\sigma$  configuration, with  $\Delta E$  of -14.2 kcal/mol, Figure 5-3c). The adsorption geometries obtained in the present work are found to be consistent with

similar calculations by Lu *et al.* employing a smaller Si<sub>9</sub>H<sub>12</sub> cluster for modelling the Si surface [16]. For benzene adsorption on Si(100)2×1, we found from a similar calculation using the same Si<sub>21</sub>H<sub>20</sub> cluster to represent the surface that the corresponding ΔE for the [4+2] adsorption state that was found to desorb molecularly at 460 K [31] to be -16.2 kcal/mol, which is very close to that of the 1,4 di-σ state for pyridine/Si(100)2×1. The TDS peak at 430 K (Figure 5-2) can therefore be attributed to the desorption of pyridine from the 1,4 di-σ adsorption geometry. From the relative values of the calculated ΔE values of the adsorption states, the TDS peak at 520 K (Figure 5-2) can then be assigned to the 2,5 di-σ configuration. The more stable N-end-on atop adsorption state is believed to be involved in other surface processes, as discussed later. The present calculation however has not considered and therefore could not be used to exclude the possibility of adsorption on defect sites and other adsorption geometries with even higher binding energies such as the double-dimer bridging configuration [24].

In addition to the molecular desorption profile, Figure 5-2 also shows the mass-4 (D<sub>2</sub>) TDS profiles with maxima at 810 K for RT exposures of d<sub>5</sub>-pyridine on Si(100)2×1. The TDS profile can be attributed to recombinative molecular hydrogen desorption from monohydride with first-order kinetics [38,39]. The slightly elevated temperature of the desorption maximum from that of monohydride desorption (by 20 K) and the broad mass-4 profile with a long tail extending above 1000 K (Figure 5-2) are related to the different sources of atomic hydrogen on the surface during the thermal desorption process. In particular, hydrogen abstraction of pyridine near or below its molecular desorption temperature could generate a comparable moiety of atomic hydrogen and other dissociated products, which could further release hydrogen mediated by the surface (both actively or *via* the availability of empty adsorption sites for H) at a temperature higher than the molecular desorption maximum. Furthermore, the shape of the observed mass-4 TDS profile (Figure 5-2) can also be affected by the presence of surface hydrocarbon species, which could not only act as a source of H but also restrict the mobility of H during the thermal desorption process. Similar TDS behaviour for hydrogen desorption has also been reported by Taylor *et al.* for the adsorption and decomposition of acetylene on Si(100)2×1 [40]. In this case [40], the corresponding hydrogen desorption peak was found to have an asymmetric shape with a

maximum slightly higher by 10 K than the desorption maximum for monohydride and a long tail extending to 980 K, which has been proposed to arise from reaction-limited scission of C–H bonds followed by desorption of molecular hydrogen. As confirmed by HREELS [41], the dissociation of adsorbed acetylene *via* cleavage of the C–H bond is shown to occur over a wide temperature range of over 150 K near 750 K (i.e. below the C<sub>2</sub>H<sub>2</sub> molecular desorption temperature). In contrast, the desorption maximum of molecular pyridine on Si(100)2×1 (near 430 K) is found to be considerably lower (Figure 5-2). Furthermore, chemisorbed pyridine would not be expected to undergo thermal dissociation from the aforementioned di-σ adsorption geometries (Figure 5-3), because the low adsorption energy ΔE of pyridine on Si(100) would enable pyridine to desorb before C–H bond activation. Hydrogen abstraction is therefore not likely to involve these di-σ states during annealing but other more stable states, such as the N-end-on atop adsorption state (Figure 5-3a) and/or other intermediate states that could be populated during the thermal desorption process.

### 5.2.2 Electron irradiation of pyridine on Si(100)2×1

In our previous TDS work on irradiation of pyridine/Si(111)7×7 by a low-energy electron beam during a LEED experiment, a distinct dissociation reaction was observed at RT, which caused rapid conversion of the modified 7×7 LEED pattern to a 1×1 pattern within 60 s [16]. However, the LEED pattern for pyridine on Si(100)2×1 observed in the present work does not exhibit any discernible change and remains as 2×1 even after a prolonged period (70 minutes) of electron irradiation at ~80 eV beam energy and 10 μA beam current. In contrast, the corresponding thermal desorption experiments show markedly different TDS profiles, which underline the different thermal surface reactions. Figure 5-4 compares the TDS profiles of the parent mass (Mass 84), Mass 28 and Mass 4 for Si(100) saturated with 100 L of d<sub>5</sub>-pyridine before and after electron irradiation at RT. Electron irradiation was performed on the Si sample (held at 80 V bias potential) for 30 minutes at 200 μA with electrons thermionically emitted from a hot W filament positioned 5 cm away. Evidently, electron irradiation greatly diminishes the desorption of Mass 84 (Figure 5-4a), suggesting a significantly smaller moiety of molecularly adsorbed pyridine on the surface likely due to electron-induced desorption [42]. For the sample without electron irradiation, the weak

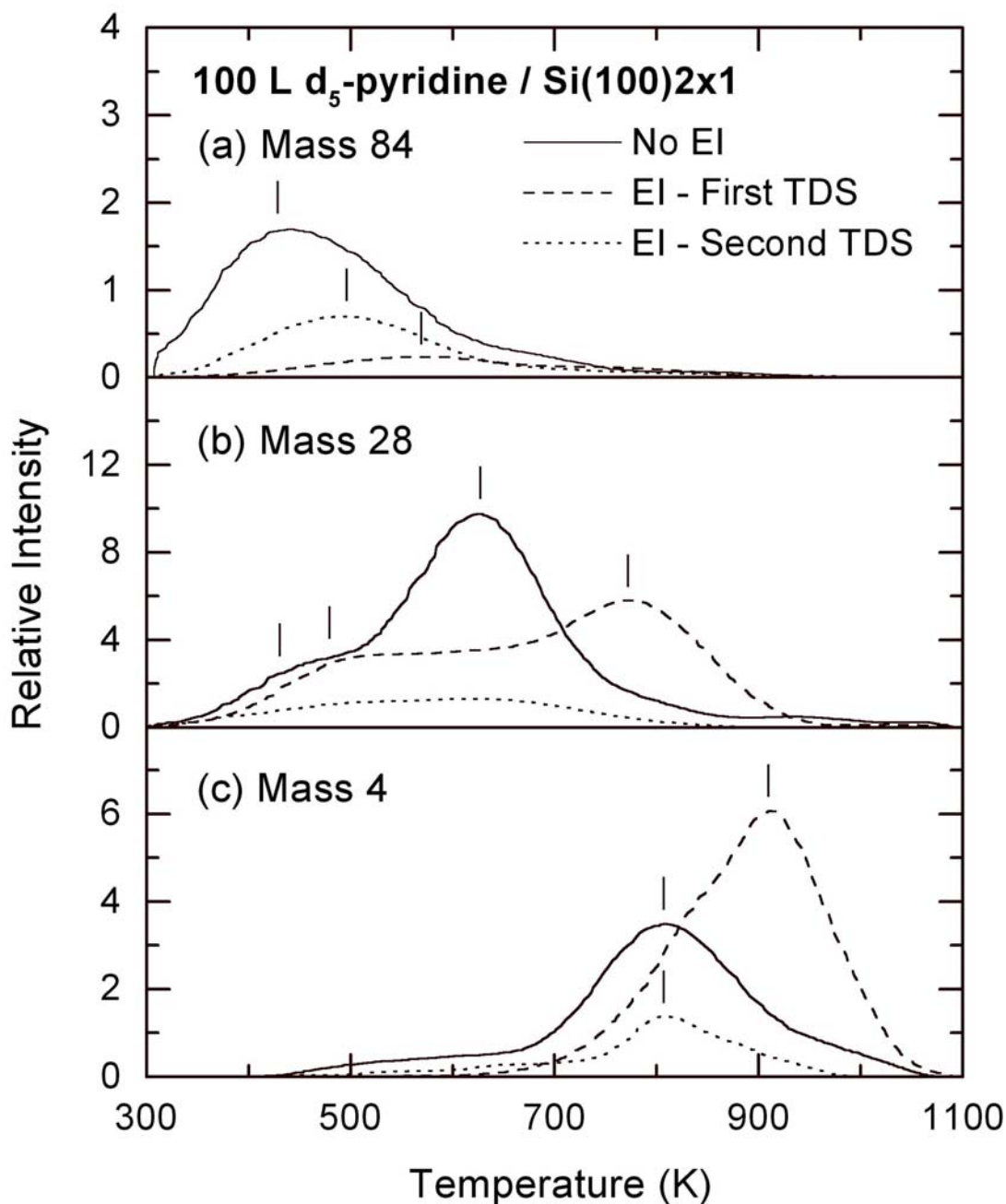


Figure 5-4 Thermal desorption profiles for (a) Mass 84 (molecular desorption) and dissociative products (b) Mass 28 and (c) Mass 4 for a 100 L room-temperature exposure of d<sub>5</sub>-pyridine with and without electron irradiation at 200 μA and 80 eV for 30 minutes. The time difference between the first and second thermal desorption spectrometry (TDS) experiments was 60 minutes.



mass-28 TDS peak at 430 K (Figure 5-4b) coincides in temperature with the broad desorption feature of the parent mass (Figure 5-4a) and can therefore be attributed to fragments of the molecularly desorbed pyridine created in the ionizer of the QMS. On the other hand, the strong mass-28 TDS peak at 630 K (Figure 5-4b) does not have any obvious correlation with features in the TDS profile of the parent mass (Figure 5-4a), and it should therefore be assigned to new desorbed products, including  $C_2D_2$  and/or CND species resulting from direct dissociative desorption of  $d_5$ -pyridine. The contribution to Mass 28 due to the cracking of desorbed  $C_2D_4$  in the ionizer can be ruled out by the lack of corresponding TDS features of Mass 30 ( $C_2D_3$ ) or Mass 32 ( $C_2D_4$ , normally with a desorption maximum near 550-580 K [43,44]). With electron irradiation, a new mass-28 TDS peak at 770 K emerges along with a mass-26 feature at the same temperature (not shown). These desorption features are characteristic of molecular desorption of  $C_2D_2$  from Si(100)2×1 [40,41], and given that no such mass-28 feature is found for the sample without electron irradiation, new  $C_2D_2$  and/or CND surface species must therefore be generated from electron-induced dissociation of the adsorbed pyridine at RT.

A considerably enhanced and broad mass-4 ( $D_2$ ) TDS profile with a maximum shifted to a higher temperature (910 K) is observed upon electron irradiation (Figure 5-4c). As with  $d_5$ -pyridine desorption without electron irradiation, the TDS feature at 810 K (appearing also as a shoulder on the lower temperature side of the broad TDS profile at 910 K) is attributed to recombinative desorption of D atoms from monohydride (Si–D) on the silicon surface, which follows first-order desorption kinetics (Figure 5-2). The emergence of a strong feature at 910 K after electron irradiation suggests a different source for the adsorbed D atoms most likely coming from new deuterated hydrocarbon species. Since the TDS features for the monohydride species arising from the more common molecular fragments of  $d_5$ -pyridine usually occur at a lower temperature (e.g. 760 K for  $C_2D_4$  [43] and 790-800 K for  $C_2D_2$  [40]) on Si(100)2×1, the new contributing species are not due to adsorbed  $d_5$ -pyridine monomers or its smaller fragments but rather their oligomers. The presence of the strong  $D_2$  TDS peak at 910 K therefore provides the first evidence of electron-induced condensation oligomerization of  $d_5$ -pyridine and/or related larger fragments on Si(100) at RT.

After completion of the TDS experiment for the electron-irradiated sample, the sample was allowed to cool for 60 minutes back to RT. A second TDS experiment was then performed on the same sample. Rather surprising results, particularly the rather strong molecular desorption of d<sub>5</sub>-pyridine (Mass 84) at 500 K, have been observed for the second TDS run (Figure 5-4a). Such phenomena have not been reported in the literature to the best of our knowledge. In general, there should not be any d<sub>5</sub>-pyridine molecule left on Si(100) after annealing to over 1000 K in the first TDS experiment. Of the 60 minutes needed for cooling the sample naturally back to RT, for a period of at least 40 minutes the temperature of the sample was sufficiently high (above 400 K) for the desorption of d<sub>5</sub>-pyridine. It is also unlikely that any re-adsorption of d<sub>5</sub>-pyridine with an even higher coverages than that during the first TDS from the surrounding back onto the sample could occur in a vacuum better than 2×10<sup>-10</sup> Torr. Furthermore, molecular desorption in the second TDS run was reproducible, though the observed intensity could vary by as much as 50%, causing the observed feature to be even higher than that found in the first TDS run (Figure 5-4a).

To explain the results of the second TDS run, we hypothesize that the d<sub>5</sub>-pyridine desorbed molecularly in the second TDS run originates from dissociation of the d<sub>5</sub>-pyridine oligomers formed as a result of low-energy electron irradiation. The dissociation of the oligomer is expected to occur at a low temperature (i.e. below 400 K), otherwise the dissociation products produced at a higher temperature would have desorbed during the cool-down period after the first TDS run. During the heating process (of the first TDS run), the interaction among the monomer units (of these oligomers) is stronger than the adsorbate-substrate interaction, and therefore the oligomers become loosely attached to the substrate surface [33]. Upon cooling, the adsorbate-substrate interaction becomes stronger than the adsorbate-adsorbate interaction of the monomers, causing oligomer dissociation. Furthermore, there should be a sufficient amount of active sites on the surface to facilitate the proposed oligomer dissociation, which are released by desorption of D<sub>2</sub> in the first TDS run. In corollary, the lack of unoccupied active sites also prevents oligomer dissociation during the first TDS run. A comparison of the second TDS run with the TDS without electron irradiation reveals a small shift in the molecular desorption peak from 430 K to 500 K (Figure 5-4a), which suggests that the d<sub>5</sub>-pyridine monomers desorb primarily in the α state (Section 3.1) with the oligomer dissociation likely occurring at a lower temperature (350-400

K). Figure 5-4c shows that the mass-4 TDS profile for the second TDS run resembles that without electron irradiation except for a lower intensity, which is consistent with the presence of a smaller moiety of monomers resulting from oligomer dissociation that leads to the hydrogen evolution. Similarly, Figure 5-4b also shows that a greatly weakened TDS profile for Mass 28 relative to that without electron irradiation, in good accord with our hypothesis. It is of interest to investigate this phenomenon with other techniques.

### 5.2.3 Surface condition studies

Figure 5-5 compares the TDS profiles for molecular desorption (Mass 84) and dissociative products (Mass 28 and Mass 4) for the  $2\times 1$  and modified Si(100) surfaces saturated with  $d_5$ -pyridine. The amorphous Si (*a*-Si) surface was produced by ion sputtering in  $4\times 10^{-5}$  Torr of Ar at 1 keV beam energy for 20 minutes, while the oxidized Si(100) surface was obtained by exposing a clean Si(100) $2\times 1$  surface with 100 L of O<sub>2</sub> at RT. The lack of any long-range order for both *a*-Si and oxidized Si surfaces was confirmed by the absence of a LEED pattern. With the sample temperature held near RT (280-300 K) by liquid-nitrogen cooling, the H-terminated Si(100) surface was prepared by exposing 3000 L of H<sub>2</sub> to a clean ( $2\times 1$ ) surface with a hot W filament positioned 2 cm away, and the surface saturation of H atoms was confirmed by a sharp  $1\times 1$  LEED pattern [45].

The general TDS features for the *a*-Si surface can be qualitatively interpreted as the corresponding features for the Si(100) $2\times 1$  surface (Figure 5-5). However, the overall desorption intensity for Mass 84 on *a*-Si is found to be considerably lower than that for the  $2\times 1$  surface (Figure 5-5a), which suggests that Ar sputtering appears to have reduced the amount of adsorption sites compatible with di- $\sigma$  bonding. Furthermore, the relative moiety of the  $\alpha$  state for molecular desorption (at 510 K) appears to be higher than the  $\beta$  state (Figure 5-2), which gives rise to the desorption maximum at 480 K in Figure 5-5a. The relative changes in the moieties of these states for the *a*-Si surface therefore suggest that the presence of defect sites on the sputtered surface would favour adsorption in the  $\alpha$  state. The feature at 370 K appears to correspond to a new desorption state for the *a*-Si surface. The weaker TDS structure of Mass 28 at 630 K compared to that for the  $2\times 1$  surface

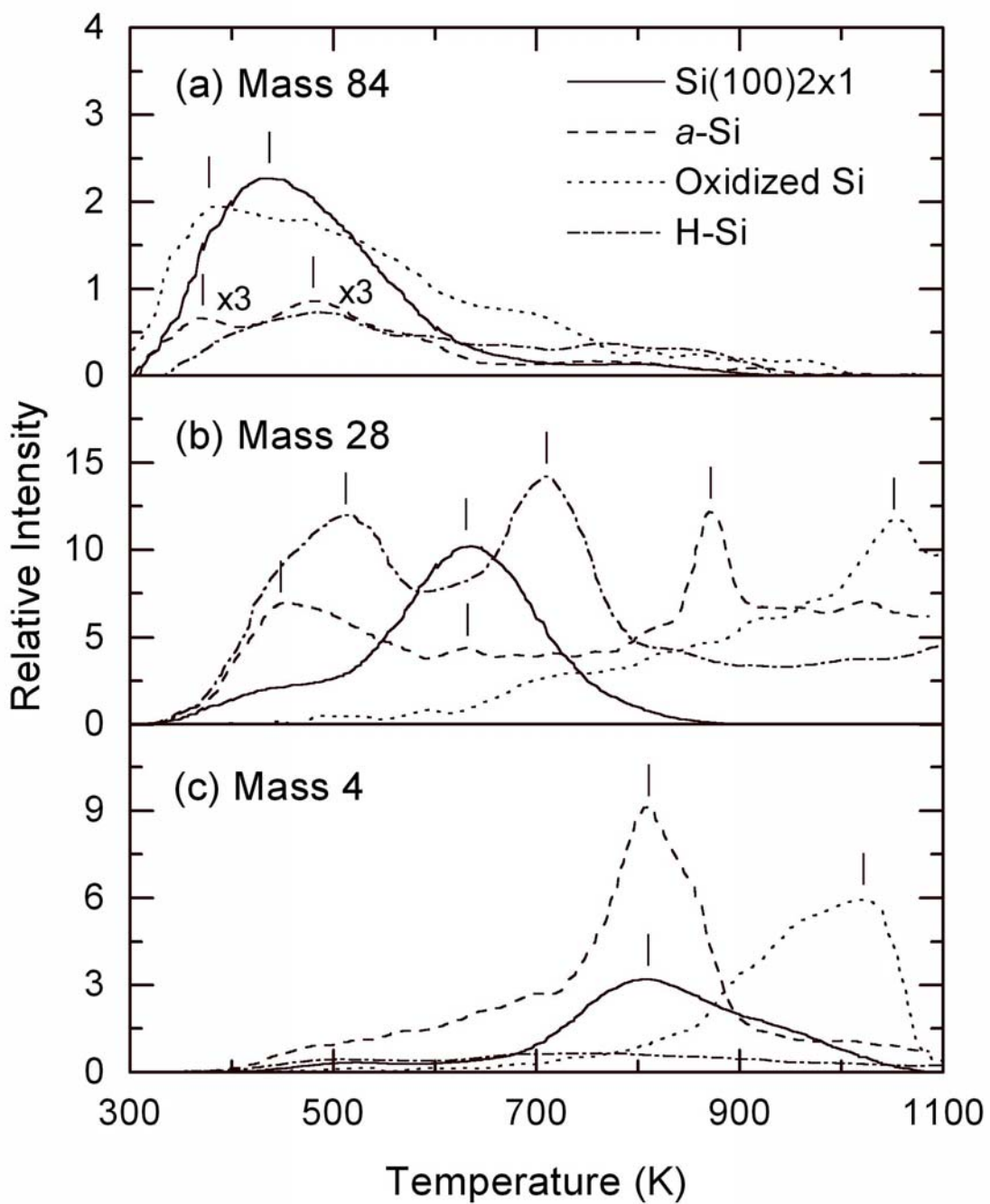


Figure 5-5 Thermal desorption profiles for (a) Mass 84, (b) Mass 28 and (c) Mass 4 for a saturation room-temperature exposure of  $d_5$ -pyridine to the  $2 \times 1$ , amorphous (a-), oxidized and H-terminated surfaces of Si(100).

(Figure 5-5b) indicates a relatively small degree of dissociation upon RT adsorption of  $d_5$ -pyridine on the sputtered surface. The distinct mass-28 TDS peak at 870 K, which appears to accompany significant desorption of Mass 40 at 880 K (corresponding to desorption of implanted Ar as a result of the sputtering process, not shown), could be attributed to dissociative desorption of fragments of hydrocarbon species from a fairly active surface. It should be noted that the strong desorption of Mass 40 observed at 880 K correlates well with a very active Si surface with intense structural rearrangement at this temperature, which could cause the hydrocarbon remnants to undergo dissociative desorption. Except for the enhanced intensity, the single mass-4 TDS peak at 810 K for the  $a$ -Si surface is very similar to that for the  $2\times 1$  surface (Figure 5-5c).

Figure 5-6 compares the TDS profiles for molecular desorption (Mass 84) and dissociative products (Mass 28 and Mass 4) for a 10 L RT exposure of  $d_5$ -pyridine to an  $a$ -Si surface before and after electron irradiation at 200  $\mu$ A and 80 eV for 30 minutes. Evidently, exposing the sputtered Si surface to low-energy electrons does not appear to produce markedly different TDS features, except for the intensity. In particular, the intensity of the mass-84 TDS profile for the  $a$ -Si surface has been greatly reduced by the electron irradiation, which again suggests electron-induced desorption of the molecularly adsorbed pyridine. On the other hand, the intensity of the mass-28 TDS profile particularly above 600 K has apparently been enhanced after electron irradiation, suggesting that there is a higher moiety of fragments that undergoes electron-induced dissociation on the amorphous surface. The mass-28 feature at 710 K (Figure 5-6b) can be attributed, as for the case of the  $2\times 1$  surface, to  $C_2D_2$  desorption [40]. Similar to the  $2\times 1$  surface, the mass-4 TDS peak is shifted to a higher temperature (i.e. from 810 to 840 K) but with a significantly enhanced intensity after electron irradiation. The apparent smaller shift in the desorption maximum to 840 K due to electron irradiation in the case of  $a$ -Si (Figure 5-6c), relative to that for the  $2\times 1$  surface (910 K, Figure 5-4c), could be due to defect sites.

Figure 5-5 also shows the TDS profiles of Mass 84, Mass 28 and Mass 4 for a 10 L RT exposure of  $d_5$ -pyridine on an oxidized Si(100) surface. The similarities in the TDS profiles of Mass 84 below 600 K suggest that both the oxidized and ( $2\times 1$ ) surfaces contain similar adsorption sites for pyridine (Figure 5-5a). On the other hand, significant differences

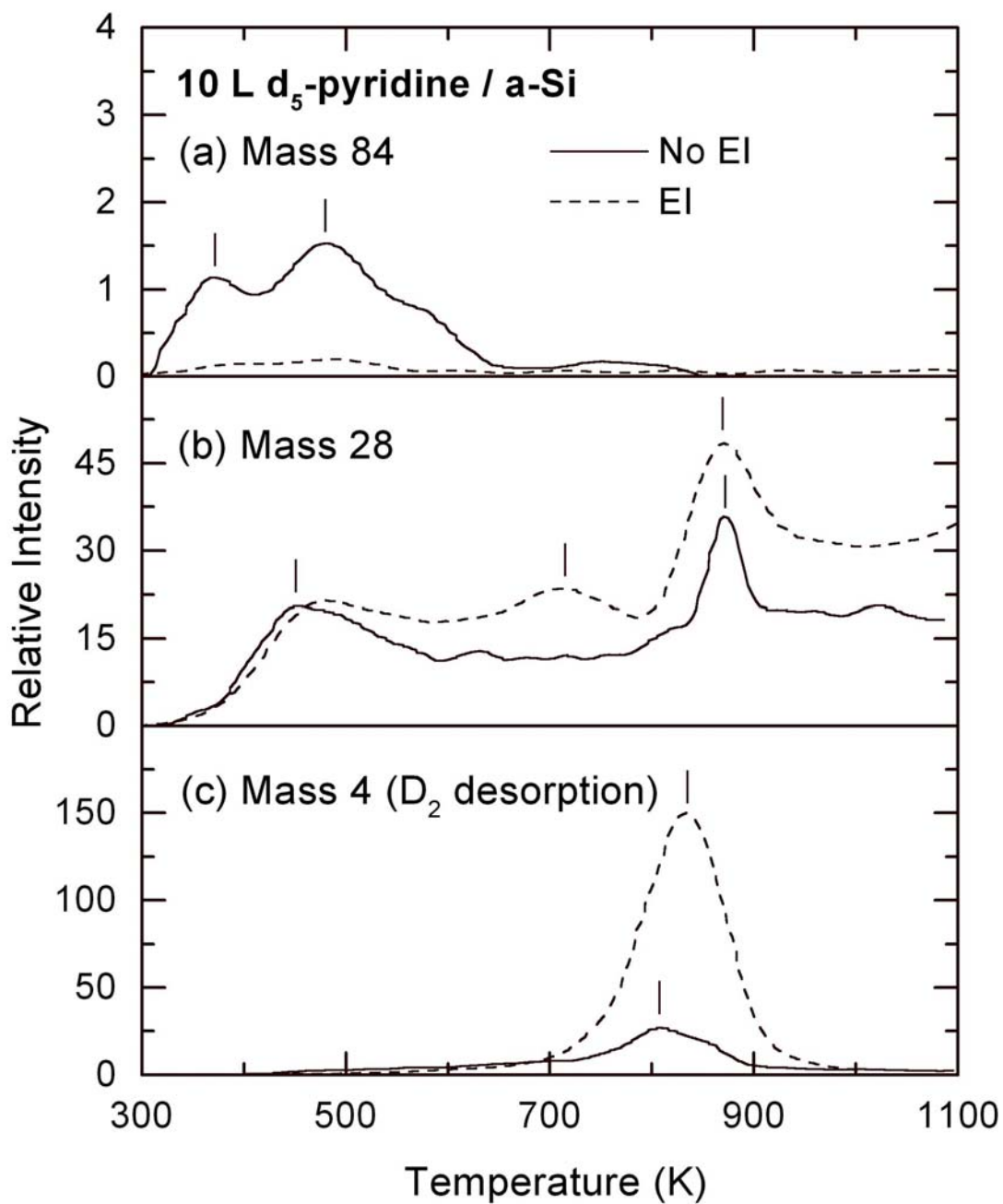


Figure 5-6 Thermal desorption profiles for (a) Mass 84, (b) Mass 28 and (c) Mass 4 for a 10 L room-temperature exposure of  $d_5$ -pyridine to an amorphous (a-)Si surface with and without electron irradiation at 200  $\mu$ A and 80 eV for 30 minutes.

in the mass-28 and mass-4 TDS profiles between the  $2\times 1$  and oxidized surfaces are observed. In particular, the new desorption peak of Mass 28 at  $\sim 1050$  K (Figure 5-5b) is found to exhibit a desorption maximum 30 K higher than that of the mass-4 desorption peak (Figure 5-5c). The lack of the corresponding lower mass fragments, e.g. Mass 26 (not shown), suggests that Mass 28 is not due to desorption of  $C_2D_2$  or  $CND$  fragments, but rather to associative desorption of  $CO$ . Since the adsorption energies of  $CO$  on  $Si(100)2\times 1$  have been estimated to be  $-17$ - $19$  kcal/mol [46] and the desorption maximum for  $CO$  on  $Si(100)$  (at 180 K) [47] is markedly lower than the present TDS peak, other dissociation channels by which  $C$  readily combines with  $O$  on the oxidized surface to produce the desorbed  $CO$  could be activated (Figure 5-5b) along with hydrogen evolution at such a high temperature (Figure 5-5c). Of particular interest is the shift in temperature of the desorption maximum for Mass 4 ( $D_2$ ) on the oxidized surface by 210 K higher than that on the  $2\times 1$  surface (Figure 5-5c). The strong mass-4 TDS peak at 1020 K can be attributed to recombinative desorption following plausible oligomer dissociation. The formation of oligomer has been proposed earlier in Section 5.2.2 as a plausible electron-induced process for pyridine on  $Si(100)2\times 1$ . The mechanism for such oligomer formation on the oxidized  $Si$  surface is however unclear but it may involve  $N-O$  interactions.

After the oxidized sample naturally cooled to RT in 60 minutes upon completion of the first TDS experiment, a second TDS run was performed and the corresponding profiles are shown in Figure 5-7. Of special interest is the reappearance of Mass 84 (molecular desorption) over its “normal” desorption temperature range (400-600 K) in the second TDS run (Figure 5-7a), which is accompanied by notable mass-4 desorption with maximum at 810 K (Figure 5-7c) and mass-28 desorption near 610 K (Figure 5-7b). As with the case of the  $2\times 1$  surface (Figure 5-5b), the mass-28 TDS feature at 610 K (Figure 5-7b) can be attributed to  $NCD$  and  $C_2D_2$  but not to  $C_2D_4$  because no Mass 30 (corresponding to  $C_2D_4$ ) is found. The changes in these desorption profiles for the second TDS run are similar to those found earlier in Section 5.2.2, which further supports that condensation oligomerization could play an important role in the observed desorption behaviour of pyridine on the oxidized  $Si$  surface.

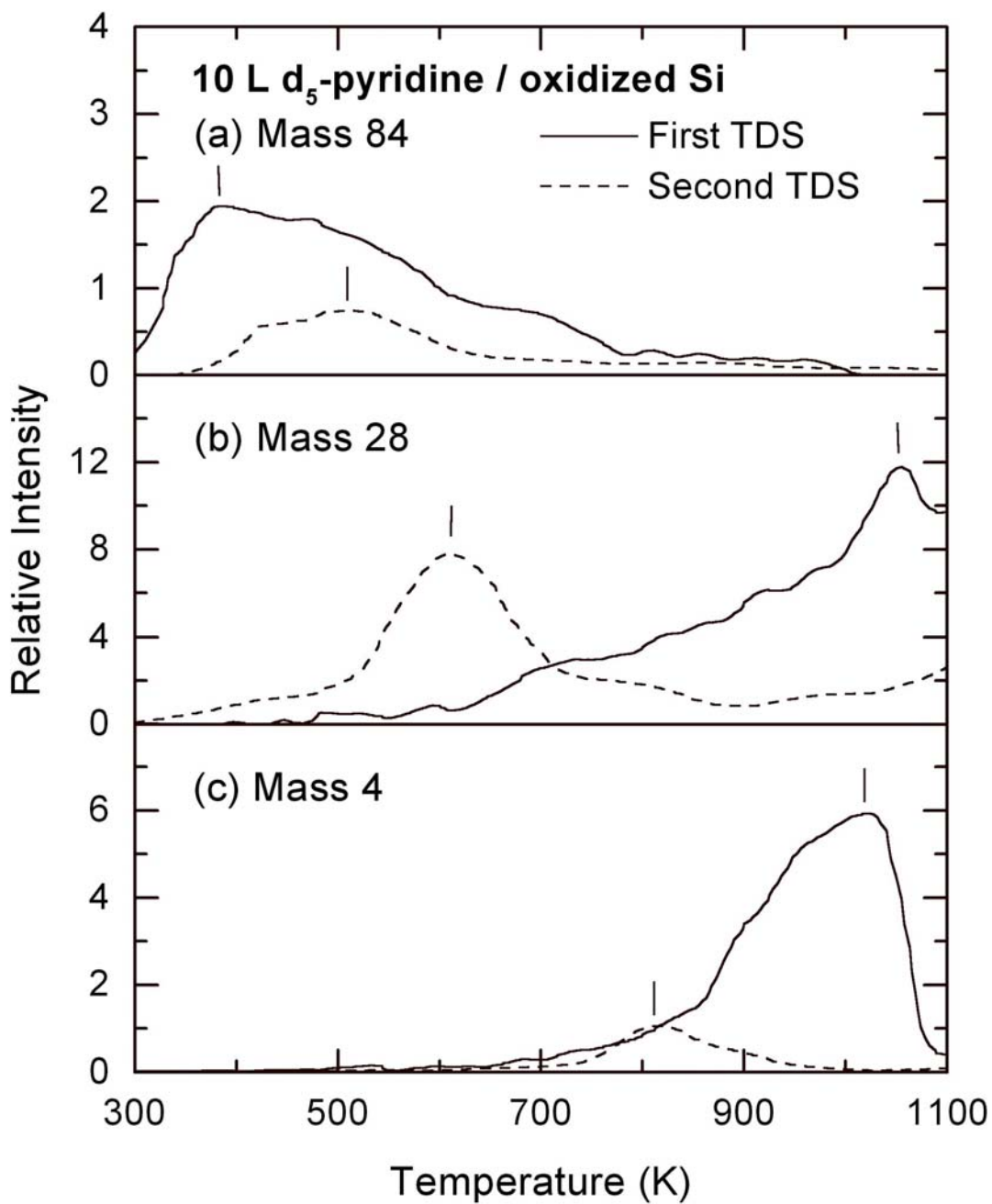


Figure 5-7 Thermal desorption profiles for (a) Mass 84, (b) Mass 28 and (c) Mass 4 for a 10 L room-temperature exposure of d<sub>5</sub>-pyridine to an oxidized Si surface. The time difference between the first and second thermal desorption spectrometry (TDS) experiments was 60 minutes.



Figure 5-5 also compares the TDS profiles of Mass 84, Mass 28 and Mass 4 for a 10 L RT exposure of  $d_5$ -pyridine on a H-terminated Si(100) surface with other surface conditions. Like the *a*-Si sample, molecular desorption (Mass 84) for the H-terminated Si(100) surface is found to be very weak (Figure 5-5a). However, unlike the *a*-Si sample where an intense mass-4 desorption peak is observed at 810 K, the corresponding mass-4 desorption for the H-terminated Si(100) surface is found to be featureless, broad and weak (Figure 5-5c). The weak mass-84 and mass-4 desorption features for the H-terminated sample would appear to suggest that pre-adsorbed H atoms have completely filled the active surface sites, hence preventing the adsorption of pyridine on Si(100) $2\times 1$ . However, the strong mass-28 TDS structure with desorption maxima at 430 K, 520 K and 710 K is found to be markedly different from that for Si(100) $2\times 1$  (630 K), *a*-Si (450 K, 630 K and 870 K) and oxidized Si surface (1050 K), which indicates different pyridine dissociation pathways for producing Mass 28 on the H-terminated Si(100) surface.

In order to investigate these perhaps more complex adsorption processes, TDS profiles of a more extended list of masses have been collected for a 10 L RT exposure of  $d_5$ -pyridine on the H-terminated Si(100) sample, shown in Figure 5-8. Unlike the weak mass-4 desorption, two strong mass-2 TDS peaks at 680 K and 790 K are found to correlate with the recombinative desorption of  $H_2$  from the dihydride ( $\beta_2$ ) and monohydride phases ( $\beta_1$ ), respectively, of the H-terminated Si(100) surface [38,39] (Figure 5-8). However, the presence of a weak mass-3 TDS peak at 800 K (near the desorption maximum of the  $\beta_1$  state of  $H_2$ ) indicates that part of the  $d_5$ -pyridine molecules adsorbed on the H-terminated surface undergoes dissociation and that the abstracted D atoms then recombine with the surface H atoms to form the desorbed HD. Furthermore, in accord with an earlier study on the interaction of atomic H with adsorbed ethylene and acetylene on Si(100) [48], the TDS feature of Mass 28 at 710 K that is accompanied by the mass-26 peak in the same temperature range can be attributed to desorption of  $C_2H_4$  [48,49]. The mass-28 feature observed at a lower temperature (520 K) can be attributed predominantly to desorption of  $C_2D_nH_{4-n}$  ( $n = 0-2$ ) fragments [48,49], while the mass-30 features at 520 K and 630 K can be assigned to desorption of  $C_2D_2H_2$ .

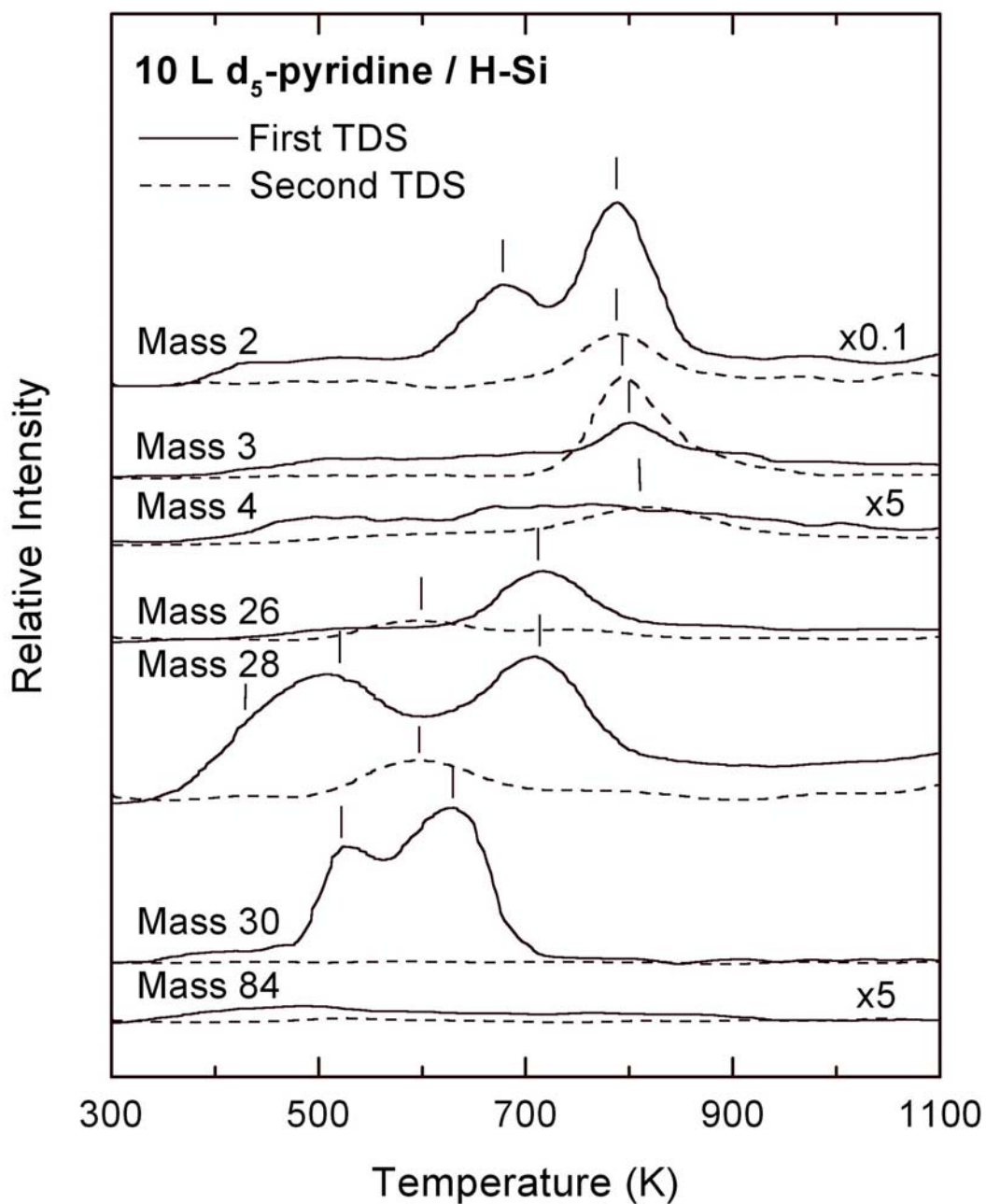


Figure 5-8 Thermal desorption profiles of Mass 2, 3, 4, 26, 28, 30, and 84 for a 10 L room-temperature exposure of d<sub>5</sub>-pyridine to a H-terminated Si(100)2×1 surface. The time difference between the first and second thermal desorption spectrometry (TDS) experiments was 60 minutes.

Figure 5-8 also shows the results of a second TDS run for the  $d_5$ -pyridine/H-terminated Si(100) sample. As expected, the overall mass-2 desorption has been significantly reduced, with only the  $\beta_1$  feature remaining. However, the TDS feature of Mass 3 at 795 K (corresponding to recombinative desorption of HD) becomes considerably more intense in the second TDS run, which suggests that the majority of the D atoms abstracted from the remaining hydrocarbon species after the first TDS run undergoes recombinative desorption with H atoms in the monohydride phase. In addition, the TDS profiles of both mass-28 and mass-26 in the second TDS run (Figure 5-8) have evidently reverted back to those found for the Si(100) $2\times 1$  sample, with a single desorption feature near 600 K (Figure 5-5b), suggesting dissociative desorption of  $C_2D_2$  and/or NCD. Furthermore, the mass-30 TDS features at 520 K and 630 K, along with the mass-28 features at 520 K and 710 K and the mass-26 feature at 710 K, could not be observed in the second TDS run (Figure 5-8). The lack of these desorption features in the second TDS run is consistent with the reduced moiety of H on the surface after the first TDS run. Unlike the earlier cases involving second TDS runs for electron-irradiated and oxidized samples, there is no evidence of oligomerization, which is consistent with our hypothesis that monomer adsorption is a required precondition.

#### **5.2.4 Post-adsorption surface-mediated oxidation and hydrogenation reactions**

Figure 5-9 shows the TDS profiles of a 30 L post-exposure of  $O_2$  to Si(100) $2\times 1$  saturated with 10 L of  $d_5$ -pyridine at RT. In particular, post-oxidation appears to reduce (Mass 84) molecular desorption from the lower temperature  $\beta$  state (at 430 K) and (Mass 4)  $D_2$  evolution with desorption maximum at 810 K. Furthermore, essentially no desorption is observed for Mass 30 upon post-oxidation (not shown), while desorption maxima for Mass 28 (Figure 5-9b) and Mass 26 (not shown) are found to shift to a higher temperature (770 K) with  $O_2$  post-exposure, which indicates that  $C_2D_2$  is likely produced through the dissociation of  $d_5$ -pyridine. This shift in the Mass 28 feature may be caused by surface interaction of dissociated fragments with coadsorbed O atoms, which produce an apparent stabilization effect. Unlike  $d_5$ -pyridine adsorption on the oxidized Si(100) surface (Section 3.3), the

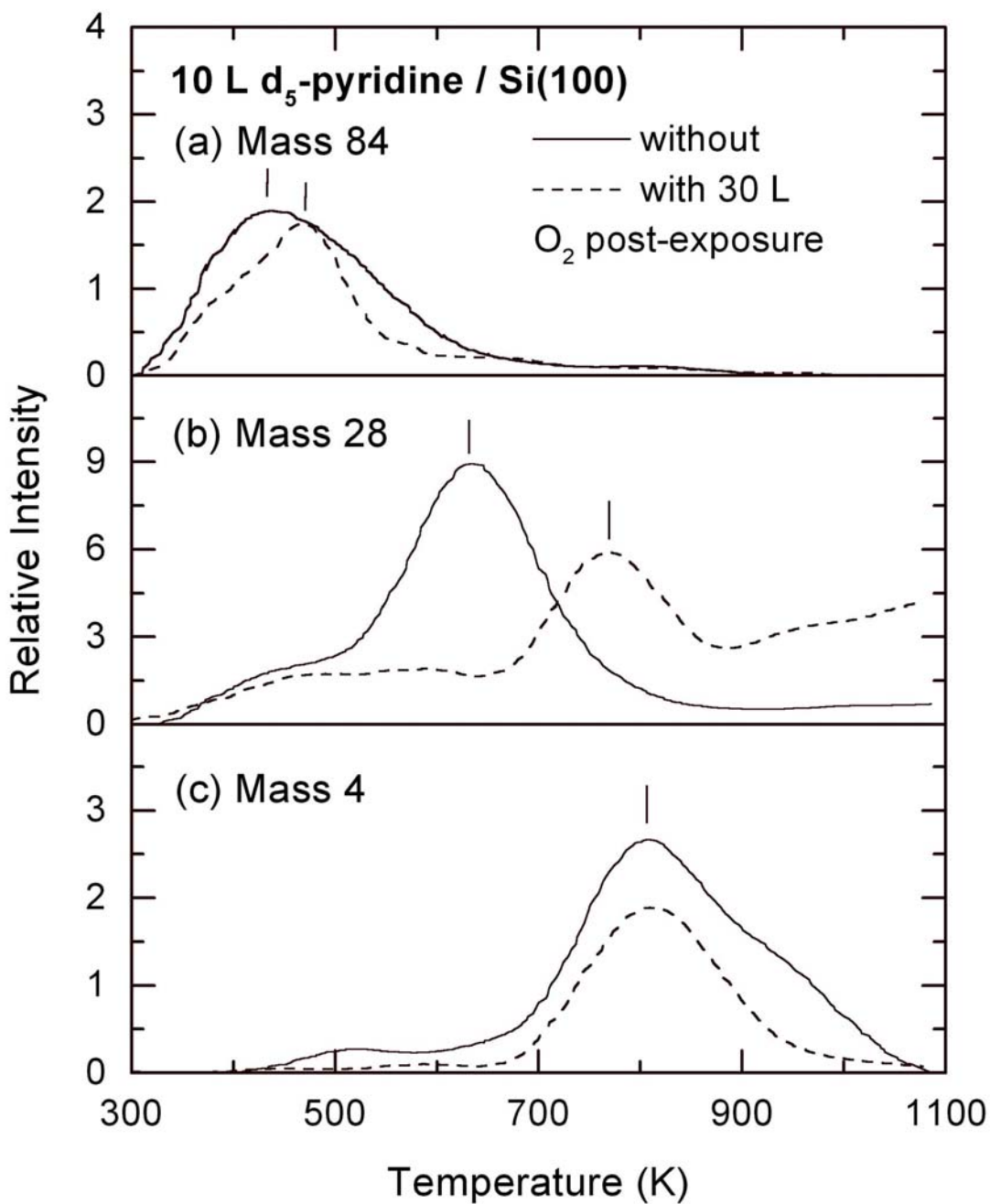


Figure 5-9 Thermal desorption profiles of (a) Mass 84, (b) Mass 28 and (c) Mass 4 for a 10 L room-temperature exposure of d<sub>5</sub>-pyridine to Si(100)2×1 with and without a 30 L post-exposure of O<sub>2</sub>.

dramatic temperature increase in the mass-4 desorption maxima as a result of plausible oligomerization is not observed in the post-oxidation experiment.

In order to investigate the interaction of atomic hydrogen with pyridine adsorbed on Si(100)2×1, the sample saturated with 10 L exposure of d<sub>5</sub>-pyridine was post-exposed with H atoms generated from 3000 L of H<sub>2</sub> with a hot W filament positioned 2 cm away. To minimize the effect of radiative heating from the hot filament during the hydrogen activation, liquid nitrogen was used to keep the sample near or below RT. Figure 5-10 shows rather weak (Mass 84) molecular desorption, and two intense TDS features of Mass 2 at 650 K and 790 K, corresponding to recombinative desorption from dihydride and monohydride, respectively [38,39]. Furthermore, desorption of Mass 4 is found to be relatively weak with respect to the desorption intensities of HD (Mass 3, at 20%) and H<sub>2</sub> (Mass 2, at 10%). The shift of the D<sub>2</sub> (HD) TDS feature by 20 K (10 K) to a higher temperature relative to the β<sub>1</sub> TDS feature of H<sub>2</sub> (Mass 2) at 790 K indicates that hydrogen evolution occurs during the thermal desorption experiment. After the RT post-exposure of H, thermally induced hydrogen abstraction of the adsorbed d<sub>5</sub>-pyridine molecules would not begin until the occupied neighboring active sites on the Si(100) surface are vacated (i.e. upon hydrogen desorption). The desorption of Mass 28 at 470 K and 730 K, along with that of Mass 26 only at 730 K, and the desorption of Mass 30 at 610 K and 730 K implicate rather complicated dissociation pathways possibly involving smaller hydrocarbon fragments such as C<sub>2</sub>D<sub>2</sub>H<sub>2</sub> [48,49]. Similar results about the adsorption and hydrogenation reactions for hexacyclic hydrocarbons (benzene, 1,3-cyclohexadiene, 1,4-cyclohexadiene, and cyclohexene) on the Si(100)2×1 surface have also been found in a combined Fourier Transform Infrared Spectroscopy and TDS study [50]. These results suggest that the C=C double bonds remaining in the chemisorbed hexacycles could react with atomic H, giving rise to a common “parent” hydrogenation product C<sub>5</sub>ND<sub>5</sub>H<sub>5</sub>. Upon reaction with the coadsorbed H atoms during the TDS process, this hydrogenation product could dehydrogenate back to a family of hexacycles C<sub>5</sub>ND<sub>m</sub>H<sub>n-m</sub> (m = 0-5, n = 5-10) with C<sub>5</sub>ND<sub>m</sub>H<sub>5-m</sub> (m = 0-5) expected to be the end-products. The weak intensity observed for Mass 84 (parent mass) and mass-28 intensity at 400-600 K could be attributed to the evolution of these dehydrogenated hexacycles. These dehydrogenated hexacycles could also undergo decomposition into smaller hydrocarbon fragments, including C<sub>2</sub>D<sub>4-m</sub>H<sub>m</sub> (m = 0-4) with plausible TDS features for masses 30, 28, and

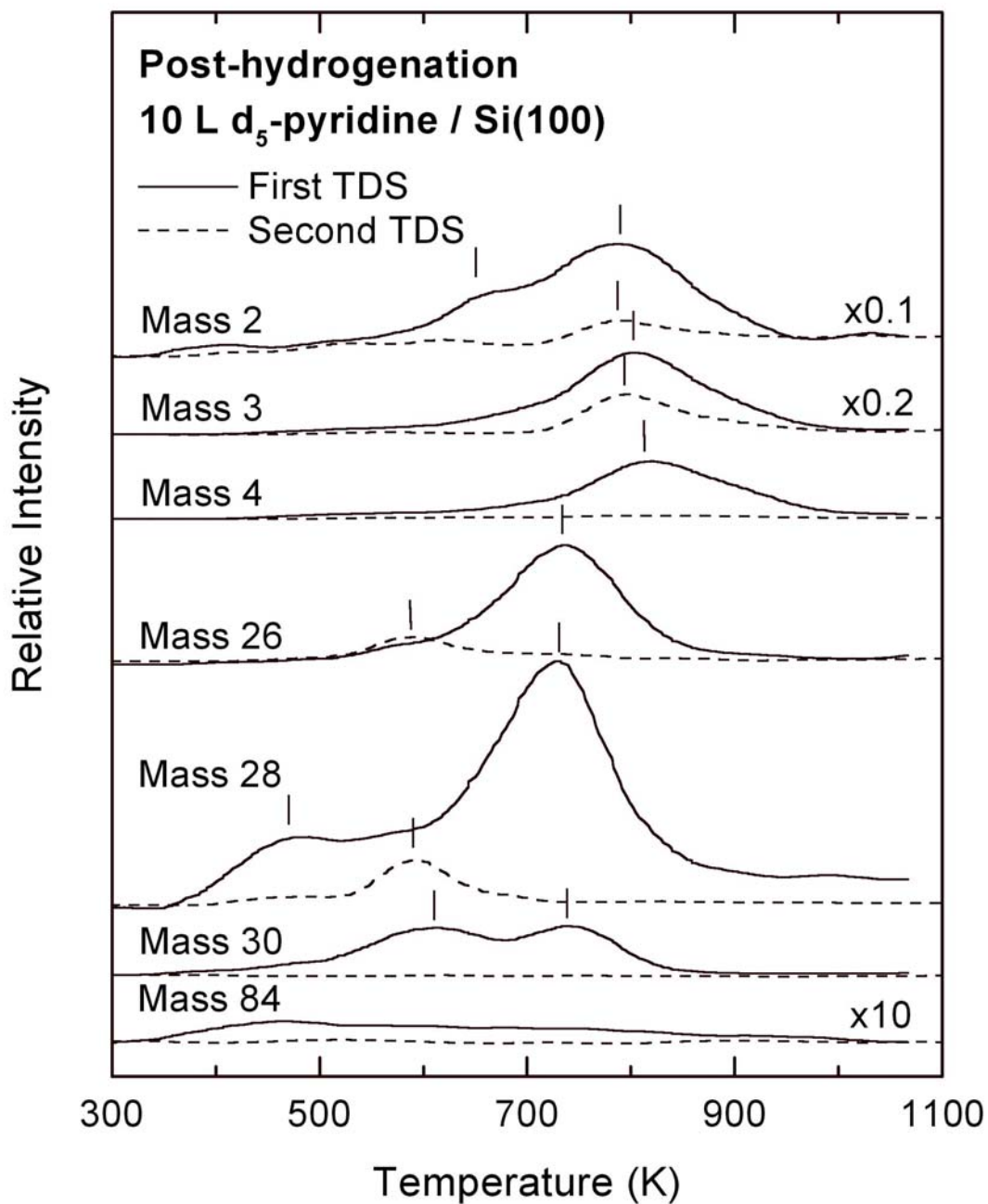


Figure 5-10 Thermal desorption profiles of Mass 2, 3, 4, 26, 28, 30, and 84 for a 10 L room-temperature exposure of d<sub>5</sub>-pyridine to a H-terminated Si(100)2×1 surface followed by post-exposure of hydrogen atoms. The time difference between the first and second thermal desorption spectrometry (TDS) experiments was 60 minutes.

26 at 610 K, and  $C_2D_{2-m}H_m$  ( $m = 0-2$ ) with mass-28 and mass-26 desorption at 730 K. In the case of  $C_2D_{4-m}H_m$  ( $m = 0-4$ ), the mass-30 feature at 730 K could be due to recombinative desorption of  $C_2D_{2-m}H_m$  ( $m=0-2$ ) with surface H or D atoms likely in a highly mobile state at this temperature.

For the second TDS run, the TDS profiles for the post-hydrogenated sample shown in Figure 5-10 resemble the corresponding profiles for  $d_5$ -pyridine on the H-terminated Si surface (Figure 5-8). In particular, as with the H-terminated Si sample, the TDS features for Mass 2, Mass 4, Mass 30, and Mass 84 appear to have diminished significantly. Furthermore, the TDS profiles of Mass 26 and Mass 28 are also found to revert back to those found for the  $2\times 1$  sample (with a desorption maximum at 590 K). In contrast to the second TDS run observed for the H-terminated Si sample (Figure 5-8), the TDS feature of Mass 3 at 790 K for the second TDS run is found to be weaker than the first TDS run. This reduction is consistent with the hydrogenation of  $d_5$ -pyridine discussed earlier, which has the effect of diluting the relative concentration of D atoms in the resulting hetero-hexacycles. Because the resulting heterocycles is the main source of the D atoms for the mass-3 desorption, the reduction in the moiety of the heterocycles after the first TDS run would therefore produce less mass-3 desorption. On the other hand, in the case of H-terminated surface, hydrogenation of adsorbed  $d_5$ -pyridine appears to be unlikely (Figure 5-8). The lack of unoccupied sites for the hydrogen abstraction of pyridine during the first TDS run limits the amount of mass-3 desorption while in the second TDS run the availability of newly released sites provides more hydrogen evolution opportunity, thus giving rise to a stronger Mass 3 desorption (Figure 5-8).

### 5.3 Concluding remarks

The adsorption and thermal reactions of pyridine on  $2\times 1$  and modified surfaces of Si(100) have been investigated by TDS, LEED and AES under UHV conditions. The AES results show that the second-order kinetics observed for pyridine adsorption on Si(100) $2\times 1$  is consistent with a more complicated process (relative to benzene) possibly involving hydrogen abstraction and/or fragmentation at RT. Furthermore, the saturation coverage of pyridine on Si(100) $2\times 1$  is found to be 0.41 ML, corresponding to two pyridine molecules for

every three Si dimers, which is higher than that of benzene (0.27 ML [19], with one benzene molecule for every two Si dimers). The (2×1) LEED pattern obtained after adsorption indicates that the overall structure of the reconstructed Si(100) surface is not significantly affected by the chemisorption of pyridine at RT. However, pyridine is found to undergo several competitive thermal reactions on Si(100)2×1, involving the N-end-on atop and di-σ bonded cycloaddition states. The 1,4 and 2,5 di-σ adsorption states are believed to give rise to molecular desorption while the most stable N-dative adsorption state could be responsible for the dissociation pathways such as hydrogen abstraction and fragmentation.

Unlike the results in our previous study of pyridine on Si(111)7×7, where rapid dissociation of adsorbed pyridine upon irradiation by low-energy electrons at RT was observed [16], pyridine was found for the first time to undergo condensation oligomerization on Si(100)2×1 mediated by low-energy electrons. This result is significant in providing a viable method for imprinting a highly “crystalline” polymer prealigned by the surface template onto a pattern generated by an electron beam writer (in a way similar to electron beam lithography). Furthermore, similar oligomerization has also been observed for an oxidized Si surface without low-energy electron mediation. These observations are supported by the shift in temperature of the desorption maximum of the TDS feature for hydrogen evolution and by a distinct molecular desorption in the second TDS run. The present work also illustrates that “repeated” TDS runs could be very useful for elucidating the consequence of surface processes upon thermal excitation and desorption.

Various thermal reactions, including molecular, dissociative and associative desorption, hydrogen abstraction, fragmentation, and oligomerization as well as oxidation, involving different adsorption states could be inferred from the coordinated evolution of hydrogen and higher fragments in the TDS profiles. As shown in the present work, these reactions have been further studied under different surface conditions, and with various pre- and post-treatments (including oxidation, hydrogenation, and low-energy electron mediation). In contrast to benzene, which was found to adsorb and desorb molecularly, pyridine evidently exhibits a more active surface chemistry on Si(100)2×1 likely due to the presence of the lone-pair electrons on the N heteroatom. It may therefore be feasible to manipulate and control the outcome of different surface processes by changing the



heteroatom in the case of heterocyclic silicon surface chemistry. More detailed *ab initio* calculations and other experimental investigations using different surface analysis techniques (such as variable-temperature scanning probe microscopy) will be of great interest to further elucidate the intricate adsorption geometries and mechanisms as well as the surface reactions (with and without electron mediation) of these important heterocyclic hydrocarbons on Si(100).

## 5.4 Reference

- [1] A. Tsumura, H. Koezuka, T. Ando, *Appl. Phys. Lett.* 49 (1986) 1210.
- [2] A. Garito, R. F. Shi, M. Wu, *Physics Today* 47 (1994) 51.
- [3] J.R. Ostrick, A. Dodabalapur, L. Torsi, A.J. Lovinger, E. W. Kwock, T. M. Miller, M. Galvin, M. Berggren, H.E. Katz, *J. Appl. Phys.* 81 (1997) 6804.
- [4] V. I. Krinichnuyi, *Phys. Solid State* 39 (1997) 1.
- [5] “Handbook of conducting polymers”, Eds. T.A. Skotheim, R.L. Elsenbaumer, J.R. Reynolds (Dekker, New York, 1998).
- [6] K.M. Baumgartner, M. Volmer-Uebing, J. Taborski, P. Bauerle, E. Umbach, *Ber. Bunsenges. Phys. Chem.* 95 (1991) 1488.
- [7] H.N. Waltenburg, J. T. Yates, *Chem. Rev.* 95 (1995) 1589.
- [8] R.J. Hamers, Y. Wang, *Chem. Rev.* 96 (1996) 1261.
- [9] R.J. Hamers, J.S. Hovis, C.M. Greenlief, D.F. Padowitz, *Jpn. J. Appl. Phys.* 38 (1999) 3879.
- [10] J.T. Yates, Jr., *Science* 279 (1998) 335.
- [11] “CRC Handbook of Chemistry and Physics”, Ed. D.R. Lide (CRC Press LLC, Cleveland, 2001).
- [12] M.N. Piancastelli, G. Margaritondo, J.E. Rowe, *Solid State Comm.* 45 (1983) 219.
- [13] M.N. Piancastelli, M.K. Kelly, G. Margaritondo, J. Anderson, D.J. Frankel, G.J. Lapeyre, *Phys. Rev. B* 32 (1985) 2351.
- [14] C.D. MacPherson, K.T. Leung, *Surf. Sci.* 324 (1995) 202.
- [15] S. Yagi, N. Shirota, M. Taniguchi, E. Hashimoto, *Surf. Sci.* 454-456 (2000) 157; N. Shirota, S. Yagi, M. Taniguchi, E. Hashimoto, *J. Vac. Sci. Technol. A* 18 (2000) 2578.
- [16] X. Lu, X. Xu, J. Wu, N. Wang, Q. Zhang, *New J. Chem.* 26 (2002) 160.
- [17] X. Lu, M.C. Lin, X. Xu, N. Wang, Q. Zhang, *Phys. Chem. Comm.* 13 (2001) 1.

- [18] F. Tao, M.H Qiao, Z.H. Wang, G.Q. Xu, *J. Phys. Chem. B* 107 (2003) 6384.
- [19] Y. Taguchi, M. Fujisawa, T. Takaoka, T. Okada, M. Nishijima, *J. Chem. Phys.* 95 (1991) 6870.
- [20] Y. Taguchi, Y. Ohta, T. Katsumi, K. Ichikawa, O. Aita, *J. Electron Spectrosc. Relat. Phenom.* 88-91 (1998) 671.
- [21] S. Gokhale, P. Trischberger, D. Menzel, W. Widdra, H. Droge, H.-P. Steinruck, U. Birkenheuer, U. Gutdeutsch, N. Rosch, *J. Chem. Phys.* 108 (1998) 5554.
- [22] M.J. Kong, A.V. Teplyakov, J.G. Lyubovitsky, S.F. Bent, *Surf. Sci.* 411 (1998) 286.
- [23] G.P. Lopinski, D.J. Moffatt, R.A. Wolkow, *Chem. Phys. Lett.* 282 (1998) 305.
- [24] G.P. Lopinski, T.M. Fortier, D.J. Moffatt, R.A. Wolkow, *J. Vac. Sci. Tech. A* 16 (1998) 1037.
- [25] B. Borovsky, M. Krueger, E. Ganz, *Phys. Rev. B* 57 (1998) R4269.
- [26] B.I. Craig, *Surf. Sci.* 280 (1993) L279.
- [27] H.D. Jeong, S. Ryu, Y.S. Lee, S. Kim, *Surf. Sci.* 344 (1995) L1226.
- [28] U. Birkenheuer, U. Gutdeutsch, N. Rosch, *Surf. Sci.* 409 (1998) 213.
- [29] R.A. Wolkow, G.P. Lopinski, D.J. Moffatt, *Surf. Sci.* 416 (1998) L1107.
- [30] P.L. Silvestrelli, F. Ancilotto, F. Toigo, *Phys. Rev. B* 62 (2000) 1596.
- [31] Q. Li, K.T. Leung, *Surf. Sci.* 479 (2001) 69. See also Chapter 2
- [32] B. Borovsky, M. Krueger, E. Ganz, *J. Vac. Sci. Technol. B* 17 (1999) 7.
- [33] See Appendix A in this thesis.
- [34] "NIST/EPA/NIH Mass Spectral Library", NIST'98 with Windows, Version 1.7, (1996).
- [35] P.A. Redhead, *Vacuum* 12 (1962) 203.
- [36] Gaussian 98 (Revision A.11.3), M.J. Frisch, G.W. Trucks, H.B. Schlegel, G.E. Scuseria, M.A. Robb, J.R. Cheeseman, V.G. Zakrzewski, J.A. Montgomery, Jr., R.E. Stratmann, J. C. Burant, S. Dapprich, J. M. Millam, A.D. Daniels, K.N. Kudin, M.C.

- Strain, O. Farkas, J. Tomasi, V. Barone, M. Cossi, R. Cammi, B. Mennucci, C. Pomelli, C. Adamo, S. Clifford, J. Ochterski, G.A. Petersson, P.Y. Ayala, Q. Cui, K. Morokuma, N. Rega, P. Salvador, J.J. Dannenberg, D.K. Malick, A.D. Rabuck, K. Raghavachari, J.B. Foresman, J. Cioslowski, J.V. Ortiz, A.G. Baboul, B.B. Stefanov, G. Liu, A. Liashenko, P. Piskorz, I. Komaromi, R. Gomperts, R.L. Martin, D.J. Fox, T. Keith, M.A. Al-Laham, C.Y. Peng, A. Nanayakkara, M. Challacombe, P.M.W. Gill, B. Johnson, W. Chen, M.W. Wong, J.L. Andres, C. Gonzalez, M. Head-Gordon, E.S. Replogle, J.A. Pople, Gaussian Inc., Pittsburgh PA (2002).
- [37] J.B. Foresman, Æ. Frisch, "Exploring Chemistry with Electronic Structure Methods", 2nd Ed., Gaussian Inc., Pittsburgh (1996); and references therein.
- [38] M. Suemitsu, H. Nakazawa, N. Miyamoto, *Appl. Surf. Sci.* 82/83 (1994) 449.
- [39] S.M. Gates, R.R. Kunz, C.M. Greenlief, *Surf. Sci.* 207 (1989) 364.
- [40] P.A. Taylor, R.M. Wallace, C.C. Cheng, W.H. Weinberg, M.J. Dresser, W.J. Choyke, J.T. Yates, Jr., *J. Am. Chem. Soc.* 114 (1992) 6754.
- [41] C. Huang, W. Widdra, X.S. Wang, W.H. Weinberg, *J. Vac. Sci. Technol. A* 11 (1993) 2250.
- [42] V.N. Ageev, *Prog. Surf. Sci.* 47 (1994) 55; and references therein.
- [43] L. Clemen, R.M. Wallace, P.A. Taylor, M.J. Dresser, W.J. Choyke, W.H. Weinberg, J.T. Yates, Jr., *Surf. Sci.* 268 (1992) 205.
- [44] C.C. Cheng, W.J. Choyke, J.T. Yates, Jr., *Surf. Sci.* 231 (1990) 289.
- [45] S.J. White, D.P. Woodruff, B.W. Holland, R.S. Zimmer, *Surf. Sci.* 74 (1978) 34.
- [46] Y. Imamura, N. Matsui, Y. Morikawa, M. Hada, T. Kubo, M. Nishijima, H. Nakatsuji, *Chem. Phys. Lett.* 287 (1998) 131.
- [47] R.Y. Young, K.A. Brown, W. Ho, *Surf. Sci.* 336 (1995) 85.
- [48] L.H. Chua, R.B. Jackman, J.S. Foord, *Surf. Sci.* 315 (1994) 69.
- [49] W. Widdra, C. Huang, S.I. Yi, W.H. Weinberg, *J. Chem. Phys.* 105 (1996) 5605.

- [50] M.J. Kong, A.V. Teplyakov, J. Jagmohan, J.G. Lyubovitsky, C. Mui, S.F. Bent, J. Phys. Chem. B 104 (2000) 3000.



## Chapter 6

### Hydrogen evolution of aromatic hydrocarbons on Si(100)

#### 6.1 Introduction

Hydrogen interaction with silicon single-crystal surfaces is of great fundamental and technological interest. With its precisely known electronic structure in quantum mechanics, the hydrogen atom is the simplest possible adsorbate. Chemisorption of H atoms therefore becomes an important benchmark process for fundamental study in surface chemistry [1]. In all our present thermal desorption experiments [2,3,4,5], hydrogen evolution plays an important role in the analysis and control of various surface structures and reactions for aromatic hydrocarbons on the Si(100) surface. Given that a voluminous amount of work, both theoretical and experimental, has been reported for the adsorption and desorption of H on Si(100) [6,7,8], the present study seeks to focus specifically on hydrogen evolution of hexacyclic hydrocarbons on Si(100), and to explore new functions of H in silicon surface chemistry.

##### 6.1.1 Hydrogen on Si(100) $2\times 1$ : Adsorption, surface phases, diffusion and desorption

The reactivity of molecular hydrogen toward silicon surfaces at room temperature (RT) is extremely weak with a sticking probability of nearly zero [8]. Hydrogen-terminated silicon surfaces therefore are usually produced by exposure to atomic hydrogen, created by thermal decomposition of H<sub>2</sub> flowing over a hot (~2000 K) tungsten filament positioned close to the Si surface. Depending on the coverage of H atoms on the Si(100) surface, the H-Si(100) surface is found to exist in different surface phases (Figure 6-1) [9]. At low coverage of H on Si(100), it is possible to form a  $2\times 1$  hemihydride structure at RT with a local coverage of 0.5 monolayer (ML) (Figure 6-1b), in which only one of the two Si dangling bonds on a Si-dimer is occupied by a H atom while the other has an unpaired electron in the so-called dangling-bond orbital. The Si dimer in the hemihydride phase is normally termed the “singly occupied dimer” (SOD). At a coverage of 1 ML, a  $2\times 1$  monohydride phase is formed, in which each end of the Si dimer is bonded by a H atom (Figure 6-1c). Such Si dimer is often

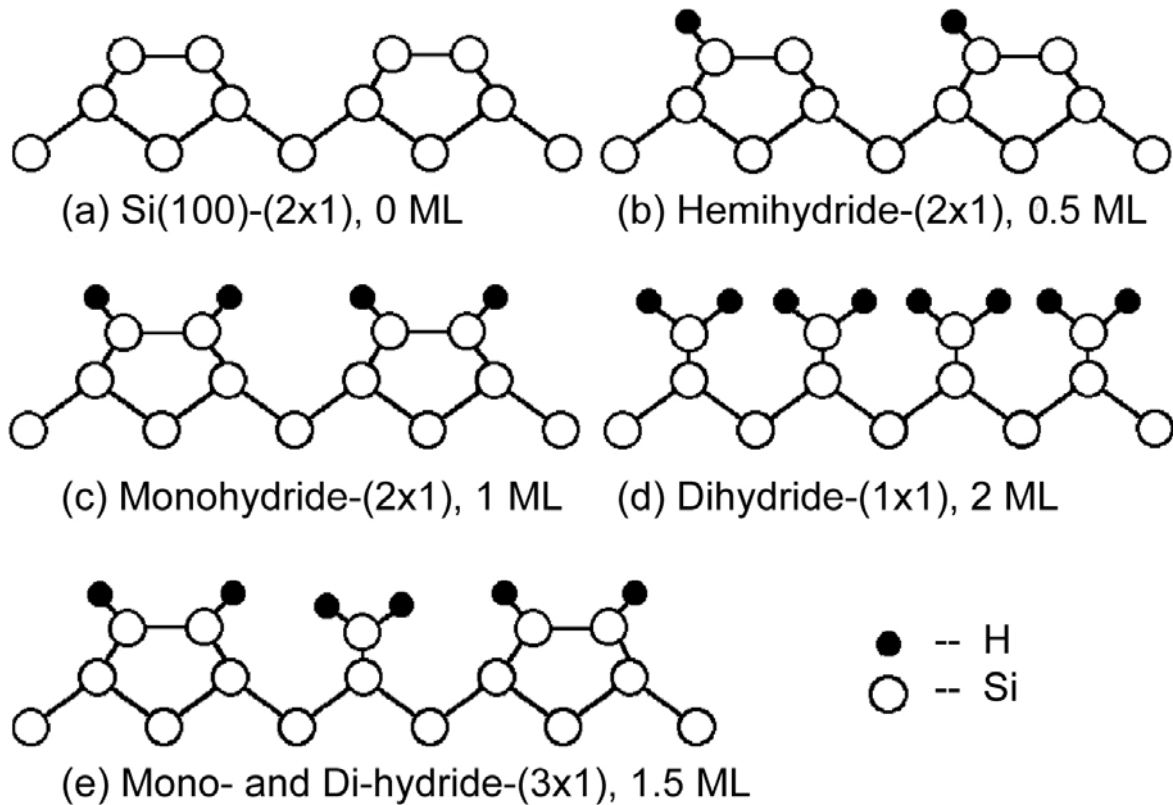


Figure 6-1. Structural model of hydrogen on Si(100) surface: (a) (2×1) reconstruction of clean Si(100); (b) (2×1) structure of hemihydride, single-occupied dimer (SOD), or Si–SiH, with a local coverage of 1/2 monolayer (ML); (c) (2×1) structure of monohydride, double-occupied dimer (DOD), or HSi–SiH, with a local coverage of 1 ML; (d) (1×1) structure of dihydride, with a local coverage of 2 ML; (e) (3×1) structure of the alternating monohydride and dihydride species, with a local coverage of 1.5 ML.

called the “doubly occupied dimer” (DOD). At a coverage higher than 1 ML, a 1×1 dihydride phase is formed, where the dimer bonds are broken, and the two dangling bonds on each surface Si atom are terminated with H atoms (Figure 6-1d). Due to its smallest mass and size, H atom exhibits more mobility than any other element on the surface, and the lateral diffusion of H becomes important to the surface processes. In particular, an unexpected 3×1 ordered phase of H-Si(100), composed of alternative rows of monohydride and dihydride (Figure 6-1e), is obtained after saturation adsorption of H at 400 K [10]. Surface phases



along with the corresponding surface reconstructions can therefore be controlled by the surface temperature and H coverage.

The TDS profile of H<sub>2</sub> for a saturated H-Si(100) surface (Figure 6-2a) exhibits two desorption states with maxima at 680±20 K ( $\beta_2$ ) and 790±20 K ( $\beta_1$ ), which correspond to recombinative hydrogen desorption of the dihydride and monohydride phases, respectively. It should be noted that the desorption temperatures for  $\beta_1$  and  $\beta_2$  are much higher than the respective H diffusion temperatures on Si(100) (i.e. 380 K for dihydride and 570 K for monohydride [9]). A quasi-equilibrium kinetics model, in which all surface species are effectively in equilibrium due to a much faster H diffusion rate during thermal desorption, can therefore be a good approximation for the thermal desorption mechanism of H on Si(100) [11].

### **6.1.2 Hydrogen evolution in chemisorption systems of aromatic hydrocarbons on Si(100)2×1**

In all of our TDS experiments on aromatic hexacyclic hydrocarbons (e.g. benzene, toluene [2], *p*-xylene [3], styrene [4] and pyridine [5]) on the 2×1 and modified Si(100) surfaces, hydrogen evolution is found to be a common process, along with molecular and dissociative desorption. Figure 6-2 compares hydrogen evolution from *p*-xylene/Si(100)2×1 and styrene/Si(100)2×1 with that from the H/Si(100)2×1 system. Different deuterated derivatives have been used in order to better distinguish the sources of the desorbed hydrogen. The lack of hydrogen desorption below 700 K for these TDS experiments suggests that no dihydride phases are formed during hydrogen abstraction from hydrocarbon adsorbates. Hydrogen abstraction is therefore not an prominent process, which is also supported by the essentially unchanged (2×1) LEED patterns obtained after the adsorption of these molecules [2,3,4,5]. Three types of desorption can be identified from their characteristic desorption temperatures and shapes of the TDS profiles for D<sub>2</sub> (Mass 4) and/or H<sub>2</sub> (Mass 2). The first type gives a similar profile shape to that for the first-order desorption of the  $\beta_1$  phase of (monohydride) H/Si(100) (Figure 6-2a), with the desorption maximum at 800-810 K (e.g. recombinative mass-2 desorption involving H abstracted from the vinyl group of styrene as shown in

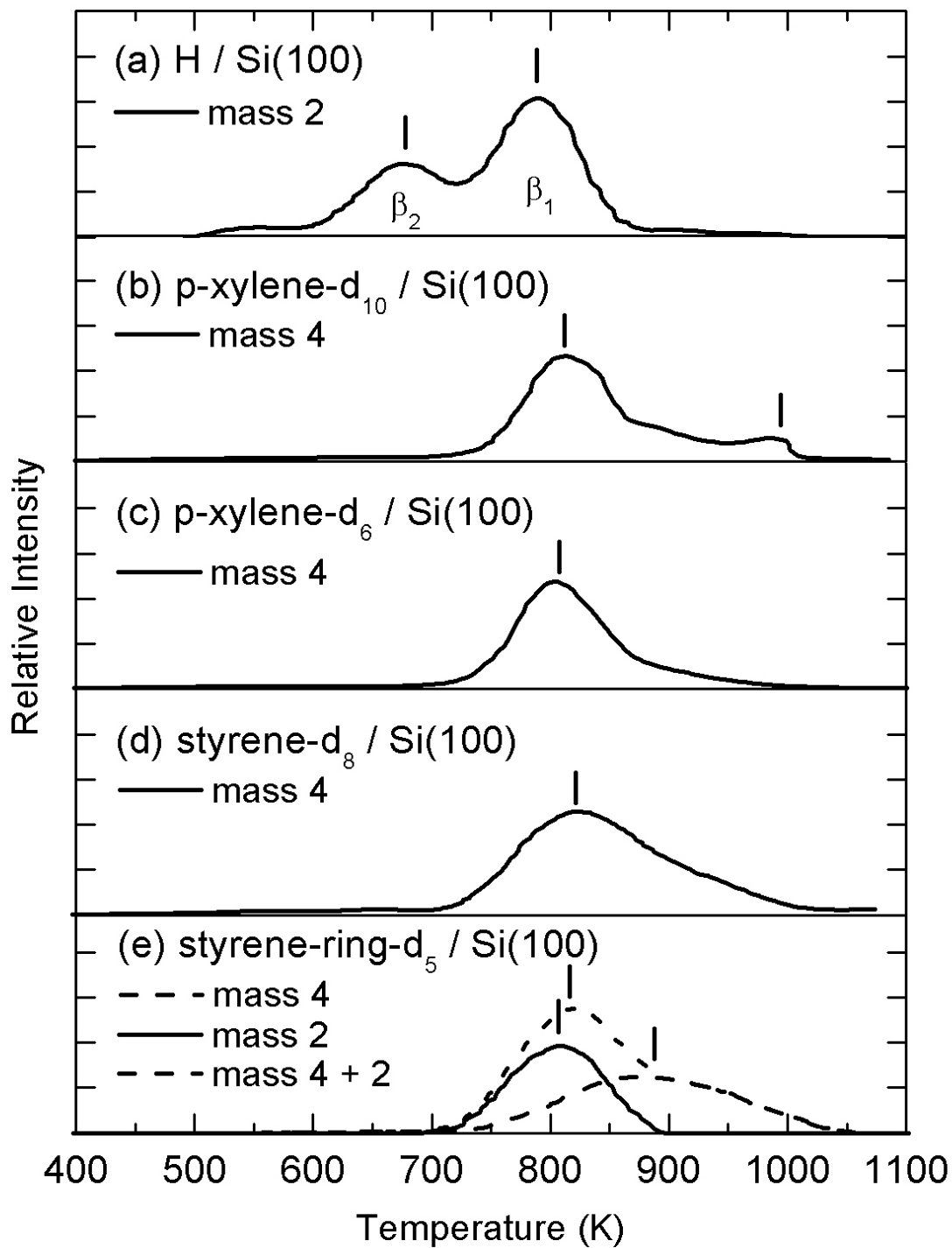


Figure 6-2 TDS profiles of D<sub>2</sub> and/or H<sub>2</sub> for (a) H/Si(100), (b) *p*-xylene-d<sub>10</sub>/Si, (c) *p*-xylene-d<sub>6</sub>/Si(100), (d) styrene-d<sub>8</sub>/Si(100), and (e) styrene-ring-d<sub>5</sub>/Si(100).

Figure 6-2e). The second type exhibits a shape characteristic of a second-order desorption profile, with the TDS maximum located at 820 K [e.g. the mass-4 desorption involving D abstracted from the methyl group of *p*-xylene (Figure 6-2c) or toluene (not shown)]. The third type of desorption involves hydrogen evolution from the phenyl groups and occurs at considerably higher temperatures than that of hydrogen desorption from monohydride [e.g. the mass-4 desorption at 1000 K from the phenyl group in *p*-xylene-d<sub>10</sub> (Figure 6-2e) and that at 880 K from the phenyl group in styrene-ring-d<sub>5</sub> (Figure 6-2b)].

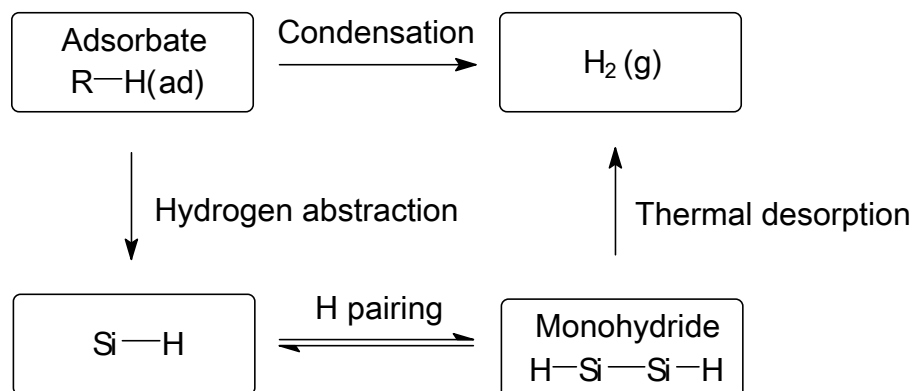


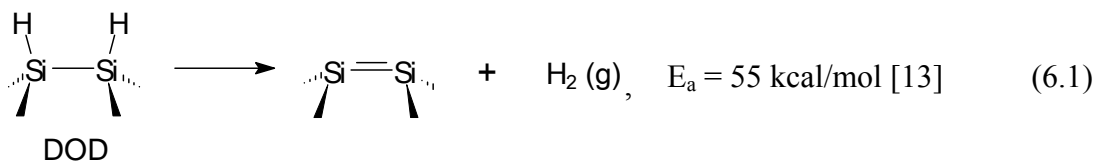
Figure 6-3 Process flow diagram for hydrogen evolution from the aromatic hexacyclic hydrocarbons adsorbed on Si(100) studied in the present work.

Figure 6-3 gives a process flow chart for hydrogen evolution in a typical hexacyclic hydrocarbon/Si(100) system. In most cases, an adsorbate first undergoes hydrogen abstraction to release H atoms onto the Si surface. As the temperature is increased, H atoms diffuse on the surface and become paired up on the Si dimers to form monohydrides in the DOD phase. The H atoms at these DOD sites then undergo recombinative desorption as H<sub>2</sub> at ~700 K. In some special conditions, hydrogen evolution is also found to occur as a side reaction as the result of condensation polymerization (oligomerization) of the adsorbates. In the following sections, three kinetics models will be discussed for hydrogen evolution in the chemisorption systems of aromatic hydrocarbons on Si(100).

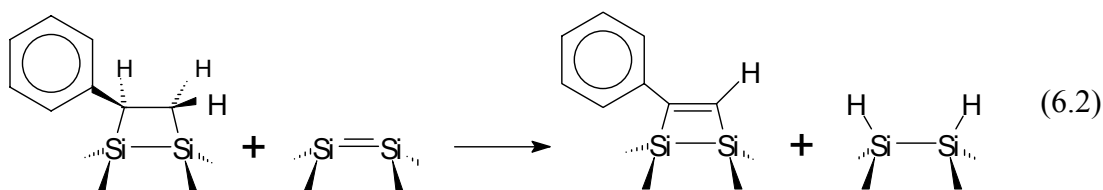
## 6.2 Model I: hydrogen evolution from the vinyl group in styrene on Si(100)2×1

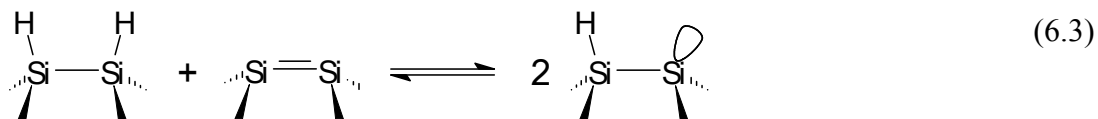
A comparison of the TDS profiles of D<sub>2</sub> (and/or H<sub>2</sub>) for styrene-d<sub>8</sub> (Figure 6-2d) and styrene-ring-d<sub>5</sub> (i.e. with the phenyl group deuterated) (Figure 6-2e) shows that the total hydrogen desorption for styrene-d<sub>8</sub> (Figure 6-2d) could be attributed to H atoms abstracted from both the vinyl group (corresponding to the mass-2 desorption with maximum at 810 K in Figure 6-2e) and the phenyl group (corresponding to the mass-4 desorption with maximum at 880 K in Figure 6-2e). A FTIR study by Schwartz *et al.* [12] also found that hydrogen abstraction from the vinyl group occurs at RT after [2+2] cycloaddition of styrene on Si(100), while hydrogen abstraction from the phenyl group takes place above 700 K.

The TDS profile of Mass 2 at 810 K corresponds to recombinative H<sub>2</sub> desorption involving the H atoms abstracted from the vinyl group of the adsorbed styrene-ring-d<sub>5</sub> (Figure 6-2e), and appears to be remarkably similar to that of H<sub>2</sub> desorption from the monohydride ( $\beta_1$  in Figure 6-2a), suggesting a similar mechanism of a first-order desorption kinetics. Since the recombinative desorption of hydrogen from the DOD occurs at a higher temperature and likely with a higher activation energy ( $E_a$ ) than the hydrogen abstraction and the H pairing processes (Figure 6-3), the desorption process can be considered as the rate-determining step:

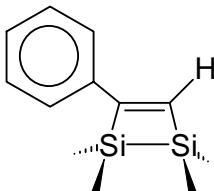
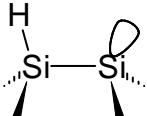
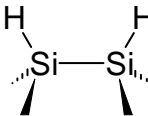
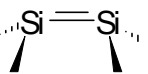


The concentration of the reactant, monohydride at the DOD, in Reaction 6.1 can be determined by the following two equilibria:





The enthalpy changes ( $\Delta H$ ) for Reactions 6.2 and 6.3 have been calculated to be  $-24.4$  kcal/mol and  $+6.0$  kcal/mol respectively by using the density functional method. The single-dimer of the Si(100) $2 \times 1$  surface is modeled by the surface of a Si<sub>9</sub>H<sub>12</sub> cluster. The large negative enthalpy change ( $\Delta H = -24.4$  kcal/mol) obtained for Reaction 6.2 suggests that it is thermodynamically favoured and the coverage of styrene remaining intact should be very low compared to that of dehydrogenated adsorbates. Moreover, since molecular desorption of styrene at 550 K [4] occurs at a lower temperature than the hydrogen desorption process, no styrene should remain on the surface at the onset of hydrogen desorption at 700 K. Only Reaction 6.3 is therefore needed in the present model, Model I. The coverages of the relevant surface species are listed as follow:

Dehydrogenated adsorbate	Singly occupied dimer (SOD)	Doubly occupied dimer (DOD)	Un-occupied dimer (UOD)
			
$\theta_a$	$\theta_1$	$\theta_2$	$\theta_0$

where  $\theta_a$ ,  $\theta_0$ ,  $\theta_1$  and  $\theta_2$  are the coverage (fraction of the occupied surface sites over the total surface sites) of the dehydrogenated adsorbate, un-occupied dimer (UOD), singly occupied dimers (SOD) and doubly occupied dimers (DOD), respectively.<sup>4</sup> Let  $\theta$  and  $\theta_H$  be the coverages of the total available sites for hydrogen adsorption and of the abstracted H on Si(100), respectively:

<sup>4</sup> The subscript is used to indicate the number of H atoms in each species.

$$\theta = \theta_0 + \theta_1 + \theta_2$$

$$\theta_H = \theta_1 / 2 + \theta_2 \quad (6.4)$$

$$\theta_a + \theta = 1$$

To simplify the analysis, the coverages (with a prime mark) were normalized with respect to the coverage of total available sites ( $\theta$ ):

$$\theta'_i = \frac{\theta_i}{\theta}, \quad \left( i = 0, 1, 2, \text{ or } H \right) \quad (6.5)$$

According to the lattice gas model proposed by D'Evelyn *et al.* [11], the equilibrium constant for Reaction 6.3 can be obtained (Appendix C) as

$$K = \frac{\theta_1^2}{\theta_0 \cdot \theta_2} = \frac{\theta_1'^2}{\theta_0' \cdot \theta_2'} = 4x \quad (6.6)$$

where  $x = e^{-\Delta H / RT}$  ( $\Delta H$  is the enthalpy change of Reaction 6.3). From Equations 6.4-6.6,  $\theta_2'$  can be solved as a function of  $\theta_H'$ :

$$\theta_2' = \theta_H' - \frac{\sqrt{x^2 + 4x(1-x)\theta_H'(1-\theta_H')} - x}{2(1-x)} \quad (6.7)$$

Equation 6.7 has the same form as that for the H-Si(100) system [11], except that  $\theta_H$  for the H-Si(100) system is replaced by the normalized coverage  $\theta_H'$  in the case of the styrene/Si(100) system.

As shown in Reaction 6.1, the hydrogen desorption comes from recombination of H in the DOD phase, and the corresponding desorption rate is given by:

$$-\frac{d\theta_H'}{dt} = \theta_2' \cdot \nu \cdot e^{-E_a / RT} \quad (6.8)$$

where  $\nu$  is the pre-exponential factor and  $E_a$  is the activation energy of hydrogen desorption from the DOD phase.

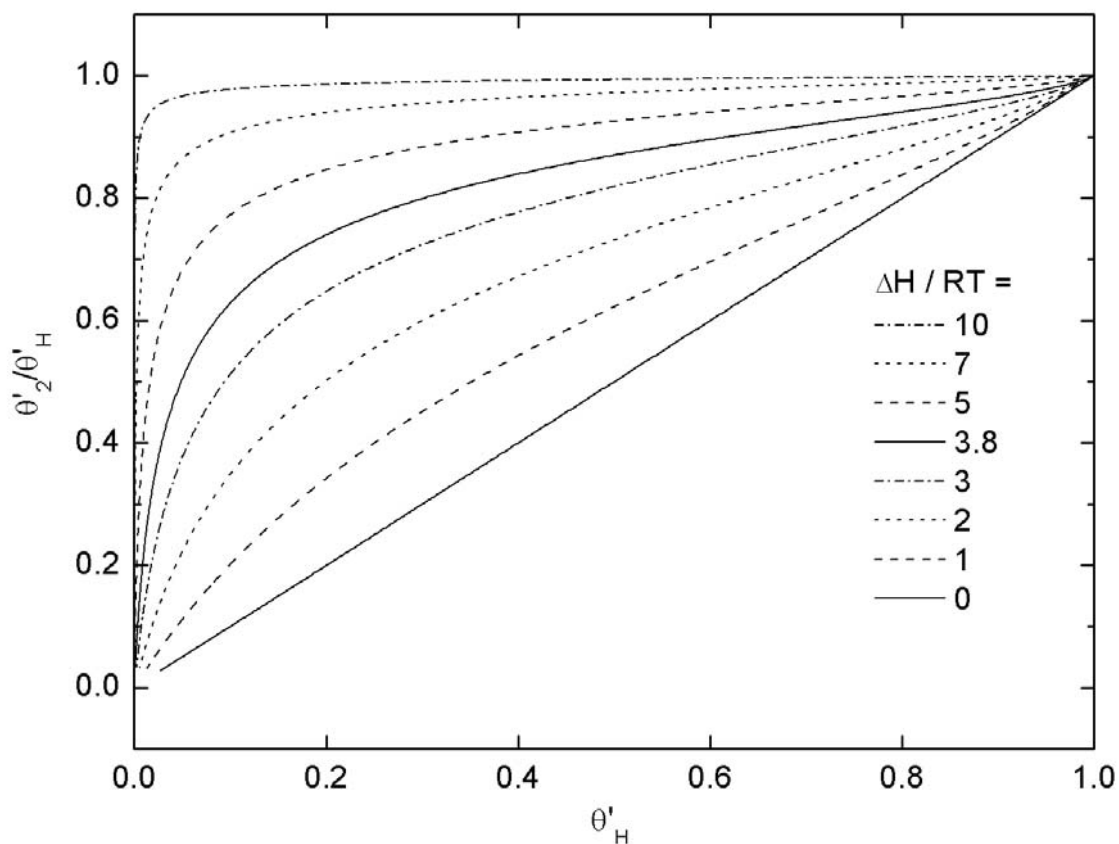


Figure 6-4 Fraction of hydrogen present in DOD as a function of total H coverage, for various values of enthalpy change for hydrogen pairing (Reaction 6.3).

If Reaction 6.3 is neither exothermic nor endothermic (i.e. As  $\Delta H \rightarrow 0$  and  $x \rightarrow 1$ ), Equation 6.7 is reduced to  $\theta'_2 = \theta_H'^2$ ,<sup>5</sup> which corresponds to a second-order desorption when substituted in Equation 6.8,. If the formation of DOD is highly thermodynamically favoured (i.e.  $\Delta H \rightarrow \infty$  and  $x \rightarrow 0$ ), Equation 6.7 is reduced to  $\theta'_2 = \theta_H'$  and corresponds to a first-order desorption. Figure 6-4 shows the fraction of H in the DOD phase ( $\theta'_2 / \theta_H'$ ) as a function of  $\theta_H'$  for various values of  $\Delta H / RT$ . This fraction is found to increase smoothly from  $\theta_H'$  to 1

$$^5 \theta'_2 \Big|_{x \rightarrow 1} = \theta_H' - \frac{d \left[ \sqrt{x^2 + 4x(1-x)\theta_H'(1-\theta_H')} - x \right] / dx}{d[2(1-x)] / dx} \Big|_{x \rightarrow 1} = \theta_H' - \frac{-2\theta_H'(1-\theta_H')}{-2} = \theta_H'^2.$$

as  $\Delta H / RT$  increases from 0 to  $\infty$ . For example, for the calculated enthalpy change of Reaction 6.3 (+6.0 kcal/mol), the curve for  $\Delta H / RT = 3.8$  in Figure 6-4 corresponds to the equilibrium of Reaction 6.3 at the temperature of the desorption maximum (800 K).

In order to illustrate the influence of T and  $\theta'_H$  on the reaction order for hydrogen desorption, the logarithm of  $\theta'_2$  is plotted against the logarithm of  $\theta'_H$  (Figure 6-5). Evidently, linear relation is observed between  $\ln\theta'_2$  and  $\ln\theta'_H$  for the  $\theta'_H$  range 0.1–0.9:

$$\ln \theta'_2 = n \ln \theta'_H \quad \text{or} \quad \theta'_2 = \theta'^n_H \quad (6.9)$$

where n is the slope of the isotherm curve. Evidently the isotherms are found to be linear to within  $\pm 5\%$  for  $\theta'_H$  between 0.01 and 0.8 for the temperature range 100–900 K. As a result, the rate of hydrogen desorption from DOD in Equation 6.8 can be approximately written as

$$-\frac{d\theta'_H}{dt} = \theta'^n_H \cdot \nu \cdot e^{-E_a/RT} \quad (6.10)$$

It is clear in Equation 6.10, the parameter n represents the reaction order for the hydrogen desorption. Equation 6.9 can therefore be used as a good method to determine the reaction order of hydrogen evolution in terms of  $\theta'_H$ . Given an equilibrium temperature T, n can be obtained from the slope of the curves in Figure 6-5.

If there is no hydrocarbon adsorbates ( $\theta_a = 0$  or  $\theta = 1$ ),  $\theta'_H = \theta_H$ , Equation 6.10 thus becomes

$$-\frac{d\theta_H}{dt} = \theta^n_H \cdot \nu \cdot e^{-E_d/RT} \quad (6.11)$$

which is the case for hydrogen desorption from H/Si(100). The similar form for Equation 6.10 and 6.11 suggests similarity in the kinetics of hydrogen evolution in both styrene/Si(100) and H/Si(100) in Model I, which is consistent with our TDS experiments (Figure 6-2a and Figure 6-2e).

In Figure 6-6, the desorption order n is plotted as a function of T and  $\theta'_H$ . As shown in Figure 6-6a, n remains to be 1 (first order) below 200 K and increases almost linearly with increasing temperature over the 400–900 K range. From the isotherm curves in Figure 6-6b,



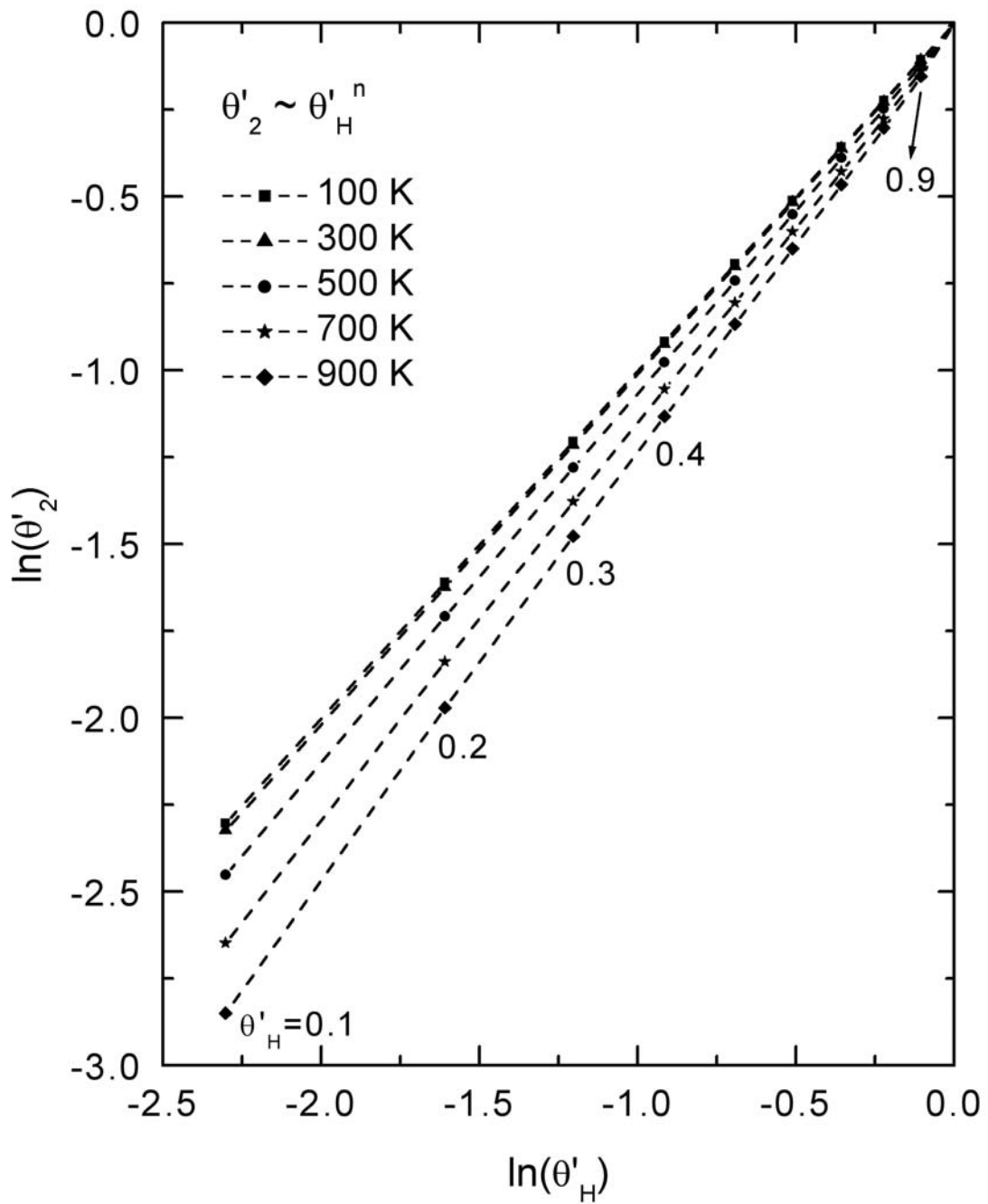


Figure 6-5 The logarithm of H coverage in DOD ( $\theta'_2$ ) is plotted as a function of the logarithm of total H coverage ( $\theta'_H$ ) at various temperatures.

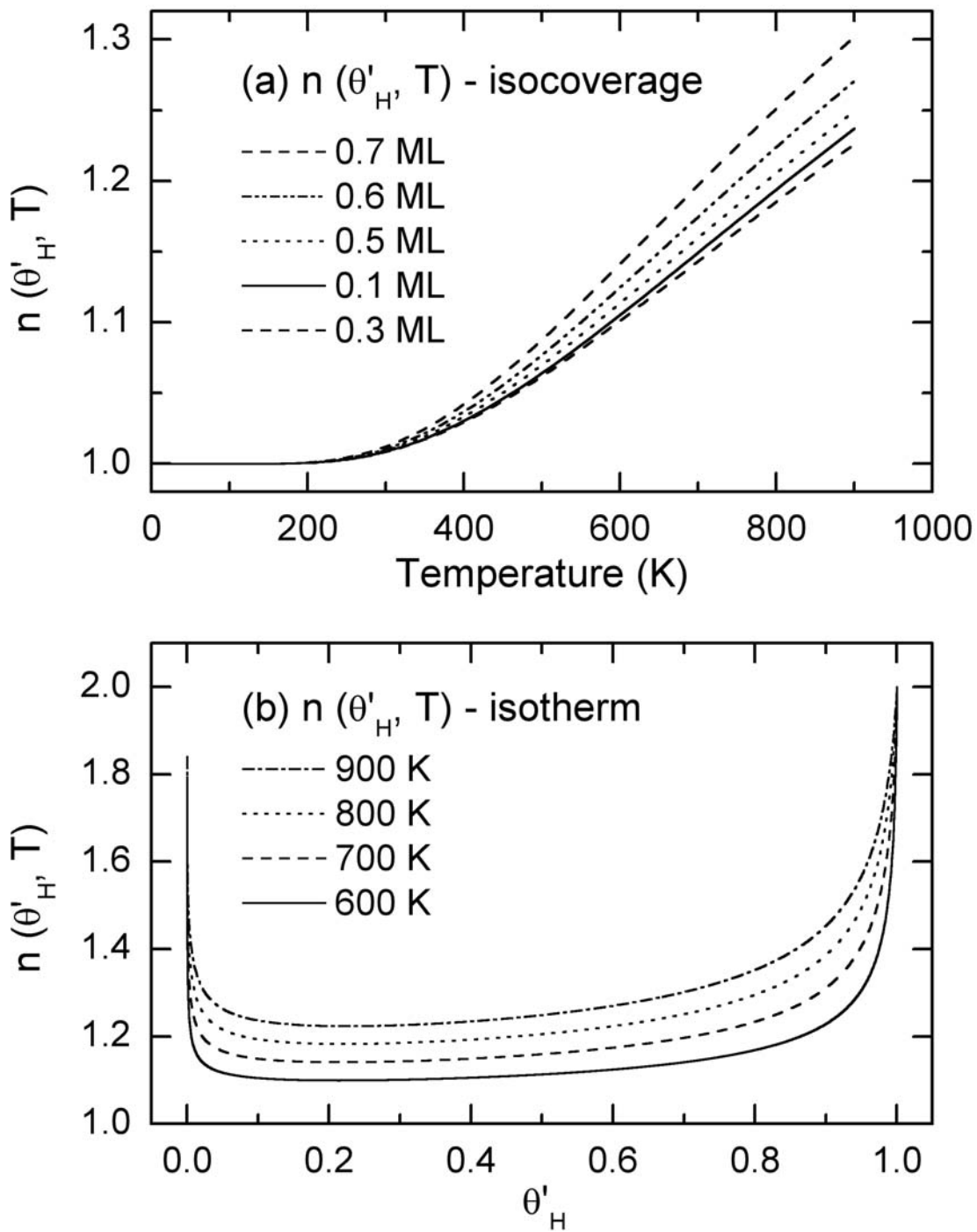


Figure 6-6 Desorption order  $n$  as a function of temperature and total H coverage for styrene-rind- $d_5$ /Si(100).

n remains essentially constant for  $0.01 < \theta'_H < 0.8$ , but increases sharply for  $\theta'_H < 0.05$  or  $\theta'_H > 0.95$ . By using the L'Hospital rule [14], n can be derived from the ratio of  $\ln(\theta'_2)/\ln(\theta'_H)$  as  $\theta'_H \rightarrow 0$  or  $\theta'_H \rightarrow 1$ . Because the derivative of  $\theta'_2$  is given as a function of  $\theta'_H$  (Equation 6.7) by

$$\frac{d\theta'_2}{d\theta'_H} = 1 - \frac{x(1-2\theta'_H)}{\sqrt{x^2 + 4x(1-x)\theta'_H(1-\theta'_H)}} \quad (6.12)$$

in the limit  $\theta'_H \rightarrow 1$ ,

$$\left. \frac{d\theta'_2}{d\theta'_H} \right|_{\theta'_H \rightarrow 1} = 1 - (1-2\theta'_H) \Big|_{\theta'_H \rightarrow 1} = 2,$$

and the corresponding desorption order n is given by

$$\begin{aligned} n \Big|_{\theta'_H \rightarrow 1} &= \ln(\theta'_2)/\ln(\theta'_H) \Big|_{\theta'_H \rightarrow 1} = \frac{d[\ln(\theta'_2)]}{d\theta'_H} \Big/ \frac{d[\ln(\theta'_H)]}{d\theta'_H} \Big|_{\theta'_H \rightarrow 1} \\ &= \frac{\theta'_H}{\theta'_2} \cdot \left. \frac{d\theta'_2}{d\theta'_H} \right|_{\theta'_H \rightarrow 1} = \frac{1}{1} \cdot 2 = 2. \end{aligned} \quad (6.13)$$

similarly, for the limit  $\theta'_H \rightarrow 0$ ,

$$\left. \frac{d\theta'_2}{d\theta'_H} \right|_{\theta'_H \rightarrow 0} = 1 - (1-2\theta'_H) \Big|_{\theta'_H \rightarrow 0} = 2\theta'_H,$$

and the corresponding desorption order n is given by

$$\begin{aligned} n \Big|_{\theta'_H \rightarrow 0} &= \frac{\theta'_H}{\theta'_2} \cdot \left. \frac{d\theta'_2}{d\theta'_H} \right|_{\theta'_H \rightarrow 0} = 2(\theta'_H)^2/\theta'_2 \Big|_{\theta'_H \rightarrow 0} \\ &= \frac{d[2(\theta'_H)^2]}{d\theta'_H} \Big/ \left. \frac{d\theta'_2}{d\theta'_H} \right|_{\theta'_H \rightarrow 0} = 4\theta'_H/2\theta'_H = 2 \end{aligned} \quad (6.14)$$

both limits therefore give rise to the second-order desorption.

As expressed in Equation 6.14 (Figure 6-6b), the deviation from the first-order kinetics for very low hydrogen coverages to second-order has also been observed by means of isothermal measurements by using optical second-harmonic generation [15]. This deviation is believed to be associated with the fact that at low coverages, the relative population of SOD becomes substantial, which in turn reduces the number of DOD phase

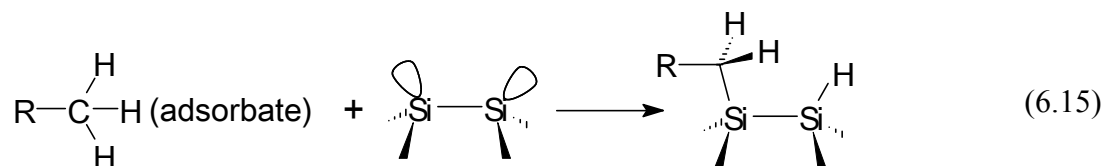
available to participate in the desorption process [15]. It is of interest to note that such deviation from the first-order to the second-order kinetics can also exist at higher H coverages as shown in Equation 6.13 (Figure 6-6b). It is however not easy to observe this behaviour in TDS because this process only occurs at the very beginning of the desorption process, and it rapidly reverts to the first-order kinetics (due to reduced H coverage as a result of the desorption) before reaching the temperature of maximum desorption. Moreover, the formation of the dihydride takes over at high coverage and this also leads to second-order desorption.

In summary, the desorption kinetics of hydrogen evolution from the vinyl group for styrene on Si(100) has been discussed by using Model I. The kinetics of hydrogen evolution for styrene/Si(100) is found to be generally similar to that for H/Si(100). This similarity can be understood, given the fact that the hydrocarbon remaining on the surface has no effect on H diffusion and desorption. The present model can therefore be applied to hydrogen evolution in all hydrocarbon/Si(100) systems in which surface diffusion of H is independent of the co-adsorbed hydrocarbons. The new method for determination of the reaction order for desorption (developed in this model) can be useful for kinetic study of other chemistries in pre-equilibrium systems, and will also be used in Model II.

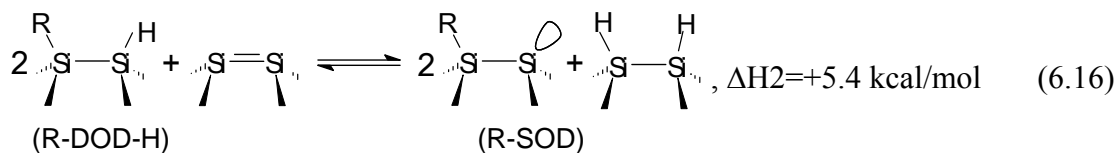
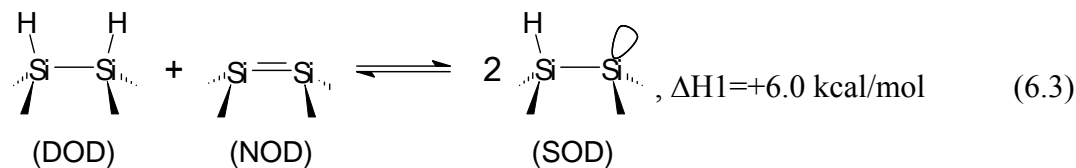
### **6.3 Model II: hydrogen evolution from the methyl group in methyl-substituted aromatic hydrocarbons (toluene, xylene) on Si(100)<sub>2</sub>×1**

In the last section, we discussed the kinetics of hydrogen evolution for the case in which the diffusion and desorption of H atoms on Si(100) is independent of the coadsorbed hydrocarbon molecules, which include all hydrocarbon adsorbates with di- $\sigma$  bonding on the Si dimers. We showed that the model for hydrogen evolution of these hydrocarbons could be treated as simply as H/Si(100). In this section, a more complicated model, Model II, will be discussed and applied to situations where the coadsorbed hydrocarbons do affect the H diffusion on Si(100). In particular, it will be used to analyse hydrogen evolution in the methyl-substituted aromatic hydrocarbons (such as toluene, *m*-xylene, *o*-xylene and *p*-xylene) on Si(100)<sub>2</sub>×1. In a FTIR study, Coulter *et al.* showed that (1) the methyl-substituted hydrocarbons chemisorb on Si(100)<sub>2</sub>×1 in much the same way as benzene that

involves di- $\sigma$  bonding through an aromatic ring with a Si dimer, and (2) hydrogen dissociates primarily from the methyl group after adsorption [16]. In our previous TDS study of toluene on Si(100)2 $\times$ 1, the majority of the adsorbed toluene is found to undergo hydrogen abstraction from the methyl group, which appears to be an irreversible process even at RT [2]. Similar results have also been found for *p*-xylene on Si(100)2 $\times$ 1 [3]. These results indicate the following picture: the methyl-substituted aromatic molecules first adsorb on Si(100)2 $\times$ 1 through di- $\sigma$  bonding between the phenyl group and the Si dimers. In certain adsorption geometries, a “dangling” methyl group of the adsorbate happens to be in close proximity to an empty Si dimer and the methyl group could then bond to a Si atom of this dimer with abstraction of a H atom onto the other Si atom of the same Si dimer, i.e.



The enthalpy change for hydrogen abstraction from the methyl group of *p*-xylene and toluene (Reaction 6.15) is calculated to be  $-44$  kcal/mol (by using the density functional method with the hybrid B3LYP density functional and a 6-31G(d) basis set on a model surface of a Si<sub>9</sub>H<sub>12</sub> cluster). Such large enthalpy change is consistent with the irreversibility of hydrogen abstraction observed in our previous TDS experiment [2]. The product in Reaction 6.15 also corresponds to a DOD geometry. Because of their lower mobilities on the surface compared to H atoms, the hydrocarbon adsorbates can be assumed to be localized at their bonding sites during H diffusion and desorption. In order to obtain desorption of one H<sub>2</sub> molecule, two H atoms are needed to form the two monohydrides in a DOD site. These H atoms could come from both a SOD site (Equation 6.3) and a DOD site (coadsorbed with both a hydrocarbon and a H atom). In addition to the three types of H-occupied dimer species in Model I (i.e. UOD, SOD and DOD), two types in Model II of hydrocarbon-occupied dimer species are also considered, including singly occupied dimer with an adsorbed hydrocarbon (R-SOD) and doubly occupied dimer with coadsorbed hydrocarbon and H (R-DOD-H). The distribution of these species can be obtained by the following equilibria:

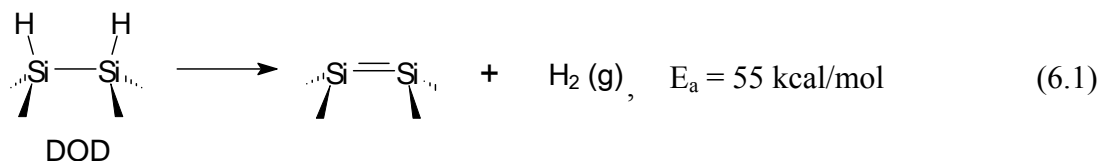


It should be noted that Equilibria 6.3 and 6.16 are proposed only to define the distributions of species expected to be present on the surface, and do not purport to indicate the mechanism by which these equilibrium distributions are established. In contrast to Reaction 6.3 where hydrogen pairing is an exothermic process, the hydrogen pairing process in Reaction 6.16 is endothermic. The magnitude of  $\Delta H$  for Reaction 6.16 is expected to be similar to that for Reaction 6.3, because both are of the order of the energy for a Si=Si  $\pi$ -bond. The enthalpy changes for Reactions 6.3 and 6.16 indicated above are calculated by using the same computational method as in Section 6.2.

If  $\theta_0$ ,  $\theta_1$ ,  $\theta_2$ ,  $\theta_R$  and  $\theta_a$ , respectively, represent the coverages of UOD, SOD, DOD, R-SOD and R-DOD-H; and  $\theta_A$  and  $\theta_H$  are the total coverage of the hydrocarbon adsorbate and H, respectively, then the following relations apply:

$$\begin{aligned}
 \theta_A &= \theta_a + \theta_R \\
 \theta_H &= \theta_a / 2 + \theta_1 / 2 + \theta_2 \\
 1 &= \theta_0 + \theta_1 + \theta_2 + \theta_a + \theta_R
 \end{aligned} \quad (6.17)$$

During recombinative desorption of  $H_2$ , the total surface H density ( $\theta_H$ ) decreases with time. As described in Model I, the desorption occurs via recombination between the two hydrogen atoms on the DOD site, i.e.



with the desorption rate given by

$$-\frac{d\theta_H}{dt} = \theta_2 \cdot v \cdot e^{-E_a/RT} \quad (6.18)$$

As in Model I, the equilibrium distribution of DOD may be obtained from a simple lattice gas model that neglects interactions between different dimers. The equilibrium constants for Reaction 6.3 and 6.16 can be derived, respectively, as Equations 6.6 and 6.19:

$$K_1 = \frac{\theta_1^2}{\theta_0 \cdot \theta_2} = 4e^{-\Delta H_1/RT} \quad (6.6)$$

$$K_2 = \frac{\theta_2 \cdot \theta_R^2}{\theta_0 \cdot \theta_a^2} = e^{-\Delta H_2/RT} \quad (6.19)$$

By combining Equations 6.17, 6.6 and 6.19 for a given set of  $\theta_A$ ,  $\theta_H$  and  $T$ , the equilibrium coverages of all the surface species can be obtained. The TDS profile of  $H_2$  for various initial coverages of hydrogen ( $\theta_H$ ) and methyl-substituted aromatic hydrocarbons ( $\theta_A$ ) can therefore be simulated. In particular, at the instant  $t_i$  ( $i=0,1,2\dots$ ),  $\theta_2(t_i)$  can be calculated numerically for  $\theta_H(t_i)$  at the surface temperature  $T(t_i)$ . The instantaneous desorption rate is then given by

$$-\frac{d\theta_H(t_i)}{dt} = \theta_2(t_i) \cdot v \cdot e^{-E_a/RT(t_i)} \quad (6.20)$$

After a short finite time interval  $\Delta t$  (0.01s in the present work),  $\theta_H$  and  $T$  are changed approximately to

$$\theta(t_{i+1}) = \theta(t_i) + \frac{d\theta_H(t_i)}{dt} \cdot \Delta t \quad \text{and} \quad T(t_{i+1}) = T_i + \beta \cdot \Delta t \quad (6.21)$$

for a linear temperature ramp  $\beta$ . Some kinetic parameters (e.g.  $\Delta H$ ,  $v$  and/or  $E_a$ ) may also be determined by fitting the simulated desorption process with the experimental TDS profiles of  $H_2$ . As shown in Figure 6-7, the TDS profile for 5 L of *p*-xylene-methyl-d<sub>6</sub> has been effectively simulated using fitted parameters  $v_d = 5.6 \times 10^{14} \text{ s}^{-1}$  and  $E_d = 53 \text{ kcal/mol}$  (similar to those for hydrogen desorption from monohydrides [13]). The shapes of both simulated and experimental TDS profiles are found to be characteristic of higher order ( $n \geq 2$ )

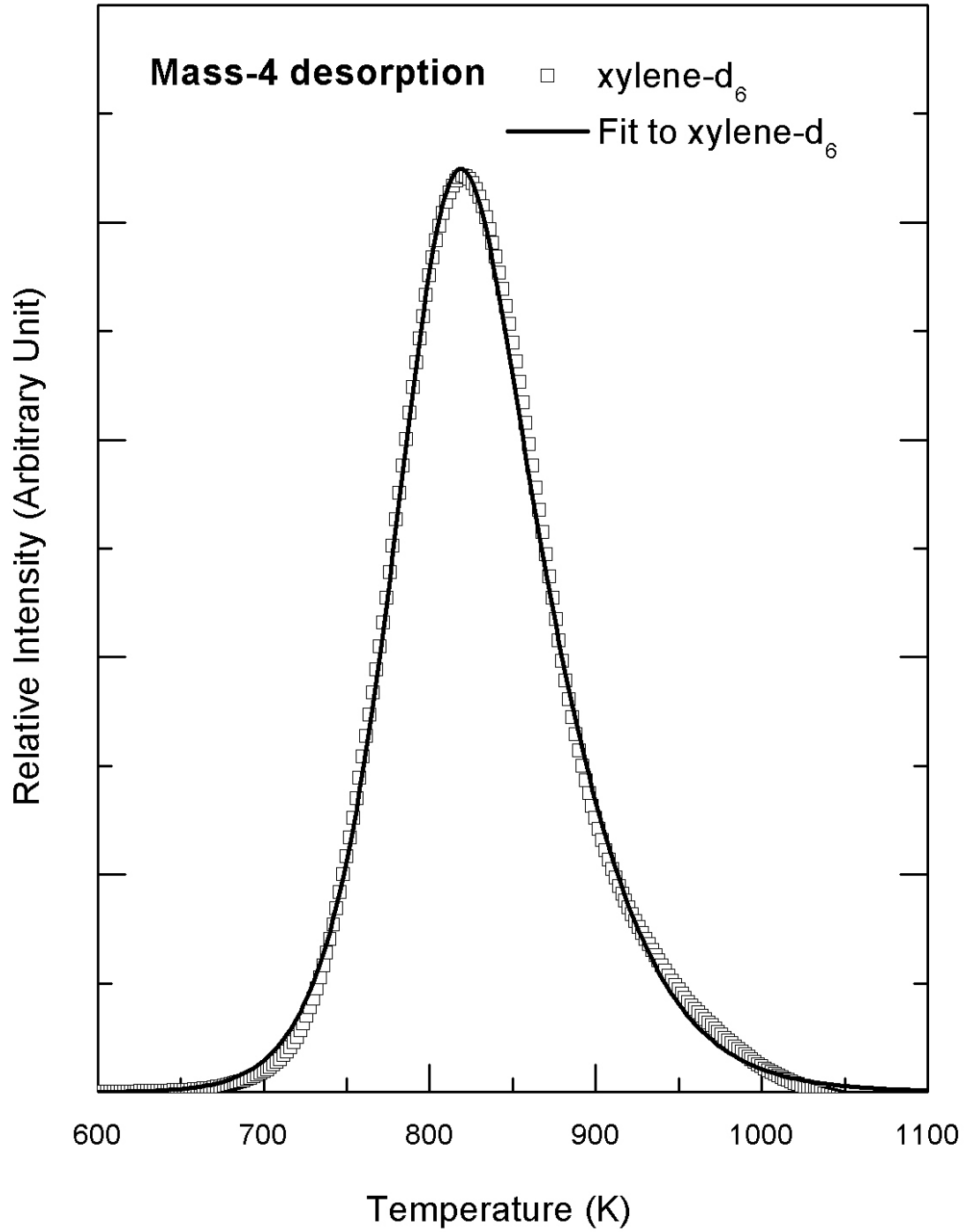


Figure 6-7 TDS profile of Mass-4 (D<sub>2</sub>) desorption for a 5 L exposure of *p*-xylene-dimethyl-d<sub>6</sub> and has been fitted with the desorption kinetics model, Model II (solid line).



desorption [17].

Figure 6-8 gives the simulated changes of  $n$  during thermal desorption for various initial hydrocarbon coverages ( $\theta_A$ ) and shows that  $n$  generally increases with increasing  $\theta_A$ . In Figure 6-8, at a low initial hydrocarbon coverages ( $\theta_A < 0.05$ ), the change in the desorption order during thermal desorption is similar to that in the H-Si(100) system described in Model I (i.e.  $n \approx 1$  below 800 K and  $n$  increases to 2 as  $\theta_H$  is reduced to 0 during thermal desorption above 800 K.) At high initial hydrocarbon coverages, however,  $n$  is found to decrease towards 2 above 850 K, because Reaction 6.3 becomes prominent over Reaction 6.16 for very small values of  $\theta_H$ . As discussed in Section 6.2, hydrogen evolution involving Reaction 6.3 would lead to second-order kinetics as  $\theta_H \rightarrow 0$ .

In summary, the kinetics of hydrogen evolution in the methyl-substituted aromatic hydrocarbons on Si(100) has been discussed in the context of Model II. The simulated TDS profiles and the estimation of the corresponding kinetic parameters (e.g.  $\nu$ ,  $E_a$  and  $n$ ) of this model are in good agreement with our TDS experiments and the results from other groups. Model II involves more complex surface chemistry than Model I, and has been satisfactorily used to simulate the effects of methyl-substituted aromatic-hydrocarbon adsorbates on hydrogen diffusion and desorption on Si(100).

#### **6.4 Model III: hydrogen evolution from the phenyl group - condensation polymerization and the collision theory for 2-dimensional diffusion systems**

In Model I and Model II, the abstraction of hydrogen only involves the smaller functional groups in the adsorbate, such as the vinyl group or the methyl group, while the phenyl group remains intact during annealing. Since hydrogen abstraction in these systems occurs at low temperature prior to the desorption, the maxima of the corresponding TDS profiles occur at a similar temperature (less than 20 K higher) to that for the H/Si(100) sample, which is related to the enthalpy change for the formation of monohydride DOD species on Si(100) (Equation 6.3). However, new desorption phases, with desorption maxima at much higher temperatures than that for the H/Si(100), have been observed in the TDS profiles for

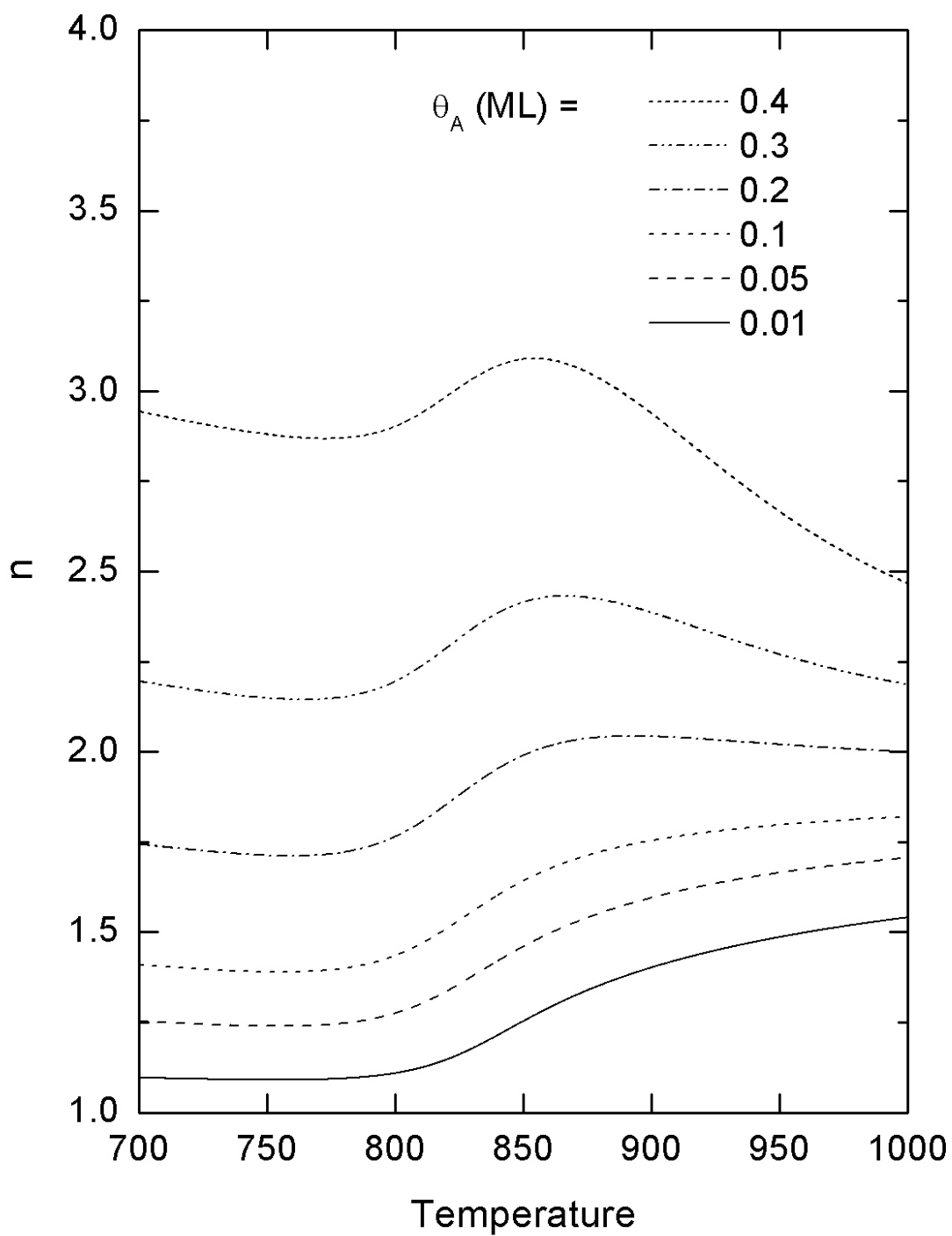


Figure 6-8 Effective order of H<sub>2</sub> Desorption as a function of temperature and initial coverage for *p*-xylene/Si(100).

*p*-xylene-d<sub>10</sub>/Si(100)2×1 (at 980 K in Figure 6-2b) and styrene-ring-d<sub>5</sub>/Si(100)2×1 (at 880 K in Figure 6-2e). In comparison with the TDS profiles for *p*-xylene-d<sub>6</sub>/Si(100)2×1 (Figure 6-2c) and styrene-d<sub>8</sub>/Si(100)2×1 (Figure 6-2d), the TDS maxima of Mass 4 in these phases can be attributed to hydrogen evolution from the phenyl group. Unlike Model I and Model II, hydrogen abstraction from the phenyl group in both styrene/Si(100) and xylene/Si(100) appears to be slower and occurs at a higher temperature than that of hydrogen desorption from monohydride. The abstraction of H from the phenyl group therefore becomes the rate-determining step of the overall hydrogen evolution process.

In the case of thermal chemistry of hydrocarbons on Si(100), hydrogen abstraction and desorption are often considered a signature of decomposition of the hydrocarbon adsorbates, which could lead to formation of SiC and monohydride. For example, the majority of the adsorbed acetylene on Si(100) is found to undergo dissociation producing chemisorbed C and H (that undergoes recombinative desorption as H<sub>2</sub>), in contrast to only less than 5% desorbed molecularly at ~750 K [18]. The observed H<sub>2</sub> desorption occurs at a slightly higher temperature than that from H/ Si(100) surface; while the carbon remaining on the surface begins to diffuse into the bulk above 800 K [18]. Of all the aromatic hydrocarbons studied in the present work, most (except benzene) are also found to undergo partial dissociation as indicated by acetylene (Mass 26 for C<sub>2</sub>H<sub>2</sub> and Mass 28 for C<sub>2</sub>D<sub>2</sub>) and hydrogen desorption in our TDS profiles [2,3,4,5]. A previous STM study on the adsorption of toluene on Si(100) has shown the formation of large carbon clusters (which were thought to be SiC) with size of the order of 100 Å separated by clean areas after annealing for 15 s at 1300 K [19]. However, at such a high temperature, most of the surface carbon atoms should have diffused into the bulk and are unlikely to form such big clusters. In addition, because of the high energy barrier that limits the SiC mobility on the Si(100) surface [20], surface diffusion of SiC would require a temperature higher than 2200 K [21]. These clusters could therefore more likely be large aromatic hydrocarbon species (instead of SiC clusters) formed through thermal diffusion and condensation polymerization of aromatic monomers through adsorbate-adsorbate interaction. This is because unlike small unsaturated organic molecules (e.g. acetylene) that undergo complete decomposition (into C and H), larger aromatic hydrocarbons with more stable structures tend to form larger molecules (clusters), or polynuclear aromatic hydrocarbons (PAH's), with an increased aromatic character [22]. For

instance, biphenyl can be formed by pyrolysis of benzene at 960 K [23], and PAH's such as tetraphenyl could be deposited on the reactor wall at 1120 K [24]. At 1000 K, there should still be a large amount of H atoms remaining on the Si surface. The proposed thermal condensation polymerization of aromatic hydrocarbons is also supported by our previous AES study, which showed that the line shape of the C(KLL) Auger peak for a 100 L RT exposure of toluene on Si(100)2×1 changes from that characteristic of tetrahedrally bonded ( $sp^3$ ) carbon between RT and 700 K to that representative of graphite ( $sp^2$  bonding) [25] upon further annealing to 1100 K for 10 minutes [2]. Furthermore, such thermal enhancement of aromatic character in hydrocarbon cluster is not limited to aromatic adsorbates on Si(100). Another earlier study by our group has shown that a graphite layer is produced upon annealing Si(111) (exposed at RT with a heavy dose of ethylene ions) to 800 K [26].

In Figure 6-3, condensation polymerization was introduced as another channel of hydrogen evolution. We further propose that hydrogen evolution from the phenyl group of the adsorbate (as shown in Figure 6-2b or Figure 6-2e) is due to condensation polymerization. Compared to the TDS profiles for hydrogen desorption from Si(100), the half width of the TDS peak of hydrogen desorption from the phenyl group appears to be broader (150–200 K) than that from H/Si(100) (~100 K), indicating more than one desorption channels with different rate constants. The rate constant depends on both the diffusion energy and the activation energy of condensation polymerization upon collision. Given that the activation energies of the condensation polymerization reactions between the phenyl groups of different molecules are expected to be similar, the differences of activation energies of the diffusion for different adspecies could therefore be used to determine the differences in the reaction rates. Generally, the larger the adsorbate, the lower is its surface mobility and consequently the lower is the rate of condensation polymerization (which corresponding to a higher temperature for the desorption maximum of  $H_2$ ).

In another example shown in Figure 6-9, the temperature of the hydrogen desorption maximum (for 100 L RT exposure of  $d_5$ -pyridine to Si(100)2×1) is found to be elevated from 810 K (without electron irradiation) to 910 K after low-energy electron irradiation (EI) at RT, while the corresponding shapes of the TDS profiles indicate a shift of desorption kinetics from second order to first order or even fractional order. These results suggest that partial

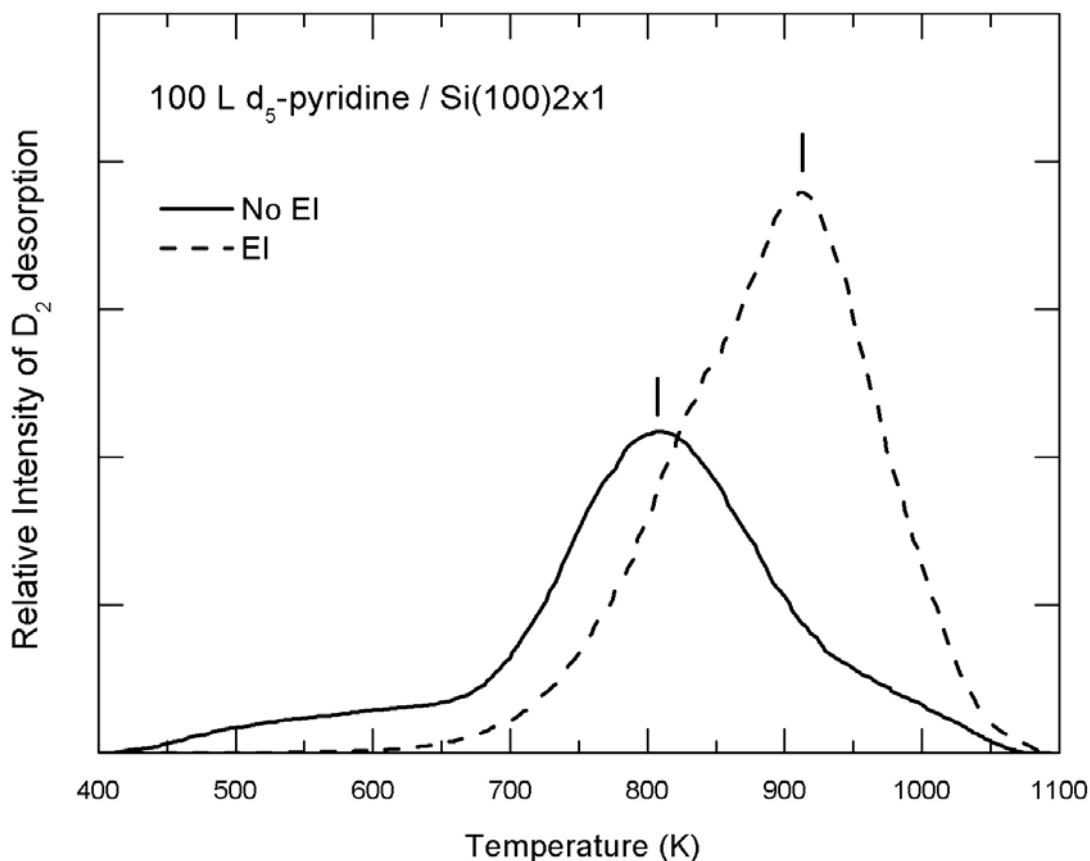
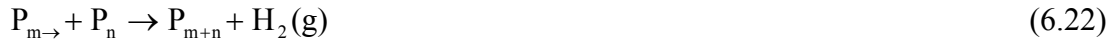


Figure 6-9 Thermal desorption profiles of Mass 4 for 100 L RT exposure of d<sub>5</sub>-pyridine to Si(100)2x1 with and without electron irradiation (EI) at 200 μA and 80 eV for 30 minutes.

condensation oligomerization occurs at RT upon EI, which leads to a different shape of the TDS profile of Mass 4 compared to those without EI [5]. Similar observations of half-order kinetics (instead of the expected second-order kinetics for recombinative desorption) have been previously reported for hydrogen evolution on metal surfaces [27,28] and even on metal-deposited graphite surface [29]. The half-order kinetics strongly suggests that the presence of two-dimensional nucleation of mobile adsorbates and that the rate-determining reaction is localized at the edge of the islands [27].

In order to study the kinetics of condensation polymerization, we introduce a new kinetic model, Model III, which can be used to explain our TDS results in consideration of condensation polymerization of aromatic hydrocarbons on Si(100). Consider a simple

reaction in which an adspecies (monomer or oligomer)  $P_{m \rightarrow}$  diffuses on the surface from its present adsorption site to a neighbouring site. If there is another adspecies  $P_n$  (where  $n$  or  $m$  identify the number of monomer units or the size of the polymer, and the arrow next to  $m$  indicates that  $P_{m \rightarrow}$  is the mobile unit), a collision between the two could occur and may produce a bigger new adspecies  $P_{m+n}$  and gaseous  $H_2$ :



According to collision theory [30], the reaction rate for Reaction 6.22  $r_{m \rightarrow n}$  is determined by the collision density  $Z_{m \rightarrow n}$  (the frequency of collisions between the diffusing particle  $P_{m \rightarrow}$  and its neighbour  $P_n$  per unit area on the surface) and the formation probability,  $e^{-E_a(m,n)/RT}$ , which corresponds to the fraction of collisions that occur with a sufficient kinetic energy along the trajectory direction in excess of the activation energy  $E_a(m,n)$ :

$$r_{m \rightarrow n} = \left. \frac{dH_2}{dt} \right|_{m \rightarrow n} = Z_{m \rightarrow n} \cdot e^{-E_a(m,n)/RT} \quad (6.23)$$

Unlike the system for H atoms on Si(100) based on the two-dimensional gas model, the lateral motion of the chemisorbed hydrocarbons is restricted by diffusion barriers [31]. According to surface diffusion theory [32], when an adspecies “jumps” from one binding site onto another with the required energy obtained from the phonon bath of the substrate, such motion is thus equivalent stochastically to a two-dimensional random-walk with an effective jump frequency  $\nu_{\text{eff}}$  if the adspecies loses its energy rapidly (compared to the periods of the vibrations involving the lateral jumps), [32]:

$$\nu_{\text{eff}} = \nu \cdot e^{-E_d/RT} \quad (6.24)$$

where  $\nu$  is the attempt frequency and  $E_d$  is the energy barrier for diffusion from an adsorption site to its neighbouring site. Assuming that each adspecies occupies one site, a collision occurs between the diffusing  $P_{m \rightarrow}$  and another adspecies  $P_n$  if  $P_{m \rightarrow}$  “jumps” onto the neighbour site occupied by  $P_n$ . The collision frequency  $Z_{m \rightarrow n}$  per available surface site therefore equals to the product of the coverage of  $P_m$  ( $\theta_m$ ), the effective-jump frequency of  $P_m$ , and the probability that  $P_n$  occupies the neighbouring surface site of  $P_m$  [or the coverage of  $P_n$  ( $\theta_n$ )]. The reaction rate for Reaction 6.22 can thus be written as

$$r_{m \rightarrow n} = \theta_m \cdot \theta_n \cdot \nu(m) \cdot e^{-E_d(m)/RT} \cdot e^{-E_a(m,n)/RT} \quad (6.25)$$

As a result, the rate of total hydrogen desorption is given by the sum over all adspecies:

$$\frac{dH_2}{dt} = \sum_{m,n} r_{m \rightarrow n} = \sum_m \theta_m \cdot \nu(m) \cdot e^{-E_d(m)/RT} \cdot \sum_n \theta_n \cdot e^{-E_a(m,n)/RT} \quad (6.26)$$

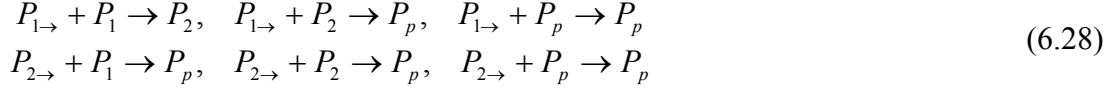
Since there is only one kind of adsorbate monomer in the TDS experiment (by assuming, for simplicity, that only the phenyl group is involved in the condensation polymerization reaction), the activation energy  $E_a(m,n)$  among different collisions can be considered identical. Furthermore, the attempt frequency  $\nu(m)$  should be inversely proportional to the square root of the mass of the adspecies ( $\nu(m) = \nu(1)/\sqrt{m}$ ) [33]. The mobility of any adspecies generally depends on the size of the particle. If the interaction between the adsorbate and the substrate does not change after condensation polymerization, the adsorption energy of  $P_m$  should be approximately proportional to its size  $m$ , and so is the diffusion energy  $E_d(m)$ , which is normally of the order of 1/10 of the binding energy on metal surface and 1/5 to even 1/2 of the binding energy on Si(100) surface ( $\sim m \cdot E_d(1) = m \cdot E_d \sim 4m$  kcal/mol) [34]. Equation 6.26 can therefore be simplified as

$$\begin{aligned} \frac{dH_2}{dt} &= e^{-E_a/RT} \sum_n \theta_n \sum_m \theta_m \cdot \nu(m) \cdot e^{-E_d(m)/RT} \\ &= \sum_m \Theta \cdot \theta_m \cdot \frac{\nu}{\sqrt{m}} \cdot e^{-(m E_d + E_a)/RT} = \sum_m R(m) \end{aligned} \quad (6.27)$$

where  $\Theta (= \sum_n \theta_n)$  is the total coverage of adsorbates on the surface. It is of interest to note that each summand in Equation 6.27 has a form similar to that of first-order thermal desorption (Equation 6.18). Hydrogen evolution can therefore be considered as contributions from different first-order desorption channels  $[R(m)]$ . As a result, the TDS profiles in Model III would be broadened due to multiple desorption channels, which is consistent with our TDS experiments (Figures 6-2e and 6-9).

Since the diffusion factor ( $e^{-E_d(m)/RT}$ ) is about  $(0.044)^m$  assuming  $E_d = 5$  kcal/mol at 800 K (near the temperature of maximum desorption),  $R(2)$  is normally much smaller than  $R(1)$ ,  $R(3)$  is much smaller than  $R(2)$ , and so on. We can therefore further simplify Equation

6.27 by considering only three types of surface species: diffusible monomers ( $P_1$ ) and diffusible dimers ( $P_2$ ) and non-diffusible polymers ( $P_p$ ) for all other adspecies with larger sizes: <sup>6</sup>



Equation 6.27 is further simplified as

$$\begin{aligned} \frac{dH_2}{dt} &= R(1) + R(2) \\ &= (\sigma_1\sigma_1r_{1\rightarrow1} + \sigma_1\sigma_2r_{1\rightarrow2} + \sigma_1\sigma_p r_{1\rightarrow p}) + (\sigma_2\sigma_1r_{2\rightarrow1} + \sigma_2\sigma_2r_{2\rightarrow2} + \sigma_2\sigma_p r_{2\rightarrow p}) \end{aligned} \quad (6.29)$$

where  $\sigma_i$  ( $i=1,2$  and  $p$ ) is the cross section of the adspecies  $P_i$ . This factor is introduced because the bigger adspecies are likely to produce more  $H_2$  than the smaller ones. An ( $i^{1/2}$ ) would be a good estimation of  $\sigma_i$  considering only the edge of the polymer is reactive for further polymerization. If a  $P_i$  collides a  $P_j$  to form  $P_k$ , the numbers of  $P_i$  and  $P_j$  are each reduced by 1 and the number of  $P_k$  will be increased by 1. The coverages of these adspecies are therefore changing during condensation polymerization with the following rates:

$$\begin{aligned} \frac{d\theta_1}{dt} &= -2r_{1\rightarrow1} - r_{1\rightarrow2} - r_{2\rightarrow1} - r_{1\rightarrow p} \\ \frac{d\theta_2}{dt} &= r_{1\rightarrow1} - r_{1\rightarrow2} - r_{2\rightarrow1} - 2r_{2\rightarrow2} - r_{2\rightarrow p} \\ \frac{d\theta_p}{dt} &= r_{1\rightarrow2} + r_{2\rightarrow1} + r_{2\rightarrow2} \end{aligned} \quad (6.30)$$

Given the initial values of  $\theta_1$ ,  $\theta_2$ , and  $\theta_p$ , the entire condensation process for Reaction 6.28 can be simulated numerically with Equation 6.30. After fitting the simulated results with the TDS profiles, the parameters of  $\nu$ ,  $E_a$  and  $E_d$  can be estimated semi-empirically.

---

<sup>6</sup> The average size of the  $P_p$  adspecies ( $p$ ) can be estimated by dividing the total size of the polymer adspecies  $P_p$  with the number of  $P_p$  adspecies:

$$p = \frac{\sum_{m \geq 3} m\theta_m}{\sum_{m \geq 3} \theta_m}$$



Figure 6-10a shows the simulated TDS profiles of hydrogen evolution from the phenyl group obtained by fitting the TDS of Mass 4 ( $D_2$ ) for 5 L RT exposure of styrene-ring- $d_5$  to Si(100). The total desorption includes the contributions involving both the mobile monomers (Figure 6-10b) and the mobile dimers (Figure 6-10c). Assuming the initial conditions (with only monomers):  $\theta_1=0.5$  and  $\theta_2=\theta_p=0$ , the parameters  $\nu$ ,  $E_a$  and  $E_d$  are estimated to be  $7\times 10^5 \text{ s}^{-1}$ , 23 kcal/mol and 4 kcal/mol, respectively. The diffusion energy (4 kcal/mol) estimated here is lower than the general estimation ( $\sim 5.5$  kcal/mol) for diffusion on the surface [13], which is of the order of 1/10 of the desorption energy (55 kcal/mol), because for the system with a high coverage, the effective travel distance to reach the neighbouring site is about half the separation between two neighbouring sites. The activation energy of condensation polymerization (23 kcal/mol) so obtained is about a half of that estimated in the gas-phase for thermal formation of biphenyl from benzene [35], possibly due to the catalytic action provided by the Si(100) surface. The pre-exponential factor ( $7\times 10^5 \text{ s}^{-1}$ ) is found to be much lower than  $\sim 10^{13} \text{ s}^{-1}$  (the benchmark for simple atomic and nondissociative molecular reactions predicted by transition state theory [17]). This result suggests that the transition state for diffusion is constrained such that the adsorbate must take on a highly specific configuration in the activated complex, consistent with the case of surface diffusion.

As a second example, Figure 6-11 shows the simulated TDS profiles of hydrogen evolution for pyridine/Si(100) with and without RT electron irradiation (EI) obtained by using a similar method. For the TDS profile obtained without EI, the initial conditions with only monomers are  $\theta_1=0.4$  and  $\theta_2=\theta_p=0$ ; while for the TDS profiles with EI, the initial conditions with only dimers are  $\theta_2=0.2$  and  $\theta_1=\theta_p=0$ .  $\nu$ ,  $E_a$  and  $E_d$  are estimated to be  $2\times 10^7 \text{ s}^{-1}$ , 27 kcal/mol and 3.5 kcal/mol, respectively. The amount of  $\theta_2$  for the case with EI indicates that dimers could be produced during RT electron irradiation on pyridine/Si(100) (the desorption feature at 810 K is the desorption from monohydride with the H atoms produced during EI). This result is consistent with our previous proposal of the RT electron-induced oligomerization of pyridine on Si(100) [2].

Although the TDS profile for *p*-xylene- $d_{10}$  as shown in Figure 6-2b is too weak for simulation, it is possible to estimate its kinetic parameters from those obtained for styrene and pyridine. If the values of the activation energy ( $E_a$ ) and pre-exponential factor ( $\nu$ ) for

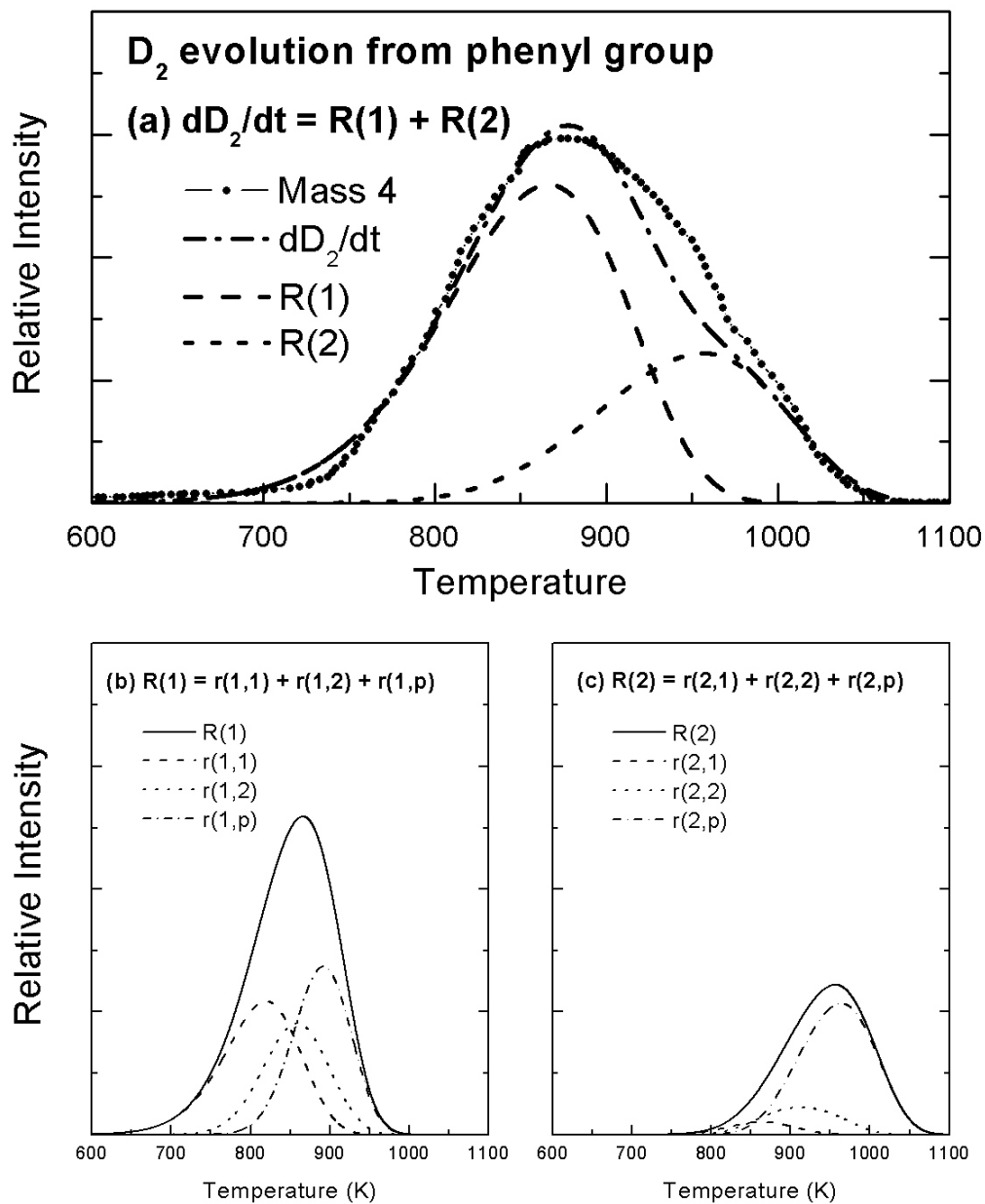


Figure 6-10 Experimental and fitted TDS profiles of D<sub>2</sub> desorption from the condensation of the phenyl groups for styrene-ring-d<sub>5</sub>/Si(100)2×1. (a) The total desorption includes the contributions involving the mobile monomers (b) and the mobile dimers (c). [Note:  $r(i,j) = \sigma_i \sigma_j r_{i \rightarrow j}$  ( $i,j = 1, 2, \text{ or } p$ )]

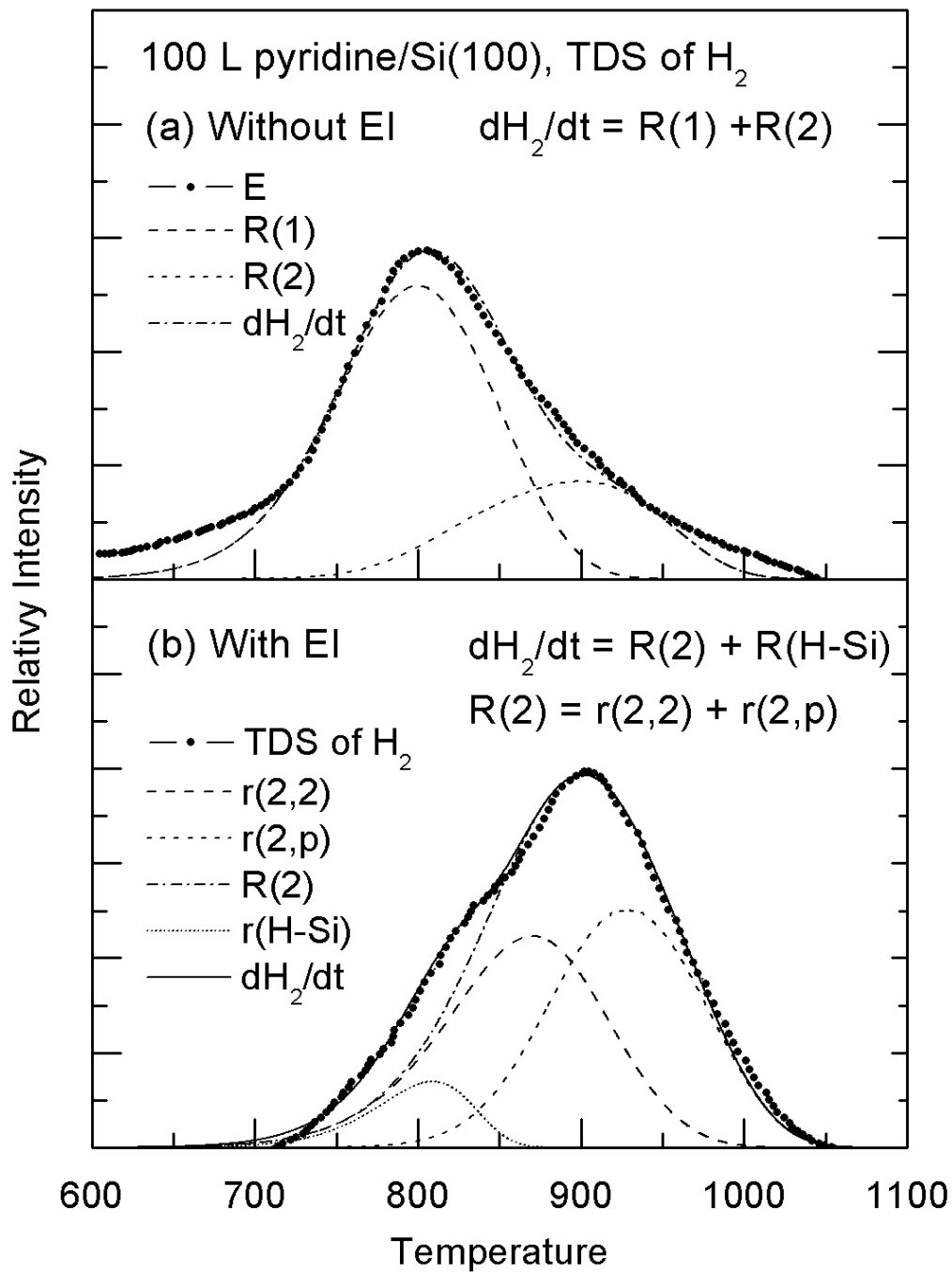


Figure 6-11 Experimental and fitted TDS profiles of H<sub>2</sub> from the condensation of phenyl groups for pyridine/Si(100)2×1. [Note:  $r(i,j) = \sigma_i \sigma_j r_{i \rightarrow j}$  ( $i,j = 1, 2, \text{ or } p$ )]

*p*-xylene are assumed to be similar to those for styrene and pyridine (due to the similar collision process between the phenyl groups), the diffusion energy ( $E_d$ ) of *p*-xylene on Si(100) can be estimated to be 9 kcal/mol which is double the value of those for styrene and pyridine. This can be understood in terms of the stronger bonding of *p*-xylene/Si(100) and/or the steric effect induced by the methyl group.

To date, the inclusion of condensation polymerization in Model III has been used to satisfactorily explain the thermal evolution of hydrogen from the phenyl group for styrene, pyridine and *p*-xylene (and/or toluene) on Si(100) surface. It could also be applied to condensation polymerization processes for other molecules on different surfaces. The development of collision theory for the diffusion system can also be generalized to both 2-dimensional (surface) and 3-dimensional (solid) crystal systems.

## 6.5 Summary

In this Chapter, we review the common process of hydrogen evolution found on Si(100) $2\times 1$  for all of the aromatic hydrocarbons studied in the present work. With reference to the kinetics of hydrogen thermal desorption on H/Si(100), three kinetic models are developed for our TDS profiles of different hydrocarbon adsorbates on Si(100). In the first two models, hydrogen abstraction involves only adsorbate-substrate interaction, and the diffusion of H atoms on the Si surface is faster than the recombination desorption from the monohydride phase. The monohydride state is thermodynamically favoured in Model I, and the behaviour of hydrogen evolution is similar to that in the H-Si(100) system, underlying the nearly first-order desorption mechanism. In Model II, the monohydride DOD phase is no longer thermodynamically favourable, and consequently the order of hydrogen evolution appears to be higher than 2. In order to analyse hydrogen evolution from the phenyl groups, the mechanism for the adsorbate-adsorbate interaction, or condensation polymerization, is studied with Model III. This model provides a new method for studying important kinetic parameters in surface chemistry (such as the activation energy, diffusion energy, and pre-exponential factor) semi-empirically with the corresponding TDS profiles. Hydrogen evolution has therefore provided an important process for us to probe the nature of organic surface chemistry. In contrast to that for a normal gas-phase chemical reaction, a new

collision theory based primarily on a two-dimensional diffusion system has been demonstrated in its application to the study of surfaces. In the future, this work may also be extended to the three-dimensional diffusion systems.

## 6.6 References

- [1] K. Christmann, Surf. Sci. Rep. 9 (1988) 1.
- [2] Q. Li, K.T. Leung, Surf. Sci. 479 (2001) 69. See also Chapter 2.
- [3] Q. Li, K.T. Leung, submitted to Surf. Sci. See also Chapter 3.
- [4] Q. Li, K.T. Leung, submitted to Surf. Sci. See also Chapter 4.
- [5] Q. Li, K.T. Leung, Surf. Sci. 541 (2003) 111. See also Chapter 5.
- [6] J.A. Schaefer, Physica B 170 (1991) 45.
- [7] J.J. Boland, Adv. Phys. 42 (1993)129.
- [8] K. Oura, V.G. Lifshits, A.A. Saranin, A.V. Zotov, M. Katayama, Surface Science Reports 35 (1999) 1.
- [9] V.G. Lifshits, A.A. Saranin, A.V. Zotov, "Surface Phases on Silicon", Wiley, Chichester, 1994.
- [10] Y.J. Chabal, K. Raghavachari, Phys. Rev. Lett. 54 (1985) 1055.
- [11] M.P. D'Evelyn, Y.L. Yang, L.F. Sutcu, J. Chem. Phys. 96 (1992) 852.
- [12] M.P. Schwartz, M.D. Ellison, S.K. Coulter, J.S. Hovis, R.J. Hamers, J. Am. Chem. Soc. 122 (2000) 8529.
- [13] M.L. Wise, B.G. Koehler, P.Gupta, P.A. Coon, S.M. George, Surf. Sci. 258 (1991) 166.
- [14] Abramowitz, M. and Stegun, I. A. (Eds.). "Handbook of Mathematical Functions with Formulas, Graphs, and Mathematical Tables, 9th printing". New York: Dover, p. 13, 1972.
- [15] U. Hofer, L. Li, T.F. Heinz, Phys. Rev. B 45 (1992) 9485.
- [16] S.K. Coulter, J.S. Hovis, M.D. Ellison, R.J. Hamers, J. Vac. Sci. Technol. A 18 (2000) 1965.
- [17] P.A. Redhead, Vacuum 12 (1962) 203.
- [18] P.A. Taylor, R.M. Wallace, C.C. Cheng, W.H. Weinberg, M.J. Dresser, W.J. Choyke, and J.T. Yates, Jr., J. Am. Chem. Soc. 114 (1992) 6754.
- [19] B. Borovsky, M. Krueger, E. Ganz, J. Vac. Sci. Technol. B 17 (1999) 7.
- [20] G. Cicero, A. Catellani, Applied Surface Science 184 (2001) 113.
- [21] K. Motzfeldt, M. Steinmo, Int. Harald A. Oeye Symp. (1995) 279.

- [22] N.M. Marinov, W.J. Pitz, C.K. Westbrook, M.J. Castaldi, S.M. Senkan, *Combust. Sci. and Tech.* 116-117 (1996) 211, and therein.
- [23] E.K. Fields, S. Meyerson, *J. Am. Chem. Soc.* 88 (1966) 21.
- [24] J. Lahaye, H.B. Palmer, R.K. Sharma, *Carbon* 6 (1968) 419.
- [25] A.K. Green, V. Rehn, *J. Vac. Sci. Technol. A* 1 (1983) 1877 and references therein.
- [26] H. Yu, K.T. Leung, *Surf. Sci.* 432 (1999) 245.
- [27] L. Chan, G.L. Griffin, *Surf. Sci.* 145 (1984) 185.
- [28] F. Healey, R.N. Carter, A. Hodgson, *Surf. Sci.* 328 (1995) 67.
- [29] J.R. Arthur, A.Y. Cho, *Surf. Sci.* 36 (1973) 641.
- [30] P. Atkins, "Physical Chemistry", 5th ed. (New York: Freeman, 1994)
- [31] K.W. Kolasinski, "Surface Science: Foundations of Catalysis and Nanoscience", John Wiley & Sons Ltd., Chichester, West Sussex, England (2002).
- [32] R. Gomer, *Rep. Prog. Phys.* 53 (1990) 917.
- [33] N.W. McLachlan, "Theory of Vibrations", Dover Publications, Inc., New York, 1951.
- [34] K. Christmann, "Introduction to Surface Physical Chemistry", Steinkopff, Darmstadt, (1991).
- [35] K.C. Hou, H.B. Palmer, *J. Phys. Chem.* 69 (1965) 863.





## Chapter 7

### Concluding remarks and future outlook

Room-temperature (RT) chemisorption of prototypical aromatic hydrocarbons (benzene, toluene, xylene isomers, styrene and pyridine) on the 2×1, sputtered, oxidized and H-terminated Si(100) surfaces, as well as the post-treatments with electron-irradiation, oxidization and hydrogenation have been studied by using TDS, AES and LEED. The present work has surprisingly revealed high reactivity of the functional groups (phenyl, methyl, vinyl, heteroatom and H atom) in various surface processes, including cycloaddition, dative adsorption, hydrogen abstraction, desorption, dissociation, diffusion, and condensation polymerization. Table 7-1 summarizes the observed involvements (with a symbol “√”) of these functional groups in different surface processes. In particular, benzene, toluene and xylene isomers are found to adsorb on Si(100) by the way of [4+2] cycloaddition (between

Table 7-1 Summary of the involvement of functional groups in different surface processes:

	Phenyl	Methyl	Vinyl	Heteroatom*	H
Cycloaddition	√		√		
Dative bonding				√	
Hydrogen abstraction		√	√		√
Desorption	√		√		√
Diffusion	√				√
Dissociation	√	√	√	√	√
Condensation polymerization	√				√

\* Pyridine is the only hetero-cyclic hydrocarbon used in the present work, and the heteroatom here is N atom.

the phenyl group and the Si dimer), while pyridine appears to have two competitive adsorption channels involving N-Si dative bonding and the [4+2] cycloaddition. The [4+2] structure may then convert to a more elaborate (and more stable) configuration involving two neighboring dimers in the same dimer row. The chemisorption of styrene is found to occur primarily with [2+2] cycloaddition through the vinyl group, with only 15% involving the phenyl [4+2] cycloaddition and/or double-dimer adsorption. Among the three types of adsorption, the vinyl [2+2] cycloaddition is observed to be stronger than the phenyl adsorption, while the dative N-Si bonding appears to be stronger than both cycloaddition phases. All three adsorption processes have little effects on the  $2\times 1$  structure of Si(100), suggesting that the adsorbed organic molecules are regulated in a well-ordered arrangement on the template provided by the Si(100) $2\times 1$  surface. The methyl and vinyl groups are found to have considerable influence on hydrogen abstraction, which stabilizes the adsorbate (on the surface) against thermal desorption and enables the adsorbed hydrocarbons to undergo further surface chemical processes (including fragmentation, hydrogen evolution, diffusion, and condensation polymerization) at higher temperatures.

Three types of hydrogen evolution are found in the TDS profiles. By using three kinetics models developed in the present work in combination with our TDS data, we demonstrate that hydrogen evolution from the vinyl group in styrene follows the nearly first-order kinetics similar to that for the H/Si(100) system with hydrogen diffusion and desorption independent of the coadsorbed hydrocarbons, while hydrogen evolution from the methyl group is affected by the methyl group and exhibits a higher order kinetics. Furthermore, hydrogen evolution from the phenyl group occurring at a much higher temperature could be successfully explained by the model involving condensation polymerization in a 2-dimensional system. In this model, a new collision theory for the 2-dimensional diffusion system has been developed with the combination of the traditional gas-phase collision theory and the diffusion theory for the crystal surface. The activation energy of the reaction in such type of systems consists of contributions from both associative collision and diffusion.

In the early studies of the hydrocarbon/Si(100) systems, hydrogen evolution has generally been considered as evidence for the dissociation of the adsorbates into smaller

hydrocarbon fragments and H atoms. The present TDS work, on the other hand, suggests the plausibility of condensation polymerization (along with hydrogen evolution during annealing) in toluene/Si(100) for the first time. Moreover, evidence of electron-induced condensation oligomerization has also been observed in pyridine/Si(100) at RT for the first time. This result is supported by the presence of a new hydrogen-evolution feature at a higher temperature and the surprising recurrence of molecular desorption in the second-run TDS experiment. Similar phenomena have also been observed in the TDS profiles for other molecules. We further propose that condensation polymerization could occur via diffusion and could involve interactions among the phenyl groups of the aromatic-hydrocarbon adsorbates on Si(100). These results are consistent with our semi-empirical studies based on the new developed kinetics model in this work. Our hypothesis of condensation polymerization has also been confirmed recently by Costanzo *et al.*<sup>†</sup> in a quantum-computational study of toluene/Si(100) based on the density functional theory.

On the Ar<sup>+</sup>-sputtered Si surface, molecular desorption with a lower adsorption energy and desorption of smaller hydrocarbon fragments at a higher temperature have been observed. On the other hand, pre-adsorbed O and H atoms are found to passivate the Si(100) surface, making the surface inert to molecular adsorption (except in the case of pyridine which is found to undergo dissociation). Post-exposure treatments have also been performed on the aromatic hydrocarbons adsorbed on Si(100). In particular, the unexpected TDS features of styrene, benzene and ethylene at 700-750 K for the styrene/Si(100) with post-exposure of atomic hydrogen have provided the first observation of surface-mediated organic chemistry driven by thermal diffusion and desorption of hydrogen. This result shows that hydrogen could be used to manipulate the outcome of different chemical processes on the modified Si(100) surfaces. Various surface processes have been found to be influenced by post-oxidization, hydrogenation and electron irradiation but not by post-UV light irradiation, suggesting that the mechanisms of these surface processes are more “chemical” (chemical bonding affected) rather than “physical” (electrical structure affected) in nature.

---

<sup>†</sup> F. Costanzo, C. Sbraccia, P.L. Silvestrelli, F. Ancilotto, J. Phys. Chem. B 107 (2003) 10209.

As one of the earliest methods used for investigating chemisorption on surfaces and with new advantages of the TDS technique explored in the present work, TDS has remained to be unparalleled in providing information about the thermal chemistry on surface. The “second-run TDS” and the multiple-ion-monitoring methods, respectively, have enable us to identify RT electron-induced oligomerization of pyridine on Si(100) and to differentiate (in the styrene/Si(100) system) the surface phase of alternating-monohydride-dihydride (with a  $3\times 1$  structure) from those of monohydride (with a  $2\times 1$  structure) and dihydride (with a  $1\times 1$  structure) for the first time.

The AES method has also been employed in a more quantitative fashion in the present work than previously used in this laboratory. In particular, a more accurate method for determining elemental adsorption coverage has been developed. The molecular adsorption coverage could be evaluated by comparing the elemental coverage of the detected adspecies with that of a standard hydrocarbon whose molecular adsorption coverage is known. Based on the Langmuir adsorption system, a means for estimating the reaction order and the rate constant of adsorption (obtained from a series of AES spectra for different exposures) has also been devised.

Along with these improvements in both the TDS and AES techniques, quantum computational techniques have also been used to study the surface chemistry of aromatic hydrocarbons on Si(100). The adsorption geometries and their corresponding adsorption energies have been calculated for a simulated model surface of a Si-H cluster by using the density functional theory with the Gaussian 98 program. The calculated results are found to be quite useful in providing a qualitative picture of the chemisorption process.

The present work seeks a better understanding of organic functionalization of Si(100) surfaces, with the ultimate goal to develop hybrid devices exploiting the intricate properties of both organic and inorganic materials. Specific challenges remain and they include:

- Improvement of the present experimental system for a more comprehensive study on the physical chemistry of organic semiconductors;
- Further study of organic functionalization of semiconductors involving other functional groups (e.g. heteroatom, halogen) and more complex hydrocarbons (e.g. oligomers);

- Extension of organic functionalization on the surface to the more practical multilayer system.
- Completion and extension of the kinetics theories developed in this work to the surface chemistry on metals.

The present experimental system has been furnished recently with an X-ray photoelectron spectrometer in order to provide the much needed chemical-state analysis of the species remaining on the surface during and after thermal desorption. Further studies by using more structural-sensitive techniques (e.g. STM and FTIR) could also be of great interest. The study of larger aromatic molecules (e.g. naphthalene and biphenyl), smaller aromatic heterocyclic molecules (e.g. pyrrole, thiophene and furan), and halogen-substituted aromatic hydrocarbons, and their surface chemistries on Si(100) and other semiconductor surfaces [e.g. Si(111) and Ge(100)] is of particular interest not only for extending the present data base but also for verifying the generality of some of the surface reactions found in the present work. Moreover, application of the monolayer organic functionalization (e.g. surface-mediated condensation polymerization) to the industrial synthesis of organic semiconductors requires better understandings in the mechanisms for depositing multiple organic layers in a controllable fashion. In order to enable the next-layer adsorption, a bifunctional or polyfunctional organic adsorbate may be needed for the first layer. This layer, in turn, may retain a reactive functional group to facilitate further adsorption.‡ The collision theory of 2-dimensional diffusion system developed for analysing condensation polymerization could also be extended for study of surface chemistries on metals. Given that diffusion is more common on the metal surfaces, and that the diffusion theory was initially used to study the migration of adspecies across the metal surface, it should be of interest to reapply the kinetics theory to surface-mediated chemistries on metal. The present work has only touched upon very limited aspects of the wonders of organosilicon surface chemistry, with much of its powers and beauty remained unexplored.

---

‡ T. Bitzer, N.V. Richardson, Surf. Sci. 144 (1999) 339.



## Appendix A

### Study of adsorption by Auger Electron Spectroscopy

In the present study, Auger electron spectroscopy (AES) is used to estimate not only the surface concentration of the adsorbate (and the surface contamination) but also the kinetic parameters of adsorption, including saturation coverage, the rate constants and the order of the chemisorption.

In this Appendix, we will discuss the common problems of conventional AES methods used to estimate the elemental coverage of surface species, and propose an effective solution for the surface-adsorption system. We will also discuss how to obtain the molecular adsorption coverage from the elemental coverage. In the last part, we will introduce a new method to estimate the rate constant and order of reaction for the adsorption process from molecular coverages obtained for different exposures.

#### A.1 Estimation of elemental adsorption coverage: A better method based on the model of binary monolayer adsorption system

Figure A-1a presents a schematic picture for a monolayer-adsorption system. For a high energy electron beam impinging on the surface, AES signals from the adsorbate (A) and substrate (S) can be obtained. The signal intensity of each element is proportional to its concentration. For example, the AES intensity ( $I_A$ ) of the adsorbate A is given by

$$I_A = S_A \cdot X_A \quad (\text{A.1})$$

where  $X_A$  is the concentration of A and  $S_A$  is the sensitivity factor for a particular Auger transition of element A. Assuming the saturation coverage of A is 1, the coverage of A can therefore be obtained by

$$\theta_A = X_A / X_{A,0} = I_A / I_{A,0} \quad (\text{A.2})$$

where the subscript 0 is used to denote saturation coverage.

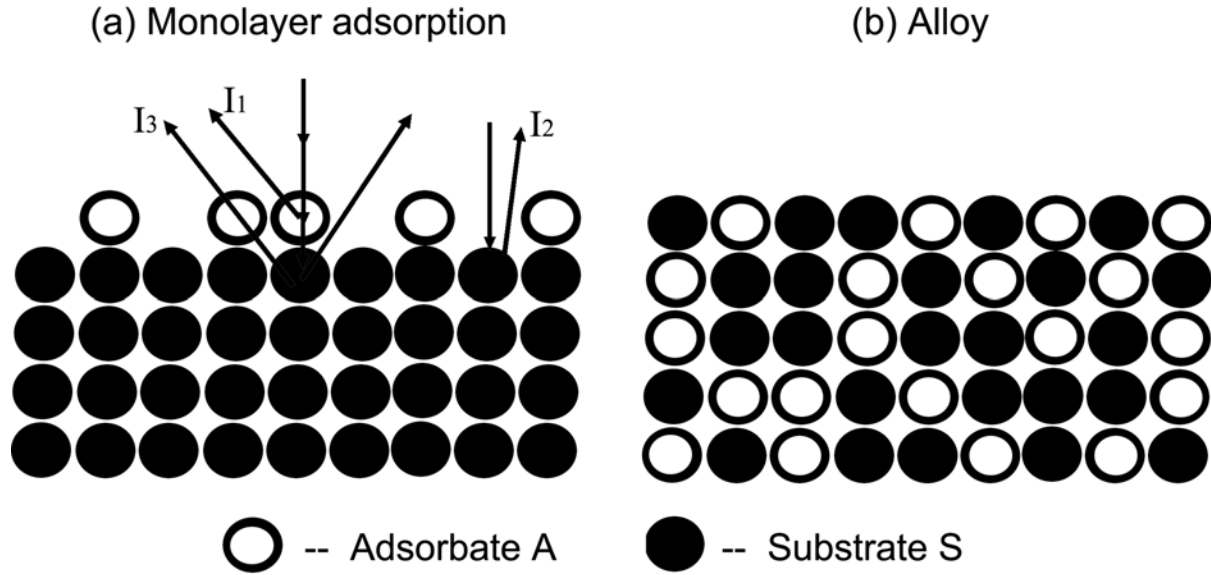


Figure A-1 Schematics of AES electron and detection models for surface concentration determination.

Due to the difference often encountered in the experimental conditions, the sensitivity factor  $S$  for a given element of the target may not be constant for different AES experiments. The absolute AES intensity therefore cannot be used to directly provide the concentration of the element of interest. However, the relative intensities of the corresponding AES signals among different elements should remain constant. For instance, since the ratio of the concentrations of two elements ( $X_A:X_B$ ) in a given sample is a constant, the ratio of their corresponding intensities ( $I_A/I_B$ ) obtained in an AES experiment should remain unchanged among different AES experiments. Consequently, for the surface of a binary A–S system  $I_A/I_S$  has been used to estimate the monolayer concentration of adsorbate A in many AES experiments (Method 1) [1,2,3], and the estimated coverage of A is given by

$$\theta_A = \frac{X_A}{X_{A,0}} = \frac{(I_A/I_S)}{(I_{A,0}/I_{S,0})} = \frac{I_A}{I_{A,0}} \cdot \frac{I_{S,0}}{I_S} \quad (\text{A.3})$$

where  $X_{A,0}$  is the saturation concentration of A, while  $I_{A,0}$  and  $I_{S,0}$  are the AES intensities of the A and S respectively for saturation adsorption of A. It should be noted that this method has assumed that the effect of adsorbate coverage on the signal of the substrate is negligible,



because the AES signal of the substrate element S is generally much stronger than that of the adsorbate element A and can be approximately treated as a constant especially for very low adsorbate coverages. However, in our AES experiment, the coverage of hydrocarbons on the Si surface is found to reduce the intensity of the Si LVV AES signal, and such influence appears to be even stronger at low coverages. For example, the AES intensity for the substrate Si for the Si(100) surface with a saturation coverage of pyridine is found to be about 2/3 of that for a clean Si(100) surface (Figure A-2). This can be understood by the fact that the sensitivity factor (S) of the substrate varies with depth, and the signal for the atoms in the sublayers is weaker than those of the same element in the top layer (due to the attenuation along the electron mean free path). Because  $I_{S,0}$  is normally lower than  $I_S$ , an underestimation of adsorbate coverage ( $\theta_A$ ) will result in Method 1 (Equation A.3).

In order to take into account of the effect of the adsorbate coverage on the AES intensity of the substrate, another method (Method 2) is employed in which

$$X_A = \frac{I_A/S_A}{I_A/S_A + I_S/S_S} \quad (\text{A.4})$$

where the sum in the denominator is the total amount of the constituents in the solid. This equation is used in the quantification routines available in many commercial AES or XPS [4]. This method works best for binary alloy materials (Figure A-1b), where the adsorbate atoms A are evenly distributed in the bulk of S. For a surface system, however, the underestimation of adsorbate coverage is not totally eliminated in Method 2.

For the monolayer adsorption system shown in Figure A-1a (Method 3), there are different AES sensitivities: one for adsorbate A and two for substrate S. Because A only appears in the top layer, the AES intensity for A ( $I_A$ ) is proportional to the coverage of A ( $\theta_A$ ), as given by

$$I_A = k_A \cdot \theta_A \quad (\text{A.5})$$

where  $k_A$  is the coverage-dependent AES sensitivity factor of A. The AES intensity of the substrate S should have contributions from the S atoms covered by A (proportional to  $\theta_A$ ) and from bare S atoms on the surface [proportional to  $(1-\theta_A)$ ], i.e.

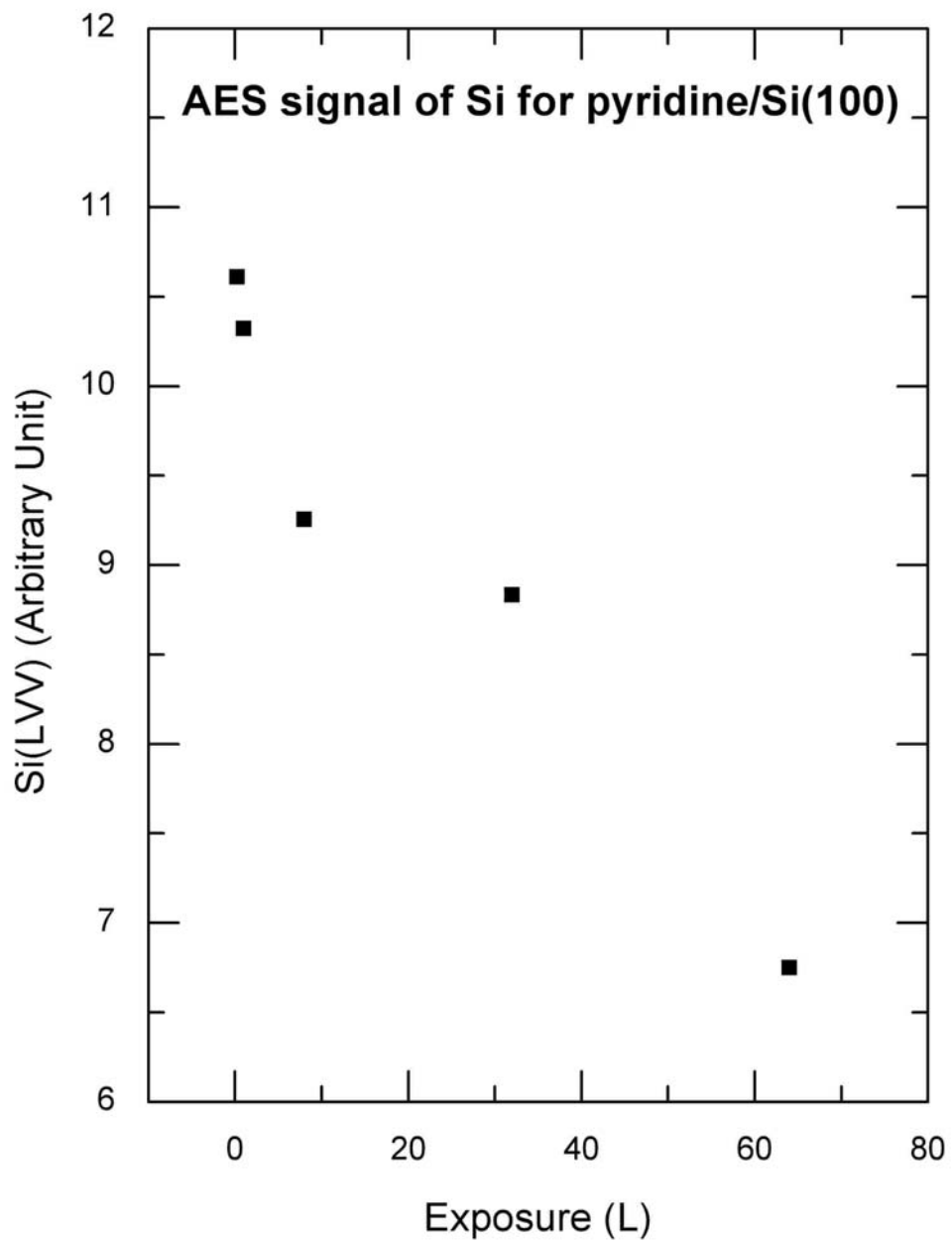


Figure A-2 AES signal for Si(LVV) at different exposures of pyridine to Si(100) surface, with a primary energy of 1500 eV.

$$I_S = k_S \cdot (1 - \theta_A) + k'_S \cdot \theta_A \quad (\text{A.6})$$

where  $k_S$  and  $k'_S$  are the AES sensitivity factors for the bare and the A-covered substrate S atoms respectively. The three sensitivity factors can be obtained from the AES spectra for the clean Si(100) surface ( $\theta_A = 0$ ) and for the Si(100) surface saturated with the adsorbate ( $\theta_A = 1$ ):

$$\begin{aligned} k_A &= I_A \Big|_{\theta_A=1} \\ k_S &= I_S \Big|_{\theta_A=0} \\ k'_S &= I_S \Big|_{\theta_A=1} \end{aligned} \quad (\text{A.7})$$

For a given A-S system, these values may change in different AES scans due to different intensities of the incident electron beam in different experiments, but the ratio among the values obtained under the same conditions (e.g.  $k_A/k_S$ ,  $k_A/k'_S$ ) should remain constant. As a result, these ratios are defined by

$$\begin{aligned} I &= I_S / I_A \\ k &= k_S / k_A \\ k' &= k'_S / k_A \end{aligned} \quad (\text{A.8})$$

where  $k$  and  $k'$  are the constants independent of experimental conditions, and can be obtained from AES intensities in the same experimental conditions by using Equation A.7.

Combining Equation A.8 with Equations A.5 and A.6, we obtain

$$\theta_A = \frac{k}{k - k' + I} \quad (\text{A.9})$$

Equation A.9 gives a more accurate expression for the adsorbate coverage  $\theta_A$  as a function of the relative AES intensity  $I (=I_S/I_A)$ .

If  $k' \rightarrow k$  (i.e., the adsorbate has no effect on AES intensity of the substrate), Equation A.9 is reduced to  $\theta_A = k(I_A/I_S)$ , corresponding to the result in Method 1. On the other hand, if  $k' \rightarrow 0$  (i.e., the overlayer of adsorbate totally blocks the AES of the substrate), Equation A.9 is reduced to  $\theta_A = \frac{kI_A}{kI_A + I_S}$ , corresponding to the alloy case considered in Method 2.

Figure A-3 compares the coverages estimated with Method 1, 2 and 3. The  $\theta_A$  values estimated in Method 1 and 2 are found to be lower than that of Method 3, especially when  $\theta$  is low. This deviation may not degrade the estimation on saturation coverages, but will create errors for the low-coverage estimation obtained by Method 1 and 2 and may therefore induce errors in estimating the rate constant and reaction order (which will be presented in section A.3).

In summary, the AES method based on Method 3 is found to be more reasonable than the usual methods based on Method 1 and 2 for estimating the adsorption coverage for a monolayer adsorption system.

## A.2 Estimation of molecular adsorption coverage for hydrocarbon/Si(100)

For the hydrocarbon/Si(100) systems, the C KLL (at 270 eV) and Si LVV (at 90 eV) are the only features in the AES spectra. Method 3 is therefore used to estimate the C coverage  $\theta_C$  for binary adsorption system. However,  $\theta_C$  obtained in Method 3 corresponds only to the coverage relative to the saturation coverage (Equation A.2) of a specific hydrocarbon molecule. In order to make it comparable among different molecules, we need to obtain the molecular adsorption coverage (number of adsorbate molecules per substrate site) by comparing the AES intensities with those for a standard molecule (a molecule with an molecular adsorption coverage that is determined separately, e.g.  $\theta = 0.5$  for ethylene and  $\theta = 0.27$  for benzene [1]):

$$\theta = \left( \frac{n_c^0}{n_c} \right) \left( \frac{I_c}{I_c^0} \right) \cdot \theta^0 \quad (\text{A.10})$$

where  $\theta$  and  $\theta^0$  are the coverages for the test molecule and the standard molecule, respectively;  $I_c$  and  $I_c^0$  are the corresponding carbon coverages derived from AES;  $n_c$  and  $n_c^0$  denote the numbers of carbon atoms in the test molecule and the standard molecule, respectively.

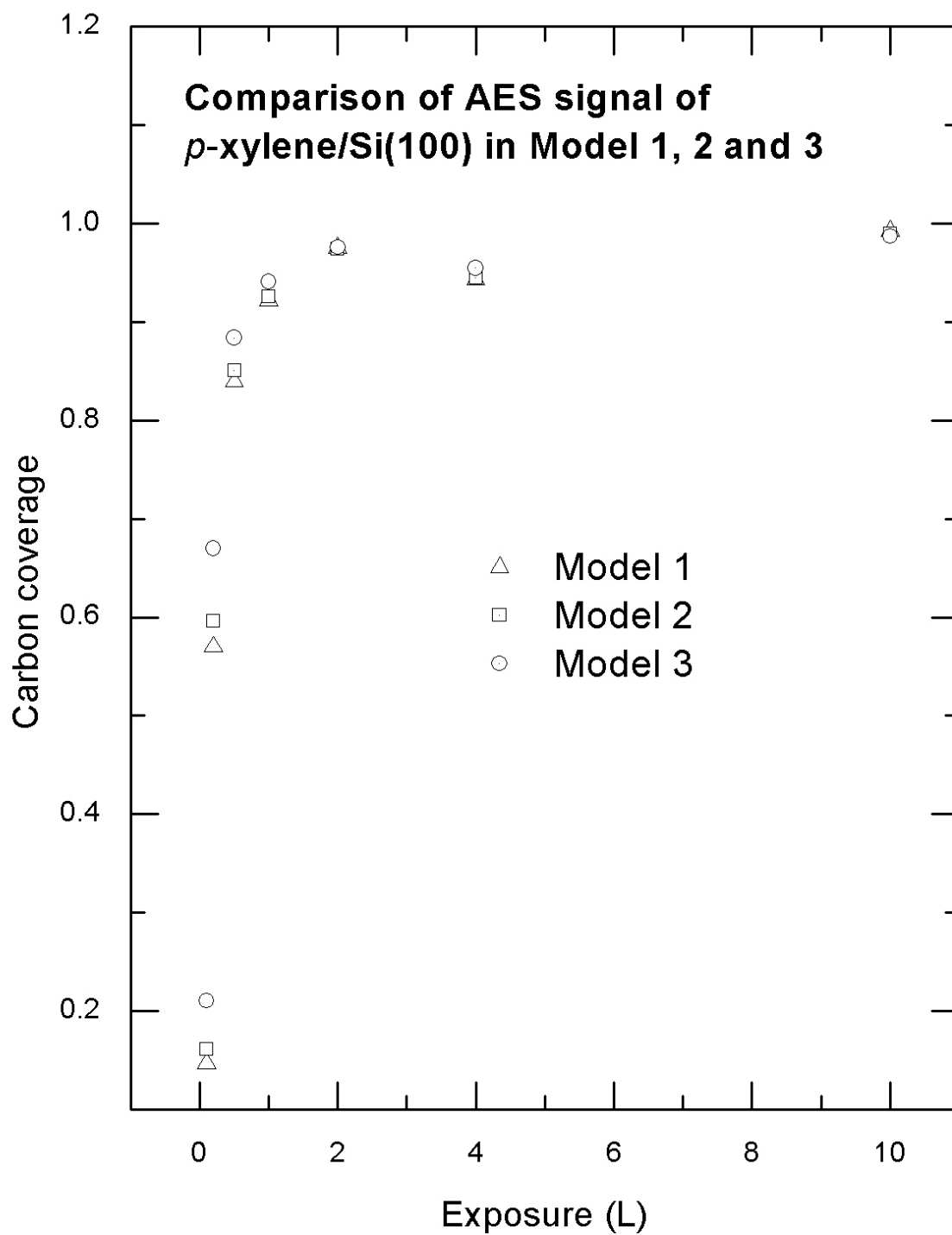


Figure A-3 Comparison of carbon coverages obtained by the three AES methods.

For example, the saturation coverage of benzene has been estimated to be 0.27 ML by Taguchi *et al.* [1]. From the ratios of saturation coverages of C for pyridine relative to benzene (1.5, obtained from the AES as described in A.1) and after taking into account the numbers of carbon atoms in pyridine (5) and benzene (6), we determine the saturation coverage for pyridine to be 0.41 ML (=0.27×6×1.5/5).

### A.3 Estimation of kinetic parameters for surface adsorption

If a surface is exposed to a gaseous chemical, the adsorption rate will be proportional to the pressure  $P$  (which is proportional to the number of molecules that hit the surface in unit area within unit period), and to the coverage of the available adsorption sites  $\theta_s$  (first-order molecular adsorption) or the square of  $\theta_s$  (second-order dissociative adsorption):

$$\frac{d\theta_A}{dt} = kP\theta_s^n = kP(1 - \theta_A)^n \quad (\text{A.11})$$

where  $\theta_A$  is the coverage of adsorbate (number of covered sites / number of total surface sites),  $(1-\theta_A)$  is the available adsorption coverage,  $k$  is the rate constant, and  $n$  is the reaction order of adsorption process. Equation A.11 is revised so that differential variables ( $\theta_A$  and  $t$ ) are separated on the two sides of the equation:

$$\frac{d\theta_A}{(1 - \theta_A)^n} = kP \cdot dt = k \cdot d\Lambda \quad (\text{A.12})$$

where the exposure of the adsorbate to the surface  $\Lambda (= P\Delta t)$  is defined as a quantity of molecular bombardment on the surface by the gaseous molecules. For first-order adsorption ( $n = 1$ ), the solution of Equation A.12 is given by

$$\theta_A = 1 - e^{-k\Lambda} \quad (\text{A.13})$$

For second-order adsorption ( $n=2$ ), the solution of Equation A.12 is given by

$$\theta = \frac{k\Lambda}{1 + k\Lambda} \quad (\text{A.14})$$

### AES analysis on *p*-xylene / Si(100)

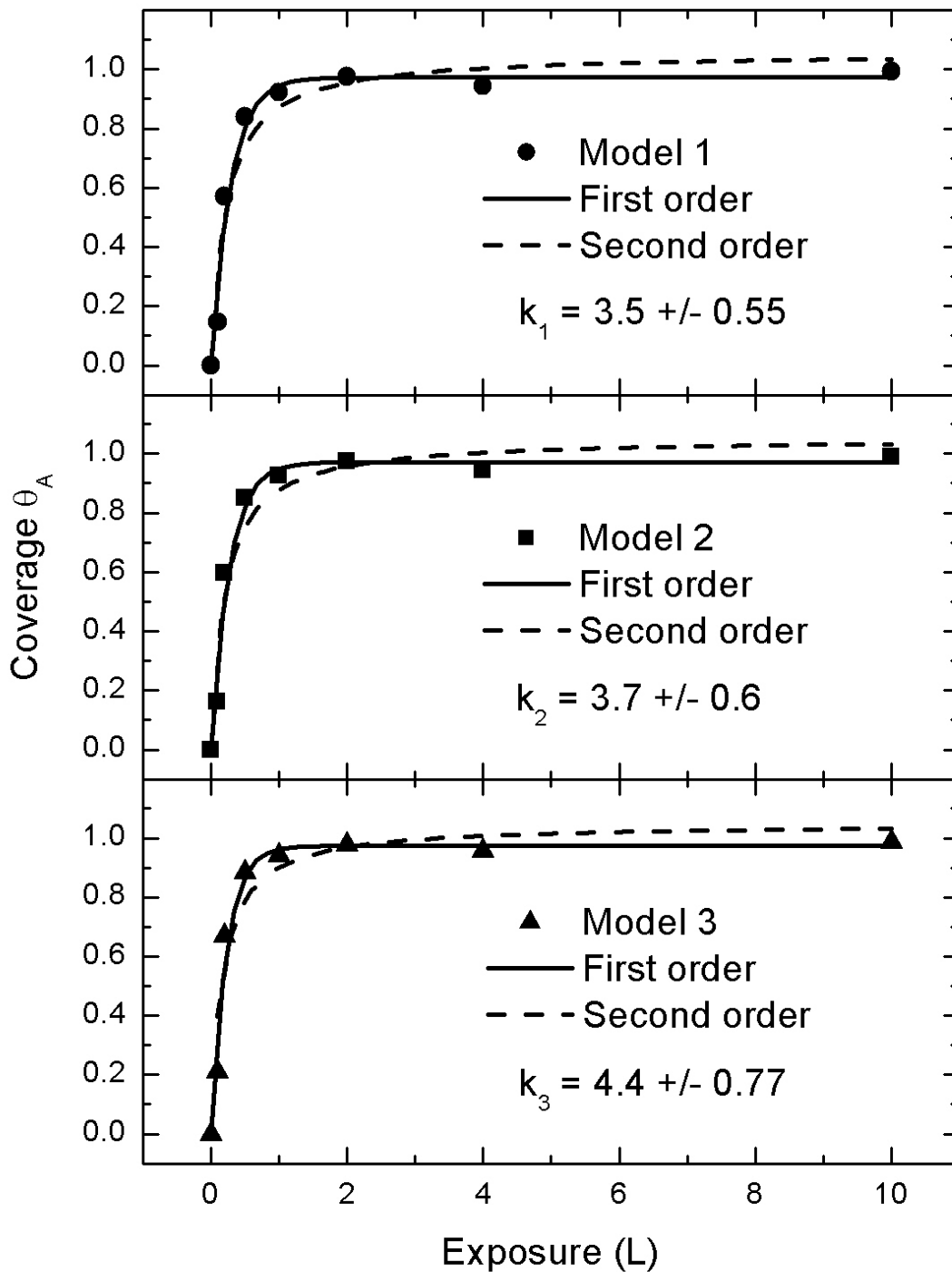


Figure A-4 Comparison of coverages fitted as a function of exposure of *p*-xylene to the Si(100) in Method 1, 2 and 3.

It is of interest to note that Equation A.14 for the second-order kinetic has the same form as the thermodynamic equilibrium of Langmuir adsorption isotherm for the first-order adsorption. From Equations A.13 and A.14, the reaction order  $n$  and the rate constant  $k$  for hydrocarbon/Si(100) can be obtained by fitting the plot of  $\theta_A$  as a function  $A$ . As an example, Figure A-4 compares the fittings of AES data for coverage of *p*-xylene as a function of the *p*-xylene exposure to Si(100), in different methods. The features for all three methods are found to be close to first-order adsorption kinetics ( $n=1$ , molecular adsorption), but the rate constants obtained by Method 1 and 2 are lower than that by Method 3. Figure A-5 shows another example for the pyridine/Si(100) system where the adsorption appears to follow the second-order kinetics ( $n=2$ , dissociative adsorption) [3].

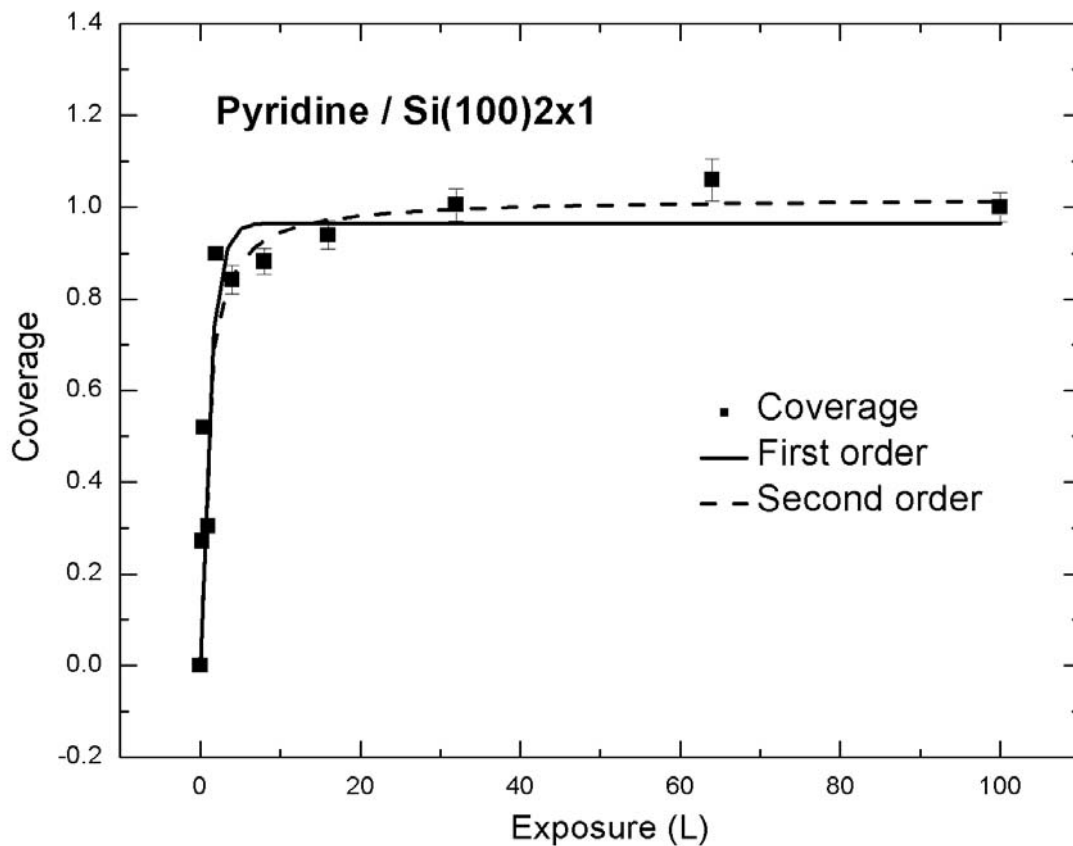


Figure A-5 Comparison of the fitting with first-order and that with second-order adsorption kinetics to the pyridine coverages (obtained from AES detection) as function of pyridine exposure to the Si(100) surface.



## **A.4 Summary**

In this appendix, theoretic and experiment research on the AES analysis of hydrocarbon/Si(100) is reported. The issues that may affect the measurement and estimation of adsorption coverage are discussed and a plausible calibration (in Method 3) to traditional methods (Method 1 and II) is developed and investigated in our experiments. In addition, a method to estimate kinetic parameters of hydrocarbon adsorption with AES is also developed and has shown results which have well compensated our TDS studies as discussed in Chapter 3 to 6.

The Method 3 could also be extended in the area of depth-profile study in surface science and materials science.

## A.5 Reference

- [1] Y. Taguchi, M. Fujisawa, T. Takaoka, T. Okada, M. Nishijima, *J. Chem. Phys.* 95 (1991) 6870.
- [2] Q. Li, K.T. Leung, *Surf. Sci.* 479 (2001) 69.
- [3] Q. Li, K.T. Leung, *Surf. Sci.* 541 (2003) 111.
- [4] D. Briggs, M.P. Seah, ed., *Practical Surface Analysis* (2<sup>nd</sup> edition) Vol. 1 "Auger and X-ray Photoelectron Spectroscopy", John Wiley & Sons, Wiley, 1990.

## Appendix B

### Wepil\_TDS - A self-developed software for TDS

In this appendix, the software Wepil\_TDS is briefly described for both the users and future developers.

#### B.1 Comments for future developers

Wepil\_TDS is composed of three parts: a graphical user interface (GUI) environment working on a host personal computer (PC), a communication interface between the PC and the mass spectrometer, and an interface between the host PC and a digital signal processing (DSP) unit that is used to control the sample temperature by manipulating the on-off distribution of the AC current passing through the Si sample.

#### B.2 Communication with the mass spectrometer

The controller of the VG quadrupole mass spectrometer (QMS) is based on an Intel 80286 operating system (OS), and can be remotely controlled by the host PC to set the QMS parameters and to acquire data when the OS is working in the MODE III option. The communication between the mass spectrometer and the PC can be conducted at 9600 baud over a distance of up to 30 m and the communication protocol is referred to as VG CP (VG Communications Protocol). All the dialogues are working in a one-way command-response mode in which the host computer always initiates dialogue by sending a command while the mass spectrometer replies with a response. All the communication signals are transferred through a RS232 serial port with VG CP script written in the text mode. The details of VG CP can be found in the *SXP ELITE OPERATOR MANUAL*. All the programming functions for the VG CP interface are written in Boland C++ 3.1, which are included in the module “MOD3.CPP”.

### **B.2.1 Temperature Control Module**

The temperature of the Si sample is controlled by a home-built DSP unit based on the TMS320c50 microprocessor [1]. The command shell that interfaces to both the AC power supply and the host PC is written in TMS320c50 Assembly language, and the proportional-integral-differential (PID) control algorithm [2] used for direct heating is written in ANSI-C (in module DSPTPD.C) and compiled into the TMS320 system codes. After resetting DSP, all the TMS320c50 codes are transferred from the host PC to the DSP through a RS232 serial port in binary mode (see the module “LOAD”).

The temperature is obtained from a thermocouple voltage readout, which is digitized by an analog-to-digital (A/D) converter (PA-ST12 AD-DA manufactured by Acqutek Corporation, Inc.) plugged in an ISA slot of the host PC motherboard. All the interface functions for the AD-DA card are contained in the module “PA-ST12”, which is also used in another software for our AES system.

### **B.2.2 Graphic User Interface (GUI) for TDS**

The GUI module (“TDS”) is written in Borland C++ 3.1, and is designed to draw windows, menus, input/output box, and data plots and to respond to different user operations through the mouse and keyboard. The GUI module is located at the highest level in the hierarchy of Wepil\_TDS (Figure B-1), which thus receives the user commands that are classified and administrated in the module “UTILITIES” of a sub-level. The module “UTILITIES” operates through the next set of modules “LOAD”, “MOD III” and “PA-ST”. Both modules “LOAD” and “MOD III” are used to communicate with the DSP and QMS respectively through the interface “COMDSP”. “DSP” and “PA-ST” are also connected to the thermal components of the experiment.

## **B.3 User manual**

Wepil\_TDS can work in both DOS and Windows 9X operation systems. Before running the software, the SXP ELITE should be checked to assure that it is working properly and has

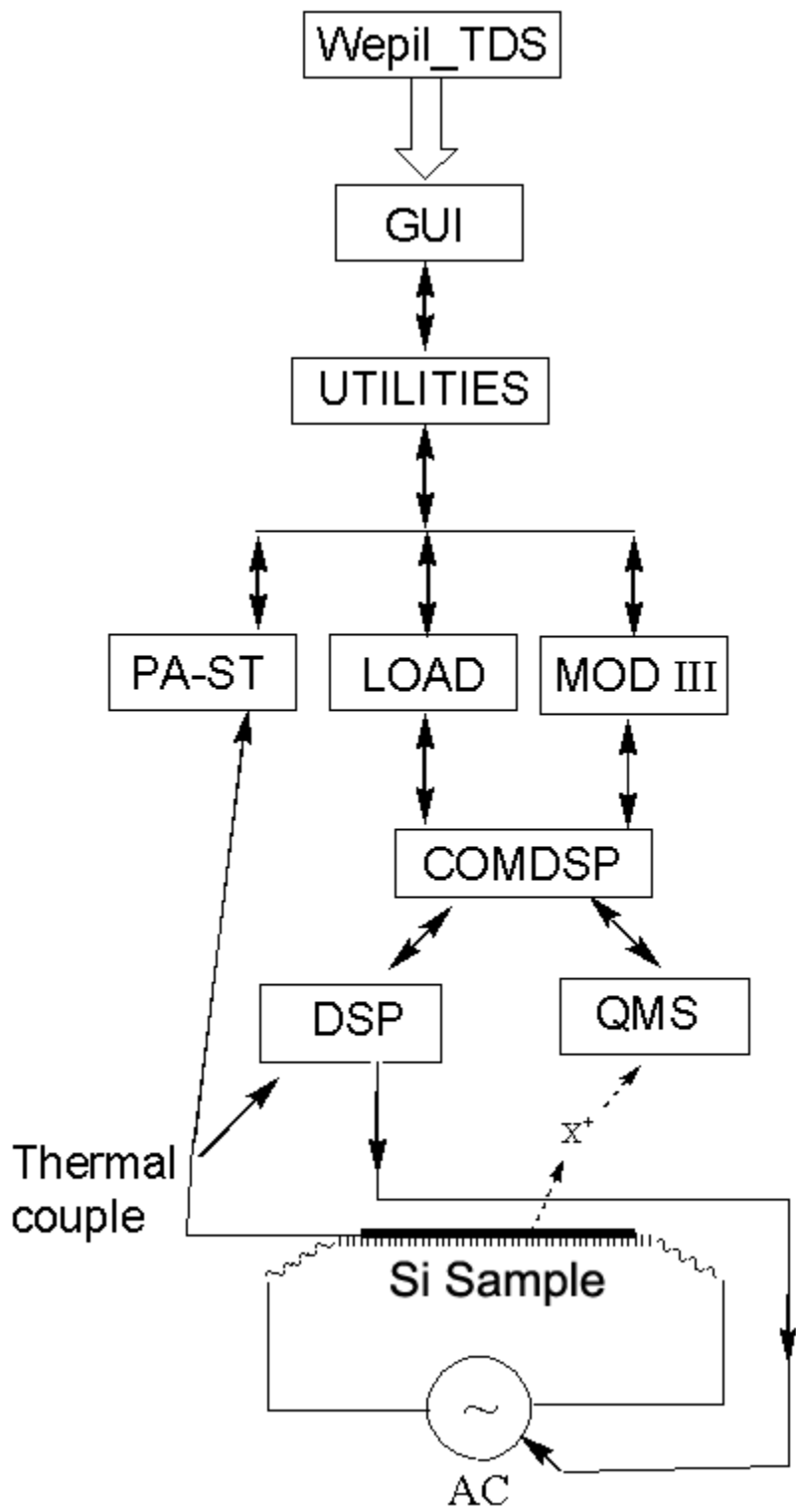


Figure B-1 Schematic hierarchy of the Wepil\_TDS.

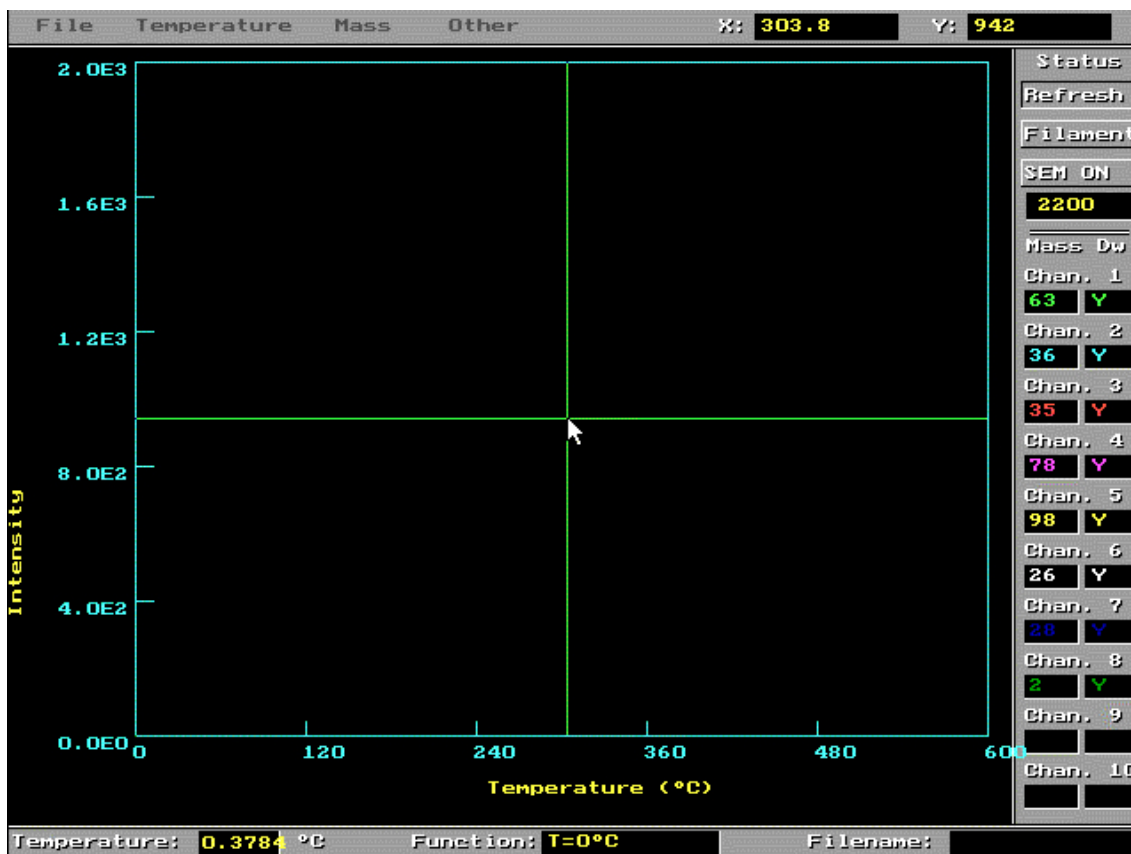


Figure B-2 Wepil\_TDS work window .

been switched to the Mode III option. The power of the DSP is set ON, and the switch on the front panel of the AC heater power supply should be set from “Manual” to “Auto” while the other switch on the right should be set to “Reset”. At the DOS command prompt or in the pop-up windows (after selecting the “Run” command from the “Start” menu in the Windows), type

*Wepil\_TDS [recipe filename] [data filename]<Return>*

where *Wepil\_TDS* is the DOS command. The [recipe filename] represents the recipe file of the multi-mass-channels, in which the recipe format is defined in the *SXP ELITE OPERATOR MANUAL*. The [data filename] gives the output file in text format with a data header followed by the thermal desorption spectra table. The TDS work window should appear (Figure B-2). The right side of the window lists the available command buttons and mass channels (in different colors) to be detected in the experiment. The horizontal

coordinate gives the temperature, and the vertical coordinate shows the intensity that can be scaled up or down by clicking the <PageUp> and <PageDown> buttons on the keyboard. The status bar at the bottom shows the present temperature value and temperature ramping function, which can be configured in the “TPD.cfg” file.

To transfer the TMS320C50 codes to the DSP unit, select the command <Load coff to DSP> in the menu “Temperature” (which could also be reached by pushing <L> on the keyboard as the menu shows up, or by pushing the shortcut key <F9> anywhere at any time). In about 10 seconds, a message “coff loaded successfully” should pop up. Clicking any key will close the pop-up window. The switch on the front panel of the AC-heater power supply should now be set from “Reset” to “Auto”. In the <Mass> menu, select the command <Run> (or press <L> key in menu, or shortcut key <F2>). This will start the TDS experiment and the intensity signals for the pre-selected masses are plotted in different colors against the increasing temperature. When the temperature reaches the preset endpoint, the TDS program will stop and the data will be automatically saved. The experiment can also be paused or terminated manually at any time by pressing any key during the TDS run.

The data file can be directly reviewed in any text or spreadsheet editor, such as MS Notepad or Excel. The data file has a standard format as shown in the following example (Figure B-3), which includes a data header that gives the name of the job, the date and time, the number of the mass channels, the mass of each channel and the number of sampling points. If the data table is to be analyzed in Origin or Sigma Plot, it should be imported after skipping the first eight lines.

The DSP unit was built by Mr. Xiang He. The subroutines are modified from the program originally written by Dr. Hui Yu for another surface science chamber employing a different mass spectrometer. Everything else has been developed by myself. The source codes of the Wepil\_TDS software, including a package of C/C++ programs of about 6000 lines and the TMS320 Assembly programs of ~1000 lines are provided upon request.

*p-xylene-d10, 10/29/2001, 21:06*

*enabled mass channels 8*

*mass1 mass2 mass3 mass4 mass5 mass6 mass7 mass8*

*116au 98au 82au 30au 28au 26au 4au 2au*

*Sample Points 268*

*TPD data:*

<i>Time(s)</i>	<i>Temperature(oC)</i>	<i>116 amu</i>	<i>98 amu</i>	<i>82 amu.....</i>
----------------	------------------------	----------------	---------------	--------------------

<i>0.054945</i>	<i>21.538263</i>	<i>0</i>	<i>1</i>	<i>0 .....</i>
-----------------	------------------	----------	----------	----------------

<i>1.373626</i>	<i>21.564837</i>	<i>0</i>	<i>0</i>	<i>0 .....</i>
-----------------	------------------	----------	----------	----------------

*.....*

Figure B-3 An example of the output data file from Wepil\_TDS.



## **B.4 References**

- [1] “Texas Instruments TMS320C5X DSP Starter Kit User’s Guide”, Microprocessor Development Systems, Texas Instruments Inc., 1994, U.S.A.
- [2] K.J. Astrom and T.Hagglund, “Automatic Tuning of PID controllers”, Instrument society of America, 1988.

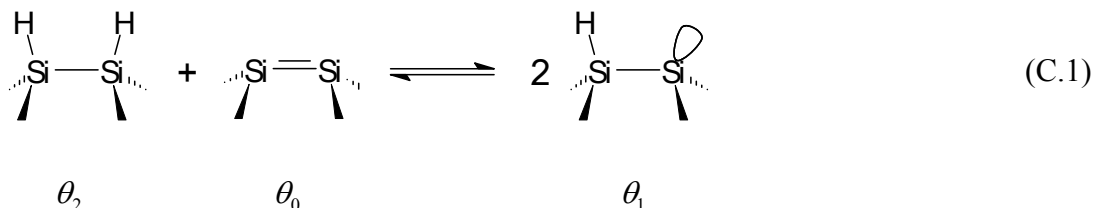


## Appendix C

### Derivation of the equilibrium equation for surface adspecies

#### C.1 Problem

In Chapter 6 (Section 6.2), the equilibrium constant for the reaction



is given by

$$K = \frac{n_1^2}{n_0 \cdot n_2} = \frac{\theta_1^2}{\theta_0 \cdot \theta_2} = 4x \tag{C.2}$$

In this Appendix, we will give details of the derivation used for Equation C.2.

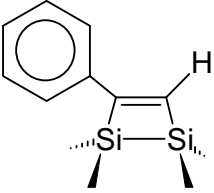
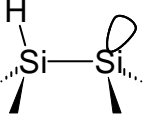
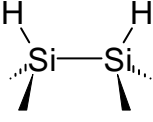
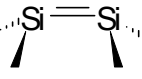
#### C.2 Solution

Consider a surface with  $N_0$  Si dimer sites on the Si(100)2×1 surface, each of which can only be one of the following four surface phases: the dimer occupied by dehydrogenated hydrocarbon adsorbate, un-occupied dimer (UOD), singly occupied dimer (SOD) and doubly occupied dimer (DOD) (Table C-1). The numbers of each species are  $n_a$ ,  $n_0$ ,  $n_1$  and  $n_2$ , respectively; and their corresponding surface coverages<sup>1</sup> are  $\theta_a$ ,  $\theta_0$ ,  $\theta_1$  and  $\theta_2$ ,<sup>2</sup> respectively. Suppose  $2M$  ( $=n_1+2n_2$ ) hydrogen atoms (with coverage of  $\theta_H$ ) are chemisorbed on the surface, and the number of total dimer sites (with the coverage of  $\theta_H$ ) that available for H

<sup>1</sup> The surface coverage of the adsorption A is defined as  $\theta = n_A/N_0$ , where  $n_A$  is the number of surface sites occupied by adsorbate and  $N_0$  is the total number of substrate adsorption sites.

<sup>2</sup> The number in the subscript gives the number of atoms in each species.

Table C-1: Distribution of the adspecies

Dehydrogenated adsorbate	Singly occupied dimer (SOD)	Doubly occupied dimer (DOD)	Un-occupied dimer (UOD)
			
$n_a, \theta_a$	$n_1, \theta_1$	$n_2, \theta_2$	$n_0, \theta_0$

chemisorption is  $N$  ( $M < N$ ). The following relations apply:

$$\theta = \frac{N}{N_0} = \frac{n_0 + n_1 + n_2}{N_0} = \theta_0 + \theta_1 + \theta_2 \quad (\text{C.3})$$

$$\theta_H = \frac{2M}{2N_0} = \frac{n_1 + 2n_2}{2N_0} = \frac{\theta_1}{2} + \theta_2 \quad (\text{C.4})$$

where  $N_0 = n_a + n_0 + n_1 + n_2 = n_a + N$ , or  $\theta_a + \theta = 1$ .

According to the simple lattice gas model proposed by D'Evelyn *et al.* [1], all the  $2M$  H atoms reside on  $M$  dimer sites in the (degenerate) ground state of the system. If  $\varepsilon$  is the energy required to form two SOD's in Equation C.1, then for  $m$  such excitations in the system

$$\begin{aligned} n_1 &= 2m, \\ n_2 &= M - m, \\ n_0 &= N - M - m \end{aligned} \quad (\text{C.5})$$

The equilibrium ratio between SOD and DOD can be calculated trivially using Equation C.5 from the equilibrium number of excitation  $m$ . Since the dimers are assumed to be non-interacting in the lattice gas model, the partition function  $Q$  for a given  $m$  can be written as

$$Q = \frac{N!}{n_0!n_1!n_2!} 2^{n_1} e^{-m\epsilon/kT} \quad (\text{C.6})$$

The  $2^{n_1}$  factor represents the degeneracy of the SOD arrangement. A good estimate of  $m$  in equilibrium would be the value of  $\langle m \rangle$  that gives the largest  $Q$  in Equation C.6. For large  $N$ , the equilibrium value of  $m$  can be approximated by determining the maximum  $Q$ , i.e. by setting the derivative of the  $\ln[Q(m)]$  to 0:

$$\frac{d}{dm} \ln(Q) = \frac{d}{dm} [\ln(N!) - \ln(n_0!) - \ln(n_1!) - \ln(n_2!) + n_1 \ln 2 + m \ln x] \quad (\text{C.7})$$

where  $x=e^{-\epsilon/kT}$ . Equation C.5 can then be simplified with Stirling's approximation [2] ( $\ln(X!) = X \ln X - X$  for any  $X$ ) as shown in the following steps:

$$0 = \ln(N - M - m) - 2 \ln(2m) + \ln(M - m) + 2 \ln 2 + \ln x ,$$

$$\ln\left(\frac{(2m)^2}{(N - M - m) \cdot (M - m)}\right) = \ln\left(\frac{n_1^2}{n_0 \cdot n_2}\right) = \ln(4x)$$

The equilibrium constant  $K$  is therefore given by

$$K = \frac{n_1^2}{n_0 \cdot n_2} = \frac{\theta_1^2}{\theta_0 \cdot \theta_2} = 4x \quad (\text{C.2})$$

### C.3 Reference

- [1] M.P. D'Evelyn, Y.L. Yang, L.F. Sutcu, J. Chem. Phys. 96 (1992) 852.
- [2] W. Feller, "An Introduction to Probability Theory and Its Applications", Vol. 1, 3rd ed. New York: Wiley, (1968).